Utah State University

DigitalCommons@USU

All Graduate Theses and Dissertations | Graduate Studies

5-2002

The Role of Bandgap in the Secondary Electron Emission of Small Bandgap Semiconductors: Studies of Graphitic Carbon

Neal E. Nickles
Utah State University

Follow this and additional works at: https://digitalcommons.usu.edu/etd

 Part of the Physics Commons

Recommended Citation

Nickles, Neal E., "The Role of Bandgap in the Secondary Electron Emission of Small Bandgap Semiconductors: Studies of Graphitic Carbon" (2002). *All Graduate Theses and Dissertations*. 1696.
https://digitalcommons.usu.edu/etd/1696

This Dissertation is brought to you for free and open access by the Graduate Studies at DigitalCommons@USU. It has been accepted for inclusion in All Graduate Theses and Dissertations by an authorized administrator of DigitalCommons@USU. For more information, please contact digitalcommons@usu.edu.



THE ROLE OF BANDGAP IN THE SECONDARY ELECTRON EMISSION OF SMALL BANDGAP SEMICONDUCTORS: STUDIES OF GRAPHITIC CARBON

by

Neal E. Nickles

A dissertation submitted in partial fulfillment
of the requirements for the degree

of

DOCTOR OF PHILOSOPHY

in

Physics

Approved:

_____	_____
J.R. Dennison Major Professor	D. Mark Riffe Committee Member
_____	_____
David Peak Committee Member	David Farrelly Committee Member
_____	_____
Tsung-Cheng Shen Committee Member	Thomas Kent Dean of Graduate Studies

UTAH STATE UNIVERSITY
Logan, Utah

2002

Copyright © Neal Nickles 2002

All Rights Reserved

ABSTRACT

The Role of Bandgap in the Secondary Electron Emission of

Small Bandgap Semiconductors: Studies of Graphitic Carbon

by

Neal E. Nickles, Doctor of Philosophy

Utah State University, 2002

Major Professor: Dr. J.R. Dennison
Department: Physics

The question of whether the small bandgaps of semiconductors play a significant role in their secondary electron emission properties is investigated by studying evaporated graphitic amorphous carbon, which has a roughly 0.5 eV bandgap, in comparison with microcrystalline graphite, which has zero bandgap. The graphitic amorphous carbon is found to have a 30% increase in its maximum secondary electron yield over that of two microcrystalline graphite samples with comparable secondary electron yields: highly oriented pyrolytic graphite and colloidal graphite. The potentially confounding influence of the vacuum level has been isolated through the measurement of the photoelectron onset energy of the materials. Other less significant materials parameters are also isolated and discussed. Based on these measurements, it is concluded the magnitude of bandgap may have an appreciable

effect on the magnitude of the secondary electron yield and further studies of this effect with annealed graphitic amorphous carbon are warranted.

In support of this work, a hemispherical two-grid, retarding field electron energy analyzer has been designed, constructed, and characterized for the present work. The advantages and disadvantages of the analyzer are discussed in comparison to other methods of measuring secondary electron emission. The analyzer has a resolution of ±(1.5 eV + 4% of the incident electron energy). A novel effort to derive theoretical, absolute correction factors that compensate for electron losses within the analyzer, mainly due to the grid transmission, is presented. The corrected secondary electron yield of polycrystalline gold is found to be 30% above comparable experimental studies. The corrected backscattered electron yield of polycrystalline gold is found to be 14% above comparable experimental studies. Corrected secondary yields for the microcrystalline graphite samples are found to range from 35-70% above those found in five experimental studies in the literature. The theoretical correction factors are estimated to have a 4-6% uncertainty. Reasons for the large discrepancy in yield measurements with the analyzer are discussed and thought to be due mainly to the lack of similar corrective factors in the previous studies. The supporting instrumentation is fully characterized, including a detailed error analysis.

(251 pages)

DEDICATION

For my father, John Nickles, without whom I would not have my drive for education, and my wife, Robin, without whom there would be nothing.

ACKNOWLEDGMENTS

Funding for this dissertation was provided by several sources: the vacuum chamber and analytical system were funded by the Air Force Office of Scientific Research; the overall funding for the surface science group was provided by the Space Environments and Effects branch of NASA; and a fellowship for my research was generously provided by the Rocky Mountain Space Grant Consortium of NASA.

I would especially like to thank my major professor, J.R. Dennison, for his guidance during the completion of this dissertation. His patient support and teaching, through broken equipment and severely exceeded deadlines, made the present work possible.

I also cannot begin to thank my wife for her personal sacrifices that have allowed me to pursue my education and for her support, especially towards the end when the situation was particularly dire. Her family, especially Bruce and Sandy Wolf, have treated me as one of their own and I will be eternally grateful. My own family has consistently provided me with unquestioned confidence in my abilities.

I would like to thank my lab mates who have assisted with many aspects of my research: Wen-Yen Chang, Robert Davies, Jason Kite, Clint Thomson, Parker Judd, Kendall Ford, Spencer Nielson, and Trevor Willey. Wen-Yen Chang deserves special acknowledgment for the many hours we spent together diagnosing all the instrumentation problems we faced. We conducted some excellent research in the

process of having a hell of a good time. Jason Kite also provided valuable support in helping to create the schematics and electron beam models in this dissertation.

My friends helped me almost keep my sanity over the years. Many raised glasses go out to the Synder-Kurtzman clan, Chuck and Joslin Werstak, Balraj Menon, Teresea Burns, and the many other friends with whom I shared all the good times.

I would like to thank Dr. Mark Riffe for his routine five-minute conversations that often came through with crucial insight, or at least much needed levity, for the work of the day. Thanks also to the supporting staff of the Physics Department, especially Donna and Deborah for pulling all those strings.

In the end, I did little more than fulfill the expectations these people saw for me. Thank you for believing in me.

Neal Nickles

CONTENTS

Page

ABSTRACT iii

DEDICATION v

ACKNOWLEDGMENTS vi

LIST OF TABLES xi

LIST OF FIGURES xii

CHAPTER

1. INTRODUCTION 1

2. BACKGROUND 5

Section A. Secondary Electron Emission 5
Section B. Bandgap and Secondary Electron Emission 13
Section C. Literature on the Secondary Electron Emission of Carbon 25

3. INSTRUMENTATION 33

Section A. Vacuum Chamber 33
Section B. Ancillary Systems 37
Section C. Sample Stage 39

Subsection 1. Modules 42
Subsection 2. Motion and alignment 47

Section D. Source Beams 49

Subsection 1. Conrad gun 50
Subsection 2. HEED gun 56
Subsection 3. Light sources 58

Section E. Hemispherical Retarding Field Energy Analyzer 59

Subsection 1. Design and construction..... 60
Subsection 2. Testing and characterization 66

Section F. Data Acquisition System 74

4. EXPERIMENTAL METHOD 84

Section A. Measurement Technique 84
Section B. Error Analysis 92

5. EXPERIMENTAL DATA 112

Section A. Sample Preparation and Characterization 112

Subsection 1. Gold 115
Subsection 2. Highly oriented pyrolytic graphite..... 116
Subsection 3. Collodial graphite..... 119
Subsection 4. Evaporated graphitic amorphous carbon..... 121
Subsection 5. Annealing of the g-C sample..... 122

Section B. Yield Measurements..... 124

Subsection 1. HOPG..... 125
Subsection 2. Aquadag™..... 128
Subsection 3. g-C 128

6. DISCUSSION OF RESULTS..... 131

Section A. SE Yield Data 131

Subsection 1. Low energy section of SE yield data..... 138
Subsection 2. High energy section of SE yield data 148

Section B. BSE Yield Data 150

7. CONCLUSIONS 153

Section A. Conclusions about the Experimental Results..... 153
Section B. Conclusions about the Experimental Apparatus and Methods..... 155
Section C. Suggested Modifications to Experimental System..... 156
Section D. Suggestions for Future Research..... 162

REFERENCES 169

APPENDICES 176

Appendix A. Vacuum Chamber Details 177
Appendix B. Faraday Cup Tests 185
Appendix C. Theoretical Calculation of Systematic Corrections for SE and BSE Yields..... 190
Appendix D. LabView Virtual Instrument Program..... 216
Appendix E. Permissions..... 231

CURRICULUM VITAE 235

LIST OF TABLES

Table		Page
2.1	Summary of experimental data on graphitic carbons	32
3.1	Summary of source beams	50
3.2	Error in current signals from linear fit to standard deviations	82
6.1	Young model fitting parameters for SE yields	133
6.2	Sternglass model fitting parameters for SE yields	133
6.3	Variable stopping power exponent model fitting parameters for SE yields	133
6.4	Summary of important material properties of graphitic carbon samples	141
A.1	Lower level port descriptions of UHV chamber	179

LIST OF FIGURES

Figure		Page
2.1	Total, SE, and BSE yield for polycrystalline gold sample.....	6
2.2	Energy band diagram for a typical insulator.....	16
2.3	Energy band diagram for a typical semiconductor.....	17
2.4	Graph of the mean free path as a function of bandgap.....	19
2.5	Graph of the maximum SE yield as a function of bandgap.....	20
2.6	Maximum SE yield as a function of calculated mean free path.....	21
3.1	Experimental UHV chamber.....	34
3.2	Lower level of UHV chamber.....	35
3.3	Calculated graph of beam current and diameter.....	38
3.4	Top and side view of sample stage.....	40
3.5	Sample stage with top plate removed.....	42
3.6	Empty 1-cm cavity sample module.....	43
3.7	Assembly drawing of 1-cm cavity OFHC copper sample module.....	44
3.8	Assembly drawing of 0.75-inch cavity OFHC copper sample module...	45
3.9	Assembly drawing of Faraday cup and tertiary aperture inside a sample module.....	46
3.10	Drawing of Conrad gun and lens column.....	51
3.11	Conrad gun power supply schematic.....	52
3.12	Conrad gun beam profiles.....	54

3.13	SimIon model of Conrad gun beam column.....	55
3.14	Beam spot of HEED gun.....	57
3.15	Cross section of HGRFA interfacing with sample stage.....	62
3.16	A preliminary version of the HGRFA and sample stage.....	65
3.17	The completed hemispherical grid retarding field analyzer.....	66
3.18	Schematic of HGRFA in UHV chamber.....	67
3.19	Normalized collector current versus suppression grid voltage bias curves.....	69
3.20	SE energy distribution of HOPG sample used for estimate of resolution of HGRFA.....	73
3.21	BSE peak of polycrystalline gold.....	74
3.22	Patch panel circuitry schematic.....	76
3.23	HGRFA circuitry schematic.....	79
4.1	A typical energy distribution of all the emitted electrons.....	90
4.2	Repeated measurement of gold sample.....	94
4.3	Beam current as a function of beam energy	98
4.4	Second-order corrections to the yields	102
4.5	Higher order corrections to the BSE yield	104
4.6	Comparison of corrected BSE yield of gold with result from literature..	107
4.7	Comparison of corrected SE yield of gold with result from literature.....	109
5.1	RGA spectra showing the partial pressure of gas inside the UHV chamber.....	114

5.2 Auger electron spectra of polycrystalline gold..... 116

5.3 Optical microscope pictures of HOPG, g-C, and colloidal graphite samples..... 117

5.4 Auger electron spectrum of HOPG sample 118

5.5 Auger electron spectrum of Aquadag™ sample..... 120

5.6 Auger electron spectrum of g-C sample 122

5.7 Optical microscope image of g-C..... 124

5.8 Linear plot of SE and BSE yield of HOPG sample..... 125

5.9 SE yield of HOPG 126

5.10 BSE yield of HOPG 127

5.11 SE yield of Aquadag™ 128

5.12 BSE yield of Aquadag™ 129

5.13 SE yield of g-C 130

5.14 BSE yield of g-C 130

6.1 Semi-log plots of HOPG, g-C, and Aquadag™ SE yields along with semiempirical fits using the Young model 132

6.2 Semi-log plost of HOPG, g-C, and Aquadag™ SE yields along with semiempirical fits using the Sternglass model 134

6.3 Semi-log plots of HOPG, g-C, and Aquadag™ SE yields along with semiempirical fits using the variable stopping power exponent model.. 135

6.4 Linear plot of low energy section of HOPG, g-C, and Aquadag™ SE yields along with semiempirical fits using the variable stopping power exponent model 139

6.5 Photoyield measurements of the HOPG, Aquadag™, and g-C samples.. 145

6.6 Linear plot of high-energy section of HOPG, g-C, and Aquadag™ SE yields along with semiempirical fits using the variable stopping power exponent model 149

6.7 Semi-log plot of HOPG, g-C, and Aquadag™ BSE yields 151

A.1 Magnetic field measurements along z-axis of UHV chamber near HEED gun focal point 181

A.2 Magnetic field measurements along z-axis of UHV chamber near the turbomolecular pump flange 182

A.3 Magnetic field measurements in UHV chamber at the HEED gun focal point 183

A.4 Magnetic field measurements in UHV chamber near the CMA focal point..... 184

B.1 Percentage efficiency of the HEED gun as measured by the module FC and the FatMan FC as a function of positive voltage bias..... 187

D.1 Front panel of the LabView VI 217

D.2 False and true cases of the meter calibration button..... 218

D.3 Monitoring the Faraday cup current before the yield measurements..... 220

D.4 Recording the Faraday cup current..... 222

D.5 Monitoring the collector and sample currents..... 223

D.6 Setting the suppression grid voltage bias..... 224

D.7 Measurement of the collector and other currents during the collection mode 225

D.8 Data analysis and file writing procedures 228

D.9 Data analysis to determine the total, SE, and BSE yields..... 229

CHAPTER 1

INTRODUCTION

Secondary electron (SE) emission is the emission of low energy electrons from a material by an incident electron beam. SE emission in large bandgap insulators is qualitatively understood, but theoretical knowledge about SE emission in semiconductors with small bandgaps is currently lacking (Iwase and Nakamura, 1997). The central question of this dissertation is whether the bandgap in these semiconductors influences SE emission in a manner similar to insulators or whether the bandgap is below a certain threshold energy needed to impact the SE emission, making the semiconductors essentially behave like metals. The distinct class of semiconductor between insulators and metals is not definitively maintained from the point of view of SE emission. Previous work has tried to infer the role of bandgap in SE emission by looking for trends in various materials with a wide range of bandgaps (Grais and Bastawros, 1982); however, SE emission depends on numerous material parameters, such as atomic number and escape or absorption coefficients (Dionne, 1975), which makes this type of investigation difficult. Current theoretical understanding of this problem is reviewed in more detail in Chapter 2.

The allotropes of carbon offer a means of addressing this central question, while minimizing confounding results due to additional material properties. Graphitic carbons are of particular interest for this study because the SE emission properties of diamond and diamond-like carbons have a large variance due to hydrogen termination

(Shih *et al.*, 1997), an additional material property, which is difficult to control and would confound results as the effects of hydrogen termination are presently not well understood. Specifically, evaporated graphitic amorphous carbon has a small bandgap, but otherwise has similar material properties to microcrystalline graphites that have nearly zero bandgap. The goal of the present work is to measure the SE emission properties of these two types of graphitic carbons and discover whether the small bandgap plays a role in SE emission through comparison. Graphitic amorphous carbon also is advantageous because the amorphous structure can be thermally annealed, causing a gradual structural change towards nanocrystalline graphite with a related reduction in bandgap (Robertson, 1986; Dallas, 1996; Dennison *et al.*, 1996). This control of the bandgap by thermal annealing makes a parametric study of bandgap possible. Attempts to anneal the amorphous carbon failed in the present study, but suggestions that may make future work possible are summarized in Chapter 7.

The motivation for the present work is mainly scientific, but there are related fields of interest. Applications that exploit the SE emission of a material are typically interested in either the highest or lowest yields possible. Graphitic carbons are currently the material of choice when low SE emission is desired and much of the seminal work in this field is reviewed in Chapter 2 for the present study. In contrast, diamond has been of very recent scientific interest because doping and hydrogen termination have been shown to result in extremely high SE emission (Shih *et al.*,

1997). Although small bandgap semiconductors typically have intermediate SE emission properties, understanding the effect of bandgap will assist efforts to precisely control their SE emission properties through doping or the introduction of defect states within the bandgap (Iwase and Nakamura, 1997).

Applications for semiconductors themselves, mainly the manufacturing of integrated circuits, use SE emission as a tool for characterizing morphology and dopant profiles with scanning electron microscopy (Castell *et al.*, 1999; Phillips *et al.*, 1999). Integrated circuits are not bombarded by electrons in their daily operation, but understanding the influence of bandgap will contribute to the interpretation of scanning electron microscope images, which is the main analytical tool of the semiconductor industry.

Another field of renewed interest in SE emission is in modeling the potential adopted by spacecraft surfaces in reaction to an incident flux of electrons from the Earth's plasma (Hastings and Garret, 1996). NASA's current model for spacecraft charging underpredicts the potentials seen on satellites in geosynchronous orbit. The poor database of SEE material parameters used by NASCAP is believed to be a significant contribution to this problem (Chang *et al.*, 1998). The SEE properties of evaporated carbon materials may be particularly important in spacecraft charging, since spacecraft surfaces often become contaminated with some form of disordered carbon in space (Davies and Dennison, 1997; Chang *et al.*, 2000).

The dissertation is organized in a standard manner. Chapter 2 will provide the

requisite background knowledge of SE emission and the current understanding of the role of bandgap in insulators and small bandgap semiconductors. Experimental work on graphitic carbon materials in the literature is also fully reviewed. Chapter 3 on instrumentation and Chapter 4 on experimental methods are relatively detailed due to the significant amount of effort in that area. The chapters attempt to document the first generation of the vacuum chamber, its supporting analytical systems, and the specific experimental apparatus and methodology that were designed, constructed, and tested for the present study. Chapter 4 also contains a detailed analysis of the random and absolute errors involved with the SE emission measurements. Before the experimental data is presented in Chapter 5, the three graphitic carbon samples are described and their preparation and characterization is discussed. In Chapter 6, the experimental data is compared with theoretical model functions from Chapter 2 and the results are discussed. The concluding Chapter 7 summarizes the significance of the experimental results, along with an evaluation of the performance of the instrumentation and suggestions for improvements. The dissertation is concluded with suggestions for future research with evaporated graphitic amorphous carbon for the study of the role of bandgap in the SE emission properties of small bandgap semiconductors.

CHAPTER 2

BACKGROUND

The following sections provide background information about secondary electron emission and the role of bandgap in the process. The chapter concludes with a literature review of the secondary electron emission properties of carbon materials, specifically graphitic carbons.

Section A. Secondary Electron Emission

Secondary electron (SE) emission is the process by which electrons within a material are emitted as the result of incident electron or ion bombardment. The emitted electrons that were originally in the material, or "true" secondary electrons, cannot be distinguished from backscattered electrons (BSE) that were originally part of the incident beam; therefore, SE's are conventionally defined by their energy as emitted electrons with between 0-50 eV, while BSE have > 50 eV of energy. The division is a historical convention, but is supported by the fact that the SE energy distribution is sharply peaked below 10 eV and most BSE are nearly elastically scattered with energies close to the incident beam energy (Seiler, 1983). The average number of SE emitted per incident electron at a given energy is the SE yield δ of a material. Likewise, the BSE yield η is defined as the average number of BSE emitted per incident electron. The sum of these yields is the total yield σ of the material. Figure 2.1 shows a typical plot of the total, SE, and BSE yields as a function of

incident beam energy. The SE yield increases at low energies as more energy is imparted to the solid. The SE yield tails off at higher energies (which is not represented well in Figure 2.1) as the penetration of the higher energy incident beam begins to exceed the mean free path length of SE's trying to escape the material. The modest variation in the BSE yield with energy in Figure 2.1, particularly above a few 100 eV, is typical for most materials.

There are many reviews of SE emission in the literature, which follow the theoretical and experimental advances in SE emission studies. The most helpful review article for the present discussion is the compilation by Dekker (1958), in which he outlines the semiempirical theories used in this dissertation. Additional insight was provided by a brief summary by Dionne (1973).

The semiempirical models for SE emission begin from similar basic assumptions. The first assumption is that SE emission is a two-step process that is

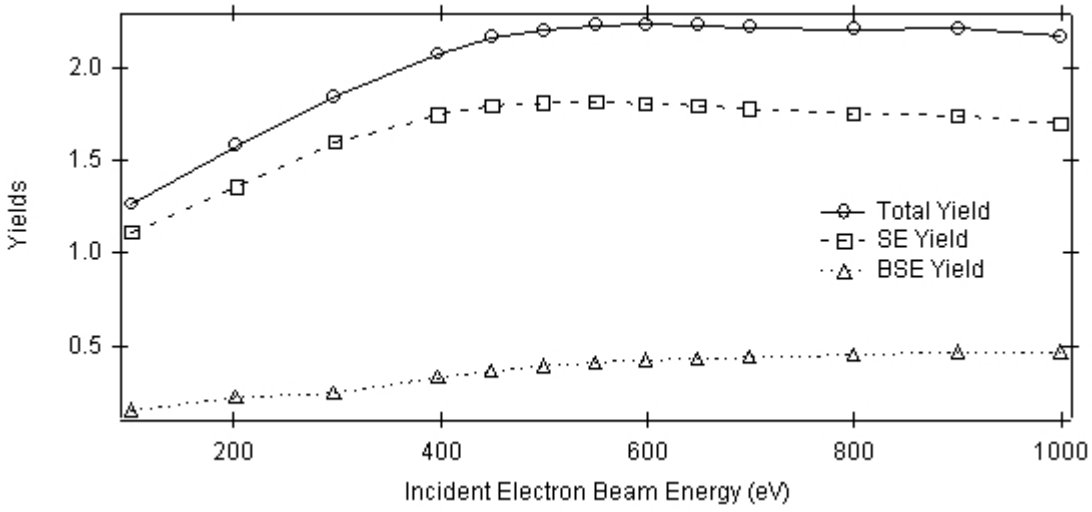


FIG. 2.1: Total, SE, and BSE yield for polycrystalline gold sample (see Subsection 5.A.1 for details of sample).

separable into the primary beam exciting a population of SE's within the material and then a diffusion process as the SE's propagate to the surface and escape the material. The combination of these two processes can be written in the form

$$\delta(E_o) = \int n(x, E_o) f(x) dx \tag{2.1}$$

where the function $n(x,E_o)$ is the average number of SE's excited by an incident beam of energy E_o in an infinitesimal layer of thickness dx a distance x below the surface and $f(x)$ is the probability of a SE reaching the surface from a distance x and being emitted. The number of SE's excited in an infinitesimal layer is related to the stopping power through $-\frac{1}{\varepsilon}\frac{dE}{dx}$, where ε is the average energy required to excite a SE within the material. The probability of a SE reaching the surface and escaping is related to an exponential absorption law $f(x) = B\exp(-\alpha x)$ because the process of SE migrating through the solid has a high scattering rate and is therefore assumed to be more closely related to diffusion. The exponential and its normalization factor B can be viewed as the product of two additionally separate terms, where the exponent governs the diffusion of SE's and the probability of escape over the surface barrier is related to the constant B (Dionne, 1973). This view leads to SE emission modeled as a three-step process with the addition of the escape probability. The result is that the SE yield depends inversely on ε and exponentially on the absorption coefficient α, which will be important in the discussion of bandgap and SE yield in Section 2.B. Inserting the

expressions for the number of SE produced and the probability of their escape, yields

$$\delta(E) = -\frac{B}{\varepsilon}\int \frac{dE}{dx}\exp(-\alpha x)dx. \tag{2.2}$$

The next step is to assume a form for the stopping power $\frac{dE}{dx}$, which is the distinguishing aspect between the semiempirical theories. There are two distinctive formulations considered here: the power law model and a formulation by Sternglass (1953a). The power law model assumes that the stopping power is inversely related to the energy, which results in more energy being deposited near the surface at lower incident beam energies. The exact relationship between energy and stopping power is left arbitrary by the inclusion of a variable exponent to give

$$\frac{dE}{dx} = -A\frac{1}{E^{n-1}}. \tag{2.3}$$

The stopping power coefficient *A* is characteristic of the material and presumably related to the absorption of the incident electrons' energy. The variable *n* will be referred to as the stopping power exponent. Eq. 2.3 can be integrated to give an expression for the energy imparted to the sample as the incident electron penetrates the sample up to a given depth:

$$E^n(x) = E_o^n - Anx. \tag{2.4}$$

The incident energy E_o is distinguished from the energy $E(x)$ at a given depth x. The maximum range of the electron beam's penetration R follows from the value of x in Eq. 2.4 that gives zero energy:

$$R = \frac{E_o^n}{An}. \tag{2.5}$$

The stopping power of Eq. 2.3 can be phrased in terms of the penetration depth R by substituting Eq. 2.5 into Eq. 2.4 and computing the appropriate derivative to yield

$$\frac{dE}{dx} = -A\left[An(R-x)\right]^{\left(\frac{1}{n}-1\right)}. \tag{2.7}$$

Substitution of Eq. 2.7 into Eq. 2.2 and a change of variable leads to a closed form solution. Baroody (1950) was the first to point out that when the SE yield and incident energy are both normalized by the maximum SE yield δ_{max} and energy at that maximum E_{max}, the SE yield data for a large number of materials follows a relatively universal curve. The practice has led to equations being phrased in terms of δ/δ_{max} and E/E_{max}, which are referred to as reduced yield curves. The energy corresponding to the maximum yield E_{max} is found by setting the derivative of the yield to zero and the maximum SE yield is defined by $\delta(E_{max})$. The reduced yield equation for the power law formulation takes the form

$$\delta(E) = \frac{B}{\varepsilon}\delta_{\max}\left(\frac{E_{\max}}{E}\right)^{n-1}\left\{1-\exp\left[-\alpha R\left(\frac{E}{E_{\max}}\right)^{n}\right]\right\} \tag{2.8}$$

where

$$\frac{B}{\varepsilon} = \frac{1}{1-\exp(-\alpha R)} \tag{2.9}$$

and

$$n = \frac{B}{\varepsilon}\left[\frac{B}{\varepsilon} - \alpha \operatorname{Re} xp(-\alpha R)\right]^{-1}. \tag{2.10}$$

The introduction of δ_{max} and E_{max} typically rids reduced yield equations of the five material constants introduced in Eq. 2.2 and 2.3 (A, B, α, R, and e), which is the main reason for the universal curve. Notice that for a given value of the stopping power exponent, the remaining parameters (B, α, R, and e) can be evaluated numerically. The value of n was widely debated during the formulation of these semi-empirical methods, but experimental work on the transmission of thin aluminum films by Young led to a value of n = 1.35 and is the generally accepted value for conducting materials (Dekker, 1958). Using Young's value for the stopping power exponent, Eqs. 2.8-10 reduce to

$$\delta(E) = 1.114\delta_{\max}\left(\frac{E_{\max}}{E}\right)^{0.35}\left\{1-\exp\left[-2.28\left(\frac{E}{E_{\max}}\right)^{1.35}\right]\right\}. \quad (2.11)$$

Eq. 2.11 will be referred to as the Young model for SE yield and will be used in Chapter 6 to fit the experimental data.

A single value for the stopping power exponent for all materials is inconsistent with the varying range of electrons in different materials, especially when semiconductors or even insulators are considered. A crude empirical formula by Feldman (1960) for the stopping power exponent has a weak dependence on atomic number:

$$n = \frac{1.2}{(1-0.29*\log_{10} Z)}. \quad (2.12)$$

Although Feldman's equation reduces the problem to the number of scattering particles, the idea of a variable stopping power exponent can be pursued in the present discussion by allowing an additional free parameter in Eqs. 2.8-10. Unfortunately, Eq. 2.10 does not have an inverse; however, the system of equations can be reduced to single variable, along with δ_{max} and E_{max}. After a fit is performed to experimental data, the stopping power exponent can be evaluated numerically. This method will be referred to as the variable stopping power exponent model, although there is no closed form solution.

Beginning again with Eq. 2.2, the thesis work of Sternglass led to his formulation of the SE yield that incorporates the interaction of the incident electrons with the electron shell structure of the sample atoms. Sternglass simplified the problem by assuming that the incident beam reaches a fairly sharply defined average depth λ_m or mean free path for the incident beam where all of the SE's are created. The integral of Eq. 2.2 with $n(E,x) \propto \delta(x-\lambda_m)$ is then a trivial expression for the total energy imparted into the sample at that depth:

$$\delta = \frac{B}{\varepsilon}(1-\eta k)E\exp(-\alpha\lambda_m). \tag{2.13}$$

The total energy E is reduced by the fraction of energy expended in producing BSE, which is given by the BSE's mean energy k and the BSE coefficient η. Careful examination of the dissertation work of Sternglass (1953a) reveals that he adds an additional overall factor to the front end of this model to correct for the effects of sample roughness. The contradictory and inappropriate uses of sample roughness to explain differences in SE yield curves will be considered in more detail during the discussion of the experimental data in Chapter 6.

The relation of the depth λ_m to the incident energy is derived from the Bethe expression for the stopping power, which includes the electronic shell structure of the atom. Sternglass makes several simplifying assumptions and approximations to show $\lambda_m \propto \sqrt{E}$. Assuming the parameters in Eq. 2.8 (B, e, η, α, and k) are constants of the

material, the equation can be put in a reduced yield as follows:

$$\delta = \delta_{max} \frac{E}{E_{max}} \exp\left[2\left(1 - \frac{E}{E_{max}}\right)\right] \tag{2.14}$$

Notice this reduced yield equation has eliminated the additional materials parameters with the introduction of reduced yield variables. Eq. 2.14 will be referred to as the Sternglass model and will be used in Chapter 6 to fit experimental data.

Section B. Bandgap and SEE

The literature dealing with the study of bandgap on SE emission is very limited (Iwase and Nakamura, 1997). The vast majority of the quantitative theoretical work in the field of SE emission has been done with free electron metals. The classical semiempirical theories have been the area where bandgap has been introduced in the explanation of the SE emission of insulators and semiconductors (Dionne, 1975; Grais and Bastawros, 1982). The more recent quantum mechanical formulations have been used to describe SE emission in metals, whose free electron assumptions make the problem somewhat tractable. The literature, which was found and will be discussed below, typically relies on the role of bandgap in SE emission to verify theoretical models or deduce other material parameters that are more difficult to measure, such as the escape probability B or absorption coeffiecent α.

For the purposes here, the two main quantities of interest have already been introduced in Eq. 2.2: (i) The average energy required to excite a secondary e and (ii)

the absorption coefficient α or equivalently the inverse mean free path (MFP) for electron scattering. In an article explaining the origins of many of the common parameters in SE emission, Dionne (1975) comments ϵ can be related to the sum of the bandgap and the electron affinity in insulators. This definition is in contrast to metals, where ϵ has been related to the work function or even the ionization potential of valence electrons in the gas phase (Sternglass, 1953a; Dionne, 1975). Although the definition for insulators is logical, notice the result in Eq. 2.2 is the SE yield then has an inverse dependence on the bandgap and electron affinity, which is contrary to experimental results that show insulators typically have much higher yields than metals (Seiler, 1983). The paradox is resolved by considering the influence of the bandgap on the absorption coefficient α or inverse MFP, which --as seen in Eq 2.2 -- has a stronger exponential relationship to the SE yield. Dionne (1975) explicitly admits the bandgap most likely controls the SE yield through its influence on the MFP rather than by determining the value of ϵ.

The MFP is influenced by the bandgap because the bandgap inhibits electron-electron scattering near the conduction band minimum. A SE is initially excited into the unoccupied energy states of the conduction band. An excited SE undergoes scattering with electrons in the valence and conduction bands, phonons due to the lattice, excitons, and plasmons from the collective behavior of the electrons. Of these mechanisms, electron scattering with the valence band dominates in most materials (Seiler, 1983). In semiconductors and insulators, the bandgap represents the minimum

energy with which a valence electron must be excited when inelastically scattering with an excited SE in the conduction band. An excited SE loses a minimum energy of the bandgap and the interacting valence electron is scattered into the conduction band, leaving behind a hole. Excited SE's in materials with a bandgap most often lose their energy through this electron-hole pair production. There has been research that supports the idea that the energy necessary to excite an electron-hole pair is three times the bandgap energy (Alig and Bloom, 1975). This minimum excitation energy for electrons in the valence band inhibits the electron-electron scattering by reducing the available states into which the valence electron can scatter. The necessity of crossing the bandgap results in a reduced probability for the interaction to take place, which translates into a longer MFP for excited SE in insulators.

The electron-electron scattering is further inhibited near the conduction band minimum. Through excited SE's losing energy and electron-hole pair production into the conduction band, the electron population in the conduction band begins to settle near the conduction band minimum. Figure 2.2 shows a qualitative energy-level diagram for an insulator with a large bandgap energy E_g in relation to the electron affinity χ. The bandgap E_g is defined as the energy needed to excite electrons at the top of the valence band to the conduction band minimum, while the electron affinity χ is the additional energy necessary for an electron to reach the vacuum level and escape the material. The vacuum level is the energy of an electron that is free from the material, typically referenced with respect to the Fermi level. The upper hatched

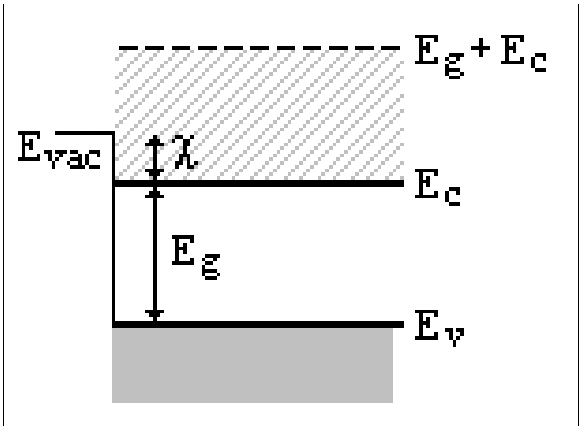


FIG. 2.2: Energy band diagram for typical insulator.

region of the diagram, between the conduction band minimum E_c and E_c+E_g, marks a region of energy were an excited SE is significantly affected by a decrease in the probability of exciting an electron-hole pair. Just below E_c+E_g, a SE cannot excite a valence electron to the conduction band minimum because the valence electron would need to scatter into the forbidden bandgap. The excited SE can still be involved in low energy scattering, typical of electron-phonon or impurity scattering, or must return to the conduction band with a single scattering event, which is more improbable due to the further reduction in possible states into which to scatter as mentioned above. The decreased probability of electron-electron scattering is demonstrated by the temperature dependence of SE yield, indicative of electron-phonon scattering, that is not seen in metals (Dekker, 1958). Studies with diamond show a distinct change in the scattering probability, clearly visible in SE energy distribution curves, below E_c+E_g that is attributable to the shift from electron-hole pair production to phonon and impurity scattering (Himpsel *et al.*, 1979; Shih *et al.*, 1997). The bandgap leads to a reduction in possible states into which to scatter that results in a decreased probability of scattering and ultimately relates back to a longer MFP, a lower value of the absorption coefficient α, and a

higher SE yield. In addition, insulators that have a low vacuum level E_{vac} within this energy region (*i.e.,* $\chi << E_g$) as shown in Figure 2.2, will emit the majority of these SE that can travel from deeper within the material. There is an overlap between E_{vac} and the energy where the excited SE population tends to settle due to their longer lifetimes and path lengths. The fact that the SE population settles near E_{vac} is evidenced by the sharp peak of the emitted SE energy distribution at low energy (Seiler, 1983). Also for this reason, any decrease in χ will lead to an increase in the SE yield. Through doping and hydrogen termination, the vacuum level of diamond can be reduced below E_g and this negative electron affinity results in SE yields of over 80 electrons/electron (Shih *et al.*, 1997).

The simple energy level arguments that explain large bandgap insulators do not translate as well to small bandgap semiconductors, which typically still have slightly higher maximum SE yields than metals. Figure 2.3 shows an energy-level diagram for a typical semiconductor with a smaller bandgap energy and a comparatively high electron affinity. The smaller bandgap means that SE energy loss due to electron-hole production is more probable. The previous arguments about the shift in scattering mechanisms below E_c+E_g still apply, but the higher vacuum

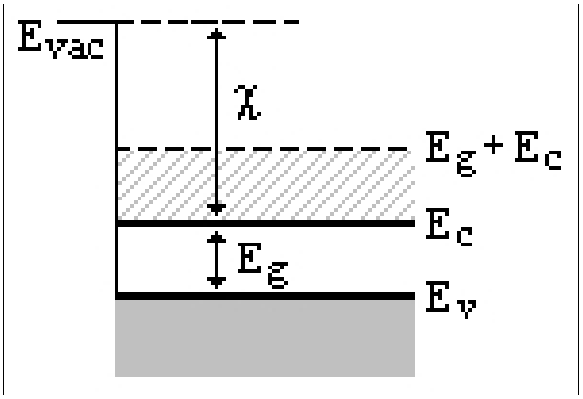


FIG. 2.3: Energy band diagram for typical semiconductor.

level decreases the probability these SE's will be part of the observed SE population.

The question is clearly whether the SE yield properties of small bandgap semiconductors have a dependence on bandgap simply to a lesser degree than insulators or whether the electron affinity acts as a threshold for the bandgap influence and small bandgap semiconductors can be treated as if they were metals. Current qualitative theories about the relationship between bandgap and SE yield do not necessarily support the idea that the SE yield of small bandgap semiconductors should be influenced by their bandgaps (Alig and Bloom, 1975; Grais and Bastawros, 1982; Schwarz, 1990).

Grais and Bastawros (1982) investigate the relationship between bandgap, MFP and SE yield in their survey of the SE emission properties of semiconductors and insulators. Using the constant loss formulation of the SE yield actually taken from Dionne's 1973 paper, they use experimental data for the maximum SE yield δ_{max} and energy at which that maximum occurs E_{max} to calculate the MFP at that energy and compare that with published values of the bandgap for over twenty semiconductors and insulators. Their results are reproduced in Fig. 2.4, which does not show a clear relationship between the MFP and the bandgap energy. In relation to the insulators considered, the MFP shows only a slight linear dependence on bandgap in the semiconductors with bandgaps less than 5 eV. This supports the idea proposed above that there is an activation energy for the bandgap to affect the MFP, but the authors make no comment about the 5 eV limit. The authors proceed to investigate the role of

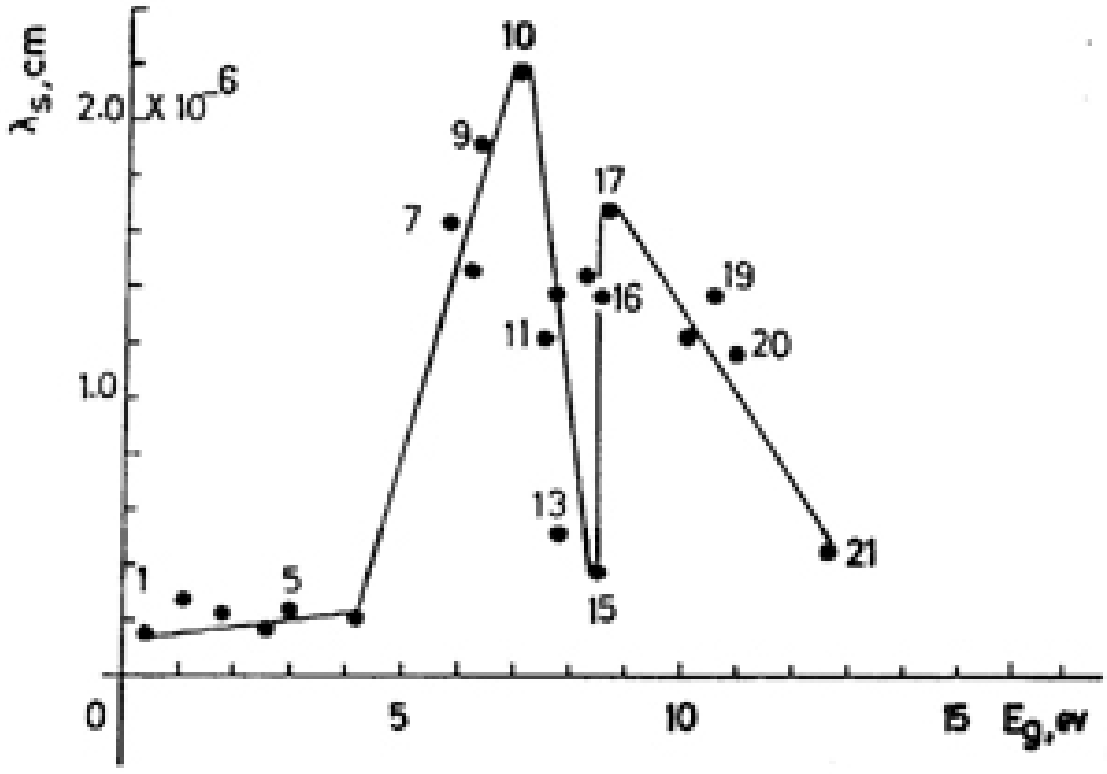


FIG. 2.4: Graph of the mean free path (labeled λ_s) as a function of bandgap (labeled E_g). Reprinted with permission from Grais, K. I., and A.M. Bastawros, 1982, "A study of secondary electron emission in insulators and semiconductors," J. Appl. Phys. **53**, 5239-5242. Copyright 1982, American Institute of Physics. The numbers refer to compounds listed in the article. The solid line is only a guide for the eye.

bandgap in SE emission with a plot of the maximum SE yield as a function of bandgap, which is reproduced in Figure 2.5. Be aware the authors have erroneously used the symbol σ_m, typically reserved for the maximum total yield, where δ_m is more accepted for the maximum SE yield. Again, the bandgap has a distinct influence on the maximum SE yield for large bandgap insulators ($E_g > 5$ eV). Notice both curves have the same general trends, which leads one to investigate the relationship between MFP and the maximum yield.

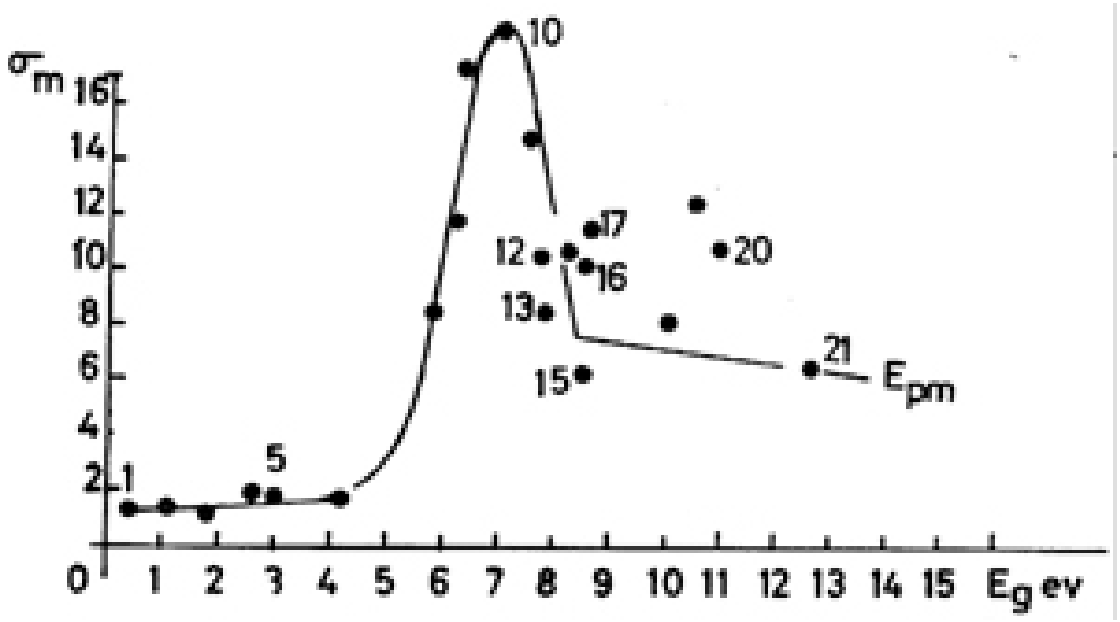


FIG. 2.5: Graph of the maximum SE yield (mislabeled σ_m) as a function of bandgap (labeled E_g). Reprinted with permission from Grais, K. I., and A.M. Bastawros, 1982, "A study of secondary electron emission in insulators and semiconductors," J. Appl. Phys. **53**, 5239-5242. Copyright 1982, American Institute of Physics. The label E_{pm} refers to the fact that the maximum SE yield occurs at the maximum primary beam energy. The numbers refer to compounds listed in the original article. The solid line is only a guide for the eye.

By taking the MFP data from Figure 2.4 and the maximum SE yield data from Figure 2.3, a much better relationship is shown to exist in Figure 2.6. Dionne (1975) predicted the maximum SE yield should be directly related to the MFP through the relation

$$\delta_{max} = 0.9\left(\frac{B}{\varepsilon}\right)[A\lambda]^{0.74}. \tag{2.15}$$

Again, B is the SE escape probability, A is the stopping power coefficient, and e is

related to the bandgap and electron affinity in insulators and semiconductors. The derivation of Eq. 2.15 proceeds from a so-called constant loss model for the SE yield, similar to the power law model, and the numerical values are computed when a value of n=1.35 is chosen for the stopping power exponent. The similarity between the shape of the curve in Figure 2.4 and power law of Eq 2.15 is close enough as to encourage a theoretical fit with the other three parameters as constants; however, this approach exemplifies the downfall of a survey like the work of Grais and Bastawros over so many different compounds. The values of the other three parameters, although they can be argued to have less of an influence than the MFP, are not constants over a wide range of materials. The point of Eq. 2.15 and the curve in Figure 2.4 is that they are strong motivation for the investigation of differences in the SE yield of materials

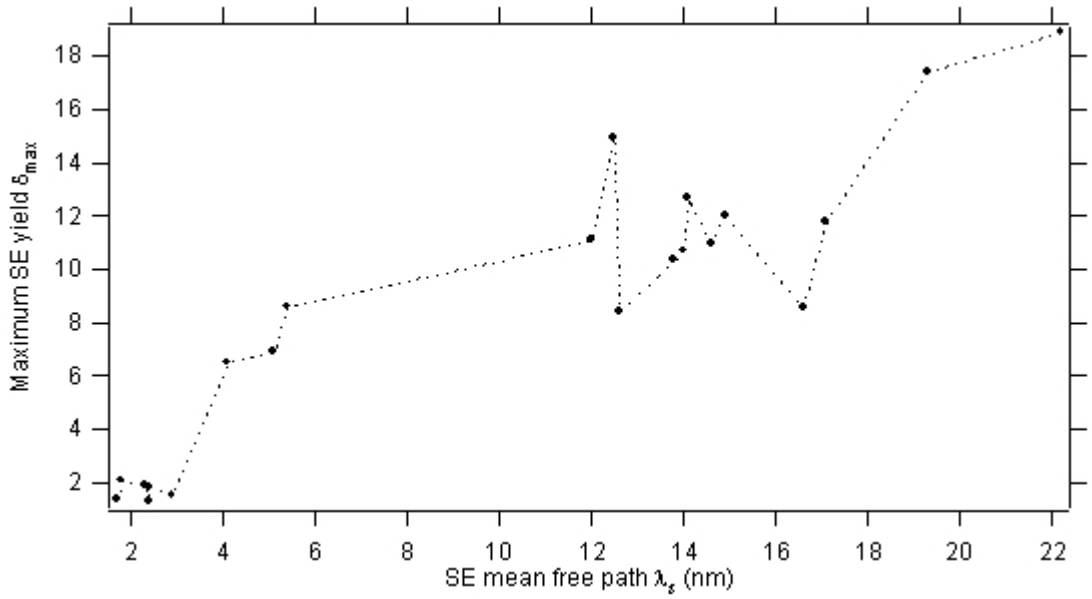


FIG. 2.6: Maximum SE yield as a function of calculated mean free path, adapted from Grais and Bastawros (1982). The numbers in the article referring to the different materials have been dropped and the data has been sorted according to mean free path.

where these other material parameters can be assumed to be constant.

The work of Grais and Bastawros demonstrates small bandgap semiconductors fall into a distinct class from insulators and for which, perhaps, the bandgap does not affect the MFP enough to impact the maximum SE yield. Again, the apparent onset energy of the bandgap influence above 5 eV is very interesting and not explained by the authors. As discussed along with Figure 2.3, the electron affinity could be too large for the bandgap in these semiconductors to impact the SE yield. The ratio of electron affinity to bandgap does vary from 12 down to 0.7 for the semiconductors considered (Grais and Bastawros, 1982), with only modest change in the maximum SE yield. The qualitative arguments presented earlier would contend that a ratio of less than 2-3 should begin to influence the SE yield. The highest ratio of electron affinity to bandgap amongst the insulators is 0.26 and this insulator displays a factor of 8 increase in maximum SE yield over the semiconductors. Using the work function for clean graphite in a vacuum (Hansen and Hansen, 2001), an estimate for the electron affinity of the graphitic amorphous carbon studied in this dissertation is roughly 4 eV above an average bandgap of 0.5 eV (Robertson, 1986), which is an electron affinity to bandgap ratio of 4 and classifies the material as a semiconductor with this criterion. The issue of the electron affinity acting as a threshold energy gains some support in this work, but there is contradictory evidence and the question is not fully addressed or resolved.

Schwarz (1990) also argues that ϵ should relate to the bandgap in insulators,

but he only uses the relationship to qualitatively explain the high SE yield of large bandgap insulators in contrast to the lower yields of metals and does not remark about semiconductors.

An interesting work by Alig and Bloom (1975) verifies that the average energy to create an electron-hole pair in a semiconductor is roughly three times E_g by employing standard semiempirical SE theory, similar to the derivations in Section 2.1. The authors are not directly investigating the role of bandgap in SE yield, but construct an empirical relationship, outlined below, between the SE escape probability B and the ratio of electron affinity to bandgap as an exercise based on their own theory about the electron-hole production energy. The authors first use standard semi-empirical theory to derive a direct relationship between the SE escape probability *B* and the average energy to excite a SE e, which is similar to the work done by Dionne (1975). Assuming that electron-hole pair production is the main mechanism for exciting SE and based on their underlying assumption that e is then related to three times the bandgap, the authors take values for the bandgap and other free parameters from the literature to derive *B*. The work to this point is a rough approximation of the work done by Grais and Bastawros (1982).

As an independent verification of their semiempirical work, Alig and Bloom proceed to derive a simplistic theoretical relationship between *B* and the ratio χ/E_g also based on their underlying assumption the electron-hole excitation energy is three times the bandgap. For simplicity, the authors assume electron-hole pair production is

the only means for an excited SE to lose energy. The implication is that below a threshold energy needed to excite another electron-hole pair, which is roughly $3E_g/2$ in their case, a SE has a 100% probability of escaping. The assumption is an overly simplified version of the previous argument there is a transition in electron energy loss mechanisms near the conduction band minimum. The authors are ultimately successful in roughly matching the distribution of their semiempirical values for B with their theoretical predictions, which is a similar goal for the work of Grais and Bastawros (1982) with less successful results. Alig and Bloom confuse the original role of B as a surface transition probability (Dionne, 1975) with the larger role of α in governing the MFP of excited SE, but this is a minor point and easily understood given the number of parameters on which SE yield depends. Although their assumptions are crude, the work of Alig and Bloom inadvertently gives credibility to the idea that bandgap plays a role in SE emission properties through inhibiting scattering below a cutoff energy related to the bandgap. Unfortunately, there is no way to draw a quantitative relationship between the bandgap and the maximum SE yield from their work beyond the qualitative ideas already discussed.

Again, there is evidence bandgap has a role in SE emission, but there are few direct studies of the relationship in small bandgap semiconductors. The articles discussed acknowledge the dependence of the SE yield on bandgap, relying on the nature of the relationship to substantiate further aspects of their theories or to derive other material parameters, which are more difficult to measure experimentally.

Section C. Literature on the Secondary Electron Emission of Carbon

The literature on the SE emission of carbon materials is sufficiently abundant. The straightforward measurements of the SE or BSE yields of carbon materials is the most pertinent to the discussions here, but other broad categories will be discussed. One of the important aspects of these SE and BSE yield studies of carbon materials is the characterization of the type of carbon being studied. A literature search for the SE yield of carbon led to several articles, which studied several different forms that still fall under the general class of carbon materials. Graphitic carbons will be the focus of the present review, but research on forms of diamond will be discussed briefly as well.

The measurement of the SE emission properties of graphitic carbon materials was originally done by Bruining (1938) in his efforts to find materials with low SE yields for use in practical applications were a low yield material would be valuable. Bruining used a spherical detector without a suppression grid to study carbon black (soot or turbostatic graphite) and Aquadag™, a colloidal microcrystalline graphite material that is discussed fully in Subsection 5.A.3. Although the spherical detector is the ideal measurement scheme for SE yield measurements, the lack of a suppression grid could have led to a significant error in the SE yield measurement because of SE's produced on the collecting sphere returning to the sample. Bruining's work also suffers from the inability to attain a high-quality vacuum environment that would ensure the samples were free from contamination. The measurements were carried out in an evacuated glass tube that included an unknown getter source, but the exact

pressure was not specified. Despite these reservations, the work is routinely cited in the CRC handbook for the maximum SE yield values of graphite and soot (Lide, 1990). Bruining also outlines what would become the standard explanation for the reduced yield of soot by noting the material has a porous surface, which recaptures a portion of the emitted SE's. The affect of surface roughness on SE yield is discussed more fully in Chapter 6 during a discussion of the experimental data.

Sternglass (1953a) replicated Bruining's SE yield measurements of Aquadag™ with a much more accurate spherical detector with a suppression grid and similar glass chamber with a vacuum of 10^{-6} torr. Sternglass was not able to measure the maximum SE yield of Aquadag™ because of his limited energy range, but his results are 20% higher than those of Bruining, which is at least the direction consistent with the addition of a suppression grid. Sternglass made an effort to correct for SE's produced on the suppression grid that return to the sample, which is a unique effort when using a spherical detector. Sternglass measured the SE yield of an amorphous carbon produced by electron-stimulated adsorption in the presence of Octoil vapors, which presumably has a higher concentration of hydrogenation and diamond-like bonding than the graphitic amorphous carbon sample discussed in Section 5.A.4 and studied in this dissertation. Following the explanation by Bruining for the differences between the carbon samples in his work, Sternglass employed the same surface roughness argument to explain the differences between the carbons he studied. As mentioned earlier in Section 2.A, Sternglass went so far as to include an additional parameter in

his model for the SE yield to account for the effects of surface roughness. The validity of this conjecture will be discussed more fully during the experimental results in Chapter 6.

The SE yield of pyrolytic graphite was measured by Whetten (1965) using a spherical detector with a suppression grid in an ultra-high vacuum (UHV) environment. The material is assumed to be similar to the highly oriented pyrolytic graphite discussed in Section 5.A.2 during the experimental data chapter. The author took further measures to reduce the affects of surface contamination by freshly cleaving the samples while under vacuum. The author reports a maximum yield in close agreement to the values for Aquadag™ by Bruining.

Another measurement of pyrolytic graphite was conducted by Wintucky *et al.* (1981) in only a slightly higher vacuum environment. The study used a cylindrical mirror analyzer to measure the higher energy BSE, but the author does not explain the technique for determining the SE yield. Soot was used as a standard for their measurements and their SE yield for soot is in agreement with Bruining's measurements. The author's SE yield of the pyrolytic graphite sample is in agreement with the measurements of Whetten, but there is no maximum yield at roughly 250-300 eV as expected, which makes the measurements suspect. The author was interested in the use of ion sputtering to roughen the surface and lower the SE yield of the graphite samples, which would then be used to increase the electron collection efficiency of the walls of a high powered traveling wave tube microwave amplifier. High levels of ion

sputtering were shown to texture the surface of the graphite samples with spires, which reduced the SE yield to lower values than the soot.

Another recent study of the use of carbon coatings to reduce the SE emission of a surface was carried out by Ruzic *et al.* (1982). Their interest was to reduce the SE emission of walls in plasma heating experiments for applications in controlled nuclear fusion. The study did not use an electron analyzer to measure the SE yield, but relied on sample bias to reject or retain SE's produced there (see Subsection 3.E.1 for details). Although the technique is questionable due to the uncontrolled field environment failing to return higher energy SE to the sample, the authors argued this error is on the order of 1% and verified their technique by comparing standard materials to values in the literature. The experiments were conducted in an adequate vacuum environment (1.5×10^{-9} torr) and the samples were sputtered with argon before and in between each measurement to rid the sample of contamination and mimic the environment in the plasma arrays. The authors studied a variety of carbon materials that include Aquadag™, Glyptal (a carbon based vacuum sealant), electrophoretically deposited lamp black (soot or turbostatic carbon), and AJT graphite, which is the commercial tile actually used in the plasma chambers of interest. All the treated samples were vacuum baked at 400° C for 1 hour in an attempt to pyrolyze hydrocarbons in the materials. Their results for the SE yield of Aquadag™ are 10% lower than the original work by Bruining. A 10% decrease in SE yield is consistent with the direction and magnitude of error typically found in the sample bias technique

of SE yield measurement (Davies, 1999). A group in Southampton has continued this work with several publications about the actual graphite panels used to limit the SE current in these types of nuclear fusion experiments (Woods *et al.*, 1985, 1987; Fahrang *et al.*, 1993).

Another source of research on carbon comes from the nuclear physics community making backward and forward yield measurements excited by high energy (keV to MeV) electron and ion bombardment of thin carbon films. Carbon targets are used in an attempt to avoid the confounding effects of carbon buildup due to stimulated adsorption from the beam, with the assumption that the carbon buildup is similar to the carbon targets (Dednam *et al.*, 1987). One such article used the simple sample bias method to determinine the forward and backward SE yield of thin "carbon" foils (10-2000 nm) in a UHV system (Caron *et al.*, 1998). Although not stated in the article, thin films of carbon are typically evaporated; however, the fraction of graphitic or diamond-like bonding depends on deposition temperature (Dennison *et al.*, 1996). The maximum SE yield of the thin carbon films is measured at over two before ion sputtering reduces the yield to agree with Bruining's work.

The most recent work in the area of SE emission properties of carbon materials has been conducted on diamond and diamond-like amorphous carbon materials. Much of the pioneering experimental work in this field has been conducted by Krainsky *et al.* (1996). Shih and Yater have also conducted substantial research in this area and have written a current review of the study of the SE emission properties of diamond

(Shih *et al.*, 1997; Yater and Shih, 2000). The interest in diamond is its extremely high maximum SE yield resulting from a negative electron affinity the material develops when terminated with hydrogen. Diamond-like amorphous carbons have also been the topic of research because the SE emission properties are more robust, although the yields are lower than crystalline diamond (Liu *et al.*, 1997; Diaz *et al.*, 1999).

Another class of SE emission studies on carbon have surrounded the use of high resolution SE energy distribution measurements to investigate the origins of fine structure in the spectra. The seminal work in this field was carried out by Willis and only a fraction of his work is referenced here (Willis *et al.*, 1972a, 1972b, 1974). The technique is typically used as a structural probe to characterize the degree of crystalline order in a sample, but has also been used to distinguish between different carbon allotropes (Hoffman *et al.*, 1991). The SE energy distributions of graphitic carbons have been the subject of study because of their interesting fine structure, but also for their use as a standard reference for sample fermi-level energy position (Oelhafen and Freeouf, 1983) or their repeatable spectra, which can be used for Auger electron spectroscopy instrument comparisons (Goto and Takeichi, 1996). This area of the SE emission characteristics of carbon materials was not fully investigated because it is not directly applicable to the current study.

The literature review of the SE emission properties of graphitic carbon materials reveals these materials are mainly of interest for their low SE and BSE yield

properties. The literature shows there are a variety of measurement techniques, with a 10-20% variability between different investigations. There is a higher level of agreement about the SE yield of microcrystalline graphite materials, like Aquadag™ and pyrolytic graphites, probably due to their repeatable structural characteristics in comparison to more highly variable amorphous and turbostatic carbons. The literature shows that sample contamination does not have as great an influence as with metals, but ion sputtering can have a significant influence on the SE yield of carbon samples. Table 2.1 summarizes much of the pertinent information about these graphitic carbon studies.

TABLE 2.1: Summary of experimental data on graphitic carbons

Ref (Year)	Material	SE yield			BSE Yield	Vacuum	Detector	Notes
		δ_{max}	E_{max} eV	E range (eV)				
Bruining (1938)	a Aquadag™ b. soot	a. 1.02 b. 0.47	a. 300 b. ~500	50-800	none	glass tubing	spherical	No suppression grid.
Sternglass (1953a)	a. Aquadag™ b. amorphous carbon with H	a. 1.2 b. not measured	a. < 300 b. not measured		0.07	glass tubing 10^{-6} torr	spherical	Theoretical correction for SE created on suppression grid. No δ_{max} for Aquadag™ due to energy range.
Whetten (1965)	pyrolytic graphite	1.0	310	100-3000	none	10^{-10} torr	spherical	Sample was cleaved *in situ*.
Wintucky *et al.* (1981)	a. soot b. pyrolytic graphite (PG) c. argon sputtered PG	a. 0.4 b. ? c. 0.35	a. 450 b. < 200 c. 450	a. 200-2000 b-c. 300-2000	a. 0.45-0.225 b. 0.15-0.05 c. 0.1-0.025		BSE used CMA, but unclear on SE method	No δ_{max} for PG (slope increasing at 200 eV). Sputtered PG with 5mA/cm^2 at 1000 eV for 6 hrs.
Ruzix (1982)	a. Aquadag™ b. Glyptal (turbostatic C with H) c. ED lamp black d. AJT panels	a. 0.91 b. 0.88 c. 0.88 d. 0.89	a. 250 b. 247 c. 250 d. 270	50-1500	none	$1.5x10^{-9}$ torr	sample bias in AES system	All samples vacuum pyrolyzed at 400° C for 1 hr. ED is electrophoretic deposition. AJT panels are a commercial graphite used in plasma chambers.
Caron *et al.* (1998)	a. 10-2000 nm carbon films	a. 1.1	b. 275	0-5000	none	10^{-10} torr	sample bias	Thin films are typically evaporated amorphous carbon, but H content depends on temperature.

CHAPTER 3

INSTRUMENTATION

The following sections describe the vacuum chamber, the ancillary systems, the sample stage, the source beams, and the electron energy analyzer involved in the present study. There are additional systems that are not involved in the present work and will not be discussed, including high energy electron diffraction (HEED), a hemispherical analyzer (HSA), a scanning electron microscope (SEM), time of flight spectroscopy, and a load-lock sample exchange system.

Section A. Vacuum Chamber

All experiments were conducted in an ultra-high vacuum (UHV) chamber, which is pictured in Fig. 3.1. The chamber is composed of two halves: The bottom section is from a Varian model FC-12E vacuum pumping station and contains the ion pumps, a popet valve, and ten 2.75 inch flanges used for gas inlet and electrical feedthrough. The top of the chamber houses the experimental systems and was custom designed by Dennison and Riffe and built by Huntington. Although the upper half of the chamber has a bewildering 36 ports, these ports are directed at only a small number of focal points. The two main focal areas inside the chamber are separated vertically by 12 inches. The source beams are mounted at this lower level, while the upper level houses the Auger electron spectroscopy (AES) and SEM systems. The lower level is diagramed in Fig. 3.2 and a list of flange information is contained in

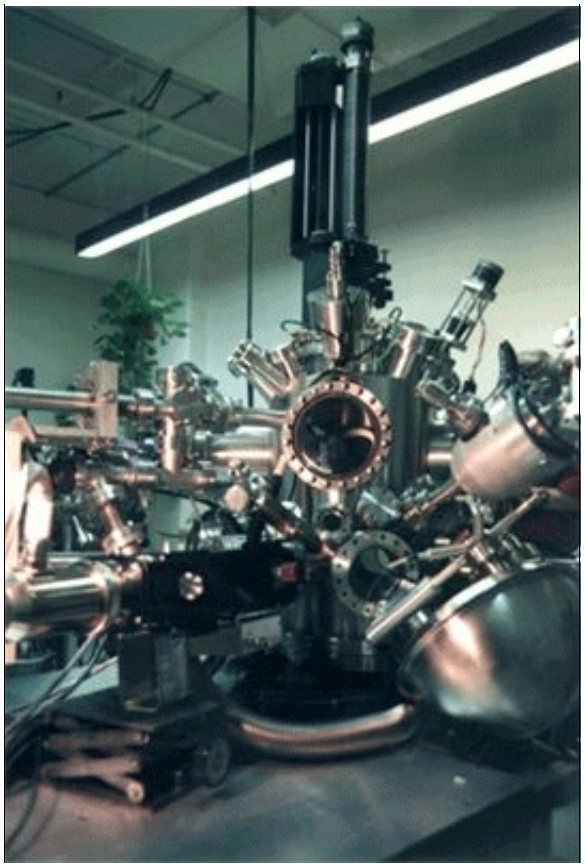


FIG. 3.1: USU UHV surface analysis chamber, referred to as "FatMan."

Appendix A.

The approximately 125-liter (1.3 m x 0.35 m ID) chamber is pumped out with a mechanical pump (Pfeiffer-Balzers Duo) to 10^{-3} torr and a 55 liter·s^{-1} turbomolecular pump (Leybold TurboVac 50) down to a high vacuum of 10^{-7} torr, after which five 40-liter·s^{-1} ion pumps (Varian) are used to maintain the chamber pressure at UHV pressures. The turbomolecular pump is also used to pump an external roughing line that runs between gas inlets, source beams that need differential pumping, and the load-lock system. A titanium sublimation pump (Varian TSP) is used periodically to assist the high vacuum pumping, especially during the switch to using the ion pumps or when outgassing other filaments.

Typical UHV pressures of 10^{-9} to 10^{-10} torr are obtained by baking the chamber at 110-125° C for 3-4 days. To bake the chamber, a temporary steel framework is constructed around the chamber and then covered with "thermoglass cloth" (trade name *Nomex*), which is the same material used to make firefighter's clothing. A set of

resistive heaters, 10 radiative heaters (220VAC at 180 ohm) plus a large heater made up of six flat heaters in parallel (220 VAC at 80 ohm), provides a total of 3300 watts to heat the air inside the cloth oven. This method was chosen over the typical use of heater tape covered with aluminum foil and has proven to be successful.

High vacuum is monitored with three convectron gauges located near the turbomolecular pump, the gas handling system, and the load-lock system. The UHV

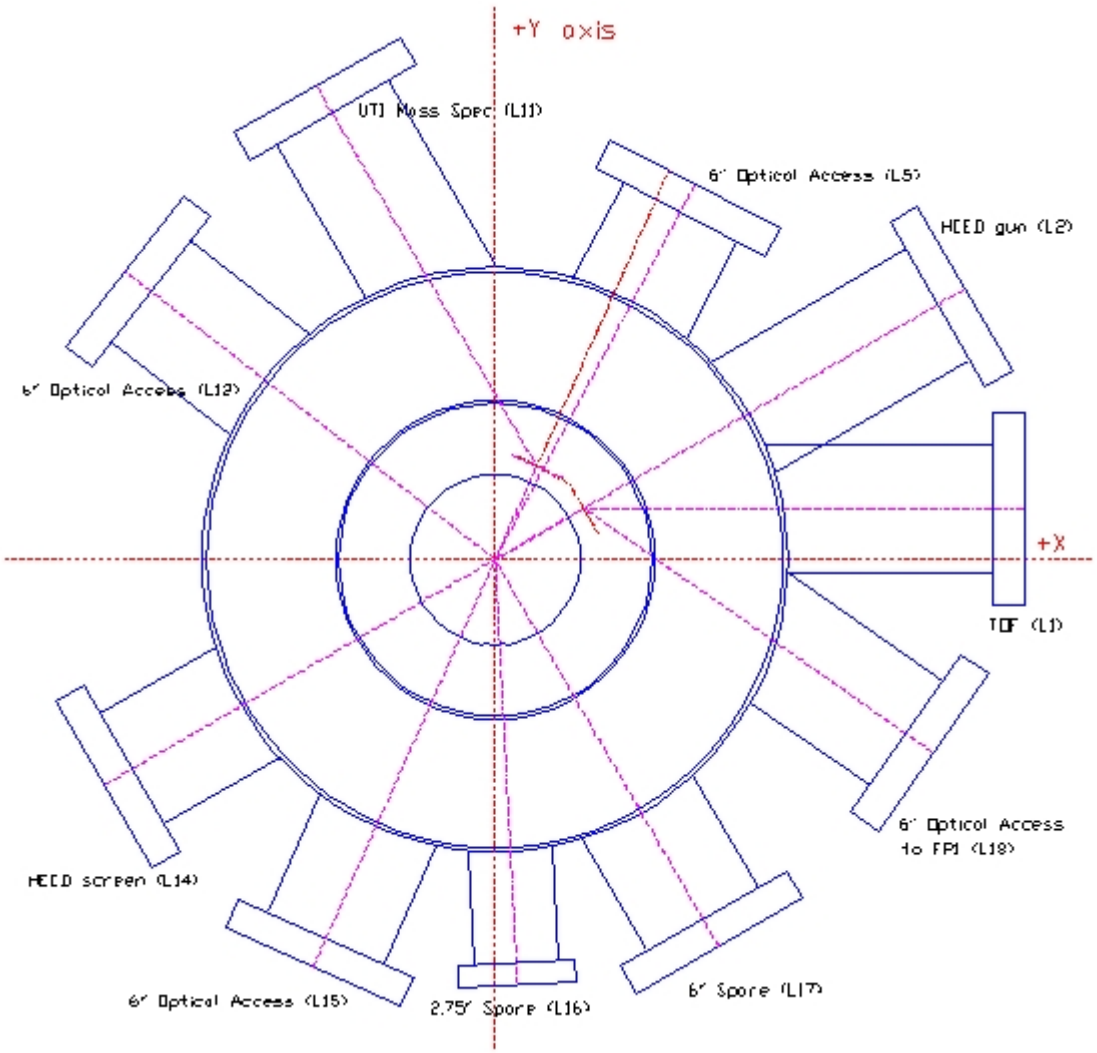


FIG. 3.2: Lower level of UHV chamber. Detailed information in contained in Appendix A.

pressure inside the chamber is monitored by three nude UHV ion gauges: A gauge at the top of the chamber, one just above the popet valve in the lower section of the chamber, and another gauge in the external roughing line to monitor outgassing from source filaments during their use. The ion gauges use a standard ion gauge controller (Granville Philips model 307). The chamber's typical base pressure is in the low 10^{-10} torr range. Outgassing of filaments during the use of the electron guns often puts the operating pressure of the chamber in the mid 10^{-10} torr range. A residual gas analyzer (RGA) (Ametek model 100 amu with electron multiplier) is used to monitor the partial pressure of gases in the vacuum. Spectra from the RGA during experiments are presented and discussed in Chapter 5 along with the experimental data.

The chamber has been fitted with a sleeve of μ-metal magnetic shielding material (custom built by Magnetic Shield Corporation) to reduce the ambient magnetic field inside the chamber that can influence low energy electron trajectories. In addition to the cylindrical sleeve of magnetic shielding, each apparatus that protrudes into the vacuum is covered with magnetic shielding. The magnetic field inside the chamber is a cumulative effect of several fields. The earth's field is roughly 460 milligauss (mG). The VG cold cathode ion gun uses a powerful magnet that, even with netic μ-metal shielding around it, leaks roughly 200 mG. The ion pump wells are surrounded by magnets that produce an unknown field in the chamber. Early measurements of the chamber's ambient magnetic shield show the field along the chamber axis averages 60 mG. Edge effects near equipment that reach far into the

chamber, such as the cylindrical mirror analyzer (CMA) or the hemispherical analyzer (HSA), show fields near 200 mG and were to be expected. The actual measurements of magnetic field profiles are discussed further in Appendix A.

Section B. Ancillary Systems

The supporting systems for this dissertation work consist of an ion gun used for sputtering samples and an Auger electron spectroscopy (AES) system used to characterize sample contamination.

The ion gun (Vacuum Generator model AG5000) uses a cold cathode structure to ionize the sputtering gas rather than a hot filament. The use of a cold cathode allows otherwise volatile gases to be used for sputtering. The sputtering gas used in the current work was argon, which does not need to rely on the cold cathode. The gun is capable of μA currents and beam energies between 300-5000 eV. The spot size can be focused, but was typically chosen to be on the order of 10 mm because of the size of the samples to be sputtered. A permanent magnet around the ionizing chamber of the gun is used to focus the beam before leaving the gun. As mentioned in Section 3.A, the magnet was shielded with μ-metal shielding from disturbing other charged particle sources.

The AES system (Varian model 981-2730) consists of a cylindrical mirror analyzer (CMA) and electron gun, along with supporting electronics. The CMA has proven to be capable of routinely operating with instrument line widths of 0.5 %, which is the measured peak-to-peak energy resolution of the instrument [Fatman II lab

notebook, p. 097y]. The electron gun was fully characterized to find the beam current density during normal operation. The electron gun was always operated at 2000 eV. Beam profile measurements reveal the minimum spot size of which the gun is capable is tightly focused around 0.3 mm [Fatman II lab notebook, p. 100w]. Although the gun is capable of nearly a μA of beam current, the gun was operated below 50 nA as a compromise between an adequate signal for the AES spectrum and high beam current densities that might contaminate the samples. Long exposure to beam current densities on the order of 90-140 $\mu A/cm^2$ has been shown to cause electron stimulated adsorption of carbon through the disassociation of vacuum chamber gases, while beam current densities of < 6 $\mu A/cm^2$ are thought to leave the sample unaffected for the total time the sample is exposed to the beam (Chang *et al.*, 2000). Figure 3.3 shows a calculation relating the beam current and diameter to this acceptable level of beam

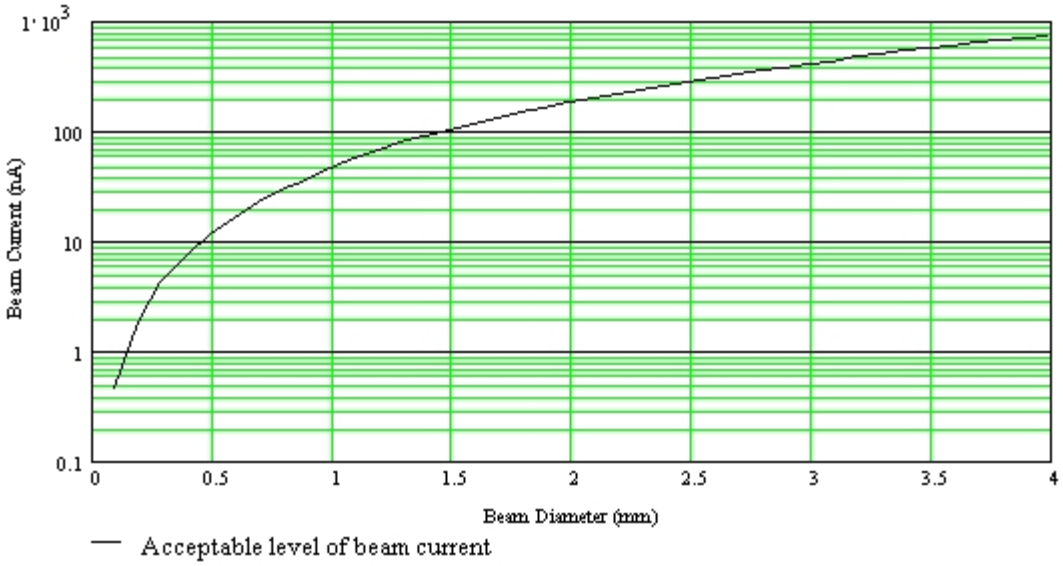


FIG. 3.3: Calculated graph of beam current and diameter showing the bound of the acceptable level of beam current density (below and to the right is acceptable).

current density. Using the minimum spot size puts an upper limit on the beam current density of 70 $\mu A/cm^2$, which is rather high in comparison to the contamination threshold. The gun's settings that resulted in 50 nA beam currents most likely also lead to a larger spot than represented by the minimum spot size, but the spot size was not measured again at these settings [Fatman III lab notebook, p. 006y]. As another precautionary measure, the samples were only exposed to the beam for the minimum time necessary to maximize the signal and obtain a spectra, which was typically no more than 10 minutes. The AES spectra for the samples are presented in Section 5.A along with a discussion of the samples.

Section C. Sample Stage

The sample stage was designed to allow for a high sample volume and quick sample transfer in response for an anticipated high volume of sample measurements for other grant work by the group. A simplified drawing of the sample stage is shown in Fig. 3.4. The sample stage is a 12-sided carousel that is suspended from a rotary feed-through on top of the chamber. Each face of the carousel is an individual module that can hold an electrically isolated sample or a small detector for observation of the source beams. The modules fit together like pieces of a pie and are held together by plates on the top and bottom. The sample stage rests on a circular base connected to a vertical rod, which is coupled to the rotary feed-through. The circular base is electrically isolated from the rod so the sample stage is electrically isolated

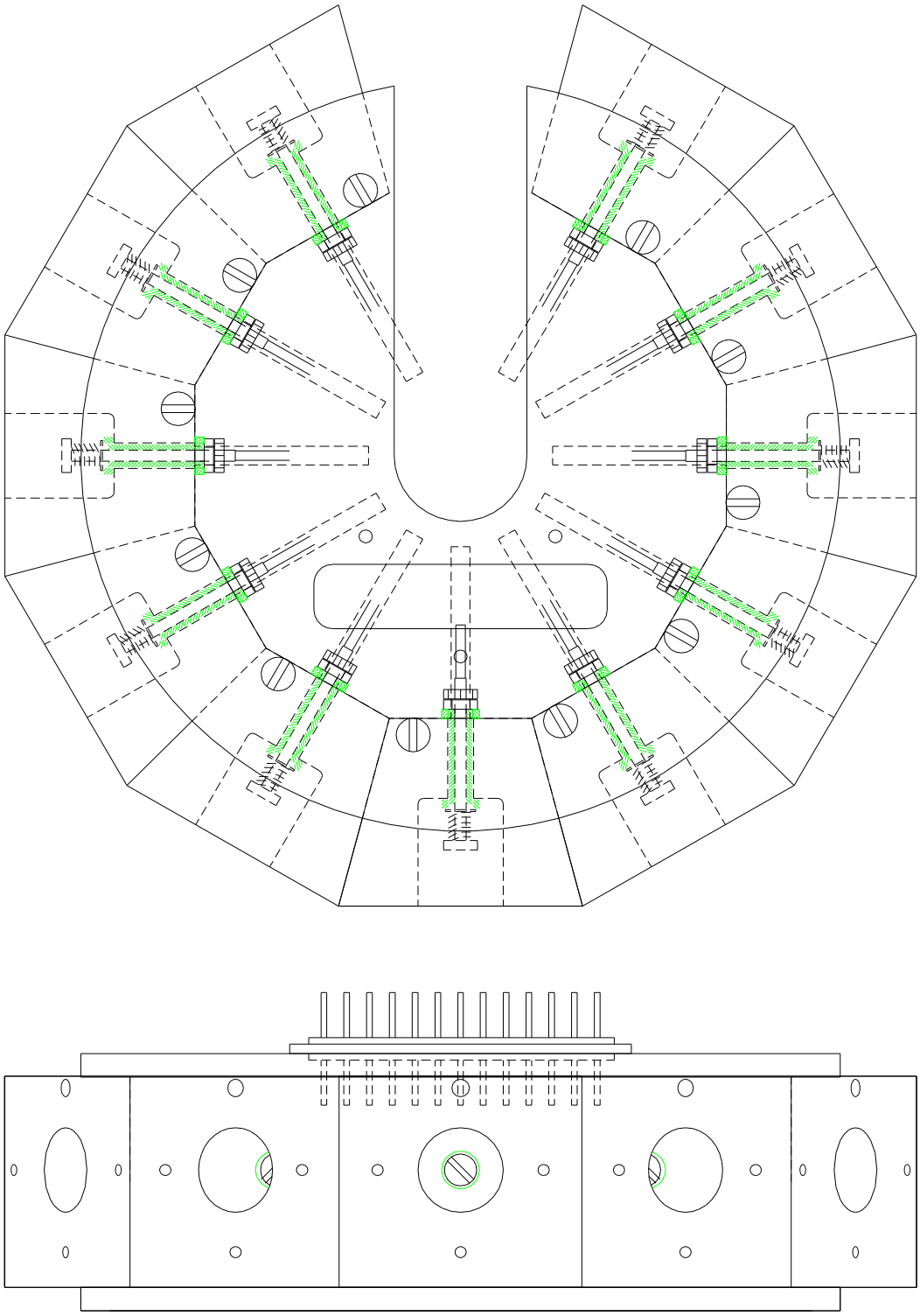


FIG. 3.4: Top and side view of sample stage. The height of a module is 28.6 mm. The diameter of the stage from module face to face is 12.7 cm.

from chamber ground and the current to the whole sample stage structure can be monitored.

The stage has been designed so it can be easily removed from the chamber. One module in the carousel is sacrificed to make way for a slot, from the center to the edge, that allows the sample stage to slip away from the circular base on which it rests. The center region of the sample stage is hollow to allow for the various wires for the back side of each module to be accumulated and pass through the top plate via a 25-pin, UHV-compatible, D-type subminiature connector (Insulator Seals Inc. part # 0981901). Figure 3.5 shows the stage without the top plate, exposing the wiring inside. The cable assembly is shown later in Fig. 3.16 during Subsection 3.E.1. The connector is necessary for the wiring to be quickly disconnected from the sample stage, which is then free to be removed from the vacuum chamber via any 8 inch port, which has been opened on that level. If the chamber is brought to atmospheric pressure with nitrogen gas, then the sample stage can be modified or replaced with a duplicate stage without a long bakeout to reach UHV pressure again. The cable is bolted to arms that hang from a disc above the base to keep the cable out of the way of the rotating detector, but has the drawback that if the top flange of the chamber is opened the cable would have to be detached before the system could be completely removed and to allow a new copper gasket to be put in place.

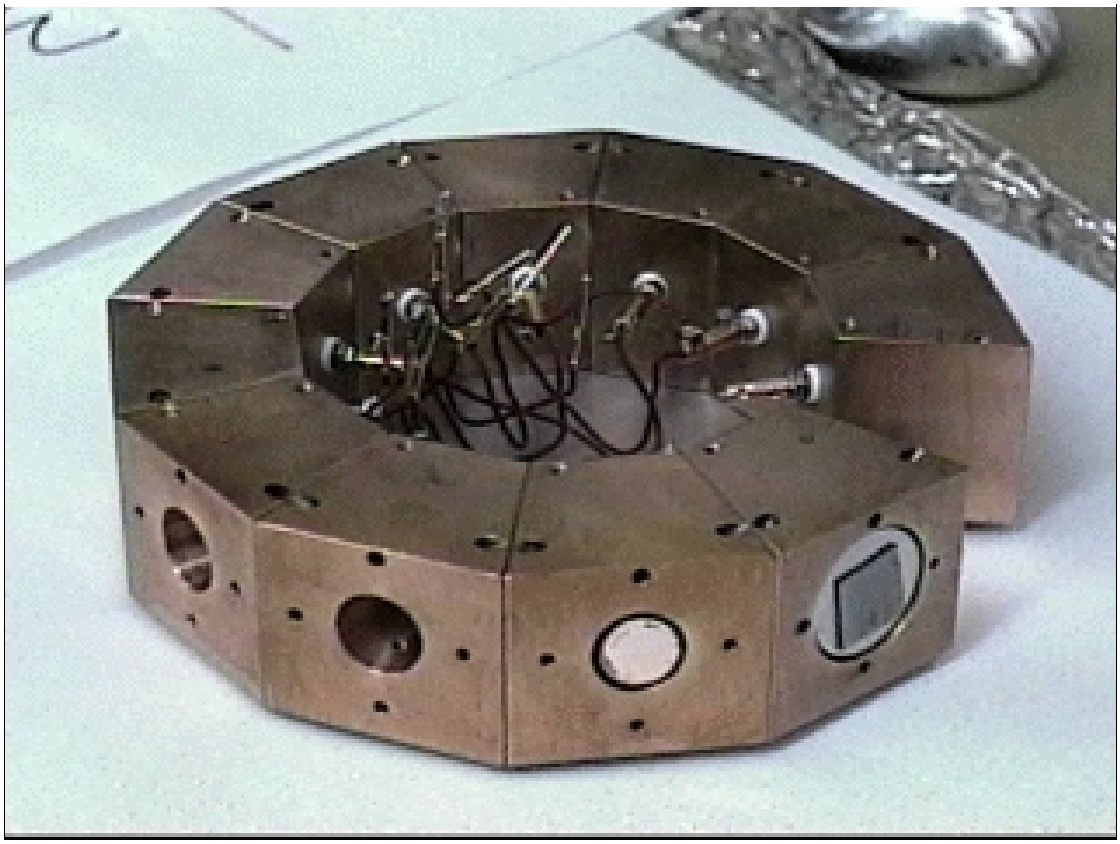


FIG. 3.5: Sample stage with top plate removed. The large cavity sample module (right) contains the HOPG sample, while the smaller cavity module (front) contains an OFHC slug.

Subsection 1. Modules

The sample modules were designed to accommodate a wide variety of samples. A typical sample module is shown in Figure 3.6. All the modules were made from OFHC copper to avoid surface charging due to an insulating oxide layer, as with aluminum, which would affect low energy electron trajectories. Samples are held in a cylindrical cavity in the face of the module. The samples must either be cylinders themselves, machined from the sample material, or flat samples attached to cylindrical

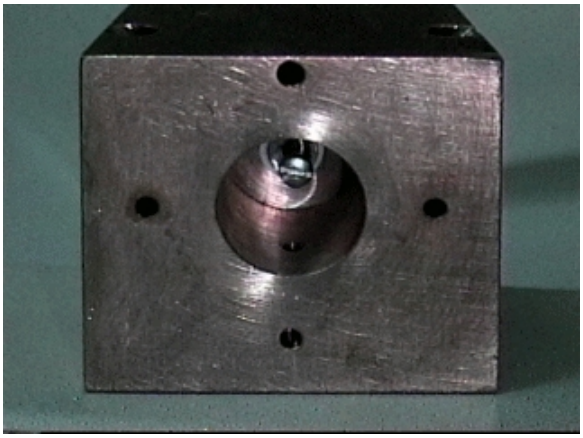


FIG. 3.6: Empty 1-cm cavity sample module.

slugs made from 304 stainless steel or OFHC copper. Two sizes were chosen for the sample cavities: The 1 cm diameter holes minimize the sample-to-collector surface area ratio, while the 0.75-inch diameter holes were intended for a wider array of sample configurations. For example, the larger cavity can hold a small sample and another cylindrical element that would be used as a tertiary detector to measure electron scatter. Drawings of the smaller and larger cavity modules are shown in Figs. 2.7 and 3.8, respectively, while an actual picture of the smaller sample module is shown in Fig.3.6.

The samples are electrically isolated from the stage to allow the measurement of a separate sample current. The sides of the sample are supported by three ceramic posts (small shaded parts in front view of Figs. 3.7 and 3.8) held in place by set screws. The holes for the ceramic posts are set back 6.4 mm from the face of the module to avoid charging the insulators. The bottom of the sample is supported by a stainless steel pin that is spring loaded to ensure contact with the sample (see top view in Figs.3.7 and 3.8). The pin extends through the back of the module in a ceramic sleeve, for electrical isolation, and into the hollow region of the sample stage. One of the 25 wires from the D-type connector is attached to the pin so the current to the

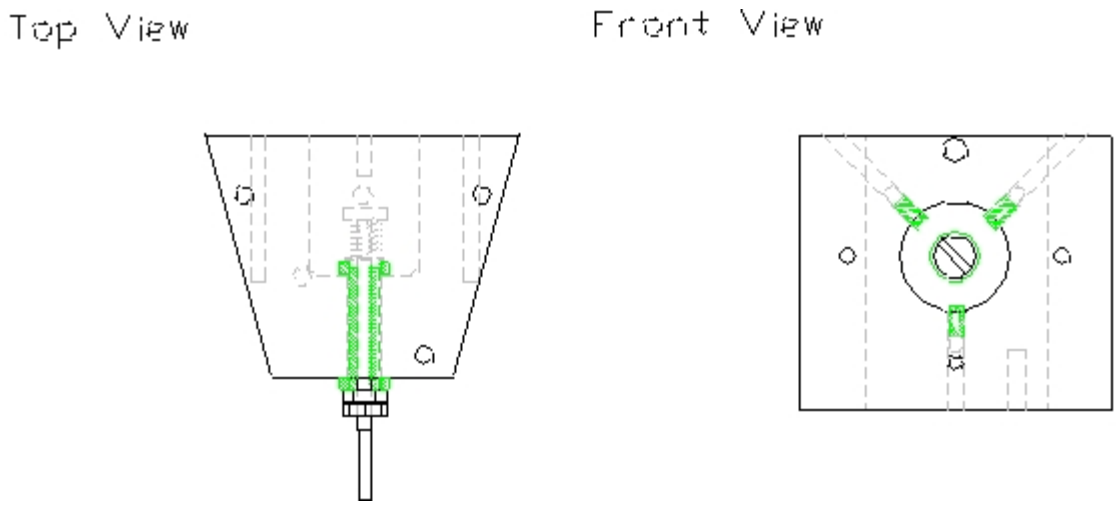


FIG. 3.7: Assembly drawing of 1-cm cavity OFHC copper sample module. The hatched regions are ceramic tubes. There is a spring in the sample cavity between the ceramic washer and the head of the 2-56 screw that makes electrical contact with the sample. The height of the module is 28.6 mm and the depth is 25.4 mm. The hole at the top of the module is a simple Faraday cup, with a 2-mm diameter and a 20-mm depth.

sample can be monitored.

There are three diagnostic modules on the stage: A Faraday cup, a phosphor screen, and a UV detector. All three are grouped together and are set behind the 25 pin connector, since the cable interferes with the SE detector motion and the diagnostic modules do not need to be studied by the SE detector.

The Faraday cup is essentially a hole used to measure the electron (or ion) beam current without losing SE's or BSE's that would effectively reduce (or increase) the actual incident current. The typical design for a Faraday cup employs a ratio of 10:1 between the depth of the hole and the diameter of the aperture so that ~97% of the electrons emitted as a result of the incident beam do not escape the Faraday cup

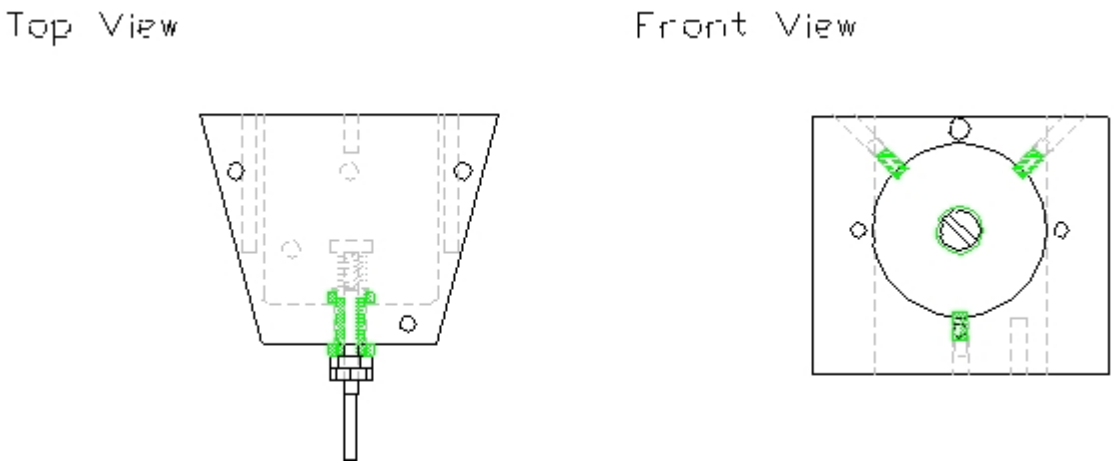


FIG. 3.8: Assembly drawing of 0.75-inch cavity OFHC copper sample module. The hatched regions are ceramic tubes. There is a spring in the sample cavity between the ceramic washer and the head of the 2-56 screw that makes electrical contact with the sample. The height of the module is 28.6 mm and the depth is 25.4 mm. The hole at the top of the module is a simple Faraday cup, with a 2-mm diameter and a 20-mm depth.

(Moore *et al.*, 1983). Conforming to this standard, the 25-mm depth of the modules limit a Faraday cup's aperture to < 2.5 mm. As shown in the front views of Figs. 3.7 and 3.8, a hole was drilled in the sample modules with a 2-mm diameter and 20-mm depth; however, when the SE detector is in front of the sample, the hole in the drift tube through the back of the detector is not large enough to deflect the beam into these Faraday cup holes.

In addition, a larger diameter aperture was needed for incident beam characterization. One solution would have been to mount a Faraday cup at an angle on the bottom of the detector's cover, but the amount of deflection necessary to reach the Faraday cup exceeded the abilities of the high energy gun and the low energy gun was mounted much too close. The solution was to use a limited depth:diameter ratio of

2.75:1 and make up for the potential loss of BSE and SE with three solutions: (i) machining an angle into the base of the hole to diffusely scatter BSE (Miller and Axelrod, 1997), (ii) coating the cup with a colloidal graphite called Aquadag™ to reduce the SE and BSE yields (Sternglass, 1953b; Ruzic *et al.*, 1982), and (iii) biasing the cup to positive voltage to retain the SE produced on the inside of the cup. Extensive tests of the Faraday cup show a +10 volt bias on the Faraday cup results in a beam current equivalent to a 10:1 design to within 0.5%. Refer to Appendix B for details of these tests. A tertiary aperture was mounted around the large aperture Faraday cup and was electrically isolated so stray currents could be measured and analyzed. The final design of the Faraday cup and tertiary aperture inside a sample module is shown in Fig. 3.9.

The phosphor screen is mainly used to verify the various charge particle beam's location and approximate size. The beam current density and energy that

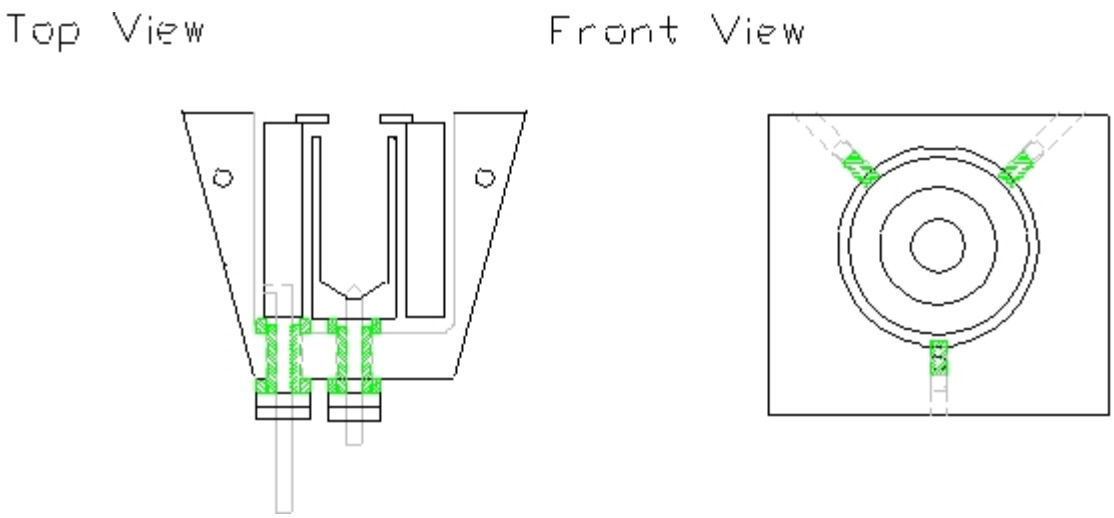


FIG. 3.9: Assembly drawing of Faraday cup and tertiary aperture inside a sample module.

results in visible luminescence makes the phosphor screen less reliable as a measure of beam current and spot size. The phosphor screen uses P43 type phosphor coated on a 19 mm OFHC copper slug by Grant Scientific. The slug itself has four Faraday cup holes; however, their small size makes them of little use. The phosphor screen has proven to be vital for the alignment procedure of the high energy electron gun.

The UV detector is mounted in a custom cavity that accommodates the square shape of the detector and two pins necessary for measuring the current output of the detector. The UV detector is a stable, high quantum efficiency AXUV-100G photodiode (International Radiation Detectors Inc.) that utilizes a p-n junction to produce a current from the excitation of electron-hole pairs. The current was measured from the p-region (anode) with the n-region (cathode) grounded.

Subsection 2. Motion and alignment

The sample stage can move along three perpendicular axes, rotate around its main column, and tilt at the top of the chamber. Planar motion (± 12.5 mm in the X and Y) and full 360° rotation are accomplished with a high precision manipulator (Varian model 891-2536). The Z-axis of the Varian manipulator is kept fixed and a 12- inch Z translation stage (McAllister model BLT27S-12) is used to move the stage between the upper AES/SEM level of the chamber and the lower experimental level of the chamber. Computer control of the Z translation with a stepper motor will soon be implemented through the work of Nielson, Reddy, Willey, and Chang. The tilt is accomplished via four gimbles on a tilt stage (McAllister McTilt 200) between the two

other manipulators.

Of these degrees of freedom, the tilt was the most difficult to align. Alignment was achieved by repeatedly rotating the stage and viewing the bottom of the stage in relation to cross-hairs etched in plexiglass on two perpendicular ports of the chamber (see ports L7 and L14 in Appendix A). This alignment uncovered a misalignment of the central rod of the stage and platform to which the stage is attached. The flaw is inherent in the manufacturing of the original rod and platform, but only accounts for ±0.5 mm variation in height as the stage completes a full rotation. After the tilt was aligned, the center of the XY plane could also be found by rotating repeatedly between perpendicular ports; however, XY alignment was accomplished by aligning the focal point of the cylindrical mirror analyzer (CMA). The CMA is very sensitive to variations in the distance to the sample and must be aligned carefully to maximize electron counts for a good AES spectra. Since the original design of the chamber put the CMA's tip-to-sample distance to within the precision of ±0.5 mm, which is better than aligning by eye, the later distance was chosen. Aligning the Z-axis is comparatively easy using the above mentioned cross-hairs and a long sighting tube to avoid uncertainty due to parallax. If the stage were perfectly aligned, the rotation from one sample to the next should then be multiples of 30°, but experience has proven the cable that conducts the currents from the electron energy analyzer can apply torque to the stage and led to gross misalignment. The resolution of the manipulators controlling the stage is on the order of ±0.1 mm translation and ±0.1° rotation and is

much less than the uncertainty in the stage alignment, which is typically ±0.5 mm and ±1°. Again, torques produced by the electron analyzer cabling can affect the alignment of the stage, but can be returned to normal with repeated rotation of the stage until the cable moves into a suitable position at the bottom of the chamber. Any modest misalignment of these degrees of freedom can be overcome by adjusting the source beam's deflection.

Section D. Source Beams

The chamber is equipped with sources of electrons, ions and photons. Two electron guns cover the low and high electron energies, a highly focused ion gun is used to study SE emission due to ion bombardment, another ion gun is used for sample sputtering, and two light sources are focused through a monochromator onto the sample to cover the near infrared, visible and UV electromagnetic spectrum. Table 3.1 summarizes the source beams used in this dissertation work. The energy ranges of the electron guns, especially the 30 keV range of the high energy electron gun, were chosen to model the energies of electrons in the earth's plasma that contribute to the problem of spacecraft charging. An overlap in the energies of the low and high energy electron guns was anticipated, but discharging and current limiting problems that will be discussed in the following subsections led to a gap between the energies of the two electron guns. For the purposes of this dissertation, the two electron guns and the light sources will be discussed in detail.

Subsection 1. Conrad gun

The electron gun used for a low energy electron beam is the third generation of a low energy electron diffraction (LEED) gun originally designed by Conrad (Cao and Conrad, 1989). A simplified drawing of the electron gun's electron optics is shown in Fig. 3.10. The gun uses on a LaB_6 filament (Kimball model ES-423E) and uses an extraction voltage to enhance emission and focus the spot on the target. Three einzel lenses (E1, E2, and E3 in Fig. 3.10) act to focus the beam further. The power supply design is novel in that the voltages supplied to these einzel lenses are a constant fraction of the beam energy. This unipotential design minimizes the need for the operator to make adjustments to the lens voltages to maintain focus while varying the beam energy (Clothier, 1991). A schematic of the modified power supply designed and built by Chad Fish, a member of our group, is shown in Fig. 3.11 (Fish, 1998).

TABLE 3.1: Summary of source beams

Source	Particle Type	Energy Range	Typical Operating Current
Conrad	electron	10-1000 eV	0-20 nA
HEED	electron	4-30 keV	0-20 nA (μA capacity)
VG Cold Cathode	ion (argon)	0-5 keV	~ μA range
Quartz Halogen	photon	Near IR to Visible 2000-300 nm 0.6-4.1 eV	N/A
Deuterium	photon	Visible to UV 400-125 nm 3.1-10 eV	N/A

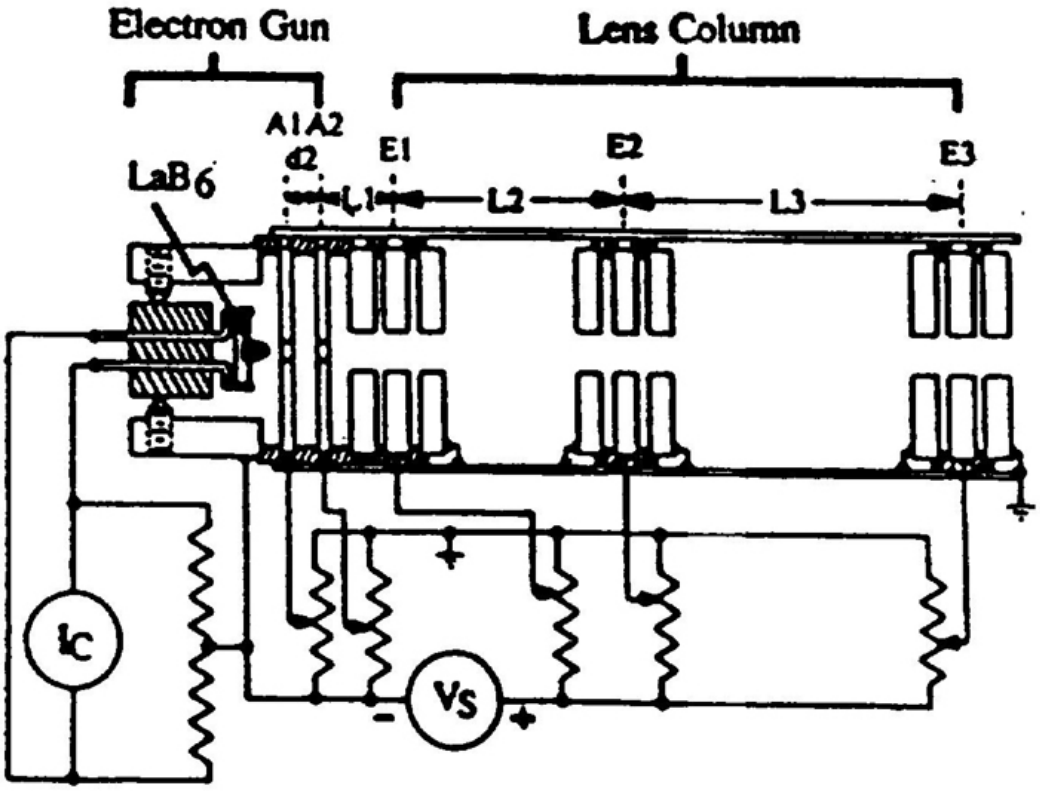


FIG. 3.10: Drawing of Conrad gun and lens column. Reprinted with permission from Cao, Y., and E. H. Conrad, 1989, "High q-resolution gun for low energy electron diffraction," Rev. Sci. Instrum. **60**, 2642-2645. Copyright 1989, American Institute of Physics. The LaB6 cathode is indirectly heated and the base is positioned using three set screws. The first anode A1 serves to extract the beam, while the second anode A2 serves to collimate the beam. The three einzel lenses, E1-E3, serve to further focus the beam. The distances, d2 and L1-L3, are beyond the scope of the present work. See Clothier (1991). The power supply is included in rough detail to give perspective. See Fish (1998). The electron energy is controlled by the supply voltage V_s. The cathode temperature is set by the current supply I_c.

The first anode control circuit has been revised so the extraction voltage can be adjusted independent of beam energy, which has proven useful to maximize the beam current. The other settings that optimize the beam current and focus the spot are as

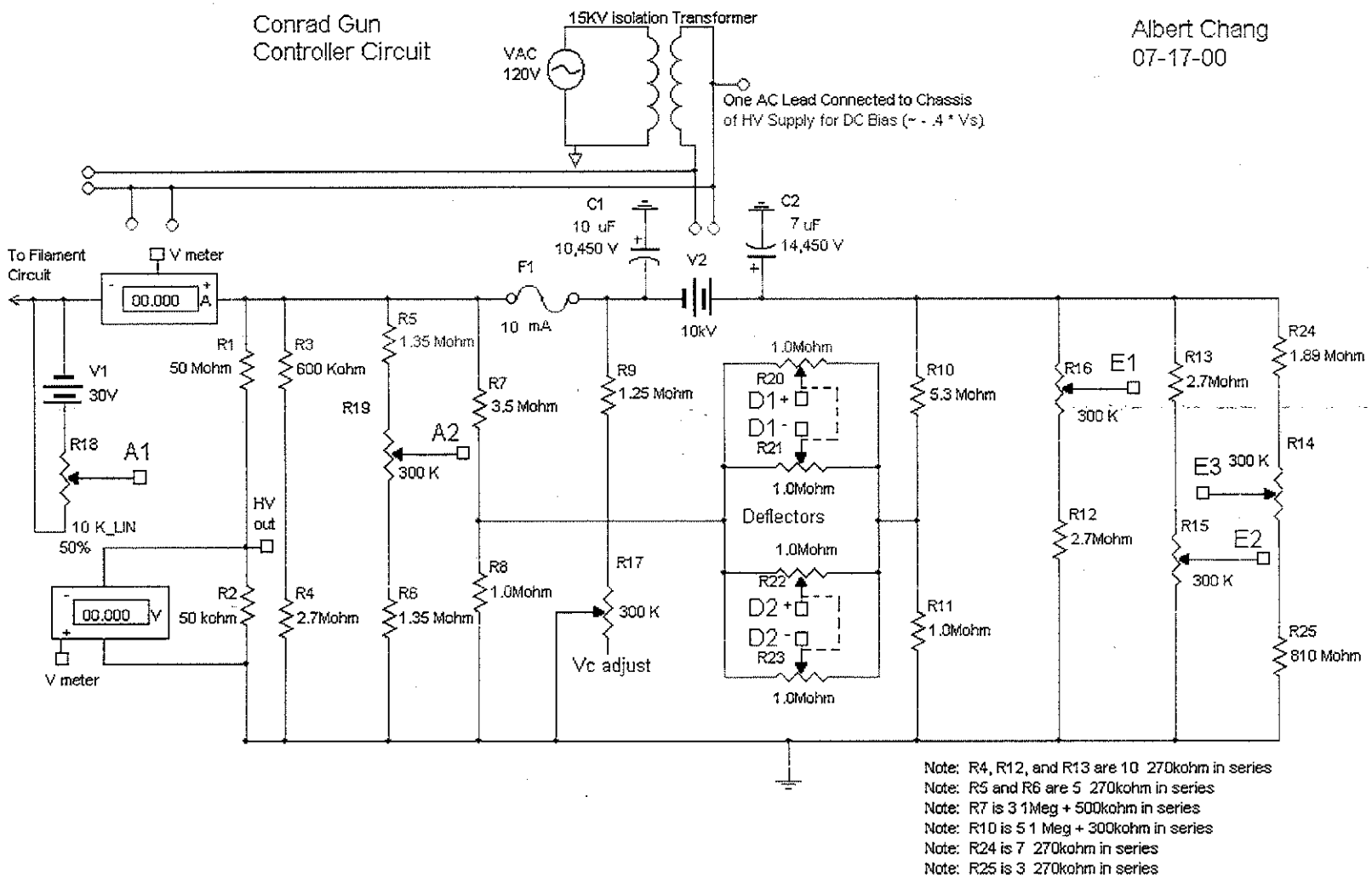


FIG. 3.11: Conrad gun power supply schematic.

follows: A1 = +15 VDC, A2 = 45% of V_c, E1 = -150% V_c, E2 = -15% V_c, and E3 = -45% V_c.

Since the Conrad gun was originally designed for LEED, the fact the gun operates at extremely low energy (down to 10 eV), but is limited at high energy is no surprise. The high energy limit over 1000 eV is caused by electrical breakdown that is thought to occur inside the filament housing of the gun. The energy spread of the gun, gleaned from the half width-half max of the inelastic BSE peak, is roughly 2.5% of the beam energy. Subsection 3.E.2 has details of this energy spread measurement.

The beam spot is adequately focused in comparison to 1 cm diameter samples, the 5 mm Faraday cup aperture, and the 5 mm ID beam pipe of the SE detector. As shown in Fig. 3.12, the beam profile was studied as a function of beam energy, which shows little variation. Beam profiles were measured by passing the edge of the Faraday cup in front of the beam spot. The plateau in the beam profile indicates the beam is inside the Faraday cup and the distance between the plateau and the background signal is the width of the beam. Notice that beam profiles were conducted in both directions because of a suspected anisotropy in the beam's shape. Using the six measurements of the beam width in Fig. 3.12, the spot size is 3.1 mm ± 0.4 mm. The beam is not perfectly round and the horizontal profile is roughly 4 mm, estimated by viewing the width in comparison to the known vertical profile on the phosphor screen.

Further studies of the electron beam behavior were carried out using the

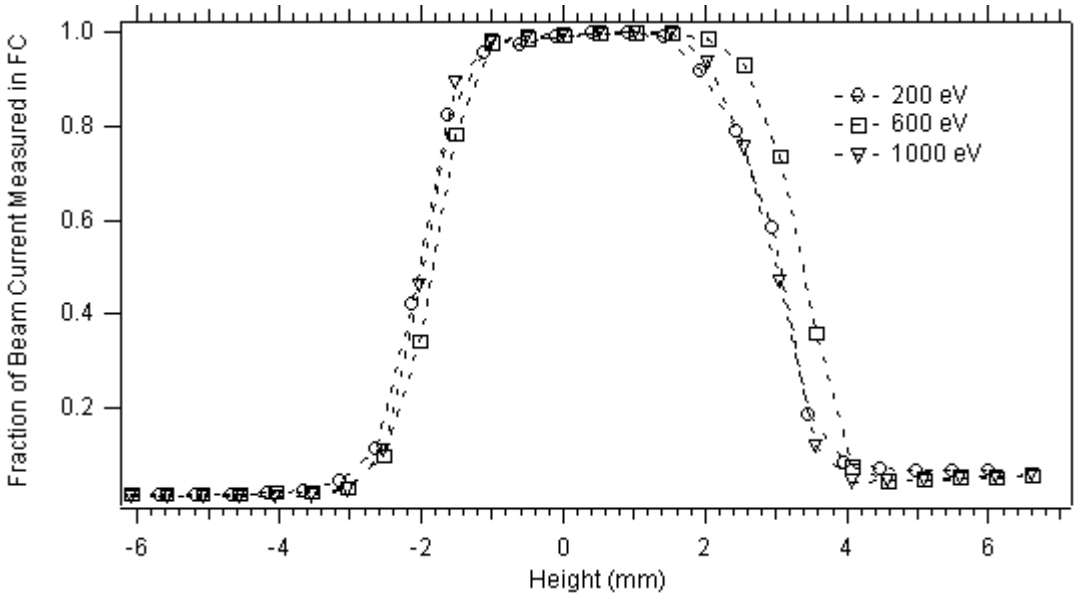


FIG. 3.12: Conrad gun beam profiles at three different beam energies. The zero point of the micrometer height is arbitrary.

SimIon™ charged particle beam modeling program. The basic geometry of the Conrad gun was reproduced and operating potentials discussed above were given to the appropriate surfaces. Figure 3.13 shows the trajectories of a beam of electrons in the gun column. The model shows a significant portion of the beam is lost due to divergence between the einzel lens elements, but the beam leaves the gun well collimated.

Beam currents in the 20-nA range were chosen as a compromise between low enough beam current densities that avoid contaminating the sample and beam currents that would maximize the resolution of the electrometers. Based on typical beam profiles (see Fig. 3.12), beam currents less than 20 nA lead to a beam current density of less than 2 $\mu A/cm^2$, well below the carbon contamination threshold (Chang *et al.*,

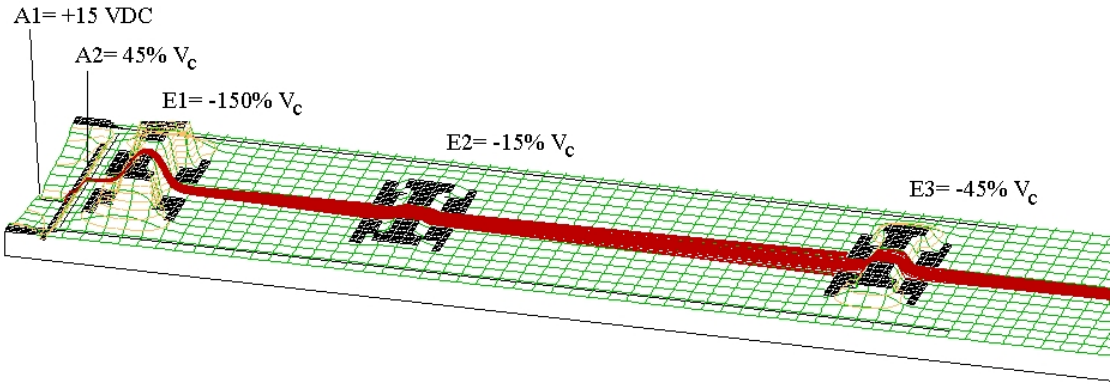


FIG. 3.13: SimIon model of Conrad gun beam column. The relief is indicative of the potential relative to the cathode voltage Vc, which happens to be 500 eV. Notice the divergence of the beam between einzel lenses E1-E3, but the relative collimation as it leaves the gun.

2000). Beam currents near 20 nA maximize the 20 nA scale on the Keithley model 619 electrometer used to measure the collector current. The custom-built electrometer used to measure the beam current via the Faraday cup has a 50-nA full scale current reading.

Once the electron gun has been allowed to warm up for 30-60 minutes, the stability of the beam is adequate over the time scale for a single measurement, which is roughly 3 minutes using the Faraday cup and only 20 seconds using the current summation technique. The typical standard deviation in the average of the beam current measured in the Faraday cup before and after a yield measurement (~ 2 minutes apart) exhibits a 1% variation. Typical variations in the beam current during the yield measurement itself have been shown to be less than 1%. Details of the two

techniques for measuring yields are discussed in Section 4.A. There is also an RC decay time as the beam current changes with energy, which is likely due to the large capacitors in the Conrad gun power supply that filter out AC fluctuations, but this relaxation time is less than a minute.

Subsection 2. HEED gun

The high energy electron gun is a commercial gun and power supply for high energy electron diffraction (HEED) (Kimball ERG-21). Similar to the low energy gun, the HEED gun also uses a LaB_6 filament. In contrast with the low energy gun, the HEED gun does not use an extraction voltage, but rather uses the first aperture to suppress emission. The HEED gun is much more flexible than the Conrad gun in that the filament housing has the ability to be mechanically aligned and the beam can be electrically aligned as well.

The gun is designed for use as a high energy electron source and its use at 30 keV is only limited by beam instability due to arc discharges inside the gun. Typical beam instabilities have limited usage to less than 20 keV. As the gun approaches relatively low energies below 5 keV, the gun begins to suffer from space charge limiting. The gun was initially thought to suffer from rollers within a UHV valve in the beam line that magnetized after the valve was used repeatedly; however, the magnetized valve only affected the overall efficiency of the gun by throwing off its ability to be precisely aligned. The real reason is that, at these lower energies, a larger fraction of the charge emitted from the filament begins to remain in the filament

housing due to the decreasing extraction field penetration into the housing. As space charge builds up in the housing, a potential gradient develops that limits the efficiency of the emission to a point where an emitted electron is not accelerated past the first aperture. Reaching energies near 4 keV is fairly typical, but is dependent on the gun's condition, which can change with each vacuum break. The energy spread has not been measured directly, but the output of the power supply only has a 2 mV peak to peak ripple, which is a negligible deviation at 5 keV [Fatman lab notebook II, p. 024y].

The beam diameter is variable with the magnetic lens in the nose of the gun. A set of beam profiles taken by using the Faraday cup as a sharp edge is shown in Fig. 3.14. As with the Conrad gun, the beam profile was measured by passing the edge of the Faraday cup in front of the beam spot. The beam spot can be a minimum of 180 microns, but was typically kept at 800 microns to avoid high beam current densities.

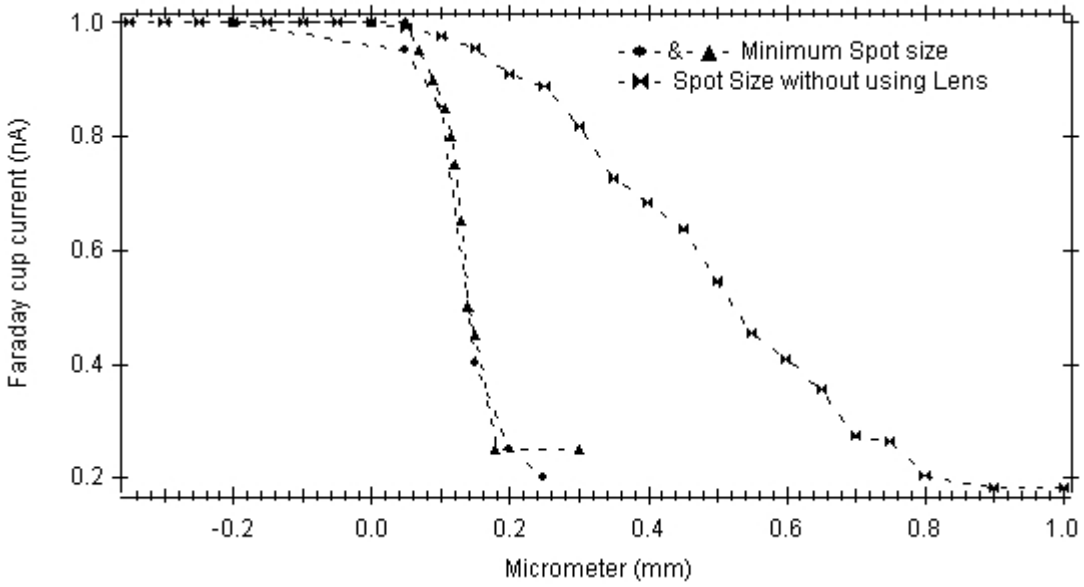


FIG. 3.14: Beam spot of HEED gun showing minimum spot size and without focusing.

Figure. 3.14 shows the effect on beam size of the focusing lens. Using the same logic as with the Conrad gun, beam currents were kept below 20 nA and the resulting beam current densities where always below 4 $\mu A/cm^2$.

The stability of the HEED gun is slightly better than the Conrad gun, with average deviations during the course of a measurement varying less than 0.5%. Even when the beam current changes, the ratio of the beam current to the emission current, or the efficiency of the gun, has been shown to be even more stable (varying less than 0.4% over the course of 10 minutes). By knowing the efficiency and monitoring the emission of the gun, the beam current can be predicted when the beam is not in the Faraday cup by multiplying the emission current by the efficiency. Work was done to show the efficiency varied linearly with the beam energy if the electrical alignment of the gun was maximized at each energy. Additional progress was made to fully characterize the electrical alignment needed to maximize the beam current at each energy of interest, but the work was abandoned after tests showed that a summation of all the currents within the electron energy analyzer estimated the beam current to within 3% of the Faraday cup current with a precision of better than 0.5%.

Subsection 3. Light sources

As summarized in Table 3.1, a quartz halogen and deuterium lamp were employed to provide a range of photon energies between 0.6 eV to roughly 10 eV. The near infrared to visible light spectrum (0.6 eV to 4.1 eV) was produced by a 100-W tungsten/halogen lamp (Sciencetech model TH1), while the visible to ultraviolet

light spectrum (3.1 eV to 10 eV) was produced by 30-W deuterium RF-powered continuum source (Hamamatsu model L7292). The range of the deuterium lamp was restricted to roughly 7 eV due to absorption from air leaking into the nitrogen purged housing for the beam line. The important energy range around the vacuum level of the materials considered (roughly 5 eV) was easily covered by the light sources. The photon beam energy is selected by using a modified Czerny-Turner monochromator (Sciencetech 9055) with typical energy steps of 1 nm (0.01 eV) and a precision of better than 0.2 nm. A manually operated "flipping mirror" is used to select the source.

The emitted light from the monochromator is refocused on the sample with a custom-designed optical array, consisting of a FL=406 mm AlMgF2-coated concave mirror (Oriel 44550) and two UV-protected aluminum flat mirrors (BSC 5BS). The beam at the sample was visually measured to be a 5 mm x 5 mm square.

Section E. Hemispherical Retarding Field Energy Analyzer

Several methods of measuring the total, SE, and BSE yields of a material were explored during the design process that ultimately led to the use of a hemispherical retarding field energy analyzer. These various methods and the reasons behind the final choice are described in the next Subsection (3.E.1), along with a description of the constructed analyzer. The testing and characterization of the instrument is discussed in Subsection 3.E.2, which provides the basis for the reliability of the measurements to follow.

Subsection 1. Design and construction

The choice of a method for measuring the total, SE, and BSE yields of a sample was a compromise between the scientific desire to obtain high quality, absolute yields and the practical design concerns of interfacing with the high sample volume of the sample stage. A brief review of the standard methods of measuring yields will be discussed to give insight into the reasoning behind the detection method chosen for the current study.

The goal of any apparatus used to measure the total, SE, and BSE yields of a material is to separate the SE and BSE yields from the total yield. Recall that a yield is defined as the average number of total, SE, or BSE electrons per incident electron from the beam. The beam is typically measured with a Faraday cup, which was described in Section 3.C.1. Measuring the current from the sample during electron bombardment is a net current due to the beam current and the SE and BSE currents together. Since SE's are defined to have < 50 eV, the SE and BSE populations can be separated by some method of energy analysis and rejection or collection of either the low energy SE or the high energy BSE populations. There were three methods initially considered for the design of an electron yield apparatus, each with their advantages and drawbacks.

The most common method is to apply a +50 volt bias to the sample, which creates an electric field that directs the SE's back towards the sample. The SE current is then given by the difference in the sample current at +50 volts and when grounded.

The advantage of this method is the ease of implementation. A standard scanning electron microscope (SEM) is able to take this type of measurement without modification (Ruzic *et al.*, 1982; Schou, 1988). The main problem is that the electric field between the +50 volt sample and the closest grounded surface (typically the holder) do not necessarily return the SE's to the sample surface. Analysis done by Davies (1999) on a similar method estimates the error in the SE yield due to uncontrolled fields near a sample holder can be >20%. This method was not pursued in favor of the next two options.

The second method points a Faraday cup, capable of energy differentiation, at the sample in an effort to measure a portion of the SE's emitted from the surface (Davies, 1999). In contrast to the previous method, a SE is distinguished from a BSE by grounding or applying -50 volts to an aperture inside the Faraday cup, which passes or rejects the SE's. The fact that the finite solid angle of the Faraday cup only measures a fraction of all the SE's emitted from the sample is overcome by integrating over the theoretical angular distribution of SE's (Jonker, 1951). The disadvantage of this method is the assumption that the emission angle of a SE is maintained until it is detected. Previous work by our group has shown the angular distribution is distorted by electromagnetic fields that are typical in UHV chambers, even with adequate magnetic shielding (Nickles *et al.*, 1998). Another disadvantage is the necessarily small apertures of the Faraday cup result in measuring picoamp (10^{-12} amp) currents, which is complicated by signal noise (Davies, 1999). Given these concerns, this

method is feasible and even has some advantages over the method that was finally chosen.

The SE detector was designed after a hemispherical, retarding-grid energy analyzer (HGRFA) similar to the apparatus used in low energy electron diffraction (LEED) (Moore *et al.*, 1983). A cross-sectional drawing of the detector is shown in Fig. 3.15. The detailed dimensions will be discussed after a general overview of the purpose of the design is reviewed. The sample is surrounded by layers of hemispheres–beginning with an inner grid, then a suppression grid, a collecting hemisphere, and an outer cover–all attached to a circular faceplate. The collector measures nearly all the electrons emitted from the surface. In front of the collector, the suppression grid can be grounded or biased to -50 volts, which acts to pass or filter

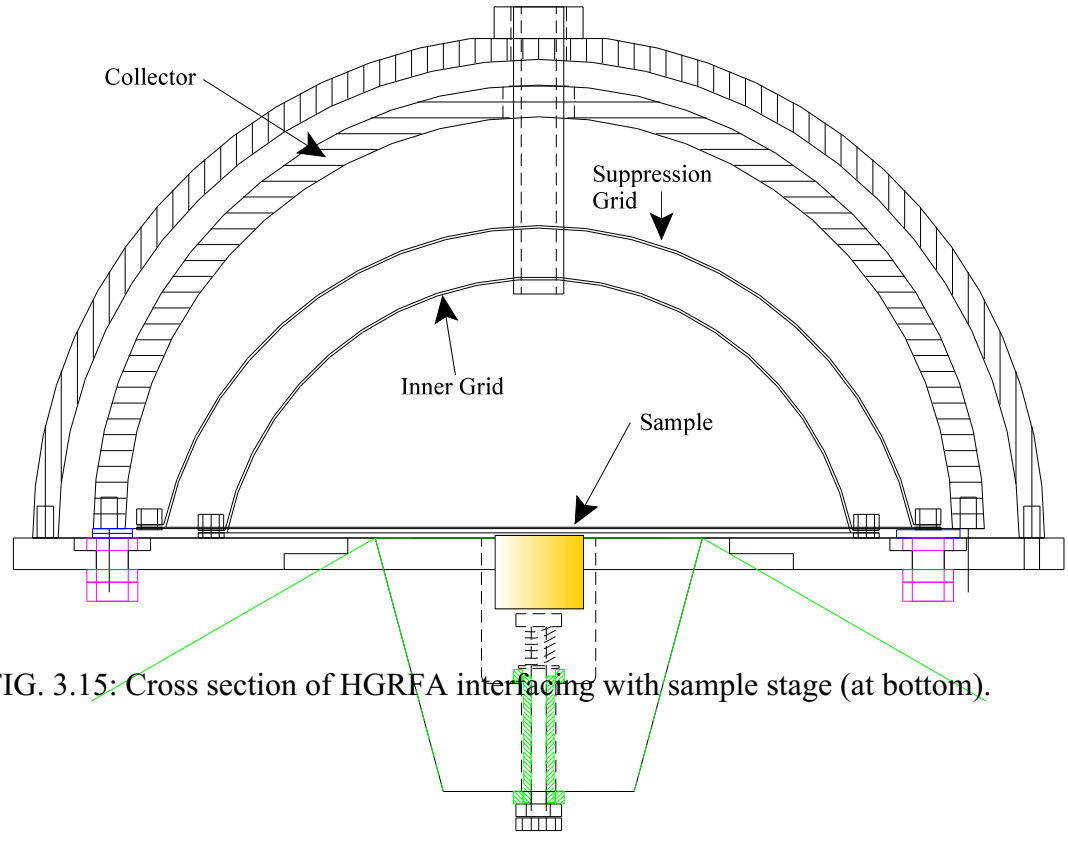


FIG. 3.15: Cross section of HGRFA interfacing with sample stage (at bottom).

out the SE current. The actual details of the SE yield measurement will be discussed in Chapter 4 on experimental methods. An inner grid at ground in front of the suppression grid ensures the fields created by voltages on the suppression grid are nearly radial, along the path of the electrons. The inner grid also creates a field free region around the sample that allows the suppression grid to be at the high potentials necessary to study BSE emission without adversely affecting the beam. A grounded tube extends from the back of the analyzer to just past the inner grid, which allows the incident electron beam to enter through the back of the detector without being affected by potentials on the suppression grid or collector.

In contrast to the Faraday cup approach, the HGRFA design does not require angular integration, the measurement of small currents, or the assumption that the SE's maintain their emission angle because the collector covers all of the 180° field of view of the sample. The main disadvantage in comparison to the Faraday cup approach is that electrons scatter off the grid wires that should otherwise be measured by the collector. These errors introduced by the HGRFA design were thought to be manageable and will be discussed in Section 4.B on error analysis.

A more typical design uses a spherical retarding grid analyzer, which obviously has a larger field of view and has the advantage of recapturing BSE emitted from the collection surface (Sternglass,1953b; Whetten, 1965; Thomas and Pattinson, 1969; Miller and Brandes, 1997). The spherical design was rejected because of practical concerns: The design restricts one to a small volume sample holder at the center of the

spherical collection surface and the placement of source beams is restricted to a vertical plane perpendicular to the samples. The HGRFA was chosen over the spherical design because it could interface with the high volume sample stage already designed and the UHV chamber accommodated the source beams in a horizontal plane around the samples. Again, the choice of the HGRFA is a compromise between the experimental concerns for high quality, absolute yield measurements and the practical concerns surrounding the sample stage and the UHV chamber.

Returning to the simplified drawing of the analyzer's cross section in Fig. 3.15, the specific dimensions and materials of the HGRFA will be reviewed. The 31.5-mm radius inner grid was custom-built from 304 stainless steel 0.004 inch diameter 20 x 20 mesh with 84% open area, following the methods outlined by Taylor (1988). The 37.6-mm radius suppression grid was built from the same wire as the inner grid and is electrically isolated from the faceplate, which allows for voltage biasing of the grid wires and the current to be monitored. Behind the suppression grid, the collecting hemisphere is a 3.18-mm thick aluminum hemispherical fence fennel, coated with Aquadag™ colloidal graphite to reduce SE production. As with the suppression grid, the collector is electrically isolated to allow for voltage biasing and current measurement. The collector is not concentric with the inner and suppression grids due to practical design and construction constraints. Encasing the collector, the outer cover is made from the same material as the collector with a slightly larger radius and is used to shield the back of the collector from stray currents. The circular faceplate to which

all the hemispheres are bolted is made of OFHC copper and the surface exposed to the interior of the HGRFA is coated with Aquadag™. The 304 stainless steel beam pipe is also coated with Aquadag™ (with 5-mm ID, 6-mm OD and 41.3-mm length) and enters through the back of the analyzer, where it is grounded to the outer cover, and reaches just past the inner grid. The whole HGRFA is designed to interface with the sample stage so the inner surface of the faceplate is aligned exactly with the surface of the sample module.

In order to access each sample in the carousel and yet still utilize the varied source beams, the HGRFA hangs from an arm on sample stage's main column that can rotate independently from the stage. A preliminary version of the detector is shown with the stage in Fig. 3.16. The analyzer rotates when this arm comes in contact with a post that is fixed in space. While the stage continues to rotate, the HGRFA stays in place and slips from one sample to the next. The HGRFA alignment with any particular sample is maintained by a pin that rests in grooves in the top plate of the sample stage (see Fig. 3.17). Once the HGRFA is aligned with the desired sample, the stage and HGRFA together rotate away from the fixed post and into position in front of the desired source beam. A spring between the HGRFA face and the arm provides tension to keep the HGRFA in line with the sample groove while moving. A picture of the completed HGRFA mounted to the sample stage inside the UHV chamber is shown in Fig. 3.17. A scale drawing of the HGRFA and the sample stage in the vacuum chamber is shown in Fig. 3.18 for perspective.

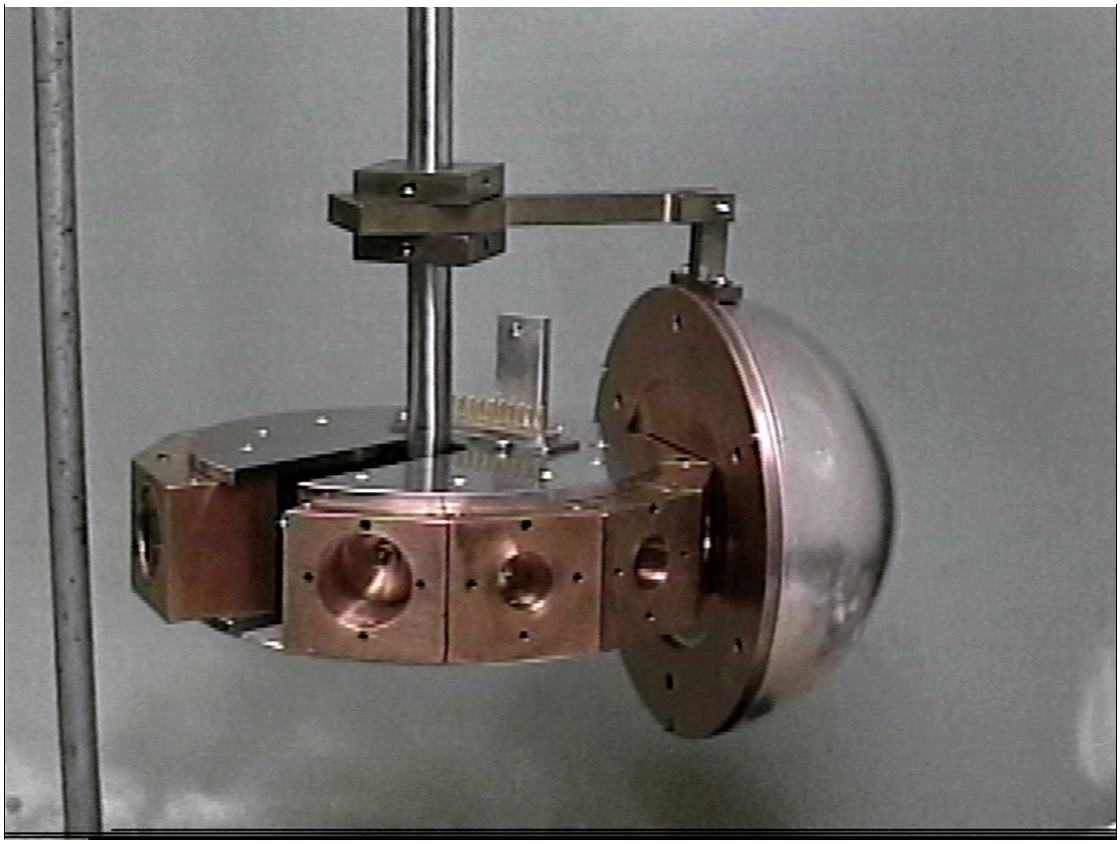


FIG. 3.16: A preliminary version of the HGRFA and sample stage, showing the detector arm.

Subsection 2. Testing and characterization

The conventional test of retarding field analyzers used for SE yield measurements is a plot of the collected current as a function of both retarding and attractive fields (Sternglass, 1953a, 1953b; Frederickson and Matthewson, 1971; Reimer and Drescher 1977). The retarding field acts to reject low energy SE's and so the collected current will tail off as more of the SE energy population fails to reach the collector. The shape of this tail will depend on the SE and BSE energies, but the conventional definition of SE means the curve should be relatively flat above 50 volts.

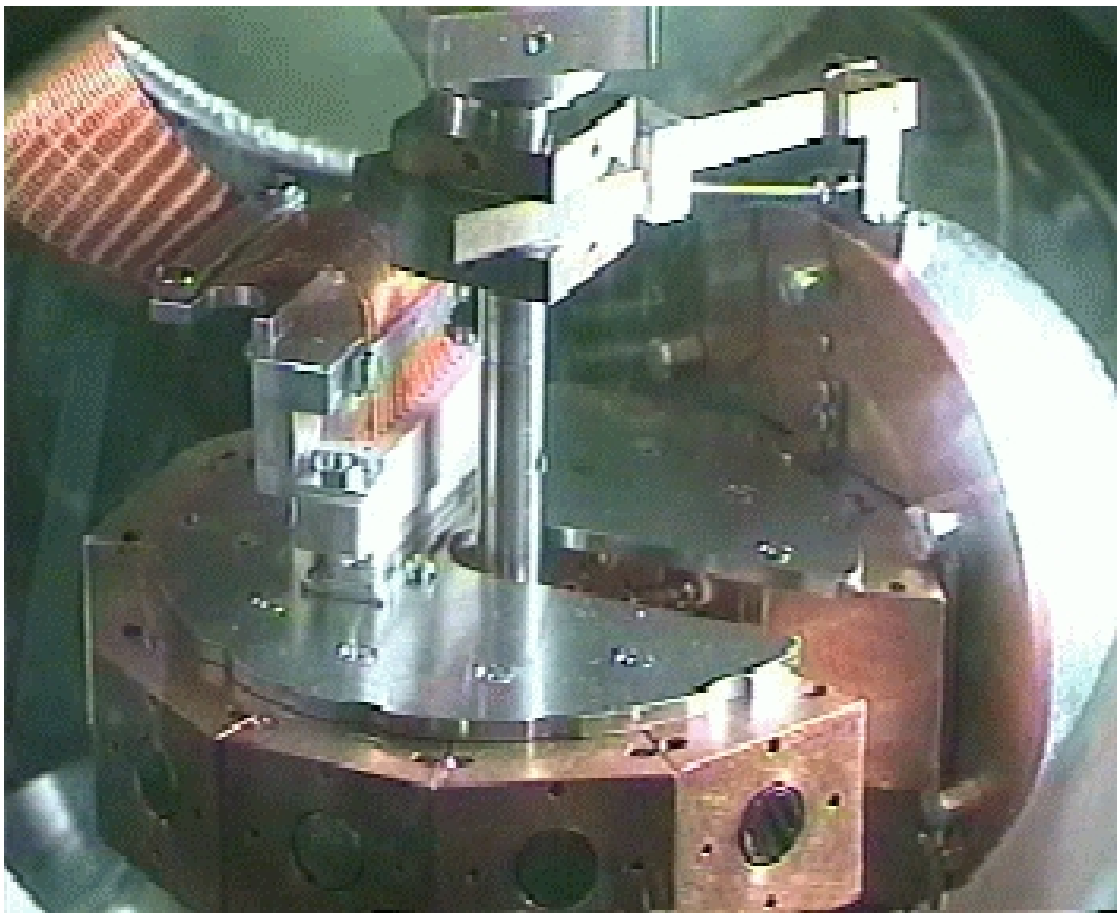


FIG. 3.17: The completed hemispherical grid retarding field analyzer.

With an attractive field, any change in collected current is due to previously uncollected electrons being focused to the collector.

In the case of the HGRFA, the plot shown in Fig. 3.19 is of collector current as a function of positive and negative voltage on the suppression grid. The HGRFA curve is compared with a similar curve from the dissertation work of Sternglass (1953a), which used a spherical detector. The collector maintains a +50 volt bias with respect to the suppression grid in order to retain SE's produced on the collector

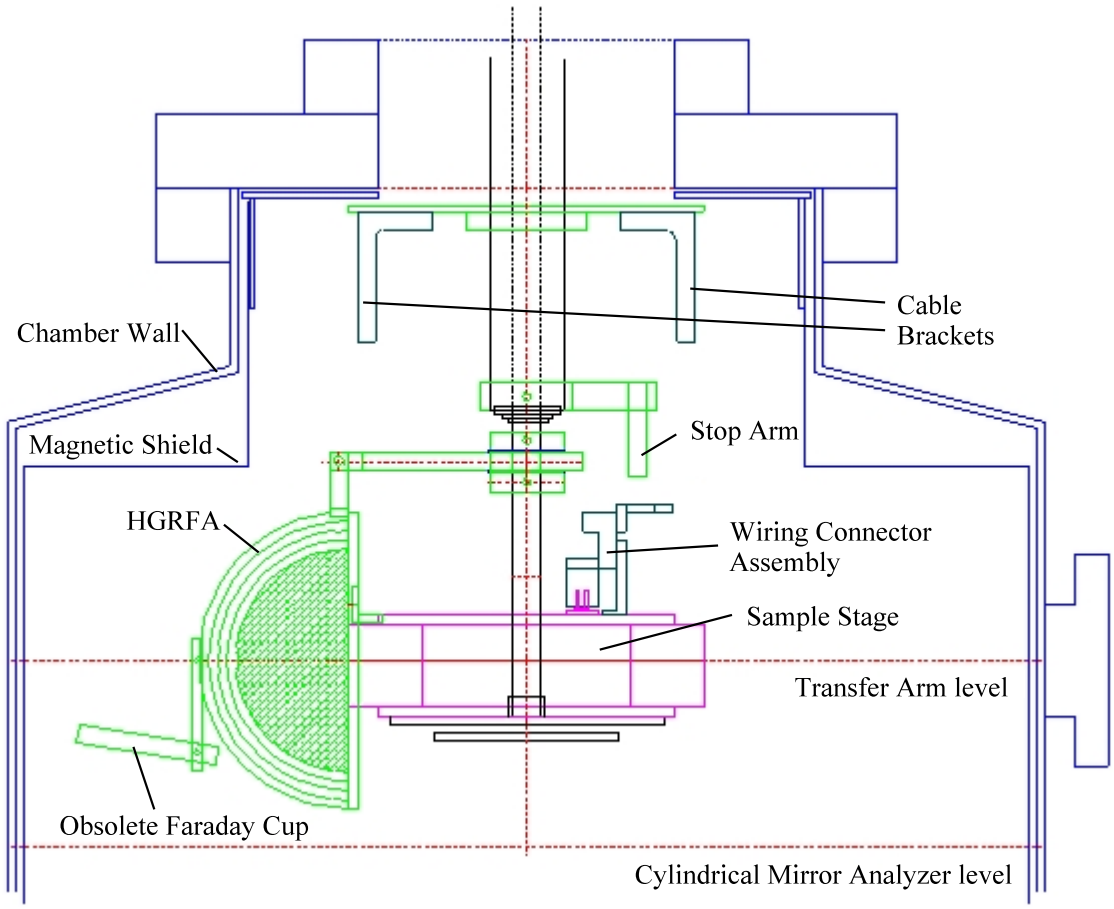


FIG. 3.18: Schematic of HGRFA in UHV chamber.

surface. The collector currents have been normalized by the beam current of each measurement separately, so differences in the total yields of each sample will offset the two curves. The HGRFA characterization was conducted with the Conrad gun at 500-eV beam energy incident on an OFHC copper sample. The Sternglass curve was measured using a tantalum sample with a 1520-eV electron beam energy. The difference in the SE yield of copper at 500 eV and tantalum at 1520 eV is on the same order as the difference in the absolute accuracy of the two detectors (Sternglass,

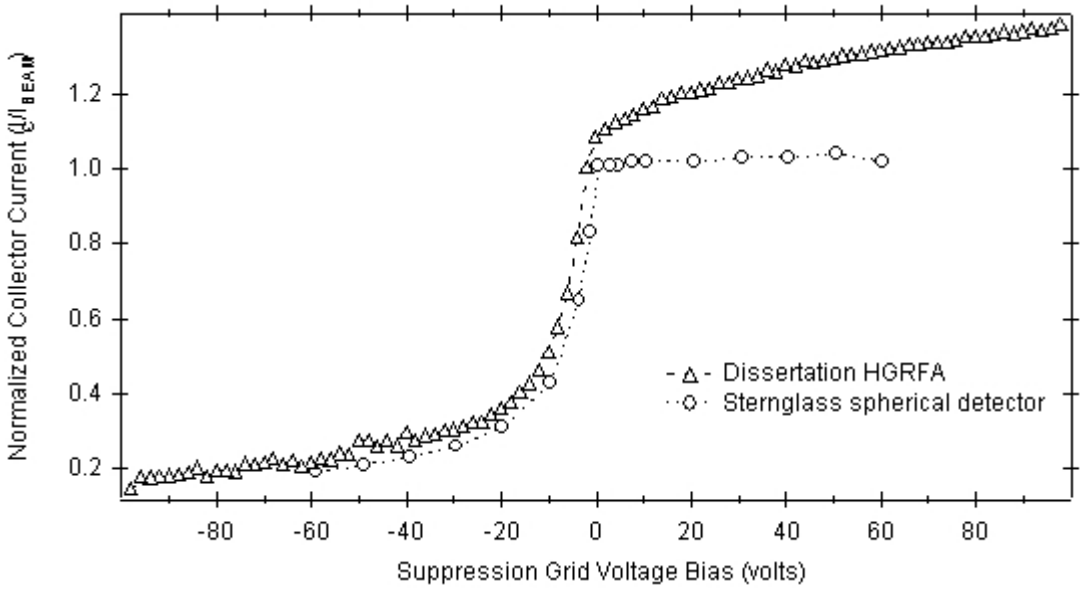


FIG. 3.19: Normalized collector current versus suppression grid voltage bias curves comparing the present HGRFA and the spherical analyzer used by Sternglass (1953b). The collectors maintain a +50-volt bias with respect to the suppression grids in both cases.

1953a), so the following discussion will refrain from comparison of the absolute scale of the curves and focus on their relative shape. The HGRFA collector current has been corrected for the drift of the electron gun current during the course of the measurement. Sternglass does make a correction for SE's produced on his suppression grid because it is part of the collection surface in his detector, but the curve in Fig. 3.19 is the uncorrected curve.

The tail of the undifferentiated SE energy distribution, which is the 0 to -100-volt region of the graph, should be characteristic of that population. Again, the conventional definition of SE's comes from the assumption there are very few SE's at and above 50 eV, which means that this tail of the curve should be relatively flat above

50 eV. Both the HRGFA and the Sternglass curve show an approximately linear increase beyond 25 eV. Sternglass does not comment on the increase in his dissertation because his correction factor for SE's produced on the suppression grid helps to flatten the curve. SE's produced on the suppression grid of the HGRFA do not affect the collected current because the suppression grid is not included in the collection surface as in the Sternglass work. The fact that the HGRFA's tail at these negative voltages has a fixed slope means the differentiated SE energy distribution will flatten at roughly 25 eV, which is consistent with typical SE energy distributions. The linear nature of the increase leads one to suspect a leakage current. The 1 nA of additional current reflects an effective resistance of roughly 10 megaohms. Experiments with the collector's leakage current, as measured under bias and without stray currents in the chamber, measures the effective resistance of the collector to be on the order of 100 teraohms. Another possible explanation could be multiply reflected BSE's that have lost enough energy so as to contaminate the SE current from the sample. A test of this theory would be to use an incident beam of extremely high energy so as to distinguish the BSE and SE populations with impunity. Another explanation is that the suppression grid is ineffectively retarding the SE population, but this seems unlikely. Poor suppression grid construction would result in poor resolution, but not a complete lack of an equal potential surface across the suppression grid and before the collector. Field penetration of that magnitude is not possible with the 1.2-mm suppression grid openings in comparison to the more than 6 mm distance

between the collector and the suppression grid.

The positive bias portion of the curve also does not flatten as expected, which does occur with the Sternglass data. Again, the exact magnitude of the disagreement is uncertain due to the unspecified beam energy of the Sternglass work. As mentioned, the most probable cause is due to current not previously collected being focused to the collector. Some focusing of SE that were previously lost by intercepting the inner and suppression grid wires was to be expected. The Sternglass curve would not reveal this behavior because his suppression grid is already part of the collection surface. In fact, the additional current collected by focusing SE's away from the suppression grid is evidence a correction factor is needed to compensate for SE's not collected at 0 volts bias due to the opacity of the suppression grid. Such a correction factor is discussed in Section 4.B on error analysis and detailed in Appendix C. An interesting experiment that would test this notion of focused SE's, which was not carried out, would be to add the HGRFA suppression grid current to the collector current.

Another troubling aspect of the HGRFA curve is that it again does not flatten beyond 50 eV, which indicates higher energy BSE that have multiply scattered are becoming part of the SE population. Another explanation is that 100 volts of positive bias does not directly translate into the focusing 100 eV electrons, which is the more likely explanation. The bias curve could not be conducted with more than a 100 volts because of the limits of the available power supply. Again, leakage current has been

ruled out. Sternglass (1953a) had similar experiences with a linear increase during positive bias, not shown here, and said the increase routinely occurred on contaminated samples and was resolved by outgassing the sample. He attributed the behavior to "field effects" without further explanation, presumably referring to contact potential differences or sample charging due to oxide layers. The OFHC copper sample had been sputtered prior to the measurement of the HGRFA collector current curve and so contamination is not an issue.

In summary, the HGRFA detector displays a different collector bias curve than the spherical collector used by Sternglass, notably the additional current collected with positive suppression grid bias. Rather than being a weakness of the HGRFA, the additional current is most likely due to the fact the suppression grid is isolated from the collector and is able to reveal the increase in collector current due to SE's focused away from the suppression grid wires that previously stopped them from reaching the collector.

The energy resolution of the HGRFA can be inferred by attempting to measure a sharp rise in collector current as a function of electron incident energy and observing the width that is actually measured. As seen in Fig. 3.20, the initial rise of the SE emission energy distribution provides a relatively sharp peak and the full width at half maximum has been measured to a resolution of 1.5 eV ± 0.4 eV, which is an upper limit of the detector's resolution. This resolution estimate is corroborated by the absence of the σ-bond peak at 7.5 eV usually observed in HOPG during higher

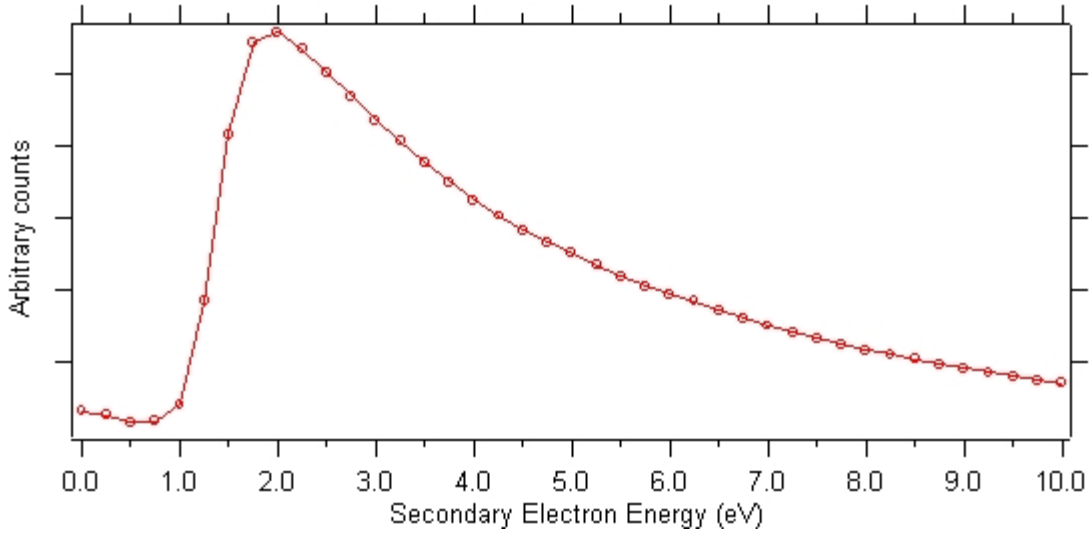


FIG. 3.20: SE energy distribution of HOPG sample used for estimate of resolution of HGRFA. The incident beam energy is 500 eV.

precision SE emission spectroscopy measurements (Oelhafen and Freeouf, 1983). An estimate of the resolution at higher energy comes from observing the inelastic BSE peak in a full electron energy spectrum, which is shown in Fig. 3.21. The BSE peak should only reflect the thermal spread of the LaB_6 filament and the energy spread of the BSE. Assuming the energy resolution is greater than both of these effects, the HGRFA resolution can be estimated from a gaussian fit to the BSE peak. The results of the fit are a full width at half maximum of 4.0 ± 0.2 eV at 81 eV incident beam energy. The results of both these estimates lead to an energy resolution of ± (1.5 eV + 4% of the beam energy) eV. The lack of better resolution is assumed to be due to the non-uniform nature of the custom-built bias grid.

Significant effort has been made to estimate the corrective factor necessary to account for SE and BSE that do not reach the collector due to the inherent geometry of

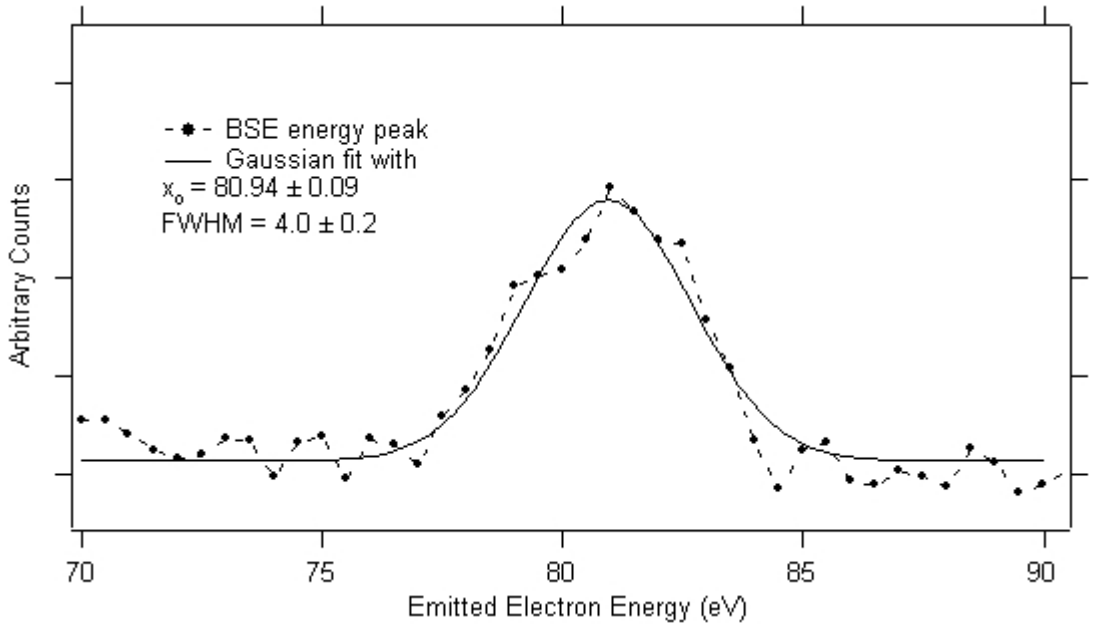


FIG. 3.21: BSE peak of polycrystalline gold using a ~ 81 eV energy beam.

the HGRFA or unwanted scatter that do reach the collector. The corrective factor is necessary to get accurate absolute SE and BSE yield measurements. A summary of this corrective factor will be discussed in Section 4.B along with an error analysis of the collector currents.

Section F. Data Acquisition System

The electronic circuitry and data acquisition will now be discussed in detail. There are two main circuits to discuss: The patch panel circuitry and the HGRFA cricuitry, which deliver currents from either the sample stage or HGRFA to an electrometer that converts the currents into voltages and then the voltages are recorded by the computer data acquisition card.

All the currents from the sample stage, which includes the stage, all the

samples, the Farday cup, and the UV detector, pass through the chamber on a 25-pin, D-type subminiature Kapton™ cable (MDC model KAP-R25) to a well shielded parallel printer cable (IEEE 1284) on the outside. The Kapton™ cable is unshielded and relies on the chamber walls for noise reduction. The external cable plugs into a panel that separates each wire to a BNC connector. Leads can be connected from any of the BNC connectors to any one of five custom made electrometers (Analog Devices 546). Unconnected leads are grounded at the BNC connectors.

The schematic in Fig.3.22 details the circuit for a single, arbitrary signal lead from the 25-pin cable as the signal is processed by the electrometer circuitry (from right to left in Fig. 3.22). The input signal enters on the shielded *SigIN* BNC input (right, Fig. 3.22). The input signal can be output to an external electrometer, connected to the *Hi/Low* output (right, Fig. 3.22), or to the internal *electrometer/isolation amplifier board* (center, Fig. 3.22). The input signal can be biased by either an external bias voltage source connected to the *ExtBias* BNC input (right, Fig. 3.22) or by a internal bias potentiometer (R18) connected across two power supplies (Lambda, model LM2200) that provide a ±60 VDC bias range. These two power supplies (bottom, Fig. 3.22) also provide ±7.5 VDC and ±15 VDC for the integrated circuits supply voltages. When using the internal bias option, the *Low* jack provides a convenient connection to monitor the bias voltage.

The electrometer and data acquisition board are protected from these potentially high common mode bias voltages by a unity gain, noninverting isolation

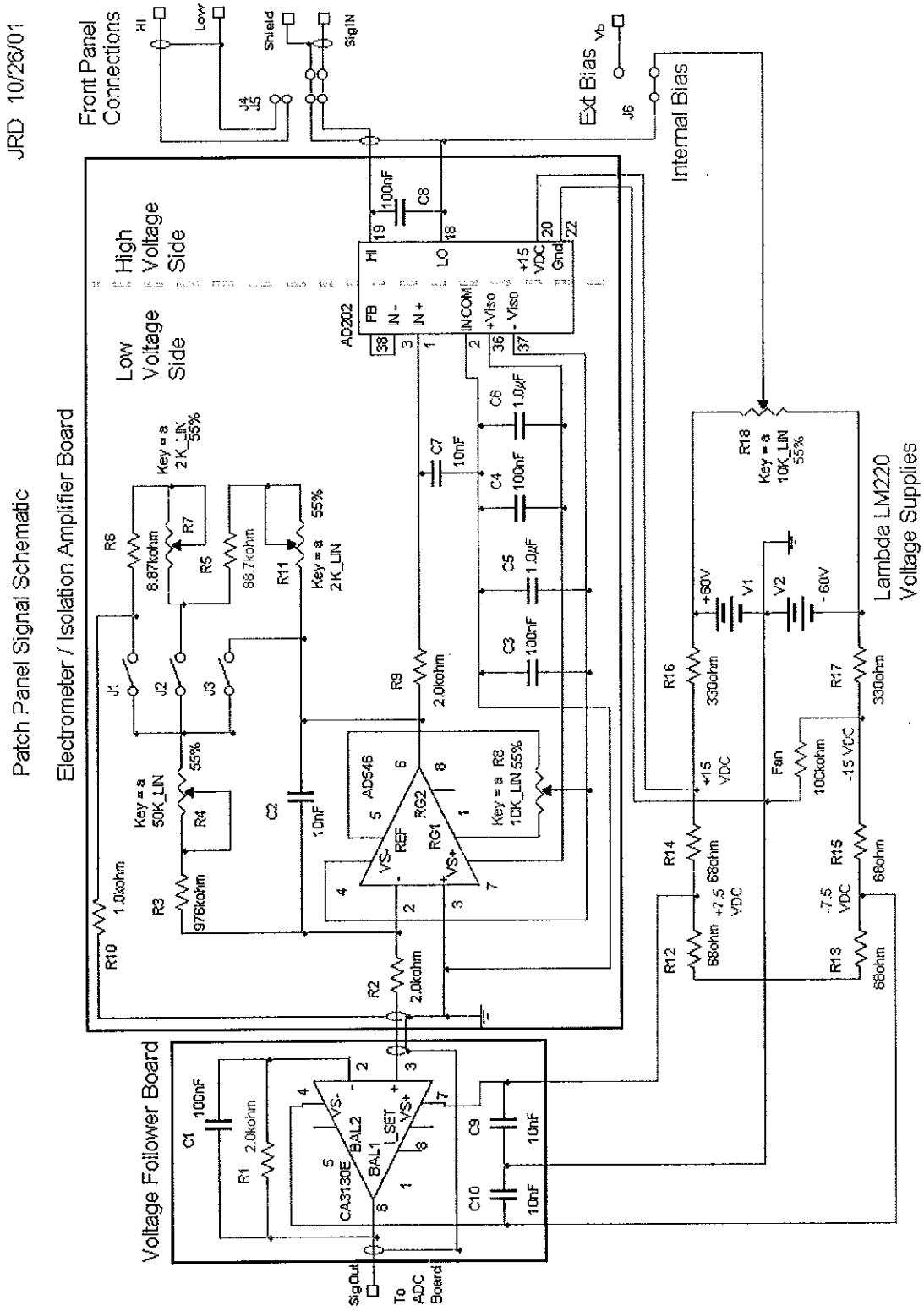


FIG. 3.22: Patch panel circuitry schematic.

amplifier (Analog Devices 202) before each electrometer that is capable of 2000-volt isolation. The isolation amplifier circuit includes a 50-kHz low pass filter on the input and a 0.1-μf capacitor between the outputs, which acts as a filter as well [FatMan II, pp. 047w & 067y]. Specifically, a signal filter is provided by C8, resulting in a typical 3-mV ripple at ±5 V output, with a signal bandwidth of ~1 kHz [refer to Fig. 13 on p. 8 of Analog Devices, 1994]. The low voltage input side of the isolation amplifier is filtered with R9 and C7, with a signal bandwidth limit of ~5 kHz [refer to Fig. 12 on p. 7 of Analog Devices, 1994]. The isolated supply voltage from the isolation amplifier used to drive the electrometer is filtered by C3-C6.

The patch panel electrometer uses a cost-effective monolithic integrated circuit (Analog Devices 546) operating in a standard current-to-voltage converter [refer to Fig. 35 on p. 10 of Analog Devices, 1989]. The electrometer current range is set by the feedback resistance factor determined by the resistance across pins 2 and 6. Closing switch SW1, SW2, or SW3 results in a fullscale range of ±50 nA with 0.01 nA resolution, ±500 nA with 0.1-nA resolution, or ±5 μA with 1-nA resolution, respectively. The feedback scheme is described in detail in Shaw (1992).

The relatively high 7-kΩ output impedance of the electrometer/isolation amplifier causes cross-talk to take place between channels of the data acquisition board which requires an input impedance of <1 kΩ. The problem with a higher source impedance is the resistance competes with the RC time constant of the multiplexer on the computer interface card, which controls the scanning of more than one signal with

the interface card. Therefore, a unity gain, low impedance operational amplifier (Intersil CA3130E) operating in the voltage follower mode follows the electrometer/isolation amplifier (left, Fig. 3.22). This voltage follower includes a 100-μf capacitor (C1) between the outputs, which again acts as a low pass filter. Final filtering is done at the input terminals for the computer analog-to-digital converter interface card (IOtech Daqboard) operating in differential analog input mode. The LO terminal for each DAC differential analog input is tied to analog common through a 100-kΩ metal foil resistor. The combined filtering limits the response time of these electrometers to roughly a second.

As shown in Fig. 3.23, the second circuit involves the collector and bias grid currents from the HGRFA. A simplistic schematic of the HGRFA is shown at left in Fig. 3.23. From the face of the HGRFA, two coaxial Kapton™-coated wires run inside a grounded shielding wire to MHV feedthroughs near the bottom of the chamber. From the MHV connectors, triaxial cables carry the currents and voltages to a dual channel electrometer (Kiethley model 619). In order to measure high energy BSE spectra, the bias grid and collector need to float to high voltage, which results in the outer shield of the MHV connection floating at high voltage. The voltage biasing of the collector and grid are actually done at the 2A input of the electrometer, which is connected to the inner shield of the triaxial connection and hence floats the shield of the coaxial cables leading back to the HGRFA. The voltage is supplied by a computer controlled voltage source (Keithley model 230), which is capable of ±110 VDC. The

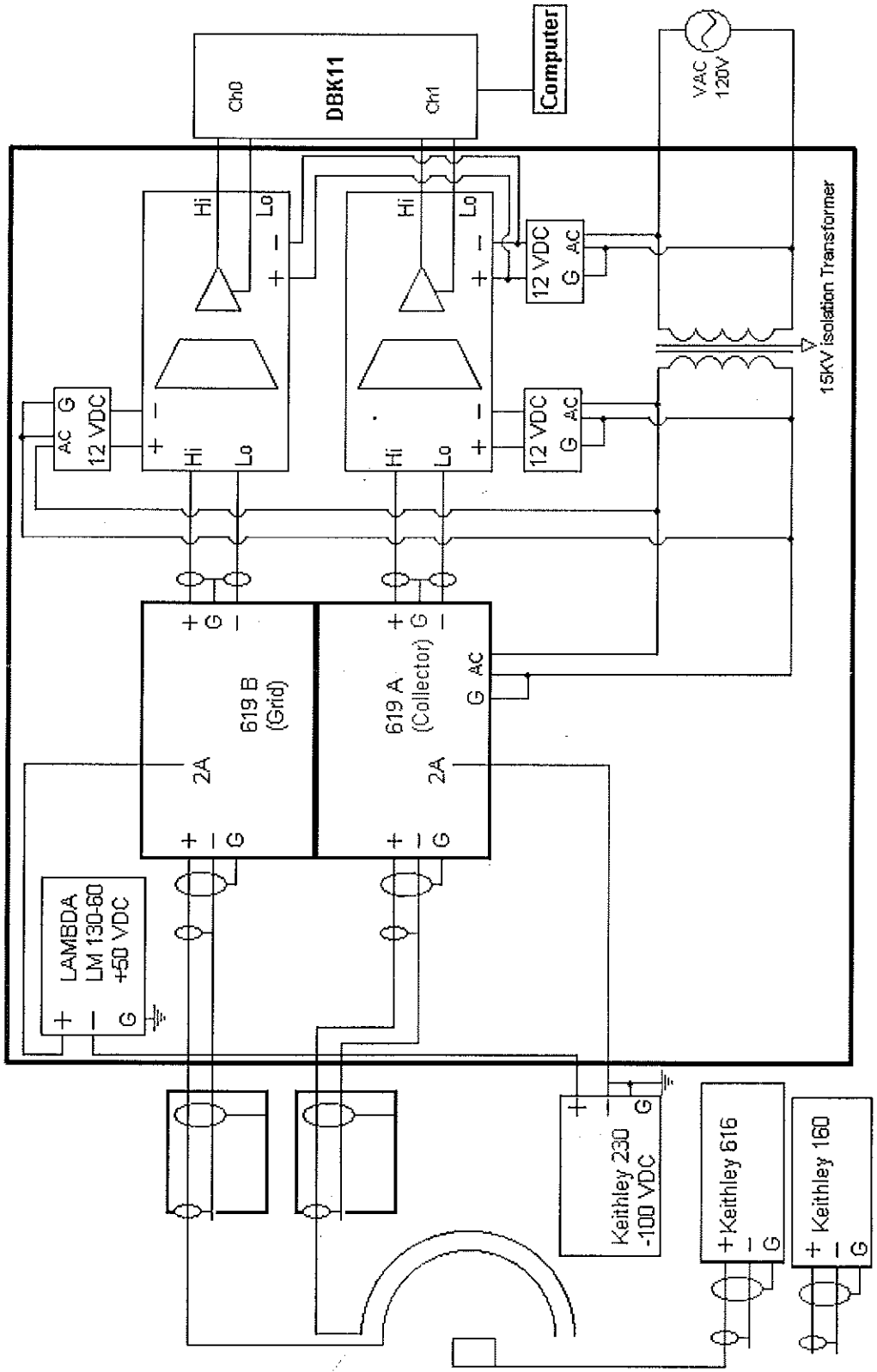


FIG. 3.23: HGRFA circuitry schematic.

suppression grid is biased with this variable voltage supply, while the collector is bias to constant +50 volts higher than the voltage delivered to the grid, using a separate supply (Lambda model LM-130-60). The electrometer can float to 250 volts, but to bias the grid and collector any higher the AC power for the electrometer is plugged into an isolation transformer which allows the case ground of the electrometer to float to 4000 rms voltage. The output voltages from the electrometer must pass through isolation amplifiers, which are capable of 3500 rms voltage isolation, to guard the data acquisition board from the high bias voltage as well. These are custom made isolation amplifiers similar to those in the patch panel, but use a different integrated circuit (Burr Brown ISO 121) capable of 3500 rms voltage isolation. Three separate 12-VDC power supplies provide operating voltages for the grid isolation amplifier high voltage side, the collector isolation amplifier high voltage side, and the isolation amplifier low voltage side.

Once the currents have passed through the 619 or patch panel electrometers, the outputed analog voltages are sampled with a data acquisition card (Iotech daqboard 200A) controlled by a Pentium PC running Windows 95 and using LabView graphical interface instrumentation control software. The data acquisition board has 16 channels capable of 16-bit analog-to-digital conversion at a maximum sample rate of 100 kHz. The 16-bit analog-to-digital conversion results in a resolution of roughly 0.004%, which far exceeds the expectations for noise reduction of the measured currents. The 16 channels are wired as eight differential inputs with the negative side referenced to

ground through an 100 kΩ, 1% accuracy metal film resistor. With all eight channels enabled, sampling is conducted at 10 kHz with a 50-μsec delay between sampling the channels to allow for the computer's RAM buffer to assimilate the information. Faster sampling is feasible, but was deemed unnecessary given the static nature of the signals.

The basis for each measurement in LabView is an average of 10,000 samples. The Kiethley 619 electrometer additionally averages four analog-to-digital conversions at 60 Hz. Subsequent analysis has shown this large amount of sampling at such a high acquisition rate leads to a correlation between the individual measurements. Specifically, the standard deviation of the 10,000 point mean is less than the standard deviation of 100 such means. The standard deviation was therefore used, rather than the standard deviation of the mean, as an estimate of the error in a 10,000 point mean, which is an overestimate of the error. While the standard deviation of the mean would have resulted in 1% of the standard deviation, analysis of the error after the collection of the data shows the standard deviation was typically a factor of 2-3 times larger than the error in repeated measurements. When low beam currents were used, the standard deviation could be 10 times larger than estimates of the error from repeated measurements. A better sampling scheme would be to take repeated measurements of a smaller number of points and then use the standard deviation of the mean for the repeated measurement (e.g., 20 measurements of 3,000 samples).

Noise in all the signals could not be reduced to negligible amounts. The average standard deviation in the signal of the collector, the suppression grid, the stage, and the sample are reported in Table 3.2 along with an estimation of the linear growth in the noise with increasing current. The intercepts of these linear fits, or the background noise suffered when the signals are low, become significant when the measured currents are below 2 nA. The background noise on the collector current signal will prove to be the driving source of error, as will be discussed in Section 4.B on error analysis. The noise in the stage and sample currents, measured with the custom-built electrometers, is due to unfiltered 60-Hz pickup and shot noise presumably from the circuit boards themselves. The noise in the collector and grid currents, measured with the Kiethley 619, are not likely due to problems with the electrometer. Using a clean input signal, the Kiethley 619 only displays a 6-7 mV ripple on its 2.5-volt output [Fatman III lab notebook, p. 033y]. The noise probably originates from within the biasing electronics associated with the electrometer, but 60-Hz pickup from the current wires in the vacuum chamber has also not been ruled out.

TABLE 3.2: Error in current signals from linear fit to standard deviations over the typical range of measurement

Current Signal	Background Noise (intercept)	Linear growth with Signal (slope)	Typical Signal Range
Collector	0.08 nA	0.01 nA	0 to 25 nA
Grid	0.08 nA	0.002 nA	-0.6 to 0.4 nA
Stage	0.4 nA	0.008 nA	0 to 20 nA
Sample	0.4 nA	0.07 nA	0 to 10 nA

The error was not resolved before measurements were conducted because the collector currents were anticipated to be nearly 20 nA, which puts the background noise below 1%.

CHAPTER 4

EXPERIMENTAL METHODS

The following sections discuss the experimental procedures and error analysis. The next section will cover the process of measuring signals used to determine the total, SE, and BSE yields. In addition, the measurement of the SE energy distribution and photoyield will be discussed. This includes the computational approaches to convert measured raw data to yield values and a description of the data acquisition algorithms. The second section presents detailed error analysis of these measurements.

Section A. Measurement Technique

The measurement of the total, BSE, and SE yields – quantities discussed in theory in Section 2.A of the background section on SE emission – are determined in practice through the measurement of currents produced by the respective populations of electrons emitted from the sample, as normalized by the incident beam current I_{beam}. Using the HGRFA, the determination of the total yield σ is accomplished by measuring the current to the collector surface while the suppression grid is grounded $I_c(0V)$.

$$\sigma = \frac{I_C(0V)}{I_{beam}} \tag{4.1}$$

The collector surface is the hemisphere behind the suppression grid and does not include either the inner or suppression grids. Other measurements schemes in the literature do include the grid currents in $I_c(0V)$ (Sternglass, 1953a; Thomas and Pattinson, 1969). The measurement of currents in Eq. 4.1 introduces the aspect of time, with the inherent assumption the two currents do not vary appreciably over the time taken for their measurement. The veracity of these assumptions will be discussed in Section 4.B when the error analysis is considered.

Measurement of the BSE yield η requires the exclusion of the SE's from the total current, which is accomplished with a -50 volt bias on the suppression grid. The current measured on the collector while the supression grid is biased to -50 volts $I_c(-50V)$ is then the BSE current and can be written as

$$\eta = \frac{I_c(-50V)}{I_{beam}}. \tag{4.2}$$

The SE yield δ is calculated from these two measurements by taking the difference between the total yield and the BSE yield as follows:

$$\delta = \sigma - \eta = \frac{I_c(0V) - I_c(-50V)}{I_{beam}}. \tag{4.3}$$

All three yield curves can be determined by measuring the three currents in the above equation as a function of incident beam energy. Measuring these currents is a

combination of manual and computer-automated processes. The automated data acquisition is controlled by a LabView virtual instrument (VI) program, which is discussed thoroughly in Appendix D and is summarized here.

The total and BSE currents are averages measured on the collector during two separate voltage bias schemes for the suppression grid and collector surface. First, the variable voltage power supply used to bias the suppression grid is grounded and the current to the collector is measured. This is the collection mode and is related to total emission current through Eq. 4.1. The collector surface is always biased +50 volts with respect to the suppression grid so an attractive field to the collector retains all the SE's produced on the collector. The collector needs to act as a measure of the current impinging on the surface without losing current to subsequent SE production. After the total current is measured, the suppression grid is biased to -50 volts and the collector current is measured again. This is the suppression mode and is related to the BSE current through Eq. 4.2. The measurement of each quantity only takes 1 second and there is a built-in 5-second pause after each voltage adjustment. Including the minimal time taken for the LabView program to communicate with the DAQ board, the measurement of the yield current during the two mode is accomplished in less than 20 seconds. Both the collection and suppression mode collector currents, including their associated random errors, are recorded for the eventual calculations that lead to the total, SE, and BSE yields once the beam current has been measured.

The beam current is measured as the sum of all the currents to surfaces within

the HGRFA, which include the collector, the bias grid, the stage, and the sample. Recall that the inner grid of the detector is grounded to the faceplate and the faceplate touches the sample stage; therefore, the stage current includes all those surfaces. Charge conservation is approximately maintained in that only a small fraction of the beam current is thought to be able to leave the HGRFA without hitting one of these surfaces (e.g., through the beam pipe). To account for temporal variations in the currents, the beam current is actually taken as the mean of the summed current during the collection and suppression modes with the HGRFA. The actual variation in the beam current during these measurements is minor because less than 20 seconds transpires as mentioned. Error in the beam current will be discussed in detail during the next section on error analysis.

Another method for measuring the beam current used for diagnostic purposes is to use the Faraday cup module. Since that module is in a different location on the sample carousel than the sample, the stage must be rotated between the Faraday cup and the sample with the detector in front both before and after the yield currents are measured. To infer the beam current at the moment when the collector current is being measured, an average is taken between the Faraday cup current measured before and after the collector current is measured. The time from the initial measurement of the beam current in the FC, rotating to and from the detector, and completing the second beam current measurement took an average of 3 minutes. The beam current is assumed to vary little and at most monotonically during the rotation. The former will

be shown to be the case in the next section on error analysis for both electron guns. Since the center of the Faraday cup and the center of the HGRFA beam pipe are not necessarily aligned so that a rotation alone moves from one to the other, the electron gun's deflection is used to maximize the Faraday cup or sample current before each measurement. Maximizing the sample current was chosen over maximizing the collector current because the sample current is larger for most points along a yield curve.

As an improvement to the FC measurement technique, the emission current of the HEED gun can actually be monitored during the time that the HGRFA is being used, which can also be used to determine the beam current. The ratio of the beam current to the emission current gives the gun efficiency. By knowing the efficiency of the gun before and after a measurement, the beam current can be inferred by measuring of the emission current at the time of the HGRFA measurements and multiplying by the mean efficiency of the gun. Experience has shown this level of effort and sophistication was unnecessary in comparison to using the sum of the currents within the HGRFA. The variation in the efficiency of the HEED gun over the average time to make a yield measurement with the FC (3 minutes) is only slightly less than the 0.5% maximum variation seen in using the current sum technique with the HEED gun.

Given the choice between the two methods of measuring the beam current, the data presented in this dissertation uses the current summation technique because of the

relative ease of the measurement. The Faraday cup measurement has been discussed and is detailed in Appendix B because it is the basis for the confidence in the current sum technique. Although the FC is the most reliable measurement of the beam current, the two methods have been compared and the small absolute error in the current sum technique will be discussed with other systematic errors in the next section on error analysis.

With the beam current measured using the current summation technique and the total and BSE currents measured during the collection and suppression modes, the simple calculations shown in Eqs. 4.1-4.3 are handled by the LabView VI (see Appendix D) and lead to the total, SE, and BSE yields. Then a new beam energy is adjusted and the process begins again.

The SE energy distribution is determined by measurement of the collector current as a negative voltage bias on the suppression grid is varied. Initially, the suppression grid is at ground. The variable power supply (Keithley model 230) to the suppression grid is then ramped over negative voltages of the desired resolution until -50 volts is reached, which defines the end of the SE population. Typical energy steps are 0.25 volts, while the precision and accuracy of the variable power supply are both 0.05% of the voltage and the power supply is capable of delivering millivolts. Measurements of the collector current are taken between each voltage step. As the negative voltage to the suppression grid is increased, more of the SE population is rejected from reaching the collector surface. Ramping the bias grid voltage up to the

beam energy rejects the BSE as well and allows the full energy spectrum to be taken. Although the voltage supply used here is limited to 100 volts, there is the capacity to use an external HV supply with a isolation amplifier. The raw data is a plot of increasingly less current measured at the collector as a function of negative voltage bias to the suppression grid. Differentiating the raw data results in a graph of the portion of the emitted electrons that were rejected at each energy step, which is the SE and/or BSE energy distribution. Figure 4.1 presents an example of an energy distribution of all the emitted electrons, using a gold sample and a roughly 80-eV beam energy. To report the energy-resolved SE yield, the beam current must be recorded in order to normalize the raw data before the derivative is calculated. This additional step was not carried out for the SE energy distributions in this dissertation.

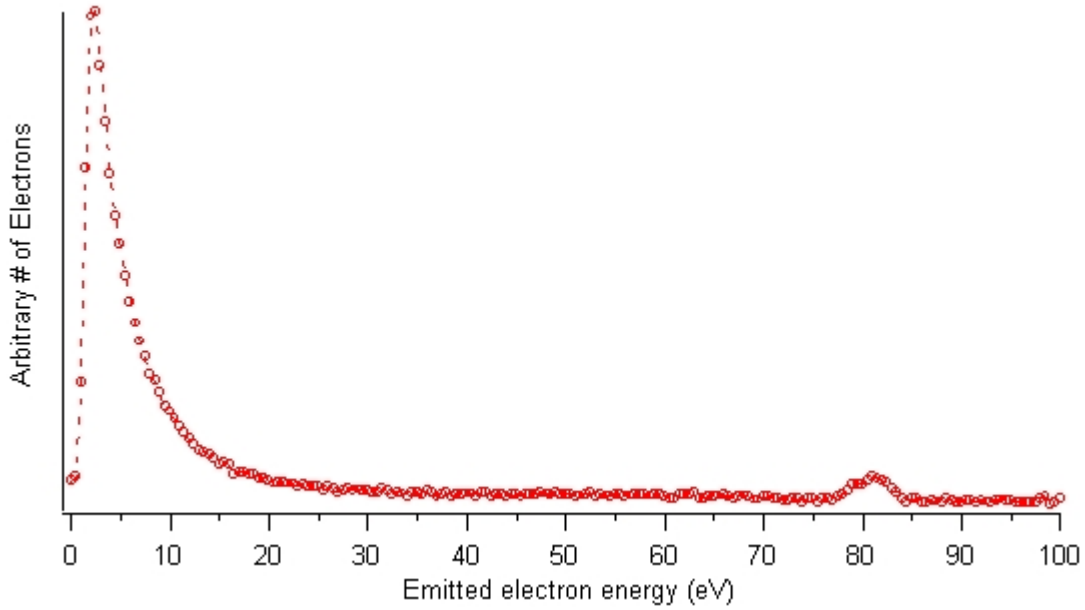


FIG. 4.1: A typical energy distribution of all the emitted electrons. The sample is polycrystalline gold and the beam energy is roughly 81 eV.

The oversight could be rectified by normalizing the first point on the undifferentiated spectrum to give the total yield measured elsewhere.

The photoyield measurement is a comparatively simple process comprised of two sets of measurements that do not involve the HGRFA. First, the sample is biased to -10 volts to prevent low energy SE's from returning to the sample and decreasing the measured current. Then, the sample current is measured as a function of incident photon beam energy. The incident photon energy steps are carried out by computer control of the light source monochromator.

The second set of measurements are of the incident photon intensity as a function of photon beam energy. This measurement is analogous to finding the incident electron beam current with which to normalize the electron induced yield measurements. The photon beam is directed onto the UV detector and the induced current is measured as the monochromator steps through the same energy spectrum used when the sample current was measured. The room lights are turned off and the view ports of the UHV chamber are covered with aluminum foil due to the sensitivity of the UV detector. The resulting current measurement is also corrected for the quantum efficiency of the photodiode. Simple division of the sample current by the corrected photodiode current leads to the photoyield as a function of incident photon energy.

Section B. Error Analysis

Since the BSE and SE yields induced by electron bombardment are the focus of this dissertation, this section provides a detailed error analysis of these yields. The accuracy of the electron gun beam energies is considered first, followed by an analysis of random errors in each of the currents that make up the yield measurements. Finally the absolute uncertainty in the yield measurements will be discussed.

The incident electron beam energy for both the Conrad and HEED guns were adjusted by hand, measured through meters on their power supplies and recorded by hand in the experimental data files. The HEED gun energy error went through a more rigorous analysis and resulted in lower absolute error than the Conrad gun. Extensive effort was made to calibrate the exact voltage delivered to the cathode with the HEED gun power supply's 0-5 volt output of the beam energy meter reading, as measured through LabView [Fatman II lab notebook, p. 52-54]. The output of the power supply was dropped over a 10,000 to 1 Fluke voltage divider and the resulting current was measured with a Kiethley 160 electrometer. This calibration of the beam voltage to the computer sampling of the meter output was better than ±5 volts and could most likely be improved using a higher precision electrometer (e.g., a Kiethley 616). The final yield measurements did not record these more exact values of the energy through LabView due to an oversight. The meter on the HEED gun power supply only has a repeatability of ±200 volts. Luckily, the dial on the HEED gun power supply was also calibrated to within ±20 volts, which is < 0.5 % error at the lowest operating

voltage setting. The precision of the HEED gun power supply at a given voltage is extremely good, with the power supply rated at better than 0.005% accuracy.

The Conrad gun power supply reports the voltage to the cathode on a digital meter on the front panel only. Verification of the actual voltage output of the power supply against the reading of the meter was never carried out. Assuming the meter is more accurate than human error in adjusting the Conrad gun power supply voltage, the energies recorded for the data are accurate to within ±1 volt. Having a custom built power supply, the precision of the voltage delivered by the Conrad gun power supply cannot be taken from the factory specifications of the commercial power supply inside the Conrad gun power supply. Analysis of the variability in the voltage delivered by the Conrad gun power supply was not carried out.

There are three sources of random error in the current measurements used to determine the SE and BSE yields as discussed in the previous section. One potentially unseen source of random error is the subjectivity introduced by maximizing the Faraday cup or sample current to ensure that the electron beam is centered in the Faraday cup or HGRFA beam pipe. If an effort is made to maximize these currents at each point along a yield curve, then the measurements are independent and the error in misaligning the beam is random. Figure 4.2 shows the repeated measurement of the SE yield of a gold sample (discussed in Subsection 5.A.1). Below 500 eV on one of the curves, no attempt was made to correct the alignment of the beam and there is a maximum of 10% error introduced as depicted on the top graph in Figure 4.2. Beyond

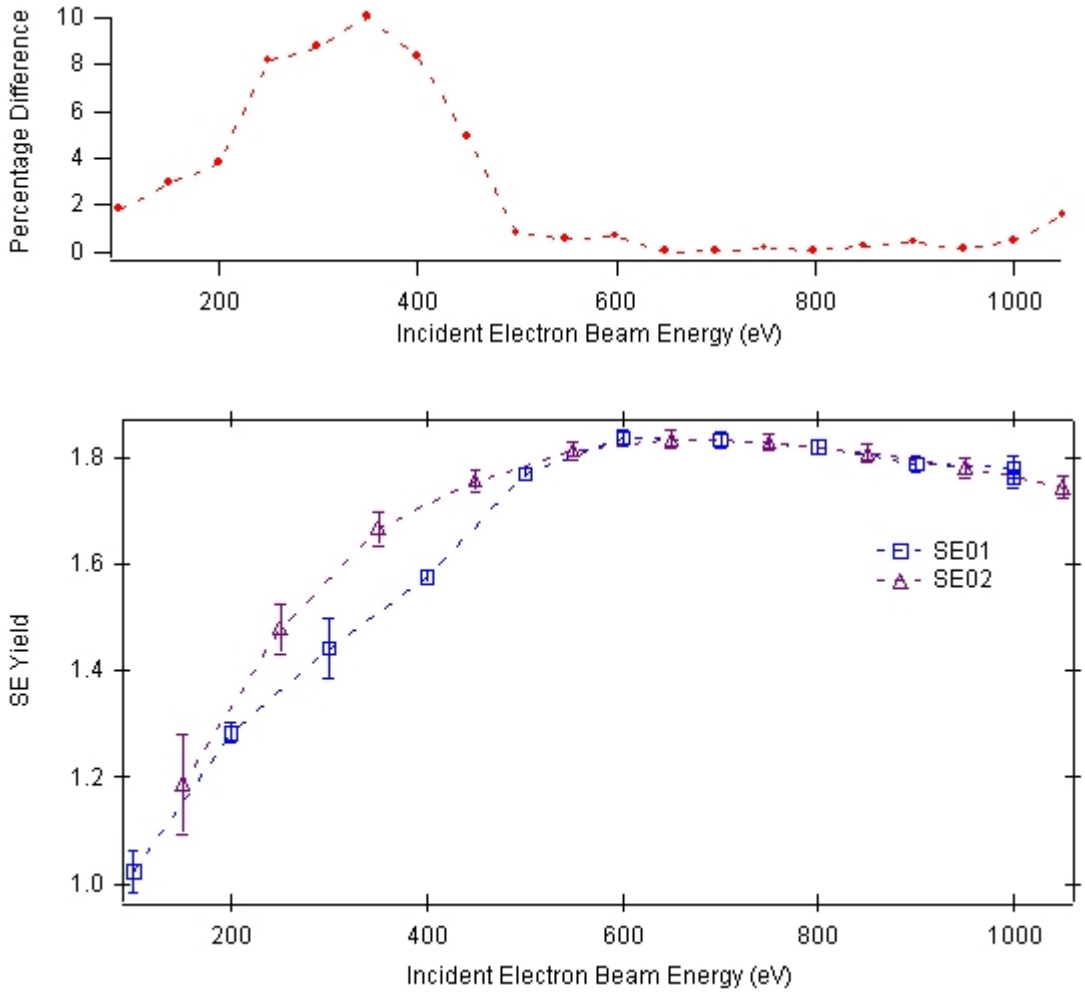


FIG. 4.2: Repeated measurement of gold sample showing possible error introduced by using poor experimental technique. The top graph plots the percentage difference between linear interpolations of the two curves on the bottom graph.

500 eV both curves demonstrates there is good repeatability in the measurements, with an average disagreement of better than 0.5%, if the procedure is followed diligently. This potential random error in the beam current is not reflected in the error bars when using the current summation technique of estimating the beam current. Error in the measurement of the beam current due to adjustment is reflected in the error bars only

when there is a measurable deviation between the two measurements of the beam current that comprise the averaged beam current. Error due to beam adjustment is mainly an issue when the Faraday cup is being used as the measure of the beam current and rotation of the HGRFA is involved in the yield measurement. In that case, continual adjustment of the beam deflection is required. Since the current summation method is used as a measure of the beam current, the beam current is averaged between measurements during the collection and suppression modes and there is no beam deflection adjustment involved between the two modes. The electron beam may drift in position as a function of energy, but the correction for that drift is adjusted between individual points on the yield curve. Inconsistent adjustment of the beam deflection between the measurement of each point along a yield curve results in a random error in the beam current that affects the yield, but is not reflected in the error bars. The magnitude of the possible error involved in the adjustment of the beam, as mentioned above, is not large enough to impact the error in the current analysis.

The next two sources of random error, variations in the measured quantities themselves and random noise on the current signals, both manifest themselves in the standard deviation of the mean current measured and are difficult to separate. As discussed in Section 3.F of the instrumentation chapter, the resolution of the data acquisition system is sufficiently high (0.004%) as to be removed from the problem.

The beam current cannot be assumed to be a static quantity and variations of the beam current in time will be included in the standard deviation reported with the

average beam current. Recall that the measured beam current is a two-point average of the summed currents within the HGRFA during the roughly 20 seconds between both the collection and suppression modes. The error in beam current used to estimate the uncertainty in yield measurements is half the separation between the two points. During the time to measure the yield currents, the Conrad gun beam current varied no more than 1% and the HEED gun varied no more than 0.5% on average for more than 200 beam current measurements taken during the data presented in this dissertation. As shown on Table 3.2, which summarizes noise on each signal, the current measurements that are summed to estimate the beam current – the collector, suppression grid, stage and sample currents – typically had a minimum error of at least 0.6 nA and increases to 2 nA at the typical full range of the currents. These errors in the individual current signals are inconsistent with the 0.5-1% errors shown in repeated measurements of the beam current, especially at low beam currents where the background noise begins to dominate. For this reason, the standard deviations of the constituent currents that go into the estimation of the beam current are thought to be due primarily to signal noise and not uncertainty in the beam current itself.

The yield currents are not assumed to vary appreciably during the 20 seconds needed to record a pair of measurements during the collection and suppression modes of the HGRFA. A variation in yield would be due to evolving contamination on the sample and is assumed not to occur given the low beam currents used (see Section 3.B). There could be an additional concern that fluctuations in the voltages supplied to

the suppression grid during the supression or collection mode might translate into added uncertainty in the yield currents. As mentioned previously, the uncertainty in the Keithley 230-variable power supply is less than 0.05% or a 25-millivolts error in the -50-volt bias during the suppression mode, which has a negligible influence in the collection current measured.

Unfortunately, the signal noise in the collector current that is the basis for the yield currents is very significant and creates an unphysical uncertainty in the yield measurements. Specifically, the 0.08 nA background noise listed in Table 3.2 for the collector current is the driving factor in the error associated with the SE and BSE yields at low energy. This background noise is less than 1% of the typically 20 nA of collector current measured during collection mode when a beam current of 20 nA is used (i.e., the SE yield is near unity for the materials of interest). Even though the BSE yields are an order of magnitude lower, the error in the collection current measured during the suppression mode with 20 nA of beam current should not exceed 4%. The error in the SE yield is made slightly worse because the SE yield is computed as the difference between two collector currents, which results in the background noise being doubled and the effective current being slightly reduced. With the expected 20 nA of beam current these errors are still less than 1%, which was the reasoning for the measurement of the data to proceed without further error analysis and refinements to the data acquisition system.

The real problem is the 0.08 nA background noise in the collector current,

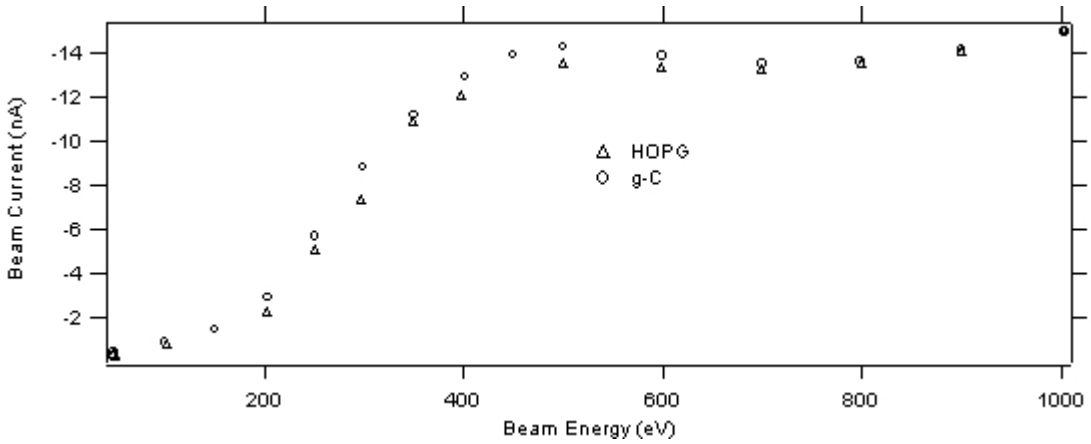


FIG. 4.3: Beam current as a function of beam energy during the HOPG and g-C yield measurements. The beam current axis has been reversed to emphasize the magnitude of the current. Error in the measurement of the currents is smaller than the symbols.

which does not vary with beam current, became significant due to a drastic reduction in the available beam current from the Conrad gun at low energies. This reduction in beam current, observed during the HOPG and g-C measurements, is shown in Figure 4.3 as a function of beam energy. As the beam current falls near 1 nA, the 0.08 nA background noise constitutes roughly a 16% error in the SE yield and potentially an 80% error in the BSE yield. Large error in the SE and BSE yield measured with the HEED gun are also a result of the low fraction of the beam current measured at the collector, due to the low SE and BSE yields at the HEED gun's high energies, and the unfortunate use of low beam current itself in some cases. As will be pointed out in Chapter 5 when the experimental data is presented, repeated measurements of the SE and BSE yields at low energy show that the repeatability is within 3%, while the error bars around those same measurements are over 60%.

In summary, the random error in the SE and BSE yield measurements depends on energy through the reduction in available beam current and the constant background noise of the collector current signal. When beam currents of near 20 nA are available, the collector current in the collection mode has a 1% error and in suppression mode has a 4% error. The contribution of the collector current to the error in the SE yield is typically 2% due to the calculation involving a difference between the collection currents. In comparison, the maximum 1% error in the measurement of the beam current only makes a significant contribution to the error in the total yield measurement, when the collection current error is comparable. In all other measurements, especially when lower than 20 nA beam currents are employed, the collection current error dominates the error in the yield measurements.

As is often the case in experimental work, an estimation of the systematic error is much more ambiguous. One obvious source of error in the measured currents is the absolute calibration of the instrumentation used to acquire the current data. The data acquisition board has been factory calibrated and no evidence for an error in this calibration could be resolved with any measurement. The Kiethley 619 used to measure the collector and grid currents was calibrated according to procedures in its operating manual [Fatman II lab notebook, p. 038w]. Using a clean input signal, the Kiethley 619 only displays a 6-7-mV ripple on its 2.5-volt output [Fatman III lab notebook, p. 033y]. There could be a slight benefit in filtering the AC power from the wall, but this improvement is beyond the scope of the present error analysis. The

custom-built electrometers in the patch panel were calibrated against a clean current supply as measured with a high precision Keithley 616 electrometer. The current supply was custom-built from an AA battery and an appropriate high precision resistor to give currents within the 20 nA range. The electrometers were connected in series and their output was displayed with LabView. The potentiometers that control the offset and slope of the electrometers were adjusted until they agreed with the current supply to within better than 0.1%. Uncertainties in the measurement of the currents were averaged out through repeated measurement with LabView. Additionally, any *in situ* offsets to the electrometers were zeroed just before yield measurements were carried out by a procedure in the LabView VI used to acquire the yield data, which is discussed in more detail in Appendix D. In summary, each current signal has been calibrated to better than 0.1% accuracy and possible offsets are compensated for by the LabView VI .

Another source of systematic error comes from the reliability of the Faraday cup current as a measure of the true beam current. The current sum technique has been compared with measurements of the beam current that employ the Faraday cup. The average disagreement between the two methods is less than 3%. The current sum technique consistently underestimates the beam current in comparison to using the Faraday cup, presumably because some charge does escape the HGRFA without detection. Again, the Faraday cup measurement of the beam current is the basis for the confidence that the current summation technique is an accurate reflection of the

true beam current. As mentioned in Subsection 3.C.1 and detailed in Appendix B, a +10 volt bias on the Faraday cup agrees with the hole in the sample module that has a 10:1 length to diameter ratio to within 0.5%. The overall accuracy of the current summation technique in estimating the beam current that would be measured by an appropriately sized Faraday cup is less than 4%.

The most important source of systematic error is the HGRFA. The intent of the detector is to collect all the electrons emitted from the sample, but the wires and other surfaces inside the detector block some fraction of these electrons from reaching the collection surface. To a smaller extent, the collector and these other surfaces also emit BSE and SE as a result of electron scatter and these unwanted electrons can reach the collector. The result is the yields of a sample as calculated in the manner mentioned at the beginning of this chapter are lower than if the all the electrons were measured on the collector without error. Theoretical correction factors have been derived to correct the SE and BSE yields based on the geometry and materials of the HGRFA. The details are presented in Appendix C and will be summarized here.

The first-order correction for either yield accounts for the opacity of the grid wires that prevent emitted electrons from reaching the collector. Using laser light, the optical transmission of the two grid system was measured. The laser light was defocused through an optical microscope lens, passed through the assembled two-grid system, and then refocused into an optical sensor. The intensity registered with and without the two grid system in the beam path were compared to determine the

transmission of the grids. Repeated measurements of different areas of the grids were averaged to best estimate the average transmission of the two grid system. The resulting estimated transmission is 70.2% with a precision of better than 0.5%.

A second-order correction to the yields accounts for (1) the limited view of the sample because of surfaces other than the grids, (2) the finite BSE yield of the collector surface, and (3) electrons lost out the beam pipe. These three loss currents that comprise the second order correction are reflected in Figure 4.4. An empirical estimate of the second-order correction due to terms (1) and (3) was determined using a light source to stimulate photoemission and subsequent calculation of the ratio of electrons leaving the sample, or the sample current, to those measured at the collector. The experiment estimates the transmission of low energy SE through the grids,

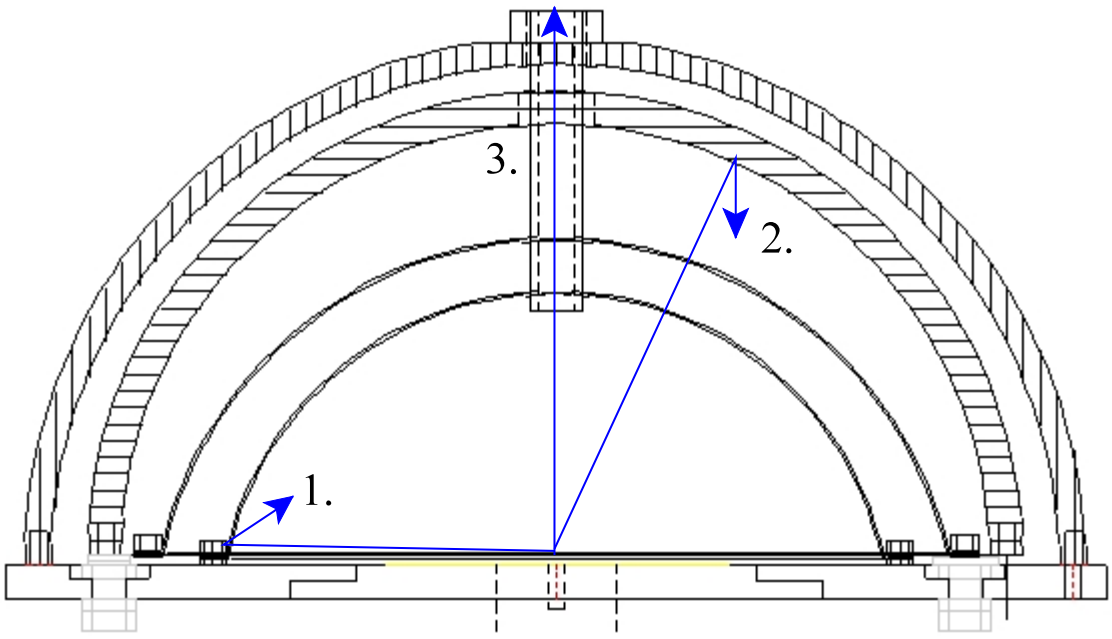


FIG. 4.4: Second-order corrections to the yields to account for lost currents due to (1) other surfaces that obscure the collector besides the grids, (2) the finite BSE yield of the collection surface, and (3) current lost out the beam pipe.

including the (1) limited view and (3) electrons lost out the beam pipe. For comparison, an independent theoretical calculation of this correction was done, based on the grid transmission measurements and geometry of the HGRFA (see Appendix C). The results of the experiment and the theoretical effective transmission of SE agree to within 3% [Chang UV source lab notebook, pp. 11-12]. The geometry factor in terms (1) and (3) should not depend on electron energy significantly, so confirmation of these terms for low energy electrons is sufficient. The BSE yield also suffers from the finite BSE yield of the collection surface, which results in lost current that would be measured in the ideal case. To minimize the BSE current leaving the collector surface, the collector was sprayed with colloidal graphite (Aquadag^{TM}) with a BSE yield of 0.07 (Sternglass, 1953b). Since the SE yield is the difference between the total and BSE yields, both of which suffer from lost BSE current from the collector, there is no need to account for term (2) in the SE yield. In order to retain SE produced on the collector surface and eliminate the need for a further correction, the collector was always biased +50 volts with respect to the suppression grid to create an attractive field.

The highest order of correction considered involves the BSE that have scattered from multiple surfaces and then return to the collector. These scattered currents are shown in Fig. 4.5. The SE yield also suffers from unwanted SE's created by these scattered BSE's bombarding the faceplate of the HGRFA or the exposed face of the module.

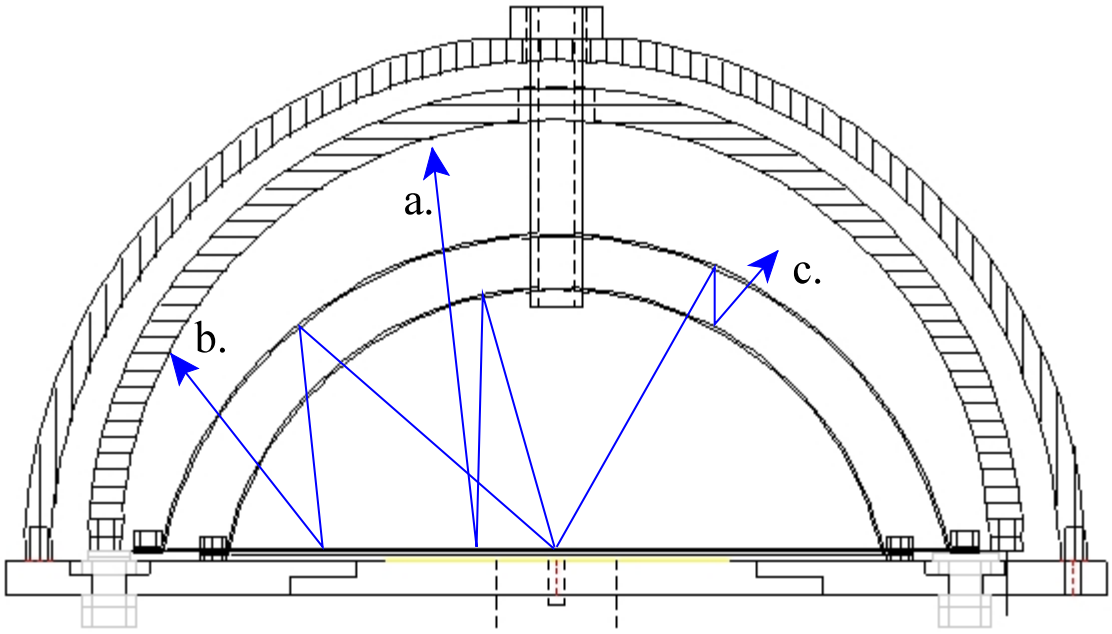


FIG. 4.5: Higher order corrections to the BSE yield due to scatter from (a) the inner grid to the HGRFA face, (b) the suppression grid to the HGRFA face, and (c) the suppression grid to the inner grid and then back to the collector surface. The SE yield suffers additionally from these scattered current creating SE's that are collected, but did not originate from the sample due to the source beam.

There are separate correction factors for the BSE and SE yields due to the different biasing scheme during their measurement. The final BSE yield correction factor is a percentage of the measured BSE yield η_m as follows:

$$\eta = \eta_m (1.52). \tag{4.4}$$

The uncertainty in the absolute correction factor for the BSE yield is difficult to estimate. Although the transmission of the two-grid system has been measured with better than 0.5% precision, the two independent estimates of the effective transmission

mentioned above disagree by 3%. Choosing one of these estimates for the effective transmission of the two grids would reduce the error because the measurements were both precise; however, the disagreement between the two is used for the uncertainty because it more honestly reflects the lack of knowledge about how SE and BSE pass through the grids. Likewise, the actual measurements of the detector geometry are known to better than 0.5% and most of the yield measurements for the materials are known to within 1-2%; however, the variation in the corrective factor due to the uncertainty in the assumptions of the model has a much greater influence. By assuming less is known about the exact paths of BSE within the detector, the corrective factor can be shown to vary by 1.5%. Assuming the BSE's undergo spectral scattering instead of diffuse scattering can be shown to have a 1.5% impact on the corrective factor. Given the three contributions discussed above (with details in Appendix C), a worst case estimate for the uncertainty in the BSE corrective factor is 6% or 1.52±0.09 (±6%).

The SE yield has two corrective factors: a percentage of the corrected BSE yield given by Eq. 4.4 that accounts for SE's created by BSE scatter and an overall factor that corrects for the effective transmission of the HGRFA grid structure. The SE yield δ is then related to the measured SE yield δ_m and the corrected BSE yield η given by Eq. 4.4 through the expression

$$\delta = [\delta_m - \eta(0.06)](1.47). \tag{4.5}$$

The nature of the SE yield correction demands that the BSE yield be corrected first before the SE yield correction factor can be determined.

The uncertainty in the SE yield corrective factor is again impacted by the disagreement between the two experimental estimates of the effective transmission discussed above, which results in a 3% uncertainty in the 1.47 overall corrective factor of SE lost before reaching the collector. Although the uncertainty in the 0.06 corrective factor is compounded by the uncertainty in the BSE correction, the fact that the BSE yield is typically 10-20% of the SE yield reduces the overall impact. The uncertainty involved in deciding whether BSE undergo spectral or diffuse scattering can change the 0.06 correction to 0.09; however, this uncertainty is less than 1% of the overall correction for a BSE yield that is 20% of the SE yield. The SE yield corrective factor has a 4% overall uncertainty.

In order to evaluate the BSE corrective factor, high energy BSE yields for a polycrystalline gold sample (see Subsection 5.A.1) measured with the HGRFA and corrected with Eq. 4.4 were compared with reputable values from the literature. A reputable measurement from the literature should combine a similar technique for measuring the BSE yield, an equivalent UHV vacuum environment, and some attention to the beam current denisty and exposure to avoid carbon contamination. The BSE yields measured with the HEED gun were chosen because of the confidence in the HEED gun performance and the fact that the BSE yield of gold at high energy is relatively flat. Figure 4.6 compares BSE yields of polycrystalline gold using the

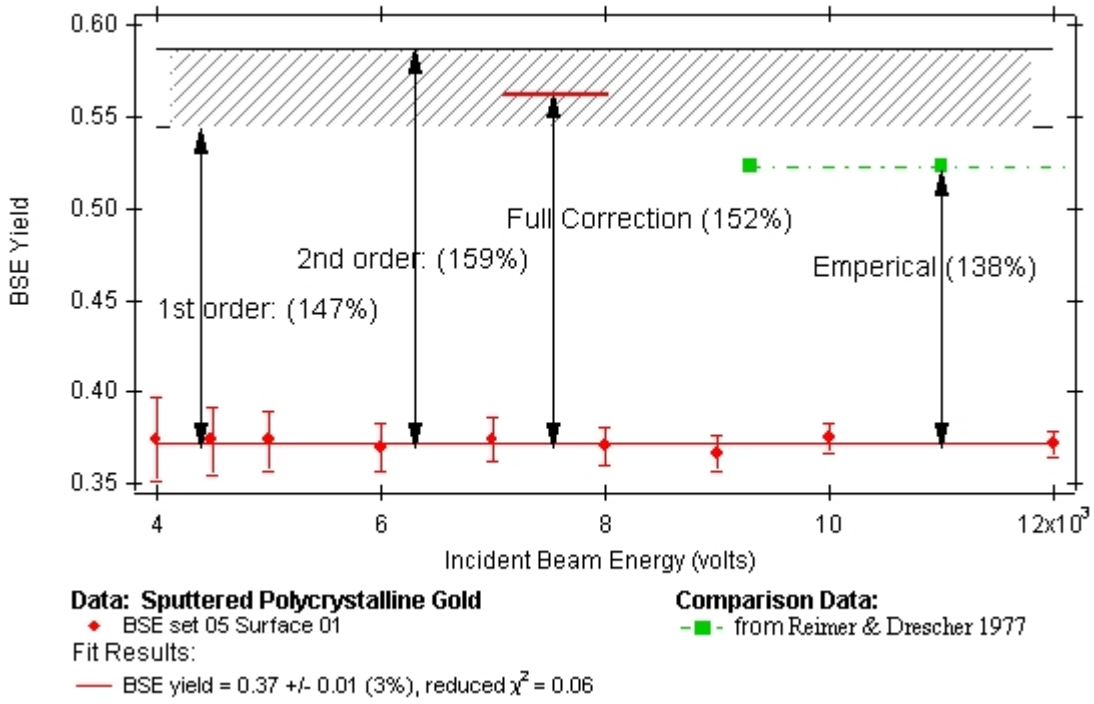


FIG. 4.6: Comparison of BSE yield of gold with corrected value using Equation 4.4 and result from literature. The correction is broken down into the three parts discussed in the text and Figs. 4.2 and 4.3, along with an empirical correction factor from the literature.

HEED gun with measurements by Reimer and Drescher, which was the best source for the high energy BSE yield of polycrystalline gold because the authors do not rely on calibrating their measurements to a previous standard (Reimer and Drescher, 1977). The figure breaks down the BSE correction into the first, second, and higher order corrections discussed above and shown in Figs. 4.4 and 4.5. The BSE corrective factor predicts a 14% higher BSE yield than that measured by Reimer and Drescher. Assuming the random uncertainty in the measurement of 3% is compounded by the absolute uncertainty of 6%, then the two separate measurements could conceivably

only disagree by 5% of the HGRFA measurement. Although their experimental methods are sound, Reimer and Drescher include their suppression grid in the collecting surface but make no mention of correcting for current lost from the grid due to BSE and SE produced on the grid wires returning to the sample. This oversight would tend to decrease the measured BSE yield by underestimating the BSE current reaching the collection surfaces. Sternglass derived such a correction for a spherical detector with a suppression grid, and has shown that the correction can be as high as 15 % for gold (Holliday and Sternglass, 1957). The work of Sternglass is arguably not directly applicable to Reimer and Drescher, who use a hemispherical grid rather than a spherical arrangement, but suggests that the descrepancy between our corrected measurements and those of Reimer and Drescher could be the result of ignoring the correction for current lost from the grid.

A comparison of the measured SE yield for the polycrystalline gold sample, using the HGRFA and the Conrad gun, against another reputable measurement by Thomas and Pattinson (1970) is shown in Fig. 4.7. The figure shows the full correction given by Eq. 4.5 (dashed line with squares) and the 147% correction that accounts for the effective grid transmission (dashed line) are nearly the same. Although the shape of the curves agrees quite well, the percentage difference between the corrected SE yield and the data from Thomas and Pattinson is roughly 30% in this case. This large disagreement is inconsistent with the 3% random uncertainty in the data and the 4% uncertainty in the SE yield correction factor. As with the Reimer and

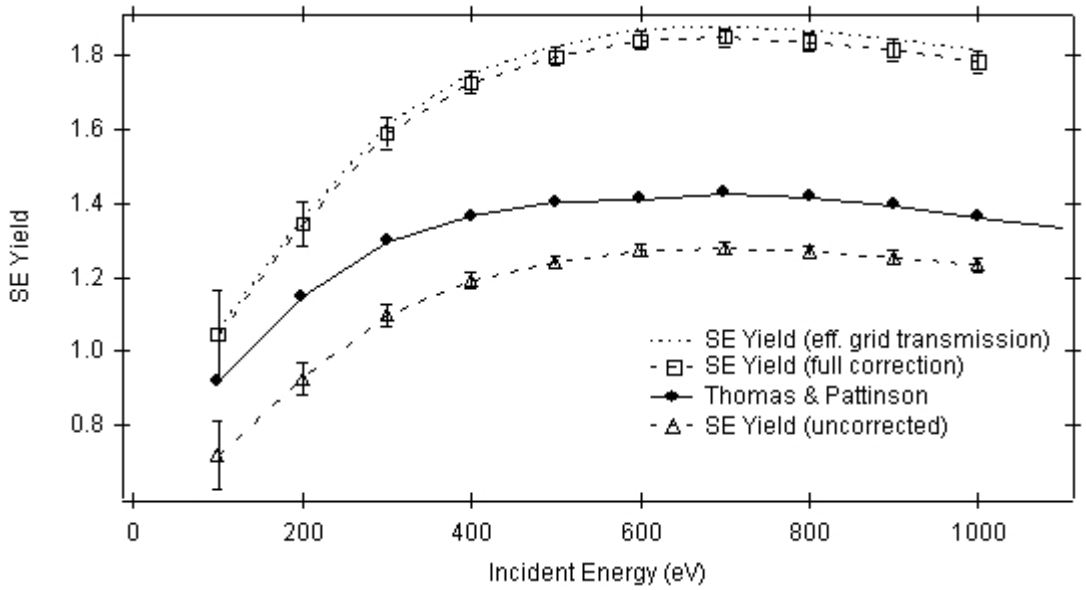


FIG. 4.7: Comparison of SE yield of gold with corrected value using Eq. 4.5 and result from literature. The first-order correction for the grid transmission is shown as well.

Drescher article, the suppression grid is included in the collecting surface and no mention is made of correcting for the current loss due to BSE and SE produced on the grid. The authors use a spherical detector and report the grid transmission (85%) and material (tungsten), but without the exact geometry of the detector the correction factor derived by Sternglass cannot be calculated. Even with the 15% correction used by Sternglass for his detector (Holliday and Sternglass, 1957), there is still more than a 10% disagreement between the experimental data.

In conclusion, both the BSE and SE corrective factors used in this dissertation are higher than comparable measurements in the literature. The BSE correction is 14% higher, but could possibly agree to within 4% if the random and absolute uncertainties are compounded. The similar structure of the detectors and the lack of

any corrective factor in the comparative work gives a fair amount of credibility to the BSE corrective factor. The large disagreement between the corrected SE yield and the comparable work is disappointing. The effective transmission of the grid system, which makes up the bulk of the correction factor, has been measured with two separate techniques and found to disagree by only 3%. The more difficult estimate of the unwanted SE produced by scattered BSE might be seen as a possible term for reducing the grid correction to agreement with the comparative work, but the low BSE yields of surfaces within the HGRFA reduce this potential correction by roughly a factor of 10 even before the opacity to BSE and SE transmission of those surfaces is considered. Although the comparable work does not apply a corrective factor for the geometry of their spherical detector, this correction is most likely on the order of 15%. Even with the random and absolute uncertainties of the SE correction factor, there is still roughly a 10% disagreement between the two sets of data. At the end of the derivation of the theoretical correction factors in Appendix C, the assumptions for the theoretical development are tested by predicting the current that should be measured on the suppression grid. Although the shape of the current with suppression grid voltage is consistent with expectations, the values are significantly different than predicted by the theoretical model.

The corrective factors of Eqs. 4.4 and 4.5 are still used without modification for the experimental data presented in Chapter 5 because the first order correction factors find both theoretical and empirical support, and are the dominate terms in the

theoretical correction factors. Again, the full derivation of the theoretical correction factors for the BSE and SE yields can be found in Appendix C.

CHAPTER 5

EXPERIMENTAL DATA

This chapter includes a description of the samples, along with their preparation and characterization. A short subsection dealing with attempts to anneal the graphitic amorphous carbon sample is also included. The experimental SE and BSE yields for each sample are then presented with a discussion of the general features and trends in the data.

Section A. Sample Preparation and Characterization

The following section describes the general properties, manufacturing source, preparation, cleaning, and characterization of the gold and carbon samples used to take the data described in the subsequent section of this chapter.

Before discussing each sample in turn, the experimental conditions common to all the samples will be discussed. In order to thoroughly assess the reliability of a SE emission experimental study, the dissertation work of Davies (1999) defines a set of parameters that should be reported along with any SE emission measurements. The following subjects will serve as a guide so the reader can successfully judge the merits of the current experimental work:

1. Sample preparation.
2. Base and operating pressures.
3. Sample smoothness.

4. Direct characterization of surface contamination (e.g., Auger electron spectra).

5. Sample treatment under vacuum (e.g., time under vacuum, sputtering, annealing).

6. Electron beam current density and time of exposure.

Again, some of the experimental conditions are common to all the samples. The samples were mounted in the vacuum chamber for 7 months prior to taking the data, but only one month after a complete bakeout of the vacuum system. The bakeout resulted in base pressures in the mid 10^{-10} torr range. Operating pressures for the guns are only slightly higher. The residual gas analyzer (RGA) spectrum at this vacuum is shown in Fig. 5.1. The RGA reveals the vacuum is limited by water and CO or N_2 even with the bakeout and a complete leak check of the system with helium gas. The cluster of peaks near the water is a signature of methane in the system, which is thought to be a byproduct of the TSP outgassing during use and is difficult to remove with ion pumps. There are also small peaks of CO_2, argon and helium that are typical in a RGA spectrum. The remaining numerous small peaks throughout the spectrum are the result of a power outage prior to the bakeout that caused backstreaming of mechanical and turbomolecular pump oils into the vacuum chamber. The absence of large hydrocarbon peaks higher than 50 amu is a positive sign of a partial recovery from the accident by the bakeout. This accident will be referred to again when the Auger spectra are considered.

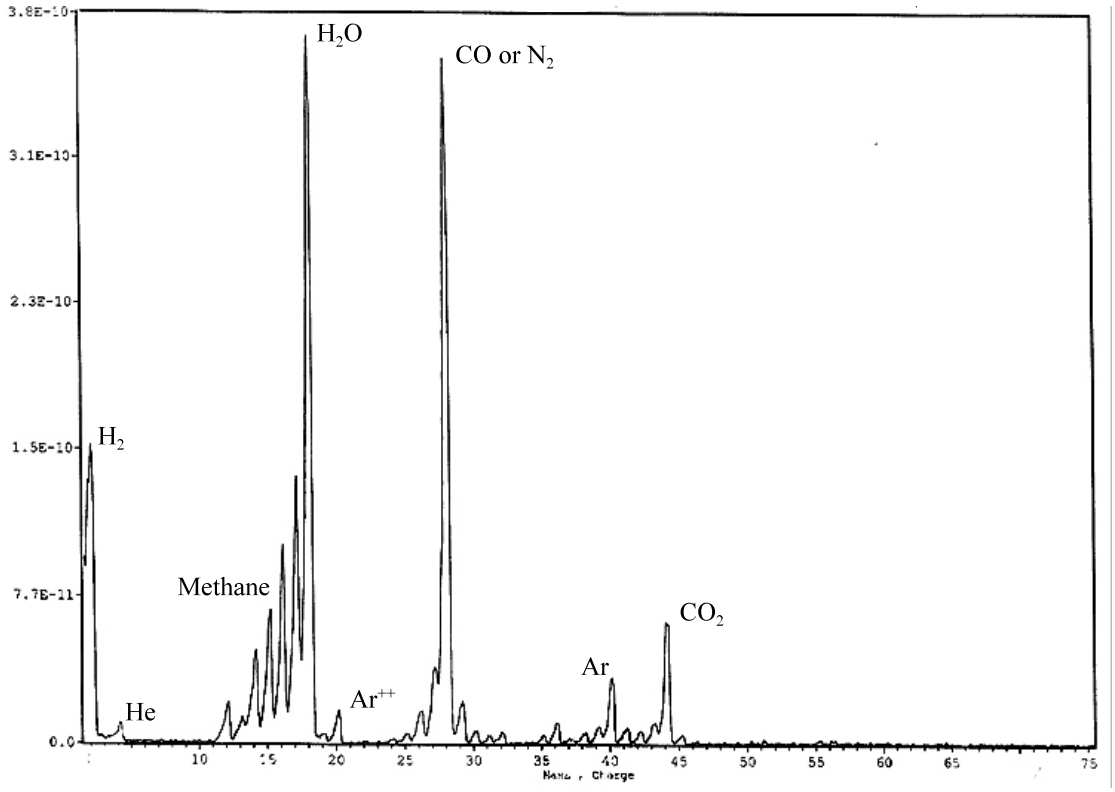


FIG. 5.1: RGA spectrum showing the partial pressures of gas inside the vacuum chamber.

The gold measurements were taken repeatedly during the months prior to the carbon measurements. The yield measurements of the HOPG and g-C samples were taken on the same day and the Aquadag^{TM} sample was studied only one week prior. As mentioned in Section 3.B, the beam current densities were always kept below 6 $\mu A/cm^2$ in an effort to reduce surface contamination due to electron beam stimulated adsorption of vacuum contaminants. The only exception was the 10 minutes of exposure to 70 $\mu A/cm^2$ beam current densities during an AES scan.

The samples, along with their preparation and characterization, will now be discussed in turn.

Subsection 1. Gold

The gold sample used to test and calibrate the instrumentation is a 6N purity neutron activation foil with polycrystalline structure. The sample roughness was measured independently with an STM to have an rms height of 8 nm over a 1.4 x 1.4 μm^2 area. Prior to insertion in the UHV chamber the sample went through a series of cleaning procedures adopted from previous work on the SE emission properties of gold by Davies (1999). The gold sample was chemically cleaned in toluene, methylene chloride, acetone, isopropyl alcohol, methanol, warm nitric acid and rinsed in distilled water. The sample was kept in distilled water prior to insertion in the UHV chamber.

The sample was glued to a 1 cm diameter stainless steel sample slug with a mixture of UHV compatible adhesive (Vacseal), acetone, and silver powder to ensure conductivity [Nickles lab notebook, p. 46]. The stainless steel slug was chemically cleaned with methylene chloride, then acetone, and finally methanol. The gold was cleaned *in situ* with argon ion sputtering by a 1keV, 4.3 μA beam for 30 minutes [FatMan III, p. 025]. As seen in Fig. 5.2, the cleanliness of the surface was verified by Auger electron spectroscopy (AES). Referring to Section 3.B, all the AES spectra presented here were taken with electron beam of 2 keV with less than 70 $\mu A/cm^2$ of beam current density. The two spectra shown in Fig. 5.2 reveal that the ion sputter has a significant effect on the level of carbon contamination, which is reduced to approximately 18% concentration on the sputtered sample. The atomic concentration

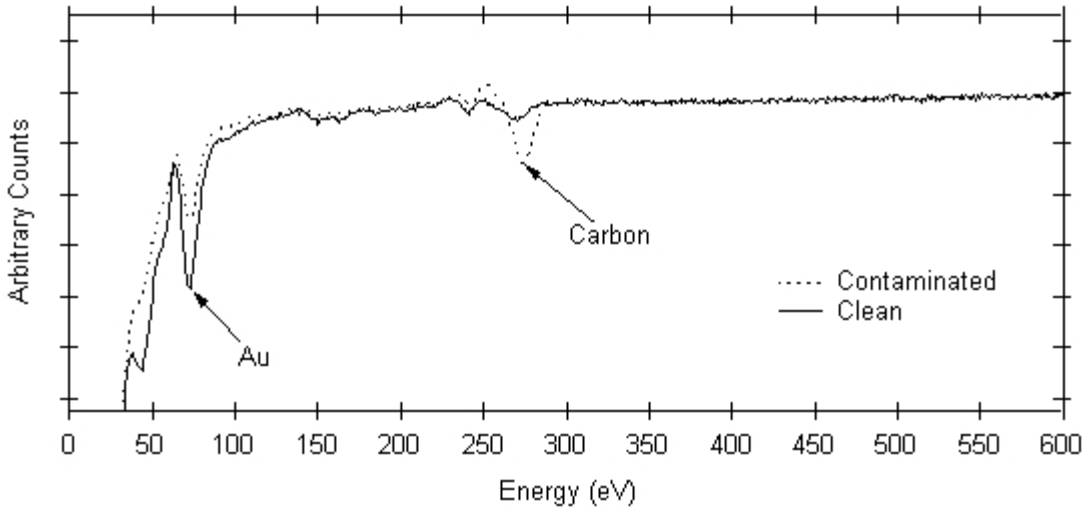


FIG. 5.2: Auger electron spectra of polycrystalline gold before and after ion sputtering. The spectrum of the contaminated gold prior to ion sputtering shows nearly 50% carbon contamination in comparison to the 18% carbon level on sputtered sample.

of carbon is only an estimate because the gold peak for which the sensitivity is known could not be resolved from the background noise.

Subsection 2. Highly oriented pyrolitic graphite

Highly oriented pyrolytic graphite (HOPG) is a manufactured graphite material that emulates the properties of naturally occurring crystalline graphite. A perfect graphite crystal is characterized by planes of hexagonal rings constructed of strong covalent bonds commonly referred to as σ bonds. The triagonal nature of the bonds around a carbon atom in graphite is referred to as an sp^2 hybridation, as opposed to the sp^3 hybridized, tetrahedronal bonds in a diamond crystal structure. The hexagonal planes of graphite are referred to as the basal planes and are bonded together by weaker π bonds, which involve the fourth atom of carbon not bonded in the plane.

Although not a perfect graphite crystal, HOPG is characterized as having roughly 1 μm of coherent hexagonal order within the basal plane and roughly 4 μm stacking order of the planes themselves (Moore, 1973). The material has the structural properties of crystalline graphite on μm length scales and therefore has macroscopic properties very similar to crystalline graphite. The most important property for the current investigation is that HOPG is a semi-metal with zero bandgap. The resistivity of HOPG across the basal plane is $4x10^{-5}$ Ω-cm and is $5x10^{-2}$ Ω-cm along the axis between the planes (Klein, 1962). The density is 2.260 gm/cm^3 (Lide, 1990). The surface of HOPG is very smooth, as demonstrated by the ability of scanning tunneling microscopy (STM) images to resolve the hexagonal ordering on an atomic scale. The optical microscope picture of the sample in Figure 5.3 confirms that the sample is extremely smooth over macroscopic distances.

The HOPG sample was donated by Greg Swain's lab and the source is most likely Advanced Ceramics Corporation in Cleveland, OH. Rather than clean the

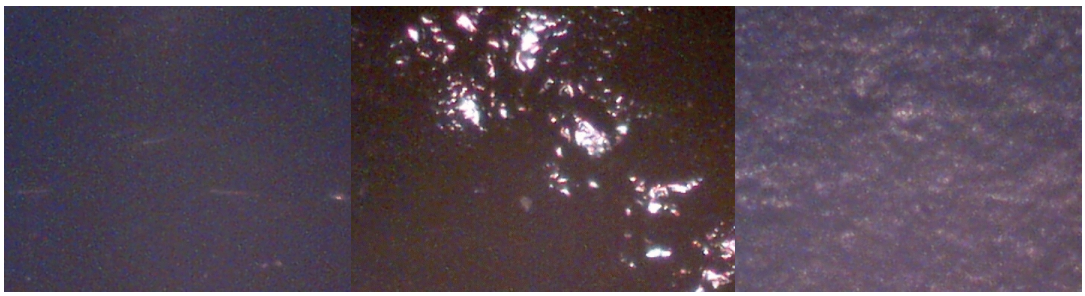


FIG. 5.3: Optical microscope pictures of HOPG (left), g-C (middle), and colloidal graphite (right). The images are 1 mm across. The magnification is approximately 50:1.

surface chemically, a fresh surface of the HOPG can be exposed by adhering tape to the surface and pulling off a layer or more of the HOPG. The weak π-bonds along the graphite planes allow the surface to be easily cleaved. As with the gold sample, the HOPG was glued to a chemically clean, stainless steel slug with the silver adhesive mixture. Since ion sputtering has been shown to change the SE emission of graphite (Wintucky *et al.*, 1981; Goto and Takeichi, 1996; Caron *et al.*, 1998), the samples were cleaned *in situ* by baking the chamber at 125° C for 4-5 days. The AES spectra in Fig. 5.4 shows the bake-out had little or no affect on surface contamination. The atomic concentrations of the contaminants are listed on the plot. The presence of silicon along with the oxygen suggests hydrocarbons from the turbomolecular pump oil accident are still contaminating the sample.

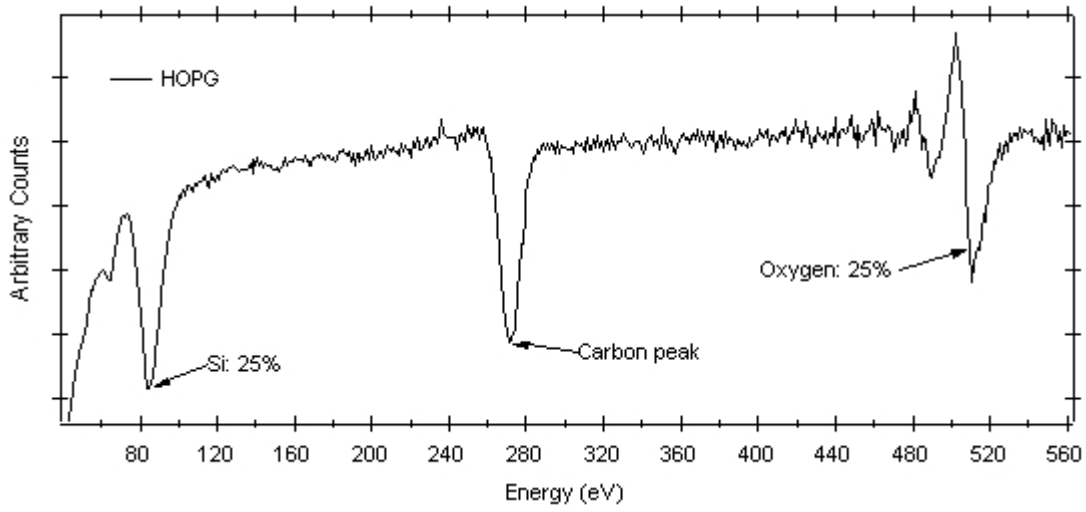


FIG. 5.4: Auger electron spectrum of HOPG sample. Types of contaminates and their relative concentration are listed near each peak.

Subsection 3: Colloidal graphite

Colloidal graphite is microcrystalline graphite powder suspended in liquid to form a paste. The crystalline nature of the powder gives the material similar properties to HOPG, but without the long range order. Colloidal graphite is crystalline graphite on 0.1-1 micron length scales.

The colloidal graphite was purchased from Ladd Research and was originally manufactured under the trade name Aquadag™ by Acheson. Aquadag™ is a solution of graphite powder, ammonia, and a proprietary dispersive agent (Derer, 2001). The dispersive agent is a natural polymeric saccharide to keep the graphite powder in solution. The ammonia is used in the liquid to keep the pH high because the sugars in the dispersive agent make the solution susceptible to bacteria. The resistivity of a dried film is estimated to be 50 Ω-cm and the density is 2.0 gm/cm^3 (Derer, 2001).

The Aquadag™ paste was diluted 2:1 with de-ionized water in order to spray the mixture onto a clean sample slug. The Aquadag™ was sprayed onto a 0.7-inch 304 stainless steel slug using an air brush sprayer with nitrogen at 25 psi. Spraying from a distance of 20-30 cm gave a spray pattern of 5-8 cm in diameter. To ensure good adhesion, the stainless steel slug was heated to above 70° C with a hot air gun before spraying and the hot air gun was used for 1-2 minutes after spraying to quickly dry the sample. Two samples of Aquadag™ were prepared with two coats of spraying on the first sample and one coat on the second sample. The coatings are estimated to be 10-100's of microns thick. Subsequent analysis confirms that there was no

difference between a single coating and two coats in the SE and BSE yields. The optical microscope picture in Fig. 5.3 shows slight roughening of the surface as a result of being sprayed onto the sample blank. There was no additional cleaning prior to insertion into the vacuum chamber. Again, ion sputtering was avoided and the bakeout was the sole means of cleaning the sample *in situ*. The dispersive agent in the Aquadag™ reportedly does not break down until temperatures of over 400° C (Derer, 2001). The AES spectrum of the Aquadag™ sample, shown in Figure 5.5, reveals almost no surface contamination. Given the similar nature of HOPG and Aquadag™, the difference in contaminant coverage is striking. The lack of contamination in comparison to the other carbon samples is most likely due to differences in the surfaces' adhesion as all the samples were exposed to the same environment in the vacuum chamber for identical lengths of time. The dispersive agent in Aquadag™

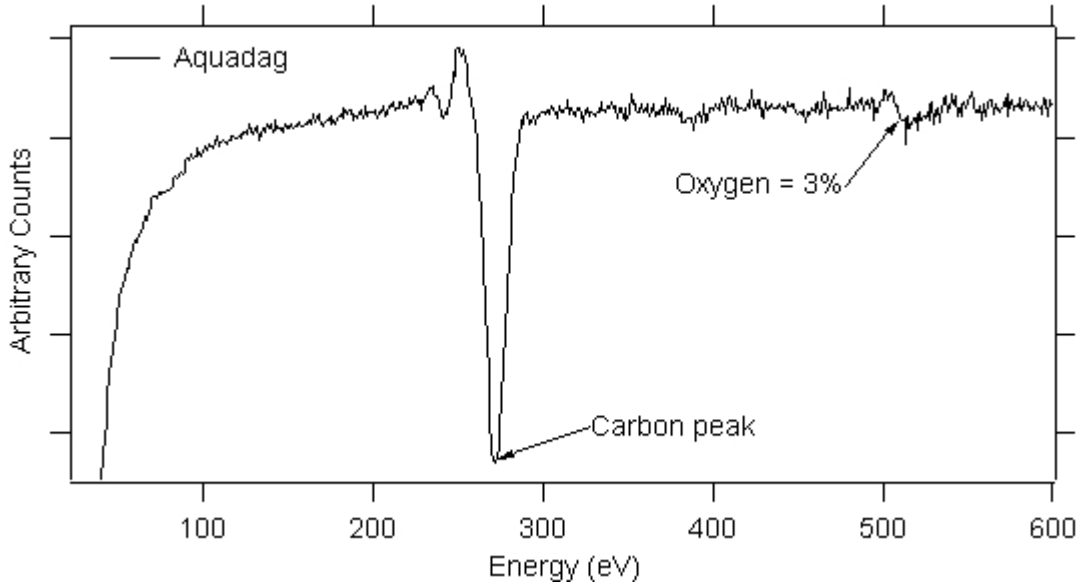


FIG. 5.5: Auger electron spectrum of Aquadag™ sample. The relative concentration of adsorbed oxygen is listed near the peak.

must inhibit the bonding of further hydrocarbons; however, the low atomic concentration of oxygen in the Aquadag™ does not support a large presence of the dispersive agent.

Subsection 4. Evaporated graphitic amorphous carbon

The defining qualities of evaporated graphitic amorphous carbon (g-C) have been in question until recent work has been able to characterize the material in relation to other forms of carbon. As the name implies, evaporated graphitic amorphous carbon is typically produced by evaporating carbon at temperatures above 200° (Dennison *et al.*, 1996). Amorphous carbons are typically classified by the ratio of their sp^2 to sp^3 bonding. The g-C is thought to have a large fraction, over 95%, of sp^2 bonding with the sp^3 bonding at the edges of 1.5-2 nm islands of multi-member rings (Robertson and O'Reilly, 1987). The level of disorder in this amorphous material is responsible for a 0.4-0.7 eV bandgap (Robertson, 1986). The resistivity of g-C is 0.5 Ω-cm (Gao *et al.*, 1989). The density is 1.82 gm/cm^3 (Stoner, 1969). The aerial density of the actual sample used in these experiments was 21.3 μgm/cm^2, which corresponds to a thickness of roughly 1.2 microns (Dennison, 1985). The amorphous carbon sample was supplied by Arizona Carbon Foils. The g-C carbon films were sent on a glass microscope slide with a surfactant detergent between the film and the slide. The surfactant allowed the film to be floated off the slide onto the surface of deionized water and then onto a chemically cleaned, stainless steel slug. Optical interferometry confirms that the samples are very smooth, with a root mean square roughness of less

than 1 nm over an area of 245x239 μm^2 (Lee, 1995). The optical microscope picture in Fig. 5.3 does reveal some blistering of the surface due to trapped water, but the surface is otherwise smooth. Again, the AES spectrum in Fig. 5.6 shows avoiding ion sputtering and relying on the bake-out to clean the g-C surface did not eliminate contamination.

Subsection 5. Annealing the g-C sample

Attempts were made to anneal the g-C, which has been shown to bring about structural changes towards nanocrystalline graphite (Wada *et al.*, 1980; Rouzaud *et al.*, 1983; Dillon *et al.*, 1984; Dallas, 1996). The structural changes were assumed to decrease the bandgap towards that of nanocrystalline graphite, which would allow for a study of the correlation between changes in the bandgap and the SE yield within the

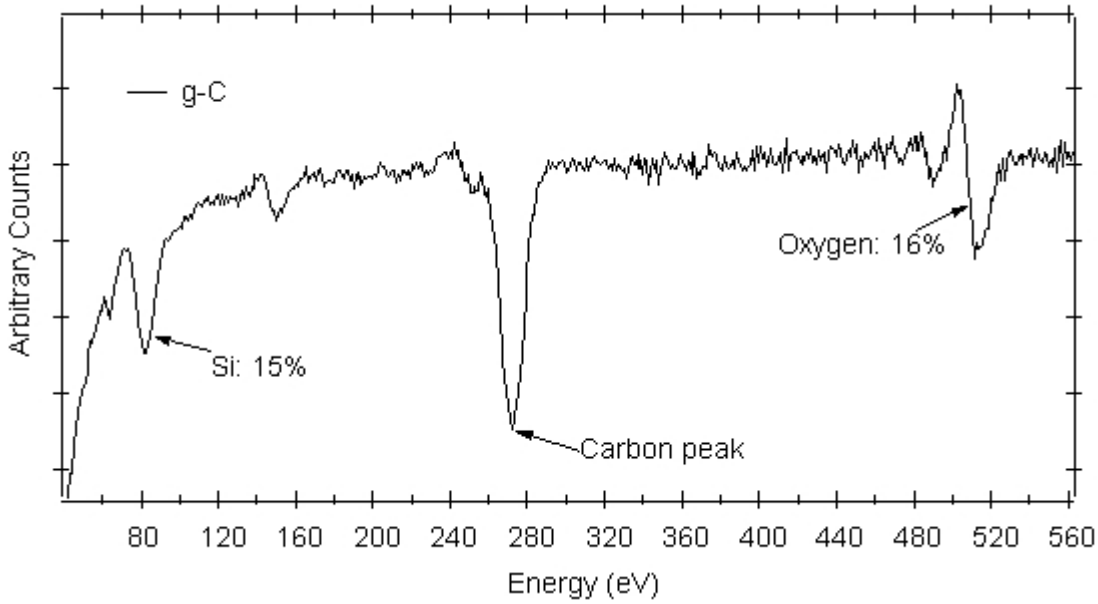


FIG. 5.6: Auger electron spectroscopy of g-C. Types of contamination and their relative concentration are listed near each peak.

same material. The annealing was done in a vacuum furnace (Lindberg model 55035) capable of a maximum temperature of 1050° C and regulates its temperature to within ±2°. The furnace was pumped by the turbomolecular pump used to rough pump the UHV chamber. Although the exact pressure was not monitored, the vacuum can be safely assumed to be better than 10^{-6} torr from experience with similar pumping arrangements where vacuum gauges were employed. Thin molybdenum 1 cm diameter discs were chosen as the substrate for the films because molybdenum's low coefficient of linear expansion ($5x10^{-6}$/degree) results in the least strain to the g-C films, whose coefficient is assumed to close to graphite ($2x10^{-6}$/degree) (Marton, 1979). Annealing temperatures were chosen at 450, 650, 850, and the maximum temperature of the furnace, 1050° C mainly because these temperatures cover the available range well. The heat treatments lasted for 1 hour, excluding the periods of heating and cooling, to correspond with the work by Dallas (1996). The 650 and 1050° C heat treatments fall on either side of the 850-950° C temperature range where carbon interstitials are gradually released and basic ring structures develop (Rouzaud *et al.*, 1983). The removal of in-plane defects is the next stage of structural change and does not occur until above 1500° C. The films would not fully graphitize until temperatures above 2000° C. Both of these stages exceed the maximum temperature of which the furnace was capable.

All of the heat treatments resulted in severe blistering of the sample surface, as seen in Fig. 5.7. The 1050° C heat treatment resulted in the g-C being completely

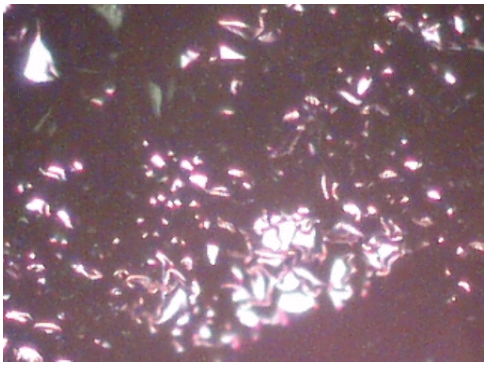


FIG. 5.7: Optical microscope image of g-C annealed at 650° C for 1 hour. The image is 1 mm across and the magnification is approximately 50:1.

removed from the disc. The blistering is due to trapped water between the sample slug and the g-C films as mentioned before. Attempts were made to preheat the samples at low temperatures to release the trapped water, but proved unsuccessful. One solution, which was not tested, would be for the manufacturer to evaporate the g-C straight onto the molybdenum discs, but adhesion to any metal is difficult (Stoner, 2001). Experimenting with thicker g-C films than 20 $\mu gm/cm^2$ (areal density) may be necessary as thin samples tend to adhere less. Annealing g-C at high temperature has proved successful on sapphire (Dallas, 1996), but using an insulator as a substrate introduces problems with charging during the SE yield measurements. A small piece of metal could be connected from the g-C film to the metal slug below the sapphire, but the charging of the insulator may still disrupt the electric fields in the HGRFA during measurements.

Section B. Yield Measurements

The SE and BSE yields will now be presented for the three carbon samples: HOPG, Aquadag™, and g-C. The yields for the gold sample are discussed in Section 4.B on error analysis as they apply to the repeatability of the measurements.

Subsection 1. HOPG

The SE and BSE yield of HOPG over an energy range of 50-16000 eV are shown in Fig. 5.8. The total yields of the carbon materials will not be presented. The BSE yields are so low (averaging 0.1) and flat the total yield only amounts to a slight shift in the SE yield curve. The curves in Fig. 5.8 are plotted together on a linear scale to give a sense of perspective. All subsequent graphs will plot the SE and BSE curves separately with the energy on a log scale to show the details of the data. The SE and BSE yields of HOPG are shown in detail on semi-log plots in Figs. 5.9 and 5.10. The plots contain two data sets covering different energy ranges, using the Conrad gun between 50-1000 eV and the HEED gun between 4.5-16 keV as the electron sources. The method of data collection and analysis that converts the measured currents into the yield curves with error bars is discussed in Chapter 4 onthe experimental methods. Fitting the data with theoretical curves will be done in Chapter 6 during the discussion

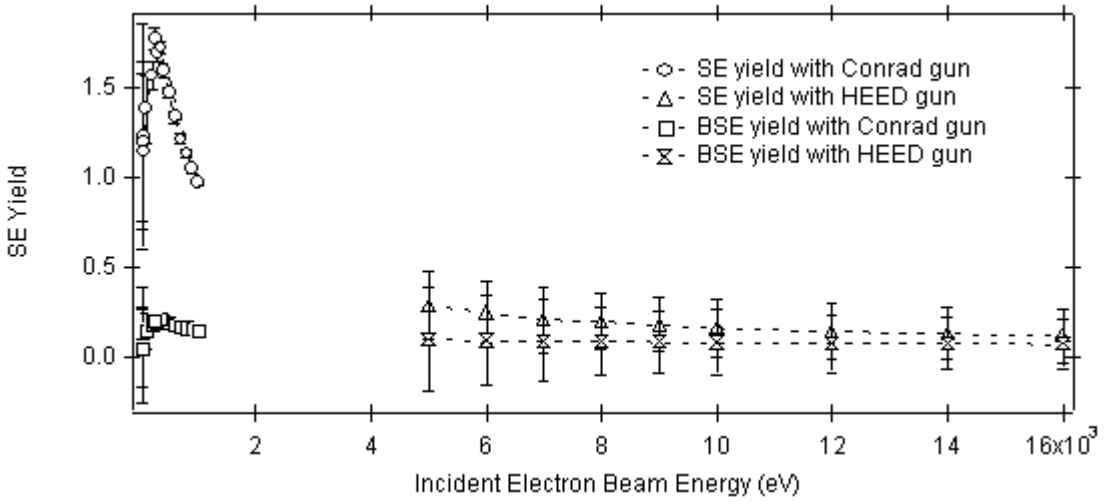


FIG. 5.8: Linear plot of SE and BSE yield of HOPG sample using the Conrad and HEED electron guns.

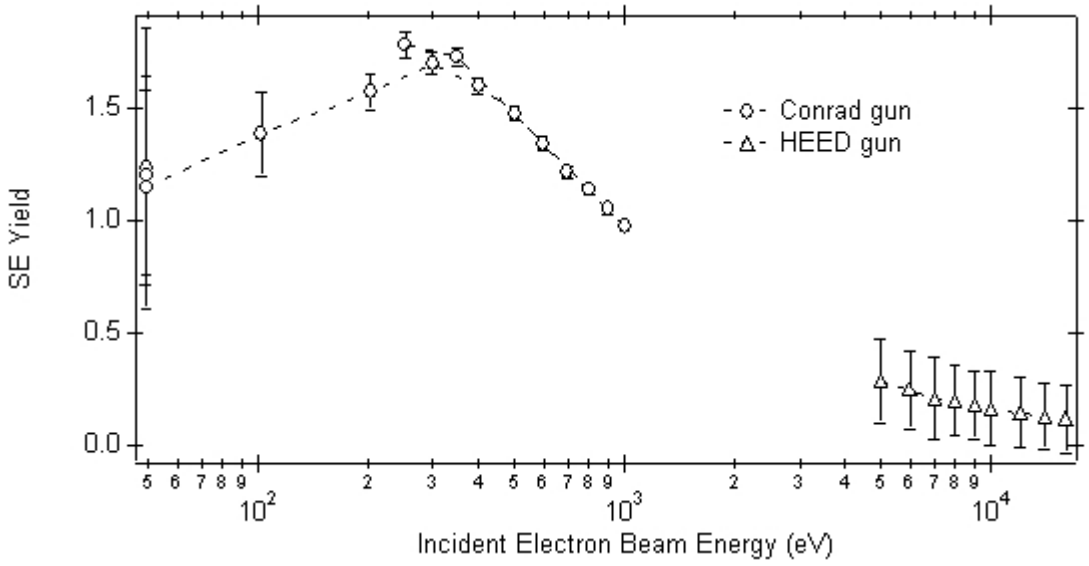


FIG. 5.9: SE yield of HOPG displayed as a semi-log plot.

of the experimental data.

Two data points on the SE yield curve in Fig. 5.9, at 250 and 350 eV, were taken out of sequence and deviate slightly from the rest of the curve. These points are slightly higher, which would indicate the beam current is being underestimated by the sum of the current within the HGRFA. The cause is most likely a change in the focus of the beam spot that results in some of the beam impacting the cover or beam pipe before reaching the sample. The error bars noticeably increase in both plots below 250 eV. As discussed in Section 4.B on error analysis, the increased error is due to a decrease in the available beam current from the Conrad gun at these energies coupled with background noise in the collector current that does not scale with the signal. The large error bars do not truly reflect the uncertainty in the SE yield. Notice the three measurements at 50 eV that agree within a standard deviation of 3%, which is much

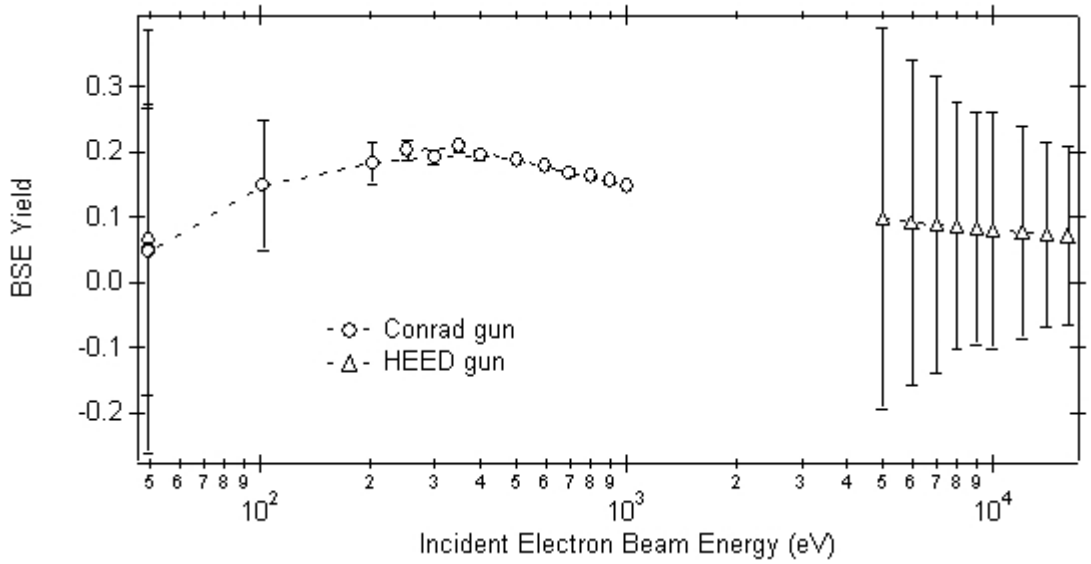


FIG. 5.10: BSE yield of HOPG displayed as a semi-log plot.

higher precision than represented by the error bars on the graph that show nearly a 60% standard deviation at that energy.

The error bars on the HEED gun portion of both yields also are a drastic overestimation of the error in the measurements. Again, the cause for the large error has been traced to the collector current, coupled with the low beam currents used to acquire the data the HEED gun data. Typical error in yields measured with the HEED gun using nearer to 20 nA of beam current is equivalent to the higher energy Conrad gun data. The agreement of the HEED gun curve with the Conrad gun data at least lends some credibility to the accuracy of the measurements. Also notice that the BSE yield in Fig. 5.10 does not decline to zero at 50 eV as expected, which points to a systematic error in the measurement or simply the fact that two populations are not separable by the conventional definition.

Subsection 2. Aquadag™

The SE and BSE yield of Aquadag™ are shown on semi-log plots in Figures 5.11 and 5.12. The data was collected and analyzed in the same manner as the HOPG, which is discussed in Chapter 4 on experimental methods. The noticeable aspect of the SE yield curve is there is poor agreement between the low and high energy data, which will be discussed further in Chapter 6. There were fewer points measured for both curves as well. Otherwise, the data has the same features as previously mentioned with the HOPG.

Subsection 3. g-C

The SE and BSE yield of g-C are shown on semi-log plots in Figs. 5.13 and 5.14. Again, the data collection and analysis was conducted in the same manner as the other carbon samples. The most noticeable aspect of both the SE and BSE yields is that the high energy data falls off as it approaches lower energies and does not seem to

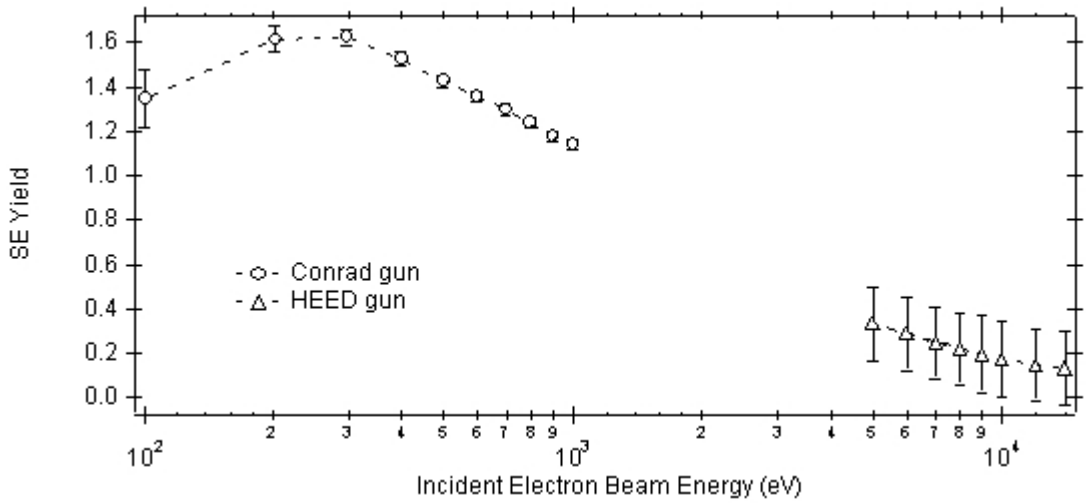


FIG. 5.11: SE yield of Aquadag™ displayed as a semi-log plot.

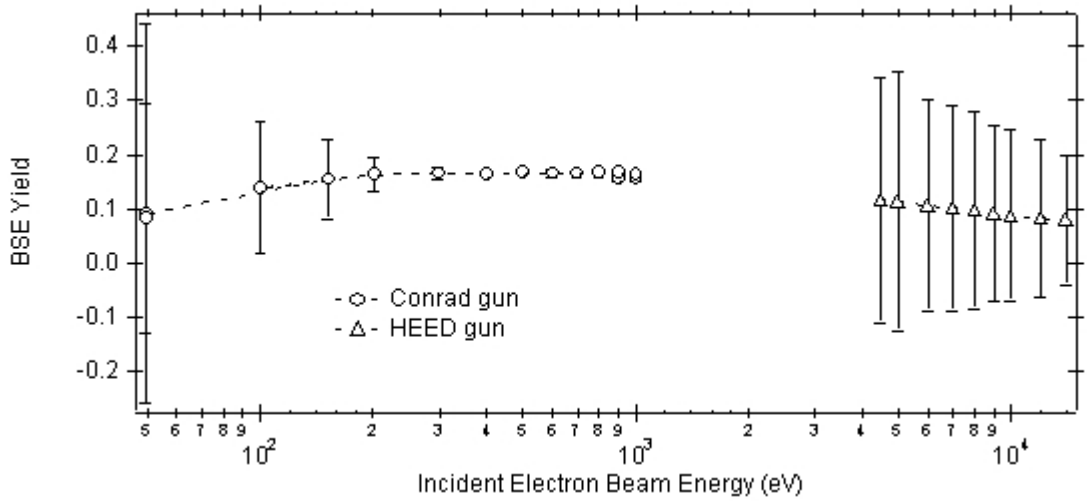


FIG. 5.12: BSE yield of Aquadag™ displayed as a semi-log plot.

be a continuation of the lower energy curves taken with the Conrad gun. The cause is most likely due to incorrect or a complete lack of adjusting the deflection to maximize sample current between each measurement. Although the values are not completely absurd, data is essentially of no use and is only included as an example of poor experimental procedure. The low energy data is excellent in comparison, although there is still the increasing error at lower energy as was seen in the previous data. As with the HOPG data, there are multiple points taken at 50 eV that again display a repeatable precision of 3% in contrast to the 40% error reflected in the error bars.

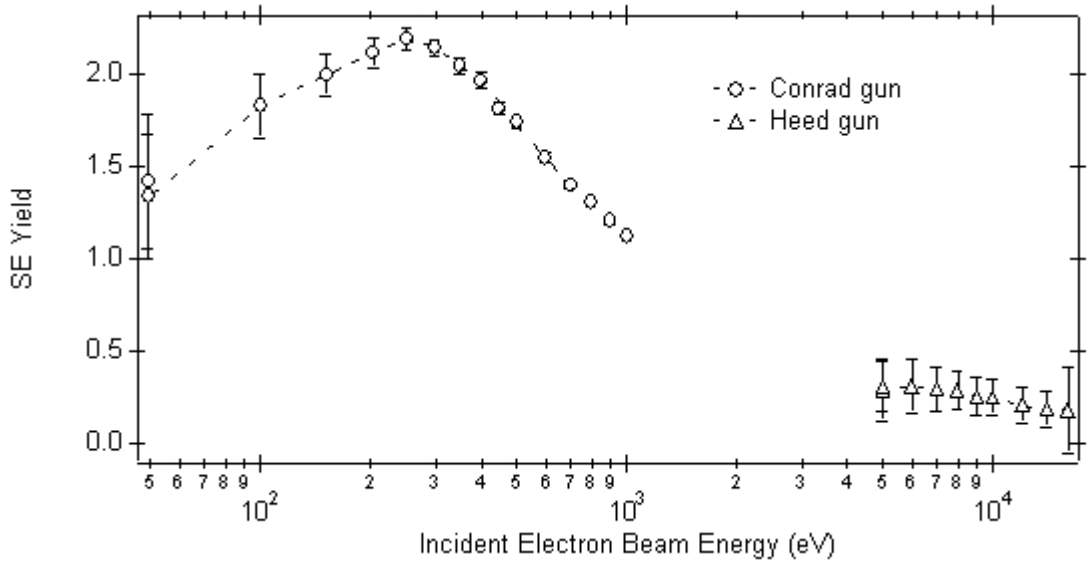


FIG. 5.13: SE yield of g-C displayed as a semi-log plot.

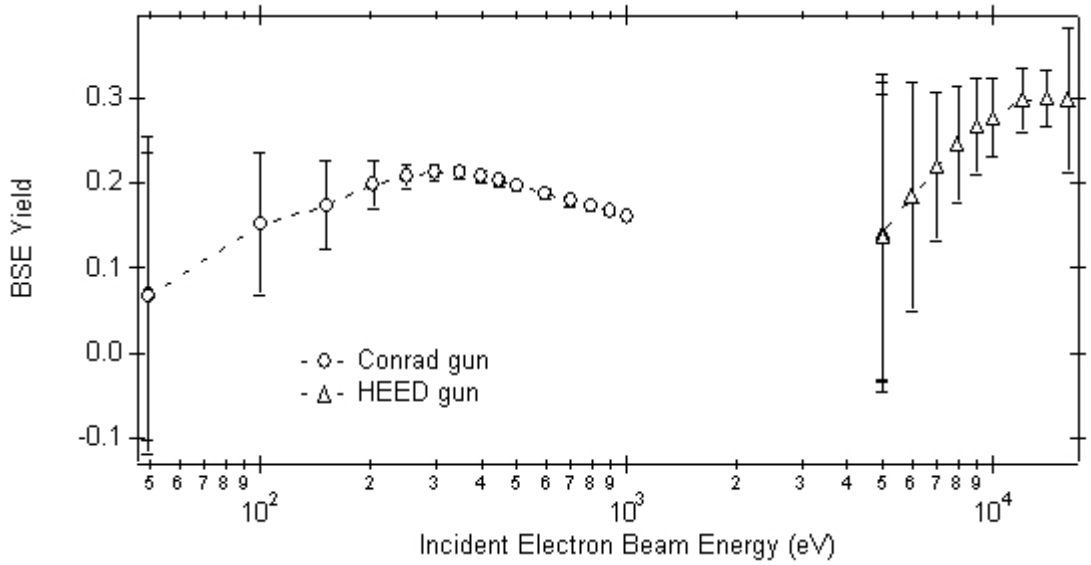


FIG. 5.14: BSE yield of g-C displayed as a semi-log plot

CHAPTER 6

DISCUSSION OF RESULTS

This chapter will focus on the SE and BSE yields of the carbon samples with an emphasis on explaining the differences in maximum SE yield of the samples. After fitting the SE yields with semiempirical models over the full energy range, the low and high energy parts of the SE yield will be discussed separately. Then the BSE yields will be discussed, except without fitting to a model function. Yields will also be compared with values found in the literature.

Section A. SE Yield Data

There were three semiempirical models reviewed in Section 2.A: The Young model of Eq.2.11, the Sternglass model of Eq. 2.14, and a variable stopping power exponent model, which is a numerical method based on Eqs. 2.8-10. Theoretical fits using each of these models to the SE yield data of the three carbon samples will now be discussed in turn.

A semi-log plot of the SE yield for HOPG, g-C and Aquadag™ with theoretical fits using the Young model from Eq. 2.11 are compared in Figure 6.1. The two fitting parameters of the Young model, the maximum yield δ_{max} and energy at which the maximum yield occurs E_{max}, are recorded in Table 6.1 along with reduced chi-squared values for an evaluation of the fits. The graph shows the model function does not fit the peaks or the high energy tails well and this is reflected in the high reduced chi-

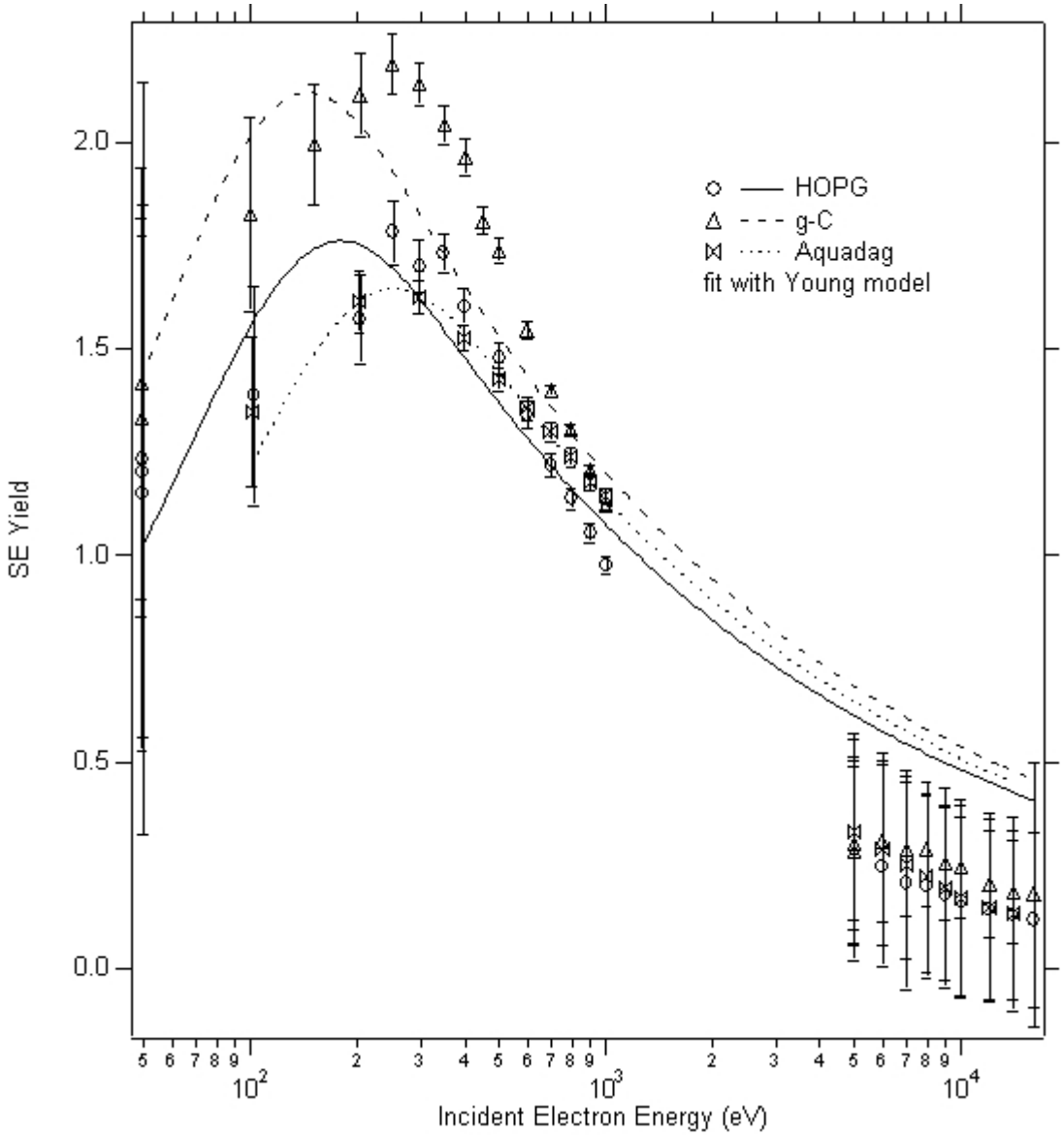


FIG. 6.1: Semi-log plot of HOPG, g-C, and Aquadag™ SE yields along with semi-empirical fits using the Young model of Eq. 2.11.

squared values. The stopping power exponent of $n = 1.35$ in the Young model is responsible for the tails of the curves being too shallow. Closer inspection reveals that the low energy section of the Aquadag™ data is a good fit to the model, but is still inconsistent with the high energy data. The fit to the Aquadag™ peak gives a

TABLE 6.1: Young model fitting parameters for SE yields

Material	δ_{max}	E_{max} (eV)	Reduced χ^2
HOPG	1.76 ± 0.08	179 ± 25	3.7
g-C	2.12 ± 0.09	144 ± 17	16
Aquadag™	1.65 ± 0.04	253 ± 17	0.94

TABLE 6.2: Sternglass model fitting parameters for SE yields

Material	δ_{max}	E_{max} (eV)	Reduced χ^2
HOPG	1.69 ± 0.03	259 ± 7	0.71
g-C	2.13 ± 0.06	230 ± 14	0.01
Aquadag™	1.54 ± 0.02	343 ± 10	2

TABLE 6.3: Variable stopping power exponent model fitting parameters for SE yields

Material	δ_{max}	E_{max} (eV)	n	Reduced χ^2
HOPG	1.74 ± 0.03	280 ± 16	1.61 ± 0.03	0.29
g-C	2.20 ± 0.04	244 ± 9	1.62 ± 0.01	0.29
Aquadag™	1.64 ± 0.03	264 ± 20	1.37 ± 0.03	0.92

convincing value for E_{max}, while the HOPG and g-C curves are inadequate fits to give suitable values.

A semi-log plot of the SE yield for HOPG, g-C and Aquadag™ with theoretical fits using the Sternglass model from Eq. 2.14 are compared in Figure 6.2. The same fitting parameters discussed above are recorded in Table 6.2 for the Sternglass model. In comparison to the shifted peaks of the Young model, the Sternglass model fits the

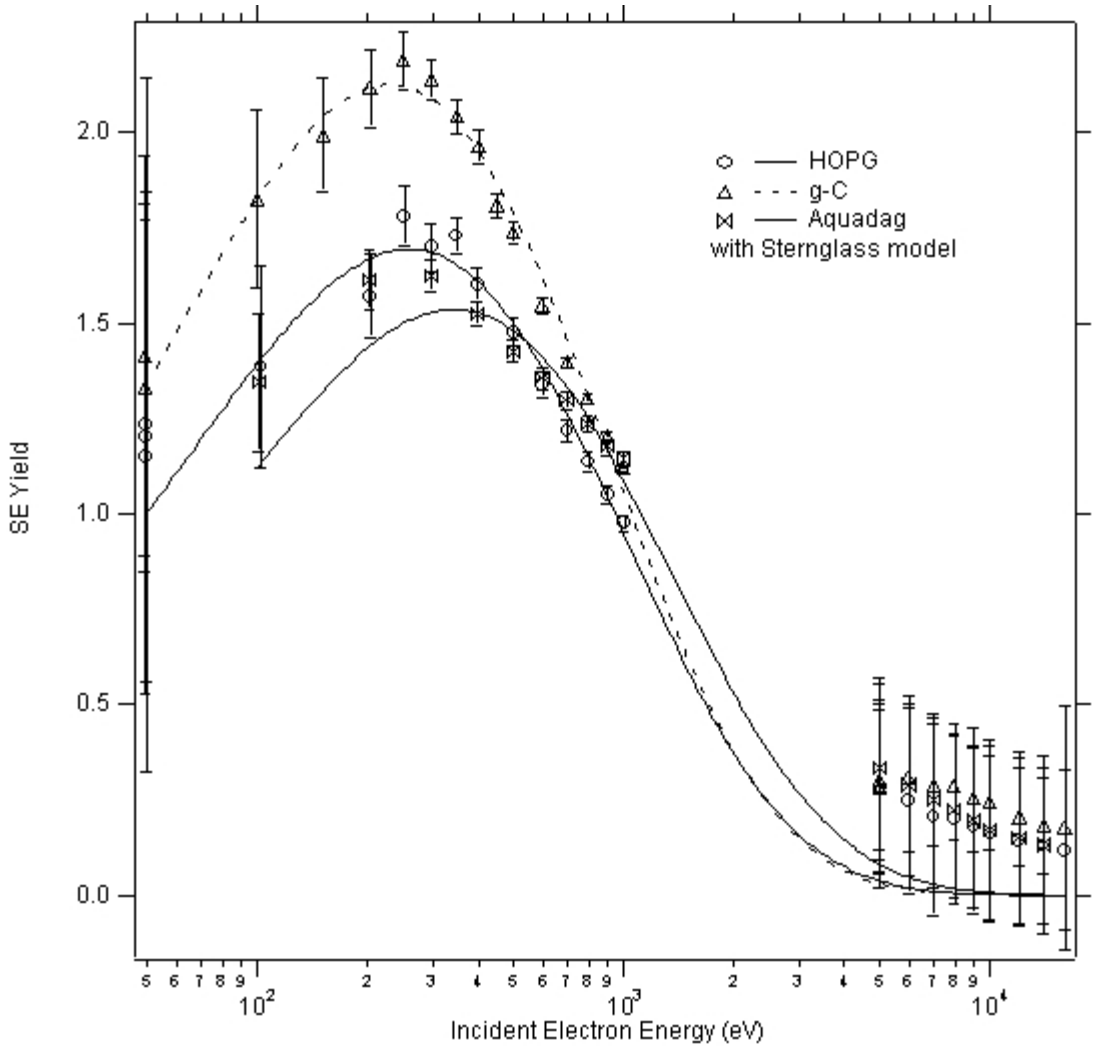


FIG. 6.2: Semi-log plots of HOPG, g-C, and Aquadag™ SE yields along with semiempirical fits using the Sternglass model of Eq. 2.14.

data well at low energy. The Sternglass model does not fit any of the high energy data well, which is typical for the Sternglass model. The large error bars of the high energy section of all the curves is the only reason the fits give suitable reduced chi-squared values, otherwise the lack of inflection in the model at lower energy would lead to poor fits for all the curves. The low reduced chi-squared values for the HOPG and g-C

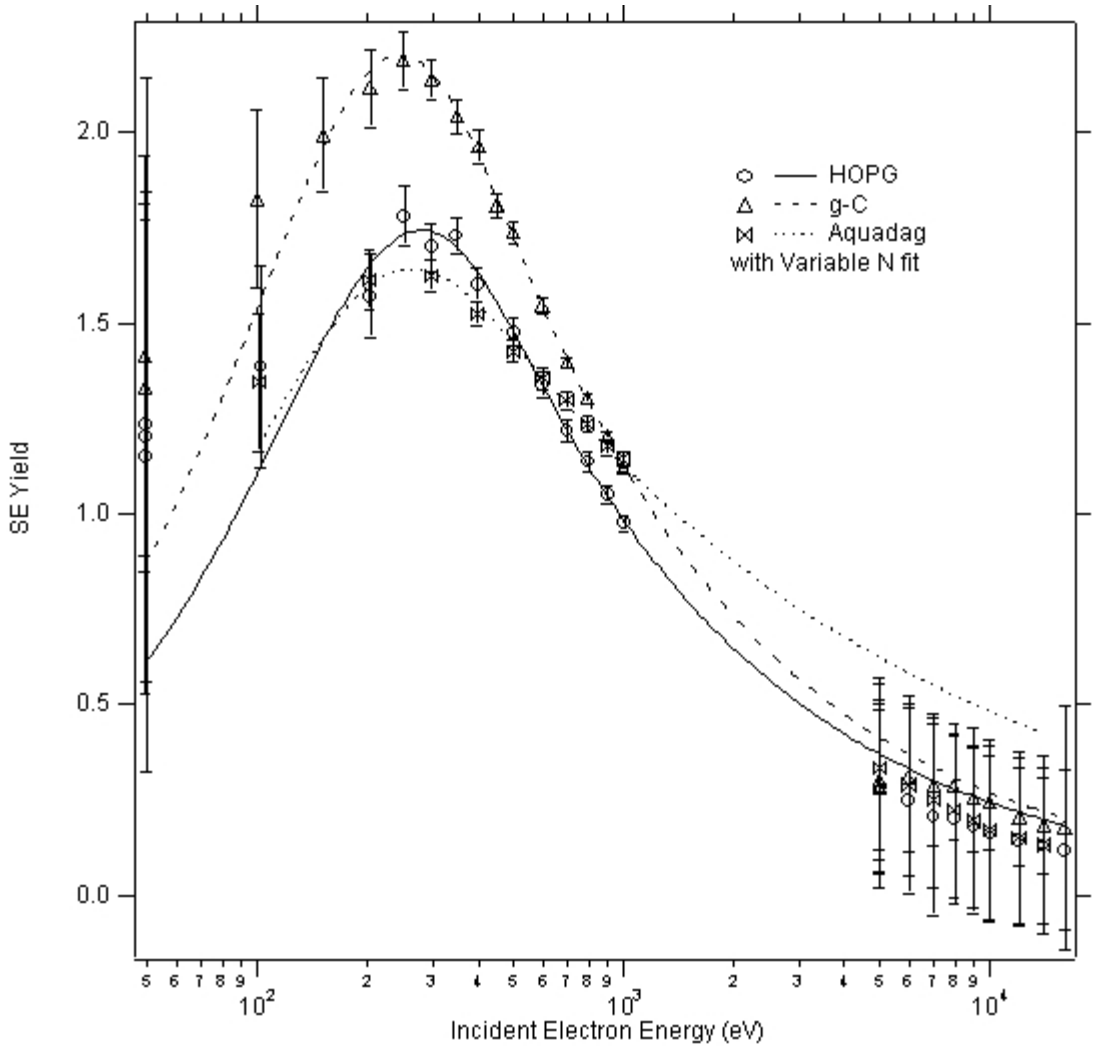


FIG. 6.3: Semi-log plots of HOPG, g-C, and Aquadag™ SE yields along with semiempirical fits using the variable stopping power exponent model.

data give credible values for E_{max}, but the shallow tail of the low energy section of the Aquadag™ data pulls that peak towards higher energy and leads to a poor fit. The poor fit to the Aquadag™ data is an indication that the shallowness of the low energy tail is due to a problem with the measurement procedure. The data might otherwise follow the HOPG and g-C data in lining up better with the high energy data.

Semi-log plots of the SE yield for HOPG, g-C, and Aquadag™ with theoretical fits using the variable stopping power exponent model are compared in Fig. 6.3. The three fitting parameters and the reduced chi-squared are recorded in Table .3. As expected, the inclusion of another free parameter leads to better fits of the data at both low and high energy. The quality of all the fits is reflected in their low reduced chi-squared values. The only exception is the high energy section of the Aquadag™ data, where the fit is dominated by the smaller error bars in the tail of the low energy section of the data. Again, this is further evidence that the shallow tail of the low energy section of the Aquadag™ may be due to experimental error. The Aquadag™ data is expected to agree with the HOPG data as they are both crystalline graphite on 100-1000 nanometer length scales. The only substantial disagreement between the two curves is the tail of the low energy section. The agreement between the HOPG and Aquadag™ at high energy, but not in the tail at low energy, is further evidence that the 5-6 data points in the tail might have suffered from an error, most likely a lack of the necessary continual adjustment of the beam position, that caused these values to be slightly higher. Additionally, the disagreement between the low energy tail of the Aquadag™ and the other two curves is exemplified by the values of the stopping power exponent for the three fits. Although the maximum SE yields of HOPG and g-C differ, the curves are in good agreement as to the value of 1.6 for the stopping power exponent. While the maximum SE yield δ_{max} and E_{max} control the height and position of the maximum, the variable stopping power exponent controls the fall-off in the tail

of the curve. The disagreement between the stopping power exponent of the Aquadag™ and the two other curves is a direct result of the shallowness in the low energy tail of the Aquadag™ data.

The stopping power exponent is a bulk property that depends primarily on the type of scattering species, which is the same in all three cases. A crude empirical equation for the stopping power exponent (Eq. 2.12), based on measurements of the electron stopping range in materials of varying atomic number, gives a value for carbon of 1.55 (Feldman, 1960). The relative agreement between the Feldman's equation and the stopping power exponent for the HOPG and g-C supports the atomic number as a dominant factor. This agreement is further evidence that a single stopping power exponent, as is used in the Young model of Eq. 2.11 and has been a common assumption (Dionne, 1975; Grais and Bastawros, 1982), is not appropriate across different materials. Eq. 2.10 of the variable stopping power exponent model relates the stopping power exponent to the product of the SE absorption coefficient α and the penetration depth R. This product of αR has also been assumed to be constant in other research (Dionne, 1975; Grais and Bastawros, 1982), which may be more justified than disregarding the dependence on atomic number because the two quantities typically counterbalance each other when they vary with other material parameters. An example of this offsetting behavior will be discussed in Subsection 6.A.1 when density is considered as a factor in the maximum SE yield. One might argue the surface contamination found on the HOPG and g-C that was absent on the Aquadag™

explains the difference, but then the high energy section of the data should disagree as well. The discussion of this disagreement in the Aquadag™ data will be discussed further as the low and high energy portions of the data are considered in more detail.

Subsection 1. Low energy section of SE yield data

The variable stopping power exponent model best represents all three carbon data sets together and will be used exclusively as the three data sets are compared in more detail. Figure 6.4 shows a linear plot of the low energy sections of the three carbon samples along with their fits to the variable stopping power exponent model.

The three carbon samples come close to agreeing on the energy E_{max} at which the maximum yield occurs. The values for E_{max} fall on the lower side of values between 275-310 eV (see Table 2.1) found in the literature (Bruining, 1938; Whetten, 1965; Wintucky *et al.*, 1981; Ruzic *et al.*, 1982; Caron *et al.*, 1998). There is a decrease in the E_{max} of g-C that deserve further consideration due to its implications about the SE escape depth that is possibly the effect of the increased bandgap. As argued previously, the stopping power of the carbon samples should be similar and therefore a decrease in E_{max} would be due to a decrease in the average escape depth of the SE's (Dionne, 1975). A decreased escape depth means the SE yield reaches a maximum at a shorter penetration depth, which occurs at a lower E_{max}. Relying on the assumption the HOPG and Aquadag™ samples should agree on E_{max}, the mean energy between the HOPG and Aquadag™ (272 ± 18 eV) does not lie beyond a statistically

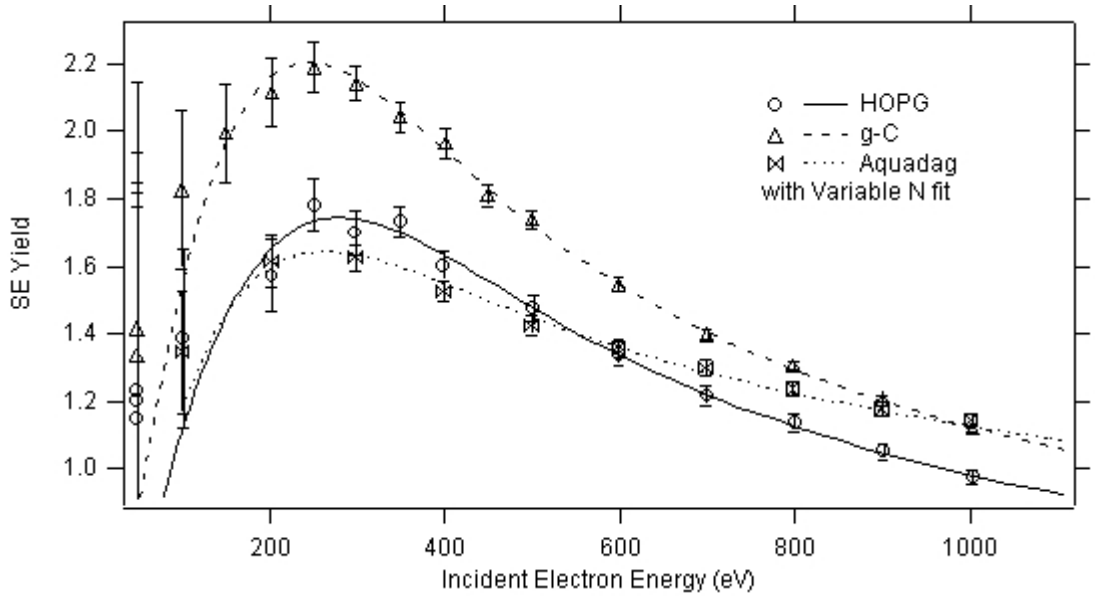


FIG. 6.4: Linear plot of low energy section of HOPG, g-C, and Aquadag™ SE yields along with semiempirical fits using the variable stopping power exponent model.

significant distance from the value for the g-C sample (244 ± 9 eV). Although the change in E_{max} between the g-C and the other forms of carbon is in the opposite direction that would be consistent with the idea of an increase in the escape depth of g-C, the data is not sufficient to fully evaluate the idea.

The maximum SE yield δ_{max} of the HOPG and Aquadag™ samples show relative agreement as they are both crystalline graphite on 100-1000 nanometer length scales. The values of δ_{max} for Aquadag™ and HOPG are 60-70% above published values (see Table 2.1) that find δ_{max} to be roughly unity (Bruining, 1938; Whetten, 1965; Wintucky *et al.*, 1981; Caron *et al.*, 1998). The disagreement is slightly larger than the correction factor used to compensate for the geometry of the HGRFA. The dissertation work of Sternglass (1953a) is the only reviewed literature to use a

correction factor and his values for Aquadag™ are 20% higher than the articles previously cited, but the present work with HOPG and Aquadag™ is still 35% higher. The disagreement with the literature is unfortunate, but is thought to be limited to the HGRFA correction and does not impact comparisons between the data that follow.

The maximum SE yield of g-C (2.2 ± 0.04) is approximately 30% higher than the HOPG (1.74 ± 0.03) and Aquadag™ (1.64 ± 0.03) curves, which is consistent with the idea outlined in Section 2.B the bandgap of g-C increases the electron mean free path or equivalently decreasing the absorption coefficient α and leads to an increased SE yield. There are other possible explanations for the increased SE yield of a material, which deserve consideration.

There is very little variation in the scattering species that could account for differences in the SE yields. The bulk material of the samples consists of carbon atoms with less than 8% impurities in the g-C samples, which is thought to be residual surfactant on the back of the sample from the preparation slide (Stoner, 1969). The film thickness is another material parameter that can be ruled out. All the samples exceed a micron of thickness, which is much larger than the mean free path in carbon at the energies of interest (Seah and Dench, 1979). Other important properties of the three samples are summarized in Table 6.4 to facilitate the further discussion of their role in the maximum SE yield of the three samples.

There is a 20% variation in the density of the HOPG (2.267 gm/cm^3) in comparison to that of g-C (1.82 gm/cm^3). The density of Aquadag™ is an

TABLE 6.4: Summary of important material properties of graphitic carbon samples

Property	HOPG (Subsection 5.A.2)	Aquadag™ (Subsection 5.A.3)	g-C (Subsection 5.A.4)
Bandgap	semi-metal (0 eV)	semi-metal	0.4-0.7 eV
Density	2.267 gm/cm^3	2.0 gm/cm^3	1.82 gm/cm^3
Structure	microcrystalline graphite with μm planar stacking	randomly oriented graphite microcrystallites	no long range order due to multi-member ring structure
Surface Roughness	< 1 nm – atomic resolution with STM	< 1 μm – visible surface roughness	< 1 nm over 245x239 μm^2
Contamination	Si: 25% Oxygen: 25%	Oxygen: 3%	Si: 15% Oxygen: 16%
Photoyield Onset	5.2 eV ± 0.05 eV	5.2 eV ± 0.05 eV	5.4 eV ± 0.05 eV
Resistivity	5 x10^{-2} Ω-cm (intraplanar) 4 x10^{-5} Ω-cm (interplanar)	~ 50 Ω-cm	5x10^{-1} Ω-cm

intermediate value (2.0 gm/cm^3). The effect of changes in density on the SE yield is not straightforward. The density is directly proportional to a material's stopping power and inversely proportional to the penetration depth; however, the density is also inversely proportional to a material's mean free path. Consider the agreement of the stopping power exponent between the HOPG and g-C. Again, the variable stopping power exponent model relates the stopping power exponent to the product of the SE absorption coefficient α (the inverse mean free path) and the penetration depth *R* in Eq. 2.10. The agreement of the stopping power exponent suggests the potentially longer

penetration depth *R* in the less dense g-C is counterbalanced by the longer mean free path and so HOPG and g-C should be regarded as equals with respect to the effects of density. There is a similar counterbalancing relationship between the product of the stopping power coefficient A and the mean free path in equations for the SE yield like Eq. 2.15. Since the density is directly proportional to the stopping power and indirectly proportional to the mean free path, the density cancels out in the product that appears in Eq. 2.15. The higher maximum SE yield is then left to depend on the other factors that influence the incident beam absorption and the SE mean free path, independent of density. The evidence in Subsection 6.A.2 supports the argument that the production of SE, related to the stopping power, is similar in all the samples, while the migration of the excited SE differs in the g-C sample due to its bandgap.

The differing structure of the samples might explain the increased maximum SE yield of the g-C sample. The argument could be made that the microcrystalline structure of the HOPG and Aquadag inhibits their SE emission by reducing the SE migration to the surface across basal planes and grain boundaries. The counter-argument is that SE migration in crystallographic directions should then be enhanced in comparison to the amorphous g-C, and could equally well lead to higher yields for the microcrystalline graphites. The relative agreement of the HOPG and Aquadag is consistent with research that found no differences in SE yield between crystals with varying orientation and polycrystalline samples, where the increased grain boundaries might impede emission (Miller and Brandes, 1997). The structure does not have a

direct influence on the maximum SE yield, other than indirectly through the creation of the bandgap.

The smoothness of a sample's surface is known to affect the SE yield (Bruining, 1938; Wintucky *et al.*, 1981; Ruzic *et al.*, 1982; Borovsky, 1988). The surface roughness argument is valid in a limited number of cases, but has been misused in the explanation of experimental data. Using the fact that the SE yield generally increases with the incident beam angle, Borovsky argues surface roughness can be viewed as a large number of tilted surfaces acting together to actually enhance emission (Borovsky *et al.*, 1988; Caron *et al.*, 1998). Although the enhanced emission of tilted surfaces is part of the reason for contrast in scanning electron microscope images, the idea surface roughness enhances the emission of a macroscopic area is not generally accepted and exemplifies how the argument has been historically misused.

The generally accepted idea is the extended structure from the surface due to roughness recaptures some portion of the SE emitted. The original argument by Bruining (1938) actually applied to porous surfaces, rather than simply roughened surfaces. The roughening of carbon samples, either by substrate sanding or ion sputtering of the sample, has been shown to decrease the SE yield (Wintucky *et al.*, 1981; Ruzic *et al.*, 1982). As mentioned in Chapter 2, Sternglass (1953a) even went so far as to include an additional parameter for sample roughness in his theoretical equation for the SE yield to explain the differences between Aquadag™ and an amorphous carbon sample derived from electron stimulated adsorption of carbon in the

presence of Octoil vapors. His results show that the amorphous carbon has a 20% higher yield than Aquadag™, which is consistent with the results presented here even though the amorphous carbon is of a different origin. Sternglass includes Bruining's soot measurements in his work and argues the increasing smoothness of the samples – from soot to Aquadag™ to amorphous carbon – is responsible for the increasing yield. The inclusion of the HOPG sample in the present work refutes the idea sample roughness alone explains these differences in SE yield. Although the optical microscope pictures in Figure 5.3 show the Aquadag™ to have a rougher surface in comparison to the STM work on g-C, the HOPG sample is known to be extremely flat from typical STM measurements. HOPG and Aquadag™ would need to have equivalent surface roughness for Sternglass's explanation to be valid, which is arguably not the case just from the optical microscope pictures in Figure 5.3. The degree of surface roughness amongst the samples is not reflected in their SE yield measurements.

The most obvious explanations for the differences in SE yield relate to the fact that the HOPG sample had more hydrocarbon contamination than the g-C sample. The contamination could be driving the HOPG yield down rather than the bandgap increasing the g-C yield. This idea is not supported by the Aquadag™ sample, which showed little contamination and yet still has a SE yield comparable to HOPG.

The g-C contamination could also serve to terminate the small fraction of dangling sp^3 bonds in the g-C with oxygen or hydrogen and reduce the electron

affinity of the g-C, which has been shown to increase the SE yield of hydrogentated diamond-like amorphous carbon (Diaz *et al.*, 1999). This explanation is not supported by the photoyield measurements of the samples shown in Fig. 6.5. The method in which the photoyield data was acquired is discussed in Chapter 4. The current emitted from the sample is measured as a function of increasing incident photon energy and then normalized by the incident photon intensity. Photoyield measurements of the HOPG had to be taken after a vacuum break due to an intermittent grounding problem between the sample and the stage when the other photoyields were measured.

The onset of the photoyield marks the minimum energy needed to emit an electron from the material. The measurement is an indication of the vacuum level of each material. In the HOPG and Aquadag™ samples, the onset energy is indicative of the work function of the sample. In the g-C sample, the onset energy is better

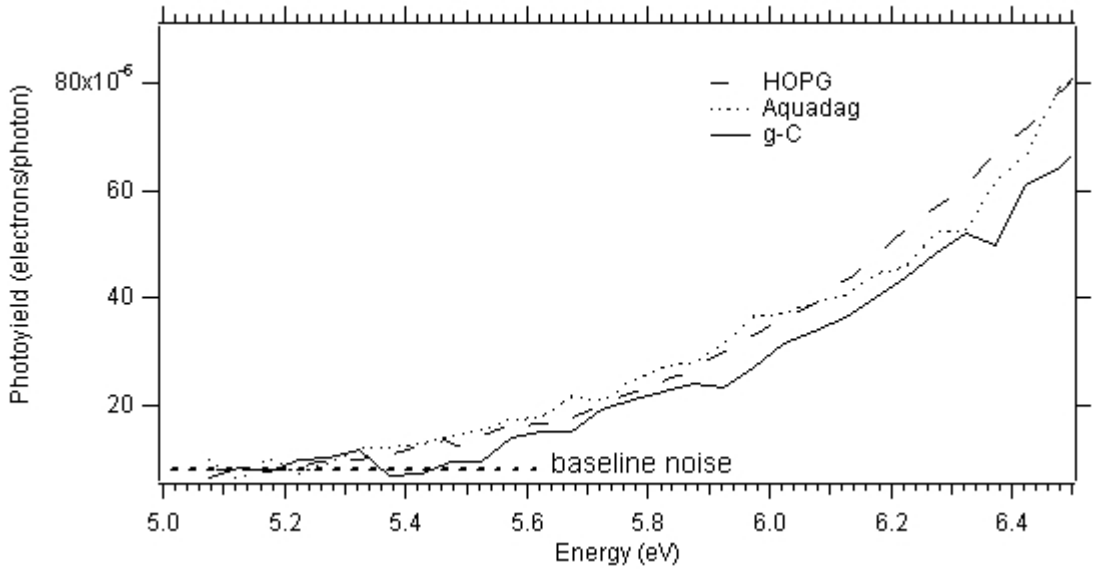


FIG. 6.5: Photoyield measurements of the HOPG, Aquadag™, and g-C samples. The data below $8x10^{-6}$ electrons/photon were assumed to be noise.

represented by the electron affinity as measured from the Fermi energy, which is typically taken to be midway through the bandgap in a semiconductor. As seen in Fig. 6.5, the fact that the g-C sample has a higher onset energy does not substantiate the idea the hydrocarbon contamination has lowered the vacuum level of the material and increased the SE yield. This argument leads to the expectation that the onset of the photoyield should occur at lower energy than the HOPG or Aquadag™. Very rough quantitative estimates of the onset energies can be made by choosing a zero level of photoyield (see Fig. 6.5). The onset energies for the photoyield (where the baseline noise intersects the photoyield) are 5.20 ± 0.05 eV for the HOPG or Aquadag™ and 5.40 ± 0.05 eV for the g-C. The difference can be interpreted as a 0.2 eV ± 0.1 eV increase in the g-C bandgap over the zero bandgap of the microcrystalline graphite. The measurement is substantially lower than the values of 0.4-0.7 eV in the literature (Robertson and O'Reilly, 1987), but the method is admittedly very crude. The result does agree better with optical absorption work done by Dallas (1996) that gives a Tauc gap of 0.1 eV. Again, the result is only meant to show the vacuum level of the g-C is not lower than the microcrystalline graphite samples. The measured difference in photoyield could have been verified by a separate technique using SE energy distribution measurements with the HGRFA. Contact potential differences between the emitting sample and the collecting surface, coated with Aquadag™, can be seen as an offset of the initial rise in the SE energy distribution curve. A difference in work functions between the sample and collector establishes a background electric field even

when both surfaces are grounded. This background field offsets the energies of the SE energy distribution. Unfortunately, the resolution needed to measure the roughly 1 eV potential difference between the g-C sample and the Aquadag™ collecting surface is beyond the roughly 1.5 eV resolution of the HGRFA (see Subsection 3.E.2).

The resistivity of the samples is indicative of the ability of free electrons to move under the influence of an electric field, which does not directly correlate to the migration process in SE emission. The low resistivity in metals is as much a reflection of the large number of available electrons for conduction as their mobility in the material. In contrast, the high resistivity of typical insulators is due to the lack of conduction electrons as a result of their bandgap, even though the electron mean free path is much longer in comparison to metals. The increased resistivity of the g-C sample in comparison to even the intraplanar resistivity of HOPG is due to the presence of the bandgap. The bandgap decreases the number of available conduction electrons at room temperature by requiring a minimum energy before conduction can take place. In this sense, the resistivity is once removed from the material parameter of interest in SE emission (the bandgap) and involves aspects of conduction that only indirectly apply to the process of SE emission, like the process of making valence electrons available for conduction. As a reflection of the bandgap, the higher resistivity of the g-C sample correlates with its higher maximum SE yield. The resistivity of the Aquadag™ sample was given by the manufacturer (Derer, 2001) and may not reflect an accurate measurement. The resistivity of the g-C sample has been

reported to be roughly equivalent to HOPG, which would make the previous discussion moot, but that estimate was based on measurements of the index of refraction and not a direct measurement (Stoner, 1969). Although the resistivity does correlate with the maximum SE yields of our carbon samples, excluding Aquadag™, the bandgap is recommended as a more direct material property of interest for SE emission.

In comparison with the ideas discussed above, the bandgap argument is the most compelling explanation for the higher SE yield of the g-C sample. Both the HOPG and Aquadag™ have zero bandgap, while the g-C is known to have a measurable bandgap. Inconsistencies or the absence of a correlation in density, surface roughness, or levels of contamination prove these explanations do not account for the increased SE yield. The one glaring difference between the g-C sample and both the HOPG and Aquadag™ samples is the presence of the bandgap.

Subsection 2. High energy section of the SE yield data

The high energy tails of the HOPG, g-C, and Aquadag™ samples are compared in Fig. 6.6. As mentioned in Section 5.2, the 5-7 keV data points of the g-C curve downward instead of the upward rise seen in the other carbon data. The discrepancy is probably due to improper alignment of the beam during the measurements. The HOPG and Aquadag™ data shows good agreement, only differing by 10%, which far exceeds the 120% uncertainty represented by the error bars. Recall from Section 5.B that the large error bars are due to an overlooked signal noise, coupled with reduced beam current. The agreement between the HOPG and Aquadag™ reaffirms the fact that the

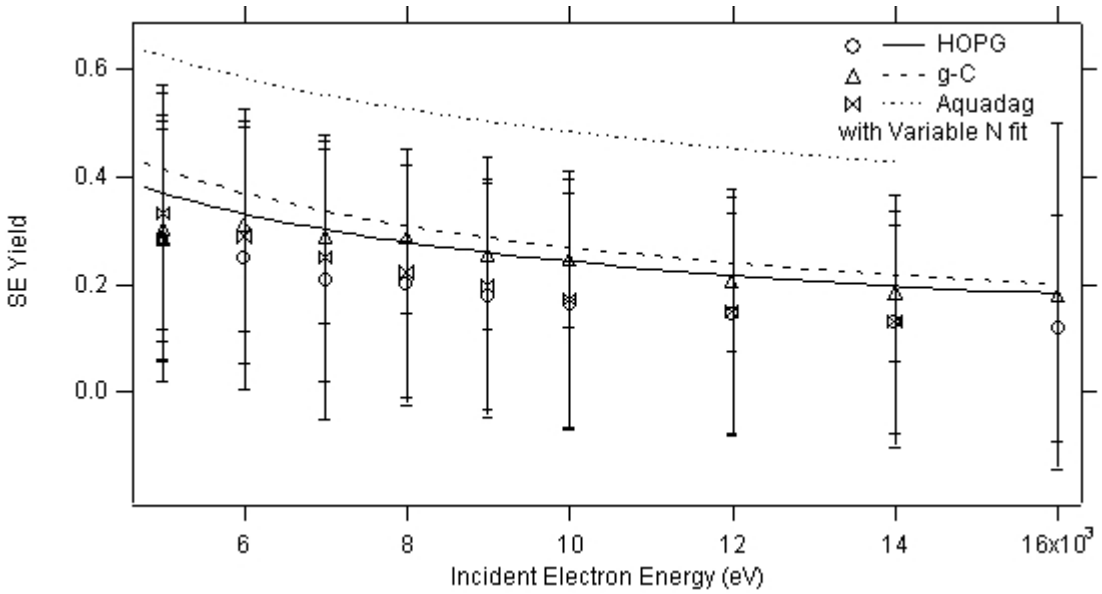


FIG. 6.6: Linear plot of high-energy section of HOPG, g-C, and Aquadag™ SE yields along with semiempirical fits using the variable stopping power exponent model.

two materials are very similar in composition. Again, the fact that the two microcyrstalline graphite data sets agree so closely at high energy casts some doubt on the tail of the low energy data for the Aquadag™ sample, which does not line up well with its high energy data nor the other carbon data at the low energy range.

Excluding the three anomalous data points between 5-7 keV in the g-C high energy SE curve, the g-C data is 30-35% higher than the HOPG and Aquadag™. The increase in the SE yield of g-C matches that seen in the low energy section and is further evidence the bandgap of g-C leads to a higher SE yield. The variable stopping power model still predicts an increased SE yield at these higher energies, but to a lesser degree than is reflected in the data itself. Given the poor experimental technqiue used to acquire the g-C data, the size of the increase is more likely somewhere in the range

between the theoretical and experimental values. The result is significant because an increased SE yield even at high energy suggests the cause of the increase is related to the migration process of the excited SE, as postulated, and not to the production process. If the reason for the increased SE yield was due to enhanced production of SE by the incident electrons, then the effect would decrease with increasing energy as the production began to take place further from the surface. The model that is consistent with the data is an essentially constant production of SE's in all our carbon samples and an increase in the depth from which the excited SE's can migrate through the g-C and still escape, which increases the SE yield at all energies.

Section B. BSE Yield Data

The BSE yield curves for HOPG, g-C and Aquadag™ are compared in Fig. 6.7. The high energy g-C data should be overlooked because its spurious results are due to poor experimental technique. There is no difference between the low energy HOPG and g-C curves outside the error bars on the data. Excluding the g-C curve, the high energy sections of the HOPG and Aquadag™ data are in excellent agreement and line up well with the low energy data. The BSE yield of all the samples was expected to be similar because the process is essentially an interaction between the incident electron and the atoms within the sample, which are carbon atoms in all cases. The general flatness of the curves agrees with the work of Sternglass, but the average BSE yield is almost double his mean value of 0.07 in the 250-2000 eV range (Sternglass, 1953b; Holliday and Sternglass, 1957). The low energy Aquadag™ data agrees with the

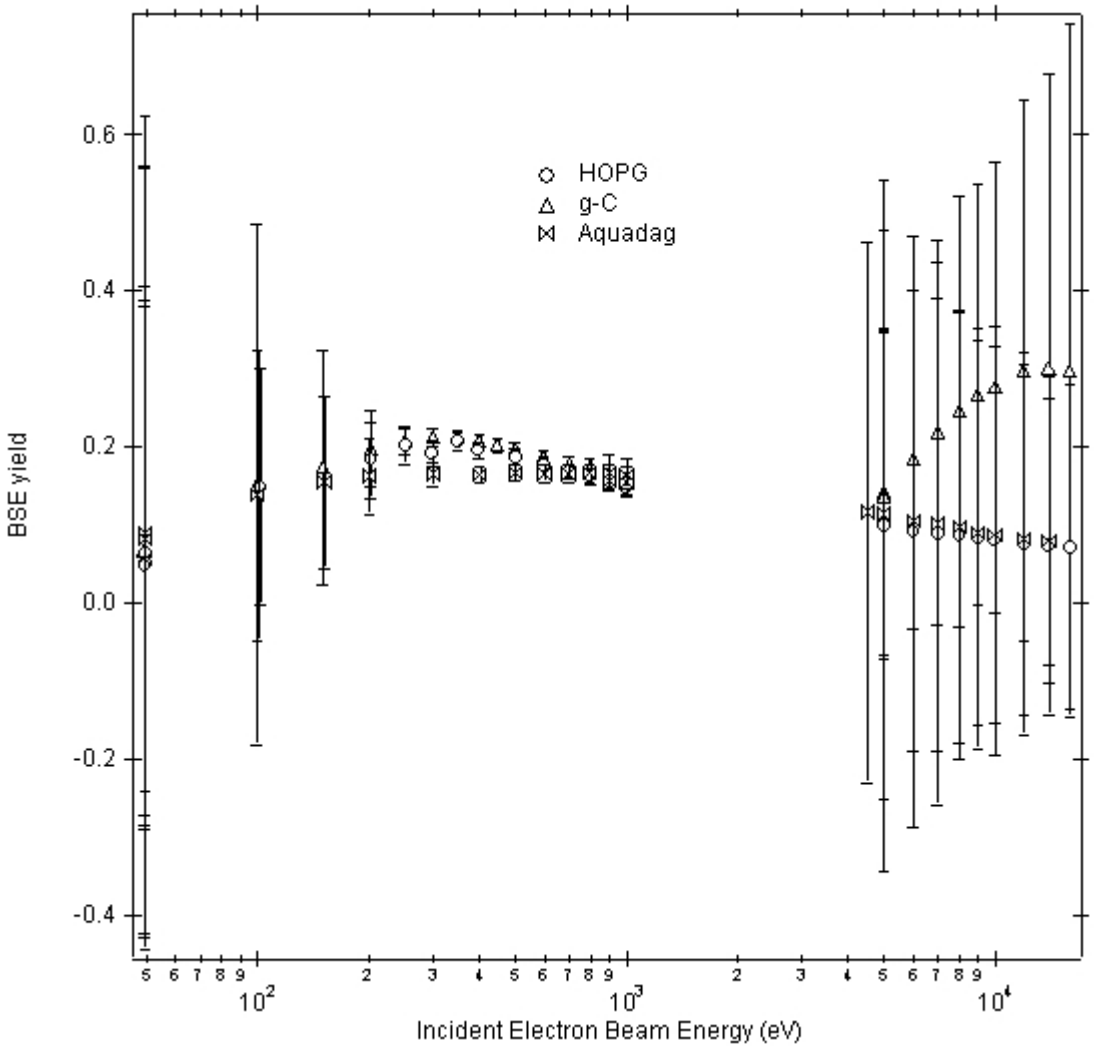


FIG. 6.7: Semi-log plot of HOPG, g-C, and Aquadag™ BSE yields.

HOPG and g-C data except in the range between 200-600 eV. The Aquadag™ data does not show the small rise around 350 eV as seen in the other two samples. The most obvious explanation is that the hydrocarbon contamination of the HOPG and g-C samples is affecting their BSE yields at low energy. This explanation is inconsistent with the fact that the BSE process is typically insensitive to surface contamination

(Chang *et al.*, 2000). Another explanation for the rise in the BSE yields of HOPG and g-C is that SE's created on the backside of the suppression grid by BSE scattering off the collection surface are significantly contaminating the BSE yield curve at low energy. This explanation is not plausible for three reasons: (i) there is no reason that the Aquadag™ should not also suffer from the unwanted current; (ii) the roughly 30% increase in the BSE yields of HOPG and g-C over the flat value represented by the Aquadag™ sample is far greater than the 2% predicted correction for this affect (see Appendix C for details); and (iii) the peak of the rise at roughly 350 eV is inconsistent with the location of the maximum SE yield at 450 eV of the 304 stainless steel grid wires (Ruzic *et al.*, 1982). There is no solid explanation for the disagreement in the BSE yields.

CHAPTER 7

CONCLUSIONS

The following chapter draws conclusions about experimental results, assesses the adequacy of the experimental apparatus, suggests modifications to the system, and provides guidance for future research.

Section A. Conclusions about the Experimental Results

The key result of this experimental investigation is the measurement of a 30% increase in the maximum SE yield of g-C over that of microcrystalline graphite samples, like HOPG and Aquadag™. From Table 6.3, the error in estimates of the maximum SE yield of these graphitic carbon samples is less than 2%. Material parameters and confounding variables, like the vacuum level of the g-C sample, have been isolated and measured so the bandgap of g-C can be said to be a dominant factor in the reason for the increased SE yield of g-C. The resistivity also correlates with the increased SE yield, but the resistivity is just an indication of the bandgap, which is the more fundamental cause for the increase. The role of the bandgap in the SE yield of a small bandgap semiconductor like g-C has been established experimentally.

This conclusion should not be understated because there was very little evidence to support the idea that the relationship would exist or be measurable in a small bandgap semiconductor. There is essentially no discussion in the literature of the role of bandgap in the SE emission properties of semiconductors and the studies that do

exist show a very weak dependence on bandgap. The proposal for this dissertation identified the electron affinity as a significant confounding variable because a reduction in the vacuum level could also explain an increase in SE yield. The effort taken to remove the electron affinity and other material parameters from the discussion has provided the confidence for the conclusion that the bandgap of g-C is responsible for the difference in maximum SE yield that was measured.

Another significant result is that the increased SE yield is maintained at high energy, which suggests the reason for the increase is related to the migration process of excited SE's and not their production. The large error in the high energy data makes the result less convincing, but the theoretical fit with the variable stopping power exponent model shows a relatively constant increase, independent of energy.

An unsuspected result of the present study is the establishment of the variable stopping power exponent model that uses Eqs. 2.8-10 as an improved alternative to the Young and Sternglass semiempirical models typically used to fit SE yield curves. The introduction of the stopping power exponent as another free parameter is supported by the close agreement between the prediction of Feldman's semiempirical model of Eq 2.12 for the stopping power (n=1.55 for carbons) with the value $n \sim 1.6$ found for the HOPG and g-C. The disagreement of the stopping power exponent for Aquadag^{TM} is discouraging, but this area of the research was unrelated and would benefit from future study.

Section B. Conclusions about the Experimental Apparatus and Methods

The instrumentation and methodology employed for the study were sufficient in that the difference in the maximum SE yield of g-C and the microcrystalline graphite was measurable and repeatable. From Fig. 4.2, the apparatus is capable of a repeatable precision of less than 1% at medium energies, although the error bars present an uncertainty that is more than double. Likewise, some of the repeated data points at low energies for the HOPG and g-C samples can be used to estimate a precision of less than 3%, while the error bars at those energies are nearly 10 times as large. Enhancements to the experimental system are discussed in the next section.

The UHV chamber and supporting surface analytical systems were well suited to the investigation. The AES system's role in determining surface contamination is crucial for any SE emission investigation because of the surface sensitivity of the phenomenon. Although the sample stage was not designed specifically for this particular investigation, the large sample volume (eight samples and three beam analysis modules) proved to be beneficial for comparative measurements between samples exposed to the same vacuum environment and experimental conditions. The electron guns were sufficiently characterized and performed well for the experiments. The unfortunate loss of UHV vacuum conditions due to the accidental venting of the chamber to mechanical and turbomolecular pump oil vapors was the most detrimental part of these experiments.

The use of the HGRFA for the SE emission measurements was a compromise

between the ideal spherical detection scheme and the design requirements of interfacing with the sample stage and multiple source beams. The primary advantage of the HGRFA is that it can used in conjunction with the sample stage to study multiple samples within the same experimental conditions. The performance of the HGRFA has been well characterized and can be said to be an adequate system in comparison to similar experimental designs. The two-grid system employed here is a unique feature. The exact sources of error in the present system are difficult to assess from collection bias curve in Fig. 3.18, which is open to a variety of interpretations (see Subsection 3.E.2 for discussion). The absolute BSE and SE yield correction factors result in yields that are 15-30% larger than reliable values found in the literature; this may result from the fact that no attempts to correct for detector error were included in the previous studies used for comparison. The comparative nature of this dissertation study reduces the impact of overestimating the SE or BSE yield. As shown in Figs. 4.4 and 4.5, the shape of the experimental curves measured with the HGRFA is in excellent agreement with comparable work in the literature.

Section C. Suggested Modifications to Experimental System

The most important area for improvement is the data acquisition system. The immediate goal would be to have the error bars accurately reflect the variation that results if the measurements are repeated. As mentioned above, the apparatus is capable of 1% precision above 500 eV and 3% uncertainty below 100 eV beam energy. A

deliberate study of the error involved in repeated measurements of a specific sample, similar to the work presented for gold in Section 4.B on error analysis, would be good to revisit. An easy and immediate improvement would be to modify the data acquisition system to sample the data in repeated sets of suitably large measurements to estimate the error involved in the yield measurements better, as discussed in Section 3.F. Reporting the standard error in the mean of 20 means from a large number of points (e.g., 3,000) could reduce the estimated error by more than 20% over the current method of using the standard deviation. That reduction is fairly consistent with current estimates of the error from repeated measurements. Further reduction in the estimated error would require more work to reduce the signal noise itself. The collector current has been identified as the dominate error responsible for the unphysical error bars seen in the experimental data. The error has been traced to a background uncertainty in the Keithley 619 signal that couples with the Conrad gun's inability to output sufficient beam current at beam energies below 500 eV. The cause of the background noise could result from the voltage bias circuitry, where the problem can be tracked down through difficult but straightforward analysis, or the noise could result in the unshielded cabling inside the UHV chamber, which is a more difficult problem to solve. Another solution would be to improve the beam current performance of the Conrad gun below 500 eV. The Conrad gun is presently capable of beam currents near 20 nA that have been shown to reduce the collector current error to roughly 1%, which is comparable to the uncertainty in the beam current of the Conrad gun. Trying to

improve the Conrad gun performance is more uncertain work than the signal analysis proposed above. A potential avenue to pursue would be to expand the voltage ranges of the einzel lenses, which currently have almost no effect on the beam, in an effort to focus more of the beam down the beam line and improve the gun's efficiency. Expanding the voltage ranges of the einzel lenses entails replacing the three resistance divider circuits for E1-E3 with a single resistance bridge (see Fig. 3.11 for schematic of Conrad gun power supply). The rewiring draws more current across the potentiometers, which means the gun will not be able to operate above 2.5 keV; however, the gun is presently limited to 1 keV due to charging anyway. If the expanded voltage ranges for the einzel lenses do not improve the gun's efficiency, then the dramatic reduction in beam current shown in Fig. 4.3 might be due to space charge limiting within the cathode housing. In any case, dismantling the Conrad gun is strongly discouraged and may result in the loss of the electron gun because of its fragile inner parts. Once the fractional error in the collector current is comparable to 1% uncertainty in the Conrad gun beam current, then the noise in the currents that comprise the beam current measurement (see Table 4.1) can be improved through rigorous signal analysis.

Another advancement in the system would be the addition of sample heating capabilities. Electron bombardment heating appears to be the easiest method of heating all the samples in the carousel. The heater would hang down from the disc above the sample stage that holds the cable in place. An optical pyrometer has been

suggested for monitoring the temperature, but the transmission through the chamber's viewports and outside air make this a complicated option. A sample module with a thermocouple could be used to calibrate the electron current with the heating of a given sample, but generalizing to other samples might be difficult. Mounting a thermocouple to a wobble stick seems to be a more practical, although expensive solution.

The HGRFA used for the present study is the first generation of the instrument and works remarkably well given the complexity of the design and construction. The detector could be better characterized if the SE and BSE yields were measured for the two different sizes of sample slugs made out of identical material. The contribution of reflected BSE's to the sample surface that creates unwanted emission could then be assessed. The assumption is that the smaller samples suffer less from the contaminating signal and would therefore have the more reliable yields, but there may not be a measurable difference. Before any modifications are made to the HGRFA, a straightforward experiment should definitely be conducted to provide internal validity to the correction factors discussed in Section 4.B and detailed in Appendix C. The suppression grid current is measured for diagnostic purposes, but is kept separate from the collector current. The opacity of the suppression grid prevents emitted electrons from reaching the collector, an effect accounted for in the theoretical correction factors. By adding the measured suppression grid current to the collector current, the suppression grid and collector surfaces can be viewed as the effective collection surface. This technique is commonly used in other SE detectors that use a suppression

grid system (Sternglass, 1953b; Thomas and Pattinson, 1969; Miller and Brandes, 1997). Including the suppression grid in the collecting surface avoids the problem of compensating for the grid opacity and worries about differences in effective transmission due to focusing when the grid is biased. Being able to avoid these problems is balanced by the additional problem of compensating for the total yield emission from the 304 stainless steel grid wires, which now would represent a current loss from the expanded collection surface. The theoretical correction factors in Appendix C would have to be revised. This exercise is an ideal opportunity to test the assumptions and methodology used to derive the correction factors. Changing the experimental method and revising the theoretical correction factors should still give the same results as before. This internal check on the validity of the theoretical correction factors could substantiate the higher yields discussed in Section 4.B. Including the suppression grid in the collection surface would have the added bonus of more closely matching experimental methods in the literature, which also benefits future comparisons like those in Section 4.B, although the inner grid is still a unique feature.

There are also more invasive improvements that are not recommended unless a complete characterization of the HGRFA has been done and the viability of the HGRFA itself is willing to be risked. One relatively easy change would be to remove the inner grid. The benefits are the HGRFA would then be more consistent with other instruments in the literature, resulting in possibly better agreement, and the transmission of the inner grid could be experimentally verified by comparison with

previous results. Once these two benefits were realized, the inner grid could be returned and the low energy SE or the incident electron beam would not be affected by high potentials on the suppression grid, necessary for the study of high energy BSE. A radical change would be to include the faceplate in the collection surface. This change would require that the faceplate be grounded to the collector and isolated from the sample stage, which are presently connected by the pin that keeps the HGRFA at the correct distance and orientation from the stage. The inclusion of the faceplate in the collecting surface would also require the suppression grid be extended across the faceplate to the edges of the sample, in order to eliminate unwanted SE emission from the faceplate. The inner grid would have to be removed and the supporting structures for the suppression grid on the face would have to be well shielded from the interior of the HRGFA, as was done with the supporting bolt and washer assemblies of the current suppression grid (Frederickson and Matthewson, 1971). The complexity of the modification would effectively mean the construction of a completely new HGRFA, which is not warranted by the present performance of the HGRFA.

Given the experience derived from building the instrumentation, some comments on the ideal detection system should be addressed. Following Sternglass (1953b), Whetten (1965), Thomas and Pattinson (1969), and Miller and Brandes (1997), a spherical detector seems ideal. The inner grid's field free region would be sacrificed and the suppression grid would be included in the collecting surface. The advantage is that BSE scattering off the collector surface would most likely miss a

small sample and return to the collector, which means there is no lost current or unwanted production of SE's at the sample. The disadvantage is that SE's are created on the suppression grid and are propelled towards the sample during the suppression mode when the sample has a positive potential with respect to the grid. As mentioned, Sternglass (1953a; 1953b) does an excellent job of correcting for this effect. The main complication with a spherical detector is that the need for a small sample surface makes the study of a number of samples under the same experimental conditions very difficult. One way to avoid this is to use a cube for the sample stage at the end of a rotatable arm. The electron beam is introduced at a right angle to the rotatable arm so that four faces of the cube, with three samples and a Faraday cup, can be individually exposed to the beam by rotating the cube faces. The complexity of mounting three samples and a Faraday cup on a suitably small cube should not be underestimated. The collecting surface might have to be expanded to compensate, as was done in the work by Thomas and Pattinson, rather than try to squeeze the samples onto a small cube. The use of a spherical detector also complicates the use of multiple sources, which were necessary for this investigation. Any number of sources could be used in the plane perpendicular to the rotatable arm, but holes would have to be drilled through the collecting surface and suppression grid for each source beam.

Section D. Suggestions for Future Research

The results of this dissertation raise questions about the electron interaction mechanisms involved in the SE emission of small bandgap semiconductors. The idea

of a threshold energy for the bandgap to play a role in SE emission, as suggested in Section 2.B, must now give way to a more complicated picture involving the probability of electron-electron scattering near the conduction band minimum. Theoretical development must be advanced beyond the simple energy band diagrams discussed in Section 2.B. The semiempirical models outlined in Section 2.A were sufficient for gauging the important parameters responsible for the increased SE yield, so perhaps providing a better theoretical understanding of those semiempirical parameters is the place to begin. For example, what is an appropriate relationship between the SE mean free path and the bandgap?

The opportunity for comparative study provided by the amorphous g-C sample along with the microcrystalline graphites raises the question of whether this same type of study could be conducted with other semiconductor materials. The graphitic carbons had the advantage of being relatively inert to adsorbed surface contamination. Other factors that may plague similar semiconductor studies are the effects of defect scattering and bandbending. The prospect of conducting a similar study in other semiconductors may be worth the difficulty for a better understanding of the important material properties in SE emission, regardless of whether bandgap can be successfully isolated.

The next step in continuing this area of research is to anneal the g-C sample and study the relationship between bandgap and the maximum SE yield as established here by varying the bandgap within essentially the same material. The g-C should be

evaporated straight onto a molybdenum substrate to avoid the blistering noted in Subsection 6.A.5 due to trapped water. The complete reduction of the bandgap may require temperatures beyond the available vacuum oven's capacity of 1050° C (Rouzaud *et al.*, 1983). There is a full discussion of annealing the g-C sample in Subsection 5.A.5. After annealing the samples, the bandgap can be characterized using optical absorption measurements and applying the Tauc equation (Elliot, 1990). In addition to the Tauc gap, there is another method for characterizing the bandgap called the E_{04} gap at which the absorption coefficient equals 10^4 cm^{-1}. The annealing and bandgap characterization might need to be iterated to find the important annealing temperatures. Similar annealing and bandgap research has been done by Ferrari *et al.* (1999) with tetrahedral amorphous carbon, but the material is so different from g-C that only the methods of the research would be applicable. Although annealing studies of the Raman spectra of amorphous carbons have been done (Wada *et al.*, 1980; Rouzaud *et al.*, 1983; Dillon *et al.*, 1984; Dallas, 1996), there are no published works relating the bandgap of g-C with annealing temperature, which would also be a noteworthy contribution. Measuring other material properties of the annealed g-C samples might also be of interest, both in general and to better evaluate the assertions in this dissertation. Measuring the resistivity with a four-point probe and the density with a gravimetric method are the two most important factors identified from the present study. Care must be taken using a four-point probe with the thin and brittle annealed g-C samples.

The annealed g-C samples would then be introduced into the vacuum chamber along with unannealed g-C, HOPG and Aquadag™ samples for a replication study. Cleaning the samples *in situ* would require some type of low temperature heating as described in Section 7.B. Sputtering with ions should be avoided to ensure a flat surface that is free of defects, but a careful study of the effects of sputtering would be of interest to compare with the available studies (Wintucky *et al.*, 1981; Goto and Takeichi, 1996; Caron *et al.*, 1998). The study would definitely benefit from not having oxidation or hydrogenation – resulting from the vacuum contamination due to venting, for example – as confounding variables like the present study. The temperature necessary for the desorption of hydrocarbons is assumed to occur below the 800° C needed to change the structure of the g-C, but no references were found during the review for this study. A careful study of the yields of the already annealed g-C as a function of sample heating would solve the dispute and might also provide interesting results.

Measurements of the photoemission onset would also be necessary to characterize the vacuum level of the samples. Instead of measuring the sample current, as was done to get the photoyield, the HSA could be used to get high precision measurements. The benefit of higher resolution with the HSA is counterbalanced by the lack of knowledge about the absolute photoyield due to the use of an electron multiplier, which amplifies the current by an unpredictable amount. The absolute photoyield is not important in characterizing the vacuum level, which requires only a

comparison of the relative photoyield onset energies. The HSA energy measurements can be precisely calibrated from the Fermi level using a distinctive peak in the SE energy distribution of HOPG or Aquadag™ (Oelhafen and Freeouf, 1983).

The straightforward question of future work is to verify there is a correlation between the bandgap and maximum SE yield. The present work suggests this should be the case. If the bandgap varies, but the yield remains unchanged, then the higher yield is probably due to a surface contamination effect. The photoyield results of the present study make this result unlikely. Secondary to the verification of the influence of the bandgap on SE yield is the way in which the gap closes. There could be a gradual reduction in the amorphous structure or a dramatic shift over a small temperature range. Either case would be of interest, not just in the investigation of SE yield, but to the community of researchers interesting in characterizing amorphous carbon materials as well. The larger question for future research is a theoretical description of the nature of the relationship. An equation like Eq. 2.15 that can relate the bandgap, or at least the MFP, to the maximum SE yield could be the basis for a theoretical fit that would pin down fitting parameters can be assumed to be constants in g-C, like the SE escape probability B or the stopping power coefficient A for the incident beam. Being able to quantify the relationship between the bandgap and the maximum SE yield would bring the theory of bandgap in semiconductors from the qualitative arguments presented in Section 2.2 into the realm of quantitative science.

The main question of this section is to decide whether the proposed study above

could be conducted with the present equipment. Assuming the full 0.5 electrons/electron variation in the SE yield between g-C and HOPG or Aquadag™ (see Table 6.1) can be spanned by the annealing process, then the present 0.04 electrons/electron error (see Table 6.1) leads to roughly five measurably distinct points within the gap. Again, the question of the reliability of the absolute yield values does not pertain to this future work. Reducing the error can now be seen as being of vital importance in increasing the resolution of the relationship between bandgap and SE yield. The capacity of the available vacuum furnace is a major weakness to the future study. The full variation in the SE yield measured here would most likely not be spanned by annealing g-C at 1050° C. The reduction in the error is all the more important. With the roughly 20% reduction in the error anticipated above, there could possibly be 10 distinct data points over the full variation in maximum SE yield. Given the success with the variable stopping power model, further reduction in the error bars might also translate into better estimates of the maximum SE yield as a fitting parameter. Although individual measurements might not be distinguishable, the fitted curves could still be measurably different. The bandgap also should not be assumed to vary linearly with annealing temperature, so predicting the ability of future work to measure changes in yield is all the more complicated. Repeated study of the phenomenon might be the only way to lend credibility to the results.

The outcome is not certain, but even modest estimates for the anticipated performance of the apparatus make the future study of the relationship of bandgap to

the SE emission properties of g-C, and the ancillary works mentioned above, too appealing to be avoided for fear of not discerning the results. Take the success of the present study in the face of the uncertainty that presented itself at the onset as the necessary encouragement.

REFERENCES

Alig, R. C., and S. Bloom, 1975, "Electron-hole creation energies in semiconductors," Phys. Rev. Lett. **35**, 1522-1525.

Analog Devices, Inc., 1989, "1 pA monolithic electrometer operational amplifiers: AD546 data sheet," Rev. A. (Norwood, MA).

Analog Devices, Inc., 1994, "Low cost, miniature isolation amplifiers: AD202/AD204 data sheet," Rev. B. (Norwood, MA).

Baroody, E. M., 1950, "A theory of secondary electron emission from metals," Phys. Rev., **78**, 780-787.

Borovsky, J. E., D. J. McComas, and B. L. Barraclough, 1988, "The secondary-electron yield measured for 5-24 MeV protons on aluminum-oxide and gold targets," Nucl. Instrum. Methods B **30**, 191-195.

Bruining, H., 1938, "Secondary electron emission," Philips Tech. Rev. **3**, 80-86.

Cao, Y., and E. H. Conrad, 1989, "High q-resolution gun for low energy electron diffraction," Rev. Sci. Instrum. **60**, 2642-2645.

Caron, M., M. Beuve, H. Rothard, B. Gervais, A. Dubus, and M. Rösler, 1998, "Experimental and theoretical study of target thickness dependent electron yields induced by electrons in carbon," Nucl. Instrum. Methdods B **135**, 436-442.

Castell, M. R., T. W. Simpson, I. V. Mitchell, D. D. Perovic, and J. M. Baribeau, 1999, "Deactivation and diffusion of boron in ion-implanted silicon studied by secondary electron imaging," Appl. Phys. Lett. **74**, 2304-2306.

Chang, W. Y., 2001, UV source lab notebook, SER rm. 21, Utah State University (unpublished).

Chang, W. Y., N. Nickles, R. E. Davies, and J. R. Dennison, 1998, "Utah State University Ground-Based Test Facility for Study of Electronic Properties of Spacecraft Materials," in *Proceedings of 6th Spacecraft Charging Technology Conference*, Boston, MA.

Chang, W. Y., J. R. Dennison, J. Kite, and R. E. Davies, 2000, "Effects of Evolving

Surface Contamination on Spacecraft Charging," in *Proceedings of the 38th Aerospace Sciences Meeting*, Reno, NV. (American Institute of Aeronautics and Astronautics).

Clothier, B. L., 1991, "Development of a High-Resolution Low Energy Electron Diffraction System," senior thesis (University of Texas, Austin).

Dallas, T., 1996, "Structural Phases of Disordered Carbon Materials," Ph.D. thesis (Texas Tech University).

Davies, R. E., 1999, "Measurement of Angle-Resolved Secondary Electron Spectra," Ph.D. thesis (Utah State University).

Davies, R. E., and J.R. Dennison, 1997, "Evolution of secondary electron emission characteristics of spacecraft surfaces," J. Spacecraft and Rockets, **34**, 571.

Dednam, C. C., S. Froneman, D. W. Mingay, and J. V. Waart, 1987, "Secondary electron emission from carbon foils resulting from fast ion bombardment," Nucl. Instrum. Methods B **24**, 366-368.

Dekker, A. J., 1958, *Solid State Physics*, edited by Seitz and Turnbull (Academic, New York).

Dennison, J. R., 1985, "(e,2e) Spectroscopic Investigations of the Spectral Momentum Densities of Thin Carbon Films," Ph.D. thesis (Virginia Tech University).

Dennison, J. R., M. Holtz, and G. Swain, 1996, "Raman spectroscopy of carbon materials," Spectroscopy **11**, 38-46.

Derer, J., 2001, Acheson Colloids, Port Huron, MI (private communication).

Diaz, J., and S. Anders, and A. Cossay-Favre, 1999, "Enhanced secondary electron yield from oxidized regions of amorphous carbon films studied by x-ray spectromicroscopy," J. Vac. Sci. Technol. A **17**, 2737-2740.

Dillon, R. O., J. A. Woollam, and V. Katkanant, 1984, "Use of raman scattering to investigate disorder and crystallite formation in as-deposited and annealed carbon films," Phys. Rev. B **29**, 3482-3489.

Dionne, G. F., 1973, "Effects of secondary electron scattering on secondary emission yield curves," J. Appl. Phys., **44**, 5361-5364.

Dionne, G. F., 1975, "Origin of secondary-electron-emission yield-curve parameters,"

J. Appl. Phys. **46**, 3347-3351.

Elliot, S. R., 1990, *Physics of Amorphous Materials* (Longman Scientific and Technical, New York).

Fahrang, H., E. Napchan, and B. H. Blott, 1993, "Electron backscattering and secondary electron emission from carbon targets: comparison of experimental results with Monte Carlo simulations," J. Phys. D **26**, 2266-2271.

Feldman, C., 1960, "Range of 1-10 keV electrons in solids," Phys. Rev. **117**, 455-459.

Ferrari, A. C., B. Kleinsorge, N. A. Morrison, A. Hart, V. Stolojan, and J. Robertson, 1999, "Stress reduction and bond stability during thermal annealing of tetrahedral amorphous carbon," J. Appl. Phys. **85**, 7191-7197.

Fatman I-III, lab notebooks, SER rm. 21, Utah State University (unpublished).

Fish, C., 1998, "Low energy electron gun power control unit," Electrical engineering senior project, Utah State University (unpublished).

Frederickson, A. R., and A. Matthewson, 1971, "Backemission of electrons from metals irradiated by 0.2 MeV to 1.4 MeV electrons," Physical Sciences Research Papers No. 463 (Air Force Cambridge Research Laboratories, Cambridge, MA).

Gao, C., Y. Y. Wang, A. L. Ritter, and J. R. Dennison, 1989, "Nature of Carbon-Carbon Bonding in Evaporated and Ion Sputtered ("Diamond-like") Amorphous Carbon Films from (e,2e) Spectroscopy," Phys. Rev. Lett., **62**, 945 - 948.

Goto, K., and Y. Takeichi, 1996, "Carbon reference Auger electron spectra measured with a high-performance cylindrical mirror analyzer," J. Vac. Sci. Technol. A **14**, 1408-1415.

Grais, K. I., and A. M. Bastawros, 1982, "A study of secondary electron emission in insulators and semiconductors," J. Appl. Phys. **53**, 5239-5242.

Hansen, W. N., and G. J. Hansen, 2001, "Standard reference surfaces for work function measurements in air," Surf. Sci. **481**, 172-184.

Hastings, D., and H. Garret, 1996, *Spacecraft-Environment Interactions* (Cambridge University, Cambridge, UK).

Himpsel, F. J., J. A. Knapp, J. A. VanVechten, and D. E. Eastman, 1979, "Quantum

photoyield of diamond (111) – A stable negative-affinity emitter," Phys. Rev. B **20**, 624-627.

Holliday, J. E., and E. J. Sternglass, 1957, "Backscattering of 5-20 keV electrons from insulators and metals," J. Appl. Phys. **28**, 1189-1193.

Hoffman, A., S. Prawer, and M. Folman, 1991, "Secondary electron emission spectroscopy: A sensitive and novel method for the characterization of the near-surface region of diamond and diamond films," Appl. Phys. Lett. **58**, 361-363.

Iwase, F., and Y. Nakamura, 1997, "Enhancement of secondary electron emission from heavily Si-implanted and Si-doped GaAs," Appl. Phys. Lett. **71**, 2142-2144.

Jonker, J. H. L., 1951, "The angular-distribution of the secondary electrons of nickel," Philips Res. Rep. **6**, 372-387.

Klein, C. A., 1962, "Electrical properties of pyrolytic graphites," Rev. Mod. Phys., **24**, 56-58.

Krainsky, I. L., G. T. Mearini, V. M. Asnin, H. Sun, M. Foygel, and A. G. Petukhov, 1996, "Auger electron spectroscopy of the hydrogen terminated chemical vapour deposited diamond surface," Appl. Phys. Lett. **68**, 2017-2019.

Lee, S. J., 1995, "Structure and Interaction Energies of Kr atoms Adsrobed on Graphitic Amorphous Carbon," M.S. thesis (Utah State University).

Lide, D. R., 1990, *CRC Handbook of Chemistry and Physics*, 71st ed. (CRC, Boca Raton, FL).

Liu, S., S. Gangopadhyay, G. Sreenivas, S. S. Ang, and H. A. Naseem, 1997, "Photoluminescence studies of hydrogenated amorphous carbon and its alloys," J. Appl. Phys. **82**, 4508-4514.

Marton, L., 1979, *Vacuum Physics and Technology* (Academic, New York).

Miller, J. B., and G. R. Brandes, 1997, "Effects of dopant concentration, crystallographic orientation, and crystal morphology on secondary electron emission from diamond," J. Appl. Phys **82**, 4538-4545.

Miller, W. R., and N. N. Axelrod, 1966, "Modified Faraday cage," Rev. Sci. Instrum. **37**, 1096-1097.

Moore, A. W., 1973, *Physics and Chemistry of Carbon* (Marcel Dekker, New York).

Moore, J. H., C. C. Davis, and M. A. Coplan, 1983, *Building Scientific Apparatus* (Addison-Wesley, Reading, MA.).

Nickles, N., R. E. Davies, and J. R. Dennison, 1998, "Applications of Secondary Electron Energy- and Angular-Distributions to Spacecraft Charging," in *Proceedings of 6th Spacecraft Charging Technology Conference*, Boston, MA.

Nickles, 1999, lab notebook, SER rm. 21, Utah State University (unpublished).

Oelhafen, P., and J. L. Freeouf, 1983, "Accurate spectrometer calibration in electron spectroscopy," J. Vac. Sci. Technol. A **1**, 96-97.

Phillips, M. R., M. Toth, and D. Drouin, 1999, "Depletion layer imaging using a gaseous secondary electron detector in an environmental scanning electron microscope," Appl. Phys. Lett. **75**, 76-78.

Reimer, L., and H. Drescher, 1977, "Secondary electron emission of 10-100 keV electrons from transparent films of Al and Au," J. Phys. D **10**, 805-815.

Robertson, J., 1986, "Amorphous carbon," Adv. Phys. **35**, 317-374.

Robertson, J., and E. P. O'Reilly, 1987, "Electronic and atomic structure of amorphous carbon," Phys. Rev. B **35**, 2946-2957.

Rouzaud, J. N., A Oberlin, and C. Beny-Bassez, 1983, "Carbon films: Structure and microtexture (optical and electron microscopy, raman spectroscopy)," Thin Solid Films **105**, 75-96.

Ruzic, D., R. Morre, D. Manos, and S. Cohen, 1982, "Secondary electron yields of carbon-coated and polished stainless steel," J. Vac. Sci. Technol. **20**, 1313-1316.

Schou, J., 1988, "Secondary electron emission from solids by electron and proton bombardment," Scan. Micro. **2**, 607.

Schwarz, S. A., 1990, "Application of a semiempirical sputtering model to secondary electron emission," J. Appl. Phys. **68**, 2382-2391.

Seah, M. P., and W. A. Dench, 1979 "Quantitative electron spectroscopy of surfaces: A standard data base for electron inelastic mean free paths in solids," Surf. and Interface Analysis, **1**, 2-11.

Seiler, H., 1983, "Secondary electron emission in the scanning electron microscope," J. Appl.. Phys. **54**, R1 -R18.

Shaw, S. Y., 1992, "An integrated-circuit based wide range electrometer implemented with automatically ranged linear display," Rev. Sci. Instrum., **63**, 3505-3507.

Shih, A., J. Yater, P. Pehrsson, J. Butler, C. Hor, and R. Abrams, 1997, "Secondary electron emission from diamond surfaces," J. Appl. Phys. **82**, 1860-1867.

Sternglass, E. J., 1953a, "An Experimental Investigation of Electron Back-Scattering and Secondary Emission from Solids," Ph.D. thesis (Cornell University).

Sternglass, E. J., 1953b, "Backscattering of kilovolt electrons from solids," Phys. Rev. **95**, 345-358.

Stoner, J. O., 1969, "Accurate determination of carbon-foil surface densities," J. Appl. Phys. **40**, 707-709.

Stoner, J. O., 2001, Arizona Carbon Foils (private communication).

Taylor, P. A., 1988, "Construction of pierced hemispherical grids," J. Vac. Sci. Technol. A. **6**, 2583-2584.

Thomas, S., and E. B. Pattinson, 1969, "Automatic measurement of secondary electron emission characteristics of TaC, TiC, and ZrC," Brit. J. Appl. Phys. **2**, 1539-1547.

Thomas, S., and E. B. Pattinson, 1970, "Range of electrons and contribution of back-scattered electrons in secondary production in aluminum," J. Phys. D **3**, 349-357.

Wada, N., P. J. Gaczi, and S. A. Solin, 1980, "'Diamond-like' 3-fold coordinated amorphous carbon," J. Non-crystalline Solids **35**, 543-548.

Whetten, N. R., 1965, "Secondary electron emission of vacuum-cleaved solids," J. Vac. Sci. Technol. **2**, 84-88.

Willis, R. F., L. D. Laude, and B. Fitton, 1972a, "Electron states and disorder in a-Ge films studied by secondary electron emission spectroscopy," Phys. Rev. Lett. **29**, 220-224.

Willis, R. F., B. Fitton, and D. K. Skinner, 1972b, "Study of carbon-fiber surfaces using Auger and secondary electron emission spectroscopy," J. Appl. Phys. **43**, 4412-4419.

Willis, R. F., B. Fitton and G.S. Painter, 1974, "Secondary electron emission spectroscopy and observation of high-energy excited states in graphite: Theory and experiment," Phys. Rev. B **9**, 1926-1937.

Wintucky, E. G., A. N. Curren, and J. S. Sovey, 1981, "Electron reflection and secondary emission characteristics of sputter-textured pyrolytic graphite surfaces," Thin Solid Films **84**, 161-169.

Woods, M. E., B. J. Hopkins, and G. M. McCracken, 1985, "Secondary electron yield measurements from limiter materials in the joint European torus," Surf. Sci. **162**, 928-933.

Woods, M. E., B. J. Hopkins, G. F. Matthews, G. M. McCracken, P. M. Sewell, and H. Fahrang, 1987, "An investigation of the secondary-electron emission of carbon exposed to a hydrogen plasma," J. Phys. D **20**, 1136-1142.

Yater, W. E., and A. Shih, 2000, "Secondary electron emission characteristics of single-crystal and polycrystalline diamond," J. Appl. Phys. **87**, 8103-8112.

APPENDICES

APPENDIX A: VACUUM CHAMBER DETAILS

This appendix includes details about the vacuum chamber, including a description of the ports at the lower surface analysis level of the chamber and measurements of the magnetic fields inside the chamber.

Table A.1 contains a list of all the flanges located at the lower level of focal points in the UHV chamber. There are two separate focal points in the lower level plane, not including the center line (CL). One focal point (X=2.084", Y=1.203", Z=6.125" where coordinates are specified in Table A.1) is for use with the HEED gun as the source and the other (0.979",2.198", 6.125") is for use with the UV light source and the HSA. The items mounted on the ports are the configuration used for this dissertation research. Refer to Section 3.A and Fig. 3.2 for further details.

The magnetic field inside the UHV chamber was measured shortly after the magnetic shielding was inserted. The magnetic field was measured with a gaussmeter using both transverse and axial probes (Bell model 640). Figure A.1 shows a set of magnetic field measurements determined by dropping the gaussmeter down into the chamber at a location near the HEED gun focal point (FP1 in Table A.1). The flux of magnetic field lines through the gaussmeter was varied from north-to-south, east-to-west, and through the z-axis itself by holding the gaussmeter perpendicular to those directions or varying the type of probe tip used by the meter. The total magnitude of the magnetic field was computed by adding the three measurements in quadrature.

Figure A.2 shows a similar set of measurements at a location near the turbomolecular pump flange (L13 in Table A.1), opposite the HEED gun focal point. A set of measurements from the HEED gun location is included on the east-to-west graph as a reference for the field's decrease in size.

The average magnetic field in the chamber is roughly 60 milligauss. Subsequent rough measurements revealed the 100-150 milligauss magnetic fields in the chamber were emanating from instruments that protruded into the chamber. Figure A.3 shows a more detailed study of the magnetic fields near the HEED gun focal point. The PHI ion gun was also studied, but was later moved to its recent location given in Table A.1. The hemispherical analzyer (HSA) is now at the previous location of the PHI ion gun when the magnetic field measurements were conducted, so similar fields can be expected due to the tip of the HSA. An angular study was conducted by moving the probe in an arc at a fixed distance from the HEED gun tip. The angle was then measured with respect to the direction the HEED gun points. Figure A.4 is a similar detailed study, but is located at the tip of the cylindrical mirror analyzer (CMA) in the upper level of the chamber.

TABLE A.1: Lower level port descriptions (distances in inches unless specified otherwise). Height Z measured up from 16½" flange mating surface. X axis along drift tube. Y axis along PHI ion gun. Azimuthal ∠ ccw from x axis (looking down). Elevation ∠ up from horizontal

Port / ID No.	Item Mounted on Port	FlangeSize / Tube OD & ID	Length (flange to CL or FP)	Azimuth& Elevation Angles	Focal Point (x,y,z)	Notes
L1 / 39	TOF Drift Tube	4½"R/2.50/2.37	10.350 to FP1	0° / 0°	(2.084, 1.203, 6.125)	1 m drift tube and TOF flange attached.
L2 / 8	HEED Gun	4½"R/2.50/2.37	10.350 to FP1	30° / 0°	(2.084, 1.203, 6.125)	End-of-gun-to sample: 2" to 2.36" Interior: 3.35" L x 2.35" OD Exterior: 18.7" L x 4.9" x 4.9"
L3 / 11	View Port	2¾"R/1.50/1.37	9.2 to FP1	30° / 22°	(2.084, 1.203, 6.125)	
L4 / 12	VG Cold Cathode Ion Gun	2¾"R/1.50/1.37	9.2 to FP1	52° / 22°	(2.084, 1.203, 6.125)	
L5 / 9	Optical Access for UV Source	6"T/4.00/3.83	10.00 to CL	62° / 0°	(0, 0, 6.125)	
L6 / 16	View Port	2¾"R/1.50/1.37	9.2 to FP2	62° / 30°	(0.979,2.198, 6.125)	
L7 / 13	Blank	4½"R/2.50/2.37	9.450 to FP2	90° / -30°	(0.979,2.198, 6.125)	Flange-to-sample: 9.45" Flange-to-tip: 8.27" (2.30" OD)
L8 / 14	Hemspherical Analyzer	4½"R/2.50/2.37	9.450 to FP2	90° / 30°	(0.979,2.198, 6.125)	Flange-to-sample: 9.0" Flange-to-tip: 7.2" Interior: 3.1" L x 1.35" OD Exterior: 4.25" L 2¾" nipple plus 7.75" L x 6.0" OD plus leak valve
L9 / 25	Blank	2¾"R/1.50/1.37	9.2 to FP2	120° / -25°	(0.979,2.198, 6.125)	
L10 /15	View Port	2¾"R/1.50/1.37	9.2 to FP2	120° / 25°	(0.979,2.198, 6.125)	

TABLE A.1 (continued): Lower level port descriptions (distances in inches unless specified otherwise). Height Z measured up from 16½" flange mating surface. X axis along drift tube. Y axis along PHI ion gun. Azimuthal ∠ ccw from x axis (looking down). Elevation ∠ up from horizontal

Port / ID No.	Item Mounted on Port	FlangeSize / Tube OD & ID	Length (flange to CL or FP)	Azimuth& Elevation Angles	Focal Point (x,y,z)	Notes
L11 / 3	View Port	4½"R/2.50/2.37	10.350 to FP2	120° / 0°	(0.979,2.198, 6.125)	Interior: 4½" L x 1.83" OD Exterior: 7⅞" L 2¾" nipple plus 1⅞" L x 2.95 OD beyond flange
L12 / 2	PHI Ion Gun	6"T/4.00/3.83	11.00 to CL	142° / 0°	(0,0,6.125)	
L13 /10	Turbo Pump	4½"R/2.50/2.37	11.00 to CL	178° / 0°	(0,0,3.625)	4½" nipple, 4½" Rt. Angle Valve, Turbo. Roughing pump line.
L14 / 4	HEED Screen	6"T/4.00/3.83	13.00 to FP1	210° / 0°	(2.084, 1.203, 6.125)	
L15 / 5	View Port	6"T/4.00/3.83	10.50 to CL	240° / 0°	(0,0,6.125)	Length and azimuthal angle are only approximate.
L16 /34	Conrad Gun	2¾"R/1.50/1.37	10.00 to CL	273° / 0°	(0,0,6.125)	
L17 / 6	View Port	6"T/4.00/3.83	10.50 to CL	300° / 0°	(0,0,6.125)	
L18 / 7	View Port	6"T/4.00/3.83	10.00 to FP1	325° / 0°	(2.084, 1.203, 6.125)	

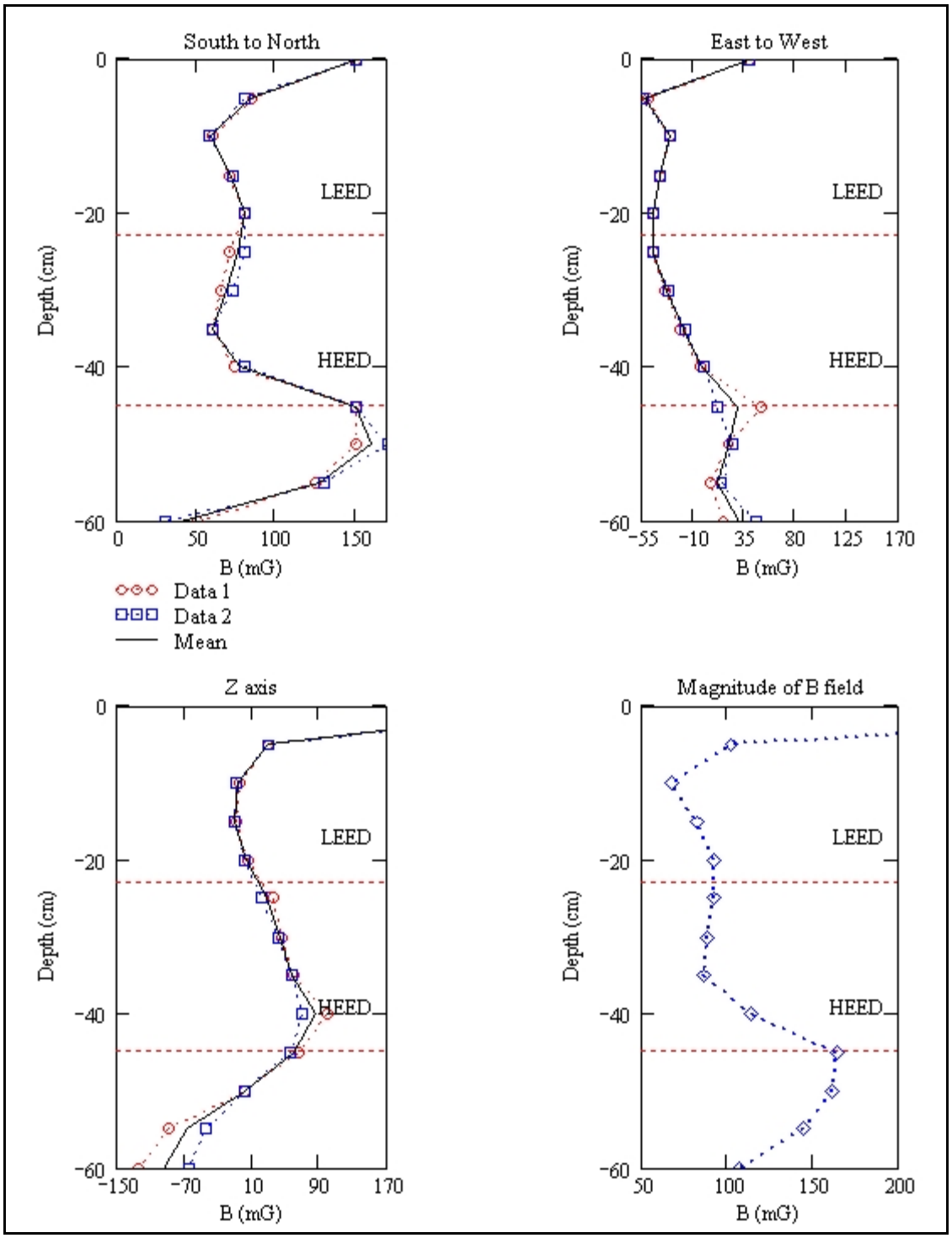


FIG. A.1: Magnetic field measurements along z-axis near HEED gun focal point. There are two sets of data and a mean. The magnitude of the magnetic field is computed and shown in the graph at lower right. The graphs are labeled LEED and HEED to correspond to the upper and lower levels of the vacuum chamber.

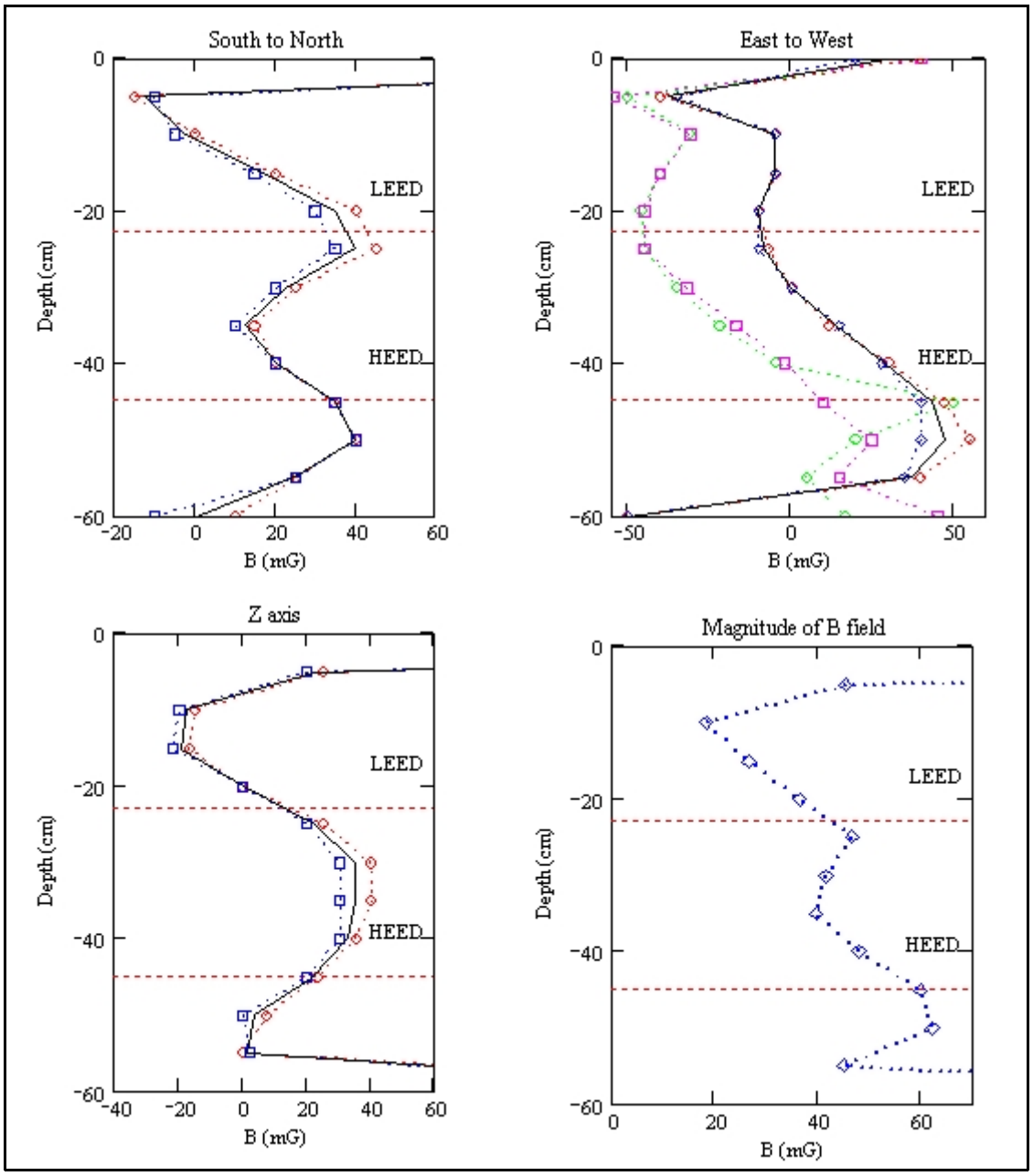


FIG. A.2: Magnetic field measurements along z-axis near the turbomolecular pump flange. There are two sets of data and a mean. The magnitude of the magnetic field is computed and shown in the graph at lower right. The graphs are labeled LEED and HEED to correspond to the upper and lower levels of the vacuum chamber. Measurements from the HEED gun focal point are included on the east-to-west graph as a reference for the decrease in the magnetic field.

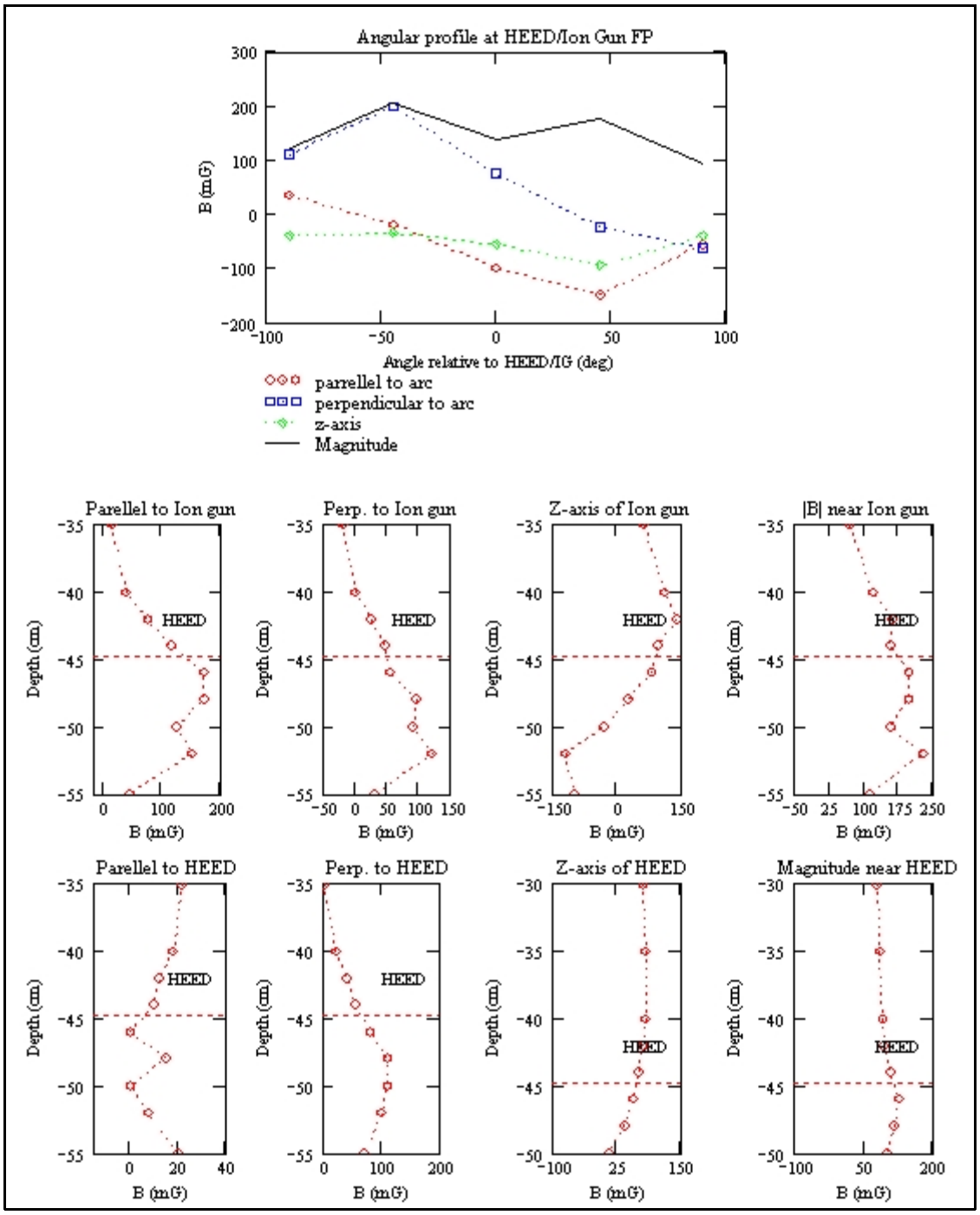


FIG. A.3: Magnetic field measurements at the HEED gun focal point. The top graph is an angular study conducted by varying the angle of the probe with respect to the direction of the HEED gun tip at a fixed distance. The remaining graphs are more detailed studies, similar to those in Figs. A.1 and A.2, at the HEED and ion gun focal points that are labeled HEED on the plots. The position of the Ion gun at the time of the measurements is presently that of the HSA.

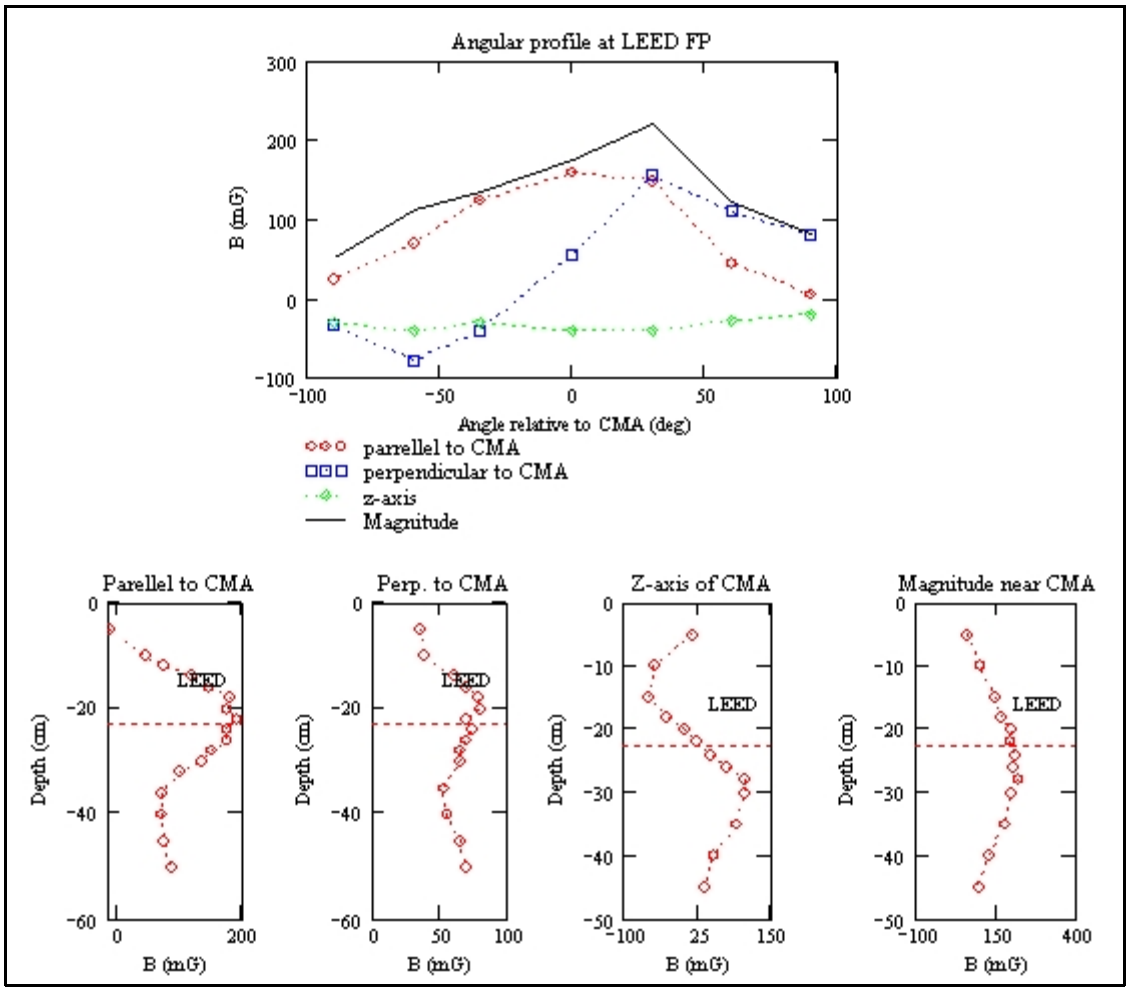


FIG. A.4 Magnetic field measurements near the CMA focal point. The top graph is an angular study conducted by varying the angle of the probe with respect to the direction of the CMA tip at a fixed distance. The remaining graphs are a detailed study of the magnetic fields, similar to those in Figs. A.1 and A.2, near the CMA focal point that is labeled LEED on the plots.

APPENDIX B: FARADAY CUP TESTS

This appendix details the experiments that establish the Faraday cup, discussed in Subsection 3.C.1, as an accurate measure of the beam current. A Faraday cup (FC) typically has a 10:1 ratio of aperture diameter to depth. The 10:1 ratio ensures the solid angle of the aperture, as seen from the bottom of the FC, is $\leq$ 3% of the emitted distribution of SE and BSE that result from the incident beam bombarding the FC. Conforming to this standard, the 25 mm depth of the sample stage module limits the diameter of a FC to < 2.5 mm. A hole was drilled at the top of each module to act as a simple FC with a 2 mm diameter and a > 20 mm depth. A larger FC was needed for characterization of the HEED and Conrad gun beam currents and spot size.

The solution was to use a limited ratio of 2.75:1, whose solid angle is roughly 11% of the full field of view. We made up for the potential loss of BSE and SE with three solutions: Machining an angle into the base of the hole to diffusely scatter BSE (Miller 1966), coating the cup with a colloidal graphite called Aquadag™ to reduce the SE and BSE yields (Sternglass; 1953b; Ruzic *et al.,* 1982), and biasing the cup to positive voltage to retain the SE produced on the inside of the cup. The final design of the FC, which will be referred to as the FatMan FC for the purposes here, and tertiary aperture inside a sample module are shown in Fig. 3.9 of Subsection 3.C.1.

To find the positive voltage of the FatMan FC that results in the measured beam current being equivalent to that measured by an FC with a 10:1 ratio of aperture

diameter to depth, the following experiment was purposed: The beam current as measured with the 2-mm diameter hole in the module would be compared with the current measured with the FatMan FC as a function of increasing positive voltage. The positive voltage needed to make the current measured by the two FC's equivalent was presumed to be < 25 volts because the SE energy distribution is peaked at much lower energy (e.g. see Fig. 4.1). The BSE's lost by the larger aperture ratio cannot be expected to be recaptured, but the Aquadag™ coating ensures that this loss is < 7% and the angle at the base also decreases the loss by diffusely scattering the BSE. The time between the two measurements must be kept to a minimum to ensure there has been little change in the actual beam current from the electron gun.

The HEED gun was chosen for the experiment because its beam spot can be focused to < 2 mm for the module's FC and has been shown to have a very stable beam efficiency (defined as the ratio of beam current to emission current) for several minutes. Initial investigations also proved large beam currents were necessary for the electrometer to adequately discern the small difference between the beam currents measured by the two FC's. A beam current of roughly 80 nA was used for the final set of experiments. Before the experiment was carried out, a beam profile was measured using the edge of the FatMan FC to ensure that the beam would fit entirely into the module FC. The current to the aperture of the FatMan FC, or the tertiary current, could also be measured and is indicative of the focus of the beam spot entering the FC. The tertiary current was measured to be < 0.1% of the beam current and shows the entire

beam enters into the FatMan FC. Initial test also revealed the offsets encountered using two separate electrometers for the module and FatMan FC were on the order of the difference in the currents being measured. The solution was to use a single, high precision electometer (Keithley 616) and simply switch cables between the two measurements. A beam energy of 4.5 keV was used to maximize the SE yield and produce as many SE as possible so the results would more closely match the situation faced by the Conrad gun at lower energies where the SE yield is higher.

The results of these experiments are presented in Fig. B.1. Notice the efficiency of the HEED gun is plotted on the y-axis and happens to be negative because of the conflicting signs of the beam and emission currents. The two measurements of the efficiency by the module and FatMan FC are shown as solid lines in Fig. B.1. The data points are the efficiency measured by the FatMan FC with increasing positive bias

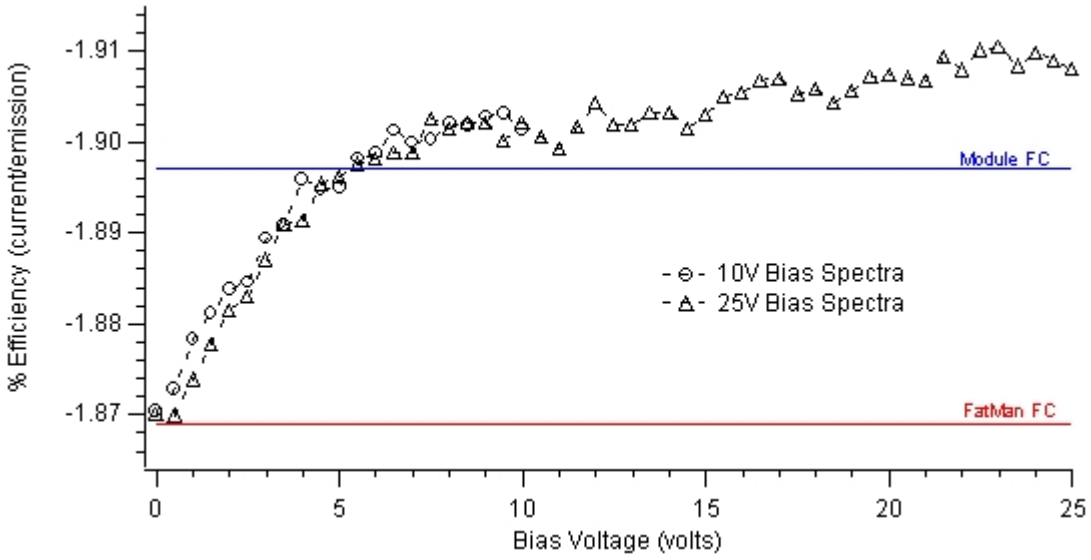


FIG. B.1: Percentage efficiency of the HEED gun as measured by the module FC and the FatMan FC as a function of positive voltage bias.

of the FC. There is a curve corresponding to one set of measurements taken to a maximum of +10 volts and another to +25 volts. Notice that the curves have two characteristic slopes. Below +6-7 volts the current is collected more rapidly than at higher levels of positive bias, where the current increases linearly. The low voltage collection of current is characteristic of recapturing low energy SE emitted by the FC surfaces. In fact, calculating the derivative of the curves in Fig. B.1 leads to a crude SE energy distribution curve. The fact that the slope changes just after the collected current begins to agree with the current measured with the module FC is not a coincidence and is further proof the majority of lost current by the FatMan FC are low energy SE's. Comparing the performance of the two FC's with the estimated performance based on geometry gives an estimate of the percentage of SE's escaping the FatMan FC. Again, the 10:1 ratio of the module FC retains 97% of the SE and the 2.75:1 ratio of the Fatman FC retains 89% of the SE just due to geometry. Assuming the asymptotic behavior of the voltage bias curve in Fig. B.1 relates to roughly 100% of the SE being retained, then the 1.5% difference in efficiency between the FC's means roughly 80% of the SE expected to escape the FatMan FC based on geometry are being retained by the voltage bias.

A value of +10 volts was chosen as the positive bias for the FatMan FC as a compromise between ensuring most of the SE are recaptured and disagreement with the Module FC. At +10 volts, the FatMan and module FC's disagree by < 0.3%. Subsequent experiments at beam energies up to 14 keV showed that the two FC's agree

to within the same precision. The result of these experiments is that all measurements of the beam current in this dissertation were taken with the FatMan FC, biased to +10 volts, and an absolute uncertainty in the beam current of < 0.5%.

APPENDIX C: THEORETICAL CALCULATION OF SYSTEMATIC CORRECTIONS FOR SE AND BSE YIELDS

NOTE: The following derivations are a printout from a Mathcad™ document that uses variable and function definitions (e.g. $x := 10 \cdot cm$) to actively compute the correction factors outlined below. The font, text spacing, and pagination will vary in this Appendix due to the Mathcad™ format.

With an ideal collector, the yields for a sample "s" are calculated from the measured currents in the following way:

Total yield $\sigma_s = \frac{I_c(0 \cdot V)}{I_b}$

BSE yield $\eta_s = \frac{I_c(-50 \cdot V)}{I_b}$

SE yield $\delta_s = \sigma_s - \eta_s = \frac{I_c(0 \cdot V) - I_c(-50 \cdot V)}{I_b}$

where

$I_c(0 \cdot V)$	Collector current in "collection" mode (grid is grounded).
$I_c(-50 \cdot V)$	Collector current in "suppression" mode (grid biased to -50 volts).
I_b	Electron gun beam current that actually hits the sample.

The point here is the collector current during either of the two modes is altered via currents lost or created by the grid wires and geometry of the detector. There are also errors due to mis-measurement of the beam current that hits the sample I_b, but that issue is largely related to the Faraday cup and the electron guns and not the internal geometry of the detector.

Consider the collector current measured during the "collection" mode $I_c(0\text{-}V)$. This measurement suffers from psuedo-source terms from unwanted scatter, and loss terms due to electrons not reaching the collector :

$$I_c(0\text{-}V) = I_b \cdot \sigma_s - I_{loss} + I_{source}$$

These source or loss terms scale with the current reflected from the sample, so we can write them as fractions of the beam current:

$$I_c(0\text{-}V) = I_b \cdot \sigma_s \cdot \left(1 - f_{loss} + f_{source}\right)$$

where the currents, I , have been replaced with a fraction f of the beam current. The total yield is then,

Corrected total yield $$\sigma_s = \frac{I_c(0\text{-}V)}{I_b \cdot \left(1 - f_{loss} + f_{source}\right)}$$

where $f_{loss} = f_{surfaces} + f_c + f_h$

$f_{surfaces}$	Electrons from the sample that hit surfaces before reaching the collector (1st & 2nd order corrections).
f_c	Electrons that backscatter off the collector (2nd order corrections).
f_h	Electrons lost out the beam pipe (2nd order corrections).

where $f_{source} = f_{2xBSE} + f_{SE}$

f_{2xBSE}	Terms involving multiple BSE scattering that get back to collector (higher order correction).
f_{SE}	Current measured at the collector due to SE produced on surfaces other than the sample (higher order correction).

Proceeding in this way, we find these terms depend on the relative size of the SE and BSE populations that make up the total yield. Since the measured BSE yield will have to be addressed separately, let's consider that measurement now. Following the same logic as before, we find:

$$\text{Corrected BSE yield} \qquad \eta_s = \frac{I_c(-50\text{-}V)}{I_b \cdot \left(1 - fBSE_{loss} + fBSE_{source}\right)}$$

All the above definitions still apply (with fBSE instead of f). We need to make the following assumptions:

ASSUMPTIONS:

1. The SE and BSE energies are sufficiently distinct as to be treated as separate populations.
2. The bias grid effectively screens out the SE's created at the sample from reaching the collector.

   Solid assumption, backed up by experimental results.

Admittedly, the situation is still complicated and we need a few more assumptions.

ASSUMPTIONS:

3. Electron trajectories are dominated by their emission angle, regardless of their energy.

   Error caused by focusing to or away from grid wires is not considered. This assumption is reasonable for all but the lowest energy electrons.

4. Electrons with < 50eV (SE) that hit any surface do not produce electrons.

   Based on yield curves for materials used in this calculation (e.g. see Section V.B), this assumption is reasonable. Yields at roughly 10 eV, where most SE are found (see Fig IV.1), are typically << 10% of the maximum yield.

With these two assumptions, we can use the opacity of the detector surfaces just due to detector's geometry and the emission angles of the electrons to calculate all the loss terms above. This effective opacity is also important since the "lost" electrons that hit surfaces $f_{surfaces}$ (and the backscatter off the collector f_{BSEc}) are ultimately the source current that creates the unwanted SE and BSE in f_{source} We begin by calculating the fraction of the total solid angle (hemisphere) that a surface subtends; however, we also weight the angles by the distribution of the SE and BSE emission angles from the sample. The SE population is included in this section for later use.

Surface's fraction of total solid angle weighted by the angular distribution of the BSE or SE emitted from the sample.

We first need to determine the relevant angles, measured from the sample normal (0 deg) to the faceplate (90 deg), for the beam pipe, tantalum ring and the edge of the inner grid.

α_1 The angle subtended by the beam pipe's hole (to ID).

Inner diameter of beam pipe: $ID_{pipe} := 0.198 \cdot in$

The distance from the beam pipe to the sample is complicated:

Length of beam pipe, minus holder width: $L_{pipe} := (1.011 - 0.135) \cdot in$
(Fatman vol I, pg. 045 yellow)

Back of cover to sample: $D_{cs} := 1.972 \cdot in$
(Autocad "cover2.dwg")

Distance from sample to beam pipe face: $R_{topipe} := D_{cs} - L_{pipe}$

The angle is then: $\alpha_1 := \operatorname{atan}\left(\frac{ID_{pipe}}{2} \cdot \frac{1}{R_{topipe}}\right)$

$\alpha_1 = 5.16 \cdot deg$

α_2 The angle to the beam pipe's OD.

Outer diameter of beam pipe: $OD_{pipe} := 0.240 \cdot in$ (estimate based on assumption the pipe fits in the 1/4" hole SDL machined in the beam pipe holder)

The angle is then: $\alpha_2 := \operatorname{atan}\left(\frac{OD_{pipe}}{2} \cdot \frac{1}{R_{topipe}}\right)$

$\alpha_2 = 6.25 \cdot deg$

α_3 The angle to ID of tantalum ring

Inner diameter of tantalum ring: $ID_{tring} := 0.32 \cdot in$ (rough estimate from video log at 8 min 14 secs)

Distance from sample to tantalum ring: $R_{totring} := (1.232) \cdot in$ (Autocad file "asmdtct2.dwg")

The angle is then: $$\alpha_3 := \operatorname{asin}\left(\frac{ID_{tring}}{2} \cdot \frac{1}{R_{totring}}\right)$$

$$\alpha_3 = 7.46 \cdot deg$$

α_4 The angle to OD of tantalum ring

Outer diameter of tantalum ring: $OD_{tring} := 0.45 \cdot in$ (rough estimate from video log at 8 min 14 secs)

The angle is then: $$\alpha_4 := \operatorname{asin}\left(\frac{OD_{tring}}{2} \cdot \frac{1}{R_{totring}}\right)$$

$$\alpha_4 = 10.52 \cdot deg$$

α_5 The angle where collector becomes blocked by inner grid ring

$\alpha_5 := 85.73 \cdot deg$ (derived from inner grid rings' ID and thickness on AutoCAD drawing "asmbdtct2.dwg")

Let: $\alpha_0 := 0 \cdot deg$ $\alpha_6 := 90 \cdot deg$

Now we wish to integrate over the discrete angles, but weight by the angular distribution of the SE or BSE emitted from the sample.

SE angular distribution: $SE_{ang}(\alpha) := \cos(\alpha)$ [Jonker 1951]

The easiest model for the BSE angular distribution is a Screened Rutherford distribution:

$RBSC(\alpha, b) := (1 + 2 \cdot b - \cos(\alpha))$

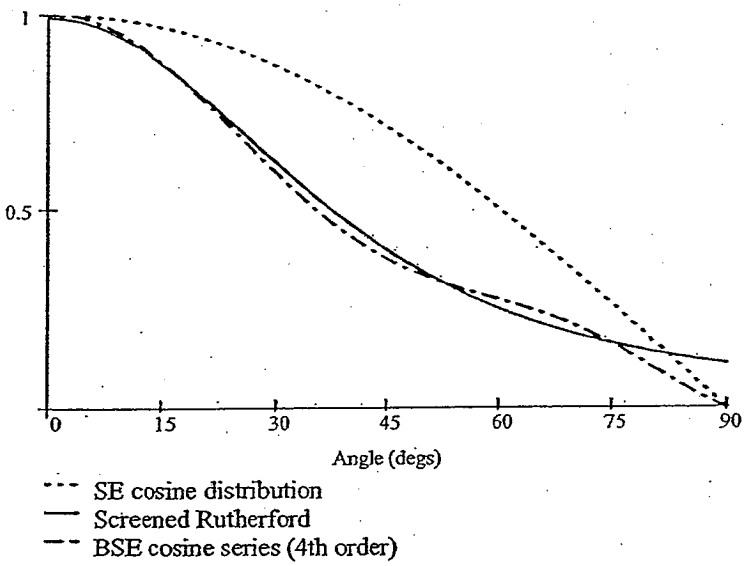
where b is the screening parameter for the sample (using the value for Au b := 0.251 from Davies [1999])

Better models for the BSE angular distribution are derived with Monte Carlo simulations, for which there is no analytical function; however, we can use a fourth order cosine series as a model [Davies 1999].

BSE angular distribution based on 4th order cosine series:

$$BSE_{ang}(\alpha) := 0.884 \cdot \left(\cos(\alpha)^4\right) + -1.17 \cdot \left(\cos(\alpha)^3\right) + 0.42 \cdot \left(\cos(\alpha)^2\right) + 0.097 \cdot \cos(\alpha)$$

We graph these functions for comparison: $\theta := 0, 1 \cdot deg .. 90 \cdot deg$



Notice the screened Rutherford distribution is non-zero at 90 degrees, which is unphysical and will impact the subsequent analysis. Using the fourth order cosine series with the coefficients that were experimentally derived for Au is justified because we are only interested in the shape, which should not be dramatically sample dependent (polycrystalline or amorphous samples).

We can calculate normalizations for the distributions:

$$SE_{norm} := \int_0^{90\cdot deg} SE_{ang}(\alpha)\cdot\sin(\alpha)\, d\alpha$$

$$BSE_{norm} := \int_0^{90\cdot deg} BSE_{ang}(\alpha)\cdot\sin(\alpha)\, d\alpha$$

Here are the discrete weighting factors, where the SE cosine distribution and the BSE cosine series are used to weight the six solid angles subtended by portions of the hemisphere outlined above:

where $i := 0..5$

$$SE_{angw_i} := \frac{1}{SE_{norm}} \int_{\alpha_i}^{\alpha_{i+1}} SE_{ang}(\alpha')\cdot\sin(\alpha')\, d\alpha'$$

Unweighted:

$$Ang_{Uw_i} := \int_{\alpha_i}^{\alpha_{i+1}} \sin(\alpha')\, d\alpha'$$

$$BSE_{angw_i} := \frac{1}{BSE_{norm}} \int_{\alpha_i}^{\alpha_{i+1}} BSE_{ang}(\alpha')\cdot\sin(\alpha')\, d\alpha'$$

The percentages of SE and BSE through the various angular regions:

	$SE_{angw_i}\cdot 100$	$BSE_{angw_i}\cdot 100$	$Ang_{Uw_i}\cdot 100$
0. lost out the beam pipe:	0.81	1.28	0.41
1. hitting end of beam pipe:	0.38	0.59	0.19
2. passing through the gap:	0.5	0.78	0.25
3. hitting the tantalum ring:	1.65	2.51	0.83
4. going through both grids:	96.11	94.41	90.87
5. hitting the inner grid ring:	0.55	0.44	7.45

The weighted distributions see more electrons lost at the near normal angles. Also notice the unweighted distribution Ang_{Uw} predicts an unphysical amount of electrons lost at oblique angles (83-90 degrees).

Recall the goal for the 1st & 2nd order BSE corrections from the beginning:

Lost BSE current in suppression mode

$$fBSE_{loss} = fBSE_{surfaces} + fBSE_{c} + fBSE_{h}$$

where

$fBSE_{surfaces}$	BSE from the sample that hit surfaces before reaching the collector (1st & 2nd order corrections).
$fBSE_{c}$	BSE that backscatter off the collector, while the SE population is retained by a 50 volt potential difference between the collector and the bias grid (2nd order correction).
$fBSE_{h}$	BSE that are lost out the beam pipe (2nd order correction).

The fraction of the BSE yield lost out the beam pipe

$$fBSE_{h} := BSE_{angw_0}$$

$$fBSE_{h} = 1.28 \cdot \%$$

We can now look at the fraction of electrons that hit surfaces before reaching the collector.

$$fBSE_{surfaces} = fBSE_{ebp} + fBSE_{tr} + fBSE_{ibg} + fBSE_{igr}$$

where

$fBSE_{ebp}$	BSE that hit the end of the beam pipe (2nd order correction).
$fBSE_{tr}$	BSE that hit the tantalum ring (2nd order correction)
$fBSE_{ibg}$	BSE that hit either the inner or bias grid wires (1st order correction).
$fBSE_{igr}$	BSE that hit the inner grid ring (2nd order correction).

Again, assuming trajectories are unaffected, the above 2nd order quantities can be defined as the surface's fraction of the hemisphere's solid angle.

$$fBSE_{ebp} := BSE_{angw_1} \qquad fBSE_{ebp} = 0.59 \cdot \%$$

$$fBSE_{tr} := BSE_{angw_3} \qquad fBSE_{tr} = 2.51 \cdot \%$$

$$fBSE_{igr} := BSE_{angw_5} \qquad fBSE_{igr} = 0.44 \cdot \%$$

The only exception is the BSE that hit either of the grid wires $fBSE_{ibg}$ Since a large part of this theoretical correction was anticipated to come from the opacity of the grid wires, an experiment was done to measure the transmission of the grid wires exactly as they are mounted in the detector.

Experimental measurement of both grids transmission: $t_{2grids} := 70.16 \cdot \%$

Although the measurement of the two grid transmission has an accuracy of better than 0.5%, the effective grid transmission as measured with photoelectrons differed by 3%, which translates directly into the same uncertainty in the corrective factor derived below.

Opacity of both grids: $p_{2grids} := 1 - t_{2grids}$

The fraction of BSE lost to either grid wires is then: $fBSE_{ibg} := p_{2grids} \cdot BSE_{angw_4}$

Weighted by BSE angular distribution vs. unweighted

$fBSE_{ibg} = 28.17 \cdot \%$ $p_{2grids} \cdot Ang_{Uw_4} = 27.12 \cdot \%$

In total, we have: $fBSE_{surfaces} := fBSE_{ebp} + fBSE_{tr} + fBSE_{ibg} + fBSE_{igr}$

$fBSE_{surfaces} = 31.71 \cdot \%$

$fBSE_c$ BSE that backscatter off the collector (the SE population is retained by a 50 volt potential difference between the collector and the bias grid).

With the effective surface opacity, we can define an effective transmission for BSE to the collector $tBSE_c$ and derive the fraction of the BSE created at the sample that reach the collector and backscatter off.

Effective transmission for BSE to collector $tBSE_c := 1 - \left(BSE_{angw_0} + fBSE_{surfaces}\right)$

Notice the BSE lost out the hole BSE_{angw_0} are subtracted from the transmission as well.

The fraction of BSE that subsequently leave the collector depends on the BSE yield of Aquadag: $\eta_{aquadag} := 7 \cdot \%$ from Sternglass [1953a]

There is also a fraction that return to the collector without going through grid wires. These BSE are emitted at oblique angles and travel through the gap between the collector surface and the suppression grid, back to the collector.

We estimate this fraction is roughly: $f_{return} := 12 \cdot \%$

Fraction of BSE not collected: $fBSE_c := tBSE_c \cdot \eta_{aquadag} \cdot \left(1 - f_{return}\right)$

$fBSE_c = 4.13 \cdot \%$

Now, summing all the terms together again, we find: $fBSE_{loss} := fBSE_{surfaces} + fBSE_c + fBSE_h$

$fBSE_{loss} = 37.11 \cdot \%$

Notice that scattering off the grid wires (1st order correction) accounts a majority of all scattering corrections: $\frac{fBSE_{ibg}}{fBSE_{loss}} = 75.91 \cdot \%$

Unwanted SE and BSE current in suppression mode

The terms of unwanted electron current to the collector during the suppression mode (higher order corrections):

$$f_{source} = f_{2xBSE} + f_{SE}$$

where

f_{2xBSE}	Terms involving multiple BSE scattering that get back to collector
f_{SE}	Current measured at the collector due to SE produced on surfaces other than the sample.

We treat the second term f_{SE} first because it is the easiest to approximate. In the suppression mode, the electric field between the inner grid and bias grid is assumed to repel all the SE, even if they are created there by subsequent BSE scatter. The term is then confined to SE produced by BSE that impact the bias grid. We make an assumption,

ASSUMPTION:

The field penetration of the attractive potential (from the collector) through the bias grid is insufficient to attract SE produced on the sample side of the bias grid back toward the collector.

ASSUMPTION:

With this assumption, the term is limited to SE produced by backscatter off the collector $fBSE_c$ hitting the bias grid and creating SE.

BSE hitting other surfaces in the region of interest (the tantalum ring and beam pipe) would increase this correction, but the percentage of the solid angle from the viewpoint of the collector BSE is assumed to be too small to justify the effort.

We proceed by defining the opacity of the bias grid, which was experimentally measured:

Experimental transmission for bias grid $t_{bg} := 84.39 \cdot \%$

Error in transmission (just experimental): $terr_{bg} := 0.21 \cdot \%$

Opacity $p_{bg} := (1 - t_{bg})$ $p_{bg} = 15.61 \cdot \%$

Instead of using this opacity, we will go further to model the difference between the opacity seen by scatter from the sample and the opacity seen through the backside of the grid.

ASSUMPTION:

1. We will assume that scatter from the sample sees the opacity of the grids as experimentally measured; however, scatter through the backside of the grids falls off as a cosine of the normal angle and includes the weighting of the BSE angular distribution. The cosine weighting is an approximation of the opacity seen by a point with the grid wire parallel to the surface.

$$p_{bbg} := 1 - t_{bg}^{\frac{\int_0^{90\cdot deg} BSE_{ang}(\theta)\cdot\cos(\theta)\cdot\sin(\theta)\,d\theta}{\int_0^{90\cdot deg} BSE_{ang}(\theta)\cdot\sin(\theta)\,d\theta}} \qquad p_{bbg} = 41.27\cdot\%$$

Notice that this is more than double the opacity from the forward direction: $\frac{p_{bbg}}{p_{bg}} = 2.64$

The source current to the back of the bias grid would then be, $fBSE_c \cdot p_{bbg} = 1.7\cdot\%$

ASSUMPTION:

The SE yield of 304 SS is a function of energy. We will take an average of the distribution by only using 80% of the maximum SE yield. This approach will be taken for all the SE yields.

SE yield of 304 SS: $\delta_{304SS} := (1.2)\cdot 80\cdot\%$ δ_{max} at 450 eV from Ruzic [1982]

$f_{SE} := \delta_{304SS}\cdot fBSE_c \cdot p_{bbg}$ $\qquad f_{SE} = 1.64\cdot\%$

The scattered BSE term f_{2xBSE} is by far the most complicated. Estimating the term involves theoretically predicting what amount of the original $fBSE_{surfaces} = 31.71 \cdot \%$ and the $fBSE_{c} = 4.13 \cdot \%$ return to the collector surface. To make the problem even marginally tractable, we make the following assumptions:

ASSUMPTION:

1. Again, forward scatter uses the experimentally measured opacity while scatter through the backside will use the cosine weighted opacity.

2. The sample, module and detector's faceplate (or sample/module/faceplate) are assumed to see a uniform distribution of the BSE that scatter from other surfaces.

The second assumption means we can account for the BSE yield of the sample/module/faceplate by defining an effective yield for the whole surface that is weighted by a constituent's fraction of the whole surface area:

Effective BSE yield of face estimation

Sternglass [1953a] chose a spherical design to avoid this whole question (pg. 22 in Sternglass dissertation). He assumes he can estimate the error from BSE hitting his target by a ratio of subtended solid angles (pg. 21).

Fredrickson [1971] deals with this problem in detail (see pg. 33), but he connects the collector and detector face and therefore only worries about BSE that reach the sample. He makes the point an isotropic flux to the face may be in error, but assuming diffuse scattering from the grids to the face seems acceptable (given that the wires are round). Scatter from the collector to the face may be influenced by the BSE angular distribution. There are two main points from Fredrickson's work: 1) He uses the ratio of sample to face areas to estimate the fraction of BSE returning that scatter from each and 2) he proposes a simple experiment to actually measure those currents.

ASSUMPTION:

The estimation of the effective BSE yield of the faceplate/module area will proceed with the assumption the BSE diffusely scatter in such a way as to uniformly cover the faceplate/module area. The effective BSE yield is then given as the sum of the BSE yields of the faceplate (coated with Aquadag) and the module (OFHC copper), weighted appropriately by their fraction of the total area. The uncertainty in this assumption versus assuming the BSE undergo spectral scattering is discussed after the calculation.

Defining the geometry and material parameters:

The BSE yield of copper: $\eta_{CU} := 0.27$ averaged from Sternglass [1953a]

The BSE yield of Aquadag: $\eta_{aquadag} = 0.07$ (from above)

Area of the faceplate: (from AutoCAD file "FacePlt.dwg) $area_{fp} := 12.41 \cdot in^2$

Inner radius of collector hemisphere: (from AutoCAD file "cover.dwg") $IR_c := 1.625 \cdot in$

Area of faceplate exposed to interior of collector: $area_{fpc} := \pi \cdot IR_c^2$

Areas covered on faceplate by the grid rings: (still coated with aquadag) $area_{bgr} := 0.961 \cdot in^2$

$area_{igr} := 0.809 \cdot in^2$

Area of square hole in face plate: (calculation based on "faceplt3.dwg") $area_{fph} := 1.8 \cdot in^2$

Area of module face: (assuming no sample) $area_{module} := 1.439 \cdot in^2$

Gaps between faceplate hole and module: $area_{lost} := area_{fph} - area_{module}$

more precise: (gaps at top & bottom only) $area_{lost2} := 1.5 \cdot in \cdot (1.2 \cdot in - 1.125 \cdot in)$

Area of centimeter sample insert: $area_{cms} := \pi \cdot (0.5 \cdot cm)^2$

Area of larger sample insert: $area_{ls} := \pi \cdot (0.35 \cdot in)^2$

Ratios (for interest):

$$\frac{area_{module}}{area_{fpc}} = 17.35 \cdot \% \qquad \frac{area_{lost}}{area_{fpc}} = 4.35 \cdot \% \qquad \frac{area_{lost2}}{area_{fpc}} = 1.36 \cdot \% \qquad \frac{area_{fph}}{area_{fpc}} = 21.7 \cdot \%$$

Effective BSE yield of face (weighted BSE yields of surfaces)

$$\eta_{face} := \eta_{aquadag}\left(\frac{area_{fpc} - area_{fph}}{area_{fpc}}\right) + \eta_{CU}\left(\frac{area_{module}}{area_{fpc}}\right) \qquad \eta_{face} = 0.102$$

The assumption that the BSE diffusing scatter from surfaces in such a way as to uniformly cover the faceplate can be challenged with the idea that the BSE undergo spectral scattering from the hemispherical surfaces and return mainly to the module. Equating the effective BSE yield of the faceplate area to that of copper, when coupled to the 3% uncertainty in the two grid transmission can be shown to have a 1.5% impact on the corrective factor derived below.

NOTE: The samples have been neglected because their contribution is small and entangles the quantity of interest into the corrective factor.

$$\frac{area_{cms}}{area_{fpc}} = 1.47 \cdot \% \qquad \frac{area_{ls}}{area_{fpc}} = 4.64 \cdot \%$$

With those assumptions, we proceed by identifying the following terms

f_{igfc} Scatter off inner grid to the sample/module/faceplate, then back to collector.

f_{bgfc} Scatter off the bias grid to sample/module/faceplate, then to collector

f_{cfc} Scatter off collector, then sample/module/faceplate, then back to collector

f_{bgigc} Scatter off the bias grid, then the inner grid and back to the collector

f_{cbgc} Scatter off collector to the bias grid, then back to collector

f_{cbgc} Scatter off collector to the inner grid, then back to collector

There are obviously an infinite number of terms here, but higher order terms are anticipated to be negligible.

f_{igfc} Error due to scatter off inner grid, then detector/module/sample face to collector.

This correction involves the BSE blocked by the inner grid, the inner grid BSE yield (η_{304SS}), the detector/module face BSE yield (η_{face}) and BSE transmission to the collector ($tBSE_c$).

We first need the opacity of the inner grid, which was not measured experimentally, but can be assumed to be equal to the bias grid opacity:

$$p_{ig} := p_{bg} \qquad p_{ig} = 15.61 \cdot \% \qquad t_{ig} := 1 - p_{ig} \qquad t_{ig} = 84.39 \cdot \%$$

We compare this to the effective surface opacity of the beam pipe edge, inner grid wires, and inner grid ring; weighted by the BSE angular distribution:

$p_{igs_i} :=$

0
1
0
p_{ig}
p_{ig}
1

$p_{igs_i} \cdot BSE_{angw_i} \cdot 100$

0
0.59
0
0.39
14.74
0.44

$$pBSE_{ig} := p_{igs} \cdot BSE_{angw} \qquad pBSE_{ig} = 16.15 \cdot \%$$

The transmission of the single grid, weighted by the BSE angular distribution and without the solid angle of the beam pipe:

$$tBSE_{ig} := 1 - \left(pBSE_{ig} + BSE_{angw_0}\right) \qquad tBSE_{ig} = 82.57 \cdot \%$$

The BSE yield of 304SS can be roughly approximated as that of iron (69% of total composition)

$$\eta_{iron} := 0.23 \quad \text{from Sternglass [1953a]}$$

$$\eta_{304SS} := \eta_{iron}$$

NOTE: There is a slight error here, since the end of the beam pipe and the inner grid ring are both coated with Aquadag, but the difference is neglected.

With the effective opacity of all the surfaces near the inner grid $pBSE_{ig}$ and the effective BSE yield of the sample/module/faceplate η_{face}, we still have to describe the transmission of those BSE. Previously, we had used the BSE angular distribution since the BSE were created from a small spot on the sample. Given the assumption the sample/module/faceplate see a uniform distribution of 2xBSE, we should no longer include the BSE angular distribution.

We define an effective transmission from the sample/module/faceplate to the collector by using the unweighted fraction of the solid angle seen from the sample Ang_{Uw} to approximate the space occupied by the various surfaces:

$t_{c_i} :=$

0
0
1
0
t_{2grids}
0

$t_{c_i} \cdot Ang_{Uw_i} \cdot 100$

0
0
0.25
0
63.76
0

$teff_c := t_c \cdot Ang_{Uw}$

$teff_c = 64.01 \cdot \%$ vs. $tBSE_c = 67.02 \cdot \%$

NOTE: Here we see some inconsistencies in the assumptions and approximation above. The inner grid ring, as seen from the sample, is $Ang_{Uw_5} = 7.45 \cdot \%$ of the solid angle; however, we are including the area of the faceplate beyond the inner grid radius, which would never be influenced by the ring upon re-scattering.

With the last piece, we can calculate the fraction of the BSE yield that scatters from surfaces near the inner grid, to the module/faceplate surface, and returns to the collector:

$$f_{igfc} := \eta_{304SS} \cdot (pBSE_{ig}) \cdot \eta_{face} \cdot teff_c \quad f_{igfc} = 0.24 \cdot \%$$

f_{bgfc} Error due to scatter off the bias grid, to face and then to collector

We include the tantalum ring (and approximate its BSE yield as that of 304SS) in the opacity of the bias grid, which is already down by the transmission through the inner grid:

$$(p_{bg} + fBSE_{tr}) \cdot tBSE_{ig} = 14.97 \cdot \% \qquad p_{big} := p_{bbg}$$

Here, as with scatter off the backside of the bias grid, we will use an effective transmission of the backside of the inner grid p_{big}

Hence, $f_{bgfc} := \left[\eta_{304SS} \cdot (p_{bg} + fBSE_{tr}) \cdot tBSE_{ig}\right] \cdot (1 - p_{big}) \cdot \eta_{face} \cdot teff_c$

$$f_{bgfc} = 0.13 \cdot \%$$

f_{bgigc} Error due to scatter off the bias grid, then the inner grid and back to the collector:

The rest is left as an exercise for the reader.

$$f_{bgigc} := \left[\left[\eta_{304SS} \cdot (p_{bg} + fBSE_{tr}) \cdot tBSE_{ig}\right] \cdot (\eta_{304SS} \cdot p_{big})\right] \cdot \left[1 - (p_{bg} + fBSE_{tr})\right]$$

$$f_{bgigc} = 0.27 \cdot \%$$

Now consider correction due to BSE created on the collector that scatter again off the grids back to the collector:

f_{cbgc} Scatter off collector, then bias grid, back to collector

$$f_{cbgc} := \eta_{304SS}\cdot\left[\left(fBSE_c\right)\cdot\left(p_{bbg}\right)\right]$$

$$f_{cbgc} = 0.39\cdot\%$$

f_{cigc} Scatter off collector, then inner grid, back to collector

This correction is the same as above, but down by the transmission through the backside of the bias grid.

$$f_{cigc} := \left[\eta_{304SS}\cdot\left[\left(fBSE_c\right)\cdot\left(1 - p_{bbg}\right)\right]\cdot p_{big}\right]\cdot t_{bg}$$

$$f_{cigc} = 0.19\cdot\%$$

f_{cfc} Scatter off collector, then module face, then back to collector

$$f_{cfc} := fBSE_c\cdot t_{bg}\cdot t_{ig}\cdot\eta_{face}\cdot teff_c$$

$$f_{cfc} = 0.19\cdot\%$$

The total of BSE that scatter back to the collector:

$$f_{2xBSE} := f_{igfc} + f_{bgfc} + f_{cfc} + f_{bgigc} + f_{cbgc} + f_{cigc}$$

$$f_{2xBSE} = 1.42\cdot\%$$

In the end, we have: $fBSE_{source} := f_{SE} + f_{2xBSE}$

$$fBSE_{source} = 3.05 \cdot \%$$

Given that we started with $fBSE_{surfaces} = 31.71 \cdot \%$ and $fBSE_{c} = 4.13 \cdot \%$

the result seems improbable; however, remember that $fBSE_{surfaces}$ still has to backscatter and most of the surfaces are 304SS grid wire, so the stray currents emitted from surfaces that could return to the collector (worst case):

$$fBSE_{surfaces} \cdot \eta_{304SS} + fBSE_{c} = 11.42 \cdot \%$$

Almost none of this backscatter can return to the collector without passing through at least one, if not both of the grids:

$$\left(fBSE_{surfaces} \cdot \eta_{304SS} + fBSE_{c}\right) \cdot t_{2grids} = 8.01 \cdot \%$$

The above numbers assume all the BSE return to the collector without hitting the sample/module/faceplate, which is by far the largest surface area in view of the collector. Assuming half of the scatter interacts with the faceplate (it is a hemisphere after all):

$$\frac{\left(fBSE_{surfaces} \cdot \eta_{304SS} + fBSE_{c}\right) \cdot t_{2grids}}{2} \cdot \left(1 + \eta_{face}\right) = 4.41 \cdot \%$$

Now we see, with three reasonable assumptions, the fraction of the beam returning to the collector is within 30%. Our more complicated derivation is probably an underestimation because we assumed every BSE must scatter twice to return to the collector. A happy medium can probably be found by assuming BSE that scatter off near-normal surfaces all return to the face, while some fraction of the BSE that scatter off oblique surfaces return to the collector through the grid wires. The deviation of the crude analysis from the full derivation shows more liberal assumptions lead to larger uncertainty in the corrective factor than the propagated error in the constituent measurements behind the full derivation.

In summary,

Corrected BSE yield $$\eta_{s} = \frac{I_{c}(-50 \cdot V)}{I_{b}} \cdot \frac{1}{\left(1 - fBSE_{loss} + fBSE_{source}\right)}$$

where $fBSE_{loss} = 37.11 \cdot \%$

$fBSE_{source} = 3.05 \cdot \%$

BSE correction factor: $$\frac{1}{1 - fBSE_{loss} + fBSE_{source}} = 151.65 \cdot \%$$

SE yield Correction

Now we turn to the correction factor needed when using the difference between collector currents during the "suppression" and "collection" modes as the SE current.

Measured SE yield $$\delta_s = \sigma - \eta = \frac{I_c(0\cdot V) - I_c(-50\cdot V)}{I_b}$$

where

$I_c(0\cdot V)$	Collector current in "collection" mode (grid is grounded).
$I_c(-50\cdot V)$	Collector current in "suppression" mode (grid biased to -50 volts).
I_b	Electron gun beam current that actually hits the sample.

Again, there are source and loss terms during the "suppression" and "collection" modes:

$$I_c(-50\cdot V) - I_c(0\cdot V) = \left(I_b\cdot\sigma_s - I_{loss} + I_{source}\right) - \left(I_b\cdot\eta - IBSE_{loss} + IBSE_{source}\right)$$

ASSUMPTIONS:

The assumption is made that, during the suppression mode, the high energy backscattered electron current to the collector is the same as that during the collection mode:

Is there any reason for the two BSE currents to be different?

The +/- 50 volt bias could make a difference to the relatively lower energy BSE. There might be focusing of the BSE during the suppression mode as they pass through the bias grid at -50 volts, which would make the open area effectively higher (avoiding the grid wires). Modeling with SimIon is one way to get a handle on the effect. We could also predict the grid current and correct by experimental results.

The correction to the BSE current due to SE's produced on the bias grids might differ.

With these assumptions, the BSE yield and correction factors cancel and we have:

$$I_c(-50\cdot V) - I_c(0\cdot V) = I_b\cdot\delta_s - ISE_{loss} + ISE_{source}$$

where

ISE_{loss}	SE produced on the sample that never reach the collector (1st & 2nd order corrections).
ISE_{source}	SE that reach the collector that are not produced by the original beam (higher order corrections).

Now we discuss each term:

ISE_{loss} SE produced on the sample that never reach the collector. Since the original source of the current is the SE produced at the sample, we can write these terms as fractions of the SE yield from the sample.

$$ISE_{loss} = I_b \cdot \delta_s \cdot \left(fSE_{surfaces} + fSE_h\right)$$

$$\text{or} \quad fSE_{loss} = \frac{ISE_{loss}}{I_b \cdot \delta_s} = fSE_{surfaces} + fSE_h$$

where

$fSE_{surfaces}$ fraction of SE from the sample that hit surfaces before reaching the collector.

fSE_h fraction of SE lost out the beam pipe.

Referring to the BSE yield error, we can write an integral over the full solid angle of the collector, weighted by the SE angular distribution and the opacity in each region. These SE are assumed to be lost (recall the BSE yield of SE's is assumed to be negligible so that 2xSE scatter is neglected).

There is an additional concern about the ambient electrostatic fields in the region before the bias grid (after which there is an assisting field to the collector) that might repel very low energy SE from the collector face. This correction is expected to be small and modeling with SimIon seems to be the best approach to this (if we can re-create the detector geometry with any accuracy).

We can define an opacity for each angular region seen by SE produced on the sample: $p_{SE_i} :=$

0. Lost out the beam pipe:	1
1. Hitting end of beam pipe:	1
2. Passing through the gap:	0
3. Hitting the tantalum ring:	1
4. Hitting either grid:	p_{2grids}
5. Hitting the inner grid ring:	1

The fraction of SE lost before reaching the collector,

$$fSE_{loss} := p_{SE} \cdot SE_{angw}$$

Weighted with the SE cosine angular distribution: Unweighted:

$fSE_{loss} = 32.07 \cdot \%$ vs. $p_{SE} \cdot Ang_{Uw} = 35.99 \cdot \%$

ISE_{source} SE that reach the collector that are not produced by the original beam.

Since the incident beam is assumed to impinge only on the sample, these source terms are due to BSE from the sample that create SE on other surfaces in the detector. All subsequent terms will scale with the sample's BSE current. Beginning with the most naive approach, we have

$$ISE_{source} = I_b \cdot \eta_s \cdot (fSE_{face} + fSE_{ig} + fSE_{bg})$$

where

fSE_{face} fraction of BSE scatter returning to the sample/module/faceplate and creating SE that reach collector.

fSE_{ig} fraction of BSE scatter hitting the inner grid and creating SE that reach collector.

fSE_{bg} fraction of BSE scatter hitting the bias grid and creating SE that reach collector.

The first term fSE_{fact} is not difficult to estimate based on the amount of BSE scatter returning to the sample/module/faceplate that was considered in our BSE analysis. Recall there were three terms:

f_{igfc} Scatter off inner grid to the sample/module/faceplate, then back to collector.

$$f_{igfc} := \eta_{304SS} \cdot (pBSE_{ig}) \cdot \eta_{face} \cdot teff_c \qquad f_{igfc} = 0.24 \cdot \%$$

f_{bgfc} Scatter off the bias grid to sample/module/faceplate, then to collector

$$f_{bgfc} := \left| \eta_{304SS} \cdot (p_{bg} + fBSE_{tr}) \cdot tBSE_{ig} \right| \cdot (1 - p_{big}) \cdot \eta_{face} \cdot teff_c \qquad f_{bgfc} = 0.13 \cdot \%$$

f_{cfc} Scatter off collector, then sample/module/faceplate, then back to collector

$$f_{cfc} := fBSE_c \cdot t_{bg} \cdot t_{ig} \cdot \eta_{face} \cdot teff_c \qquad f_{cfc} = 0.19 \cdot \%$$

We will need to replace the effective BSE yield of the sample/module/faceplate with an effective SE yield δ_{face}

,

where the SE yield are defined by 80% of their maxima (an average value). Data from CRC [Lide 1990].

$\delta_{aquadag} := (1)\cdot 80\cdot\%$

$\delta_{CU} := (1.3)\cdot 80\cdot\%$

Effective SE yield of module/faceplate:

$$\delta_{face} := \delta_{aquadag}\cdot\left(\frac{area_{fpc} - area_{fph}}{area_{fpc}}\right) + \delta_{CU}\cdot\left(\frac{area_{module}}{area_{fpc}}\right)$$

$\delta_{face} = 0.81$

As with the effective BSE yield of the faceplate/module area, the assumption is the BSE scatter diffusely and are therefore distributed across the area uniformly. If the BSE scatter spectrally, the effective SE yield would be dominated by the copper module. Estimating the uncertainty between the two assumption can be done by simply using the SE yield of copper.

The fraction of the BSE yield from the face that gets counted as SE yield during the collection mode.

$$fSE_{face} := \left[\begin{array}{l}\eta_{304SS}\cdot\left[pBSE_{ig} + \left[\left(p_{bg} + fBSE_{tr}\right)\cdot tBSE_{ig}\right]\cdot\left(1 - p_{big}\right)\right] \cdots \\ + fBSE_{c}\cdot t_{bg}\cdot t_{ig}\end{array}\right]\cdot\delta_{face}\cdot teff_{c}$$

$fSE_{face} = 4.48\cdot\%$

The next two source terms are more complicated:

fSE_{ig} fraction of BSE scatter that hit the inner grid and creating SE that reach collector.

fSE_{bg} fraction of BSE scatter that hit the bias grid and creating SE that reach collector.

The complication arises from estimating what portion of the SE produced on the grids is due to BSE yield from the sample or due to subsequent scatter, then determining whether those two populations of SE actually return to the collector.

ASSUMPTIONS:

1. We know the SE created on the grids by BSE straight from the sample scatter mostly in a forward direction (see SEM pictures of a grid [Creekside SAM manual]); however, the cosine distribution of SE emission angles is not as tight as the BSE distribution, so the assumption that NONE of these SE reach the collector is definitely an underestimate of these correction terms. Having said that, we have no easy way of estimating this error, so we make the later assumption for simplicity alone.

2. In contrast, we assume that ALL the SE's created on the grids due to BSE that hit the backside of the grids (facing collector) are directed towards the collector in the same fashion as SE that were originally created on the sample.

With these assumptions, we only have to worry about BSE to the backside of the inner grid. Remember the correction due to SE created on the backside of the bias grid returning to the collector was counted in the BSE correction. To find the BSE current to the backside of the inner grid, return to terms for 2xBSE scatter from the previous analysis:

f_{bgigc} Scatter off the bias grid, then the inner grid and back to the collector:

$$f_{bgigc} := \left[\left[\eta_{304SS}\cdot\left(p_{bg} + fBSE_{tr}\right)\cdot tBSE_{ig}\right]\cdot\left(\eta_{304SS}\cdot p_{big}\right)\right]\cdot\left[1 - \left(p_{bg} + fBSE_{tr}\right)\right]$$

$$f_{bgigc} = 0.27\cdot\%$$

f_{cigc} Scatter off collector, then inner grid, back to collector

$$f_{cigc} := \left[\eta_{304SS}\cdot\left[\left(fBSE_{c}\right)\cdot\left(1 - p_{bbg}\right)\right]\cdot p_{big}\right]\cdot t_{bg}$$

$$f_{cigc} = 0.19\cdot\%$$

Adding the two source together and using the average SE yield for 304SS, we have:

$$fSE_{ig} := \left[\left[\left[\eta_{304SS}\cdot\left(p_{bg} + fBSE_{tr}\right)\cdot tBSE_{ig}\right] + \left[\left(fBSE_{c}\right)\cdot\left(1 - p_{bbg}\right)\right]\right]\cdot\left(\delta_{304SS}\cdot p_{big}\right)\right]\cdot\left(t_{bg}\right)$$

$$fSE_{ig} = 1.96\cdot\%$$

The fraction of the BSE yield that gets counted as SE yield during the collection mode:

$$fSE_{source} := fSE_{face} + fSE_{ig}$$

$$fSE_{source} = 6.44\cdot\%$$

Returning to the original goal:

$$I_c(-50\cdot V) - I_c(0\cdot V) = I_b\cdot\delta_s - ISE_{loss} + ISE_{source}$$

where ISE_{loss} SE produced on the sample that never reach the collector

ISE_{source} SE that reach the collector that are not produced by the original beam.

Again, the source and loss terms are fractions of two different currents. Substitution yields,

$$I_c(0\cdot V) - I_c(-50\cdot V) = I_b\cdot\delta_s - I_b\cdot\delta_s\cdot fSE_{loss} + I_b\cdot\eta_s\cdot fSE_{source}$$

$$\frac{I_c(0\cdot V) - I_c(-50\cdot V)}{I_b} = \delta_s - \delta_s\cdot fSE_{loss} + \eta_s\cdot fSE_{source}$$

Corrected SE yield $$\delta_s = \left(\frac{I_c(0\cdot V) - I_c(-50\cdot V)}{I_b} - \eta_s\cdot fSE_{source}\right)\cdot\frac{1}{\left(1 - fSE_{loss}\right)}$$

where $$\frac{1}{1 - fSE_{loss}} = 147.2\cdot\%$$

and $$fSE_{source} = 6.44\cdot\%$$

Bias Grid current

To verify our theory, we extend the previous results and try to predict the current that will be registered on the bias grid during the suppression mode. The bias grid current during suppression mode is a tractable problem because only the BSE are assumed to be able to reach the bias grid and all of the SE produced there are rejected.

Current measured on bias grid during "suppression" mode: $I_{bg}(-50\cdot V)=I_b\cdot\eta_s\cdot\left[f_{bgsource}\cdot\left(1-\sigma_{304SS}\right)\right]$

where

$f_{bgsource} := \left(p_{bg}+fBSE_{tr}\right)\cdot tBSE_{ig}+fBSE_c\cdot p_{bbg}$ Fraction of BSE currents hitting the bias grid

and $\left(p_{bg}+fBSE_{tr}\right)\cdot tBSE_{ig}$ Opacity of bias grid and tantalum ring, down by transmission through the inner grid.

$fBSE_c\cdot p_{bbg}$ BSE scatter off collector that hits the back of bias grid.

There are other terms in $f_{bgsource}$; however, they are higher order terms and are assumed to add little.

Since the detector geometry and surface materials are fixed, we will want to calculate the ratio of the currents measured on the collector and bias grid wires. Notice:

Current measured on bias grid $I_{bg}(-50\cdot V)=I_b\cdot\eta_s\cdot\left[f_{bgsource}\cdot\left(1-\sigma_{304SS}\right)\right]$

Current measured on collector $I_c(-50\cdot V)=I_b\cdot\eta_s\cdot\left(1-fBSE_{loss}+fBSE_{source}\right)$

$$\frac{I_{bg}(-50\cdot V)}{I_c(-50\cdot V)}=\frac{f_{bgsource}\cdot\left[1-\left(\delta_{304SS}+\eta_{304SS}\right)\right]}{1-fBSE_{loss}+fBSE_{source}}$$

$$\frac{f_{bgsource}\cdot\left[1-\left(\delta_{304SS}+\eta_{304SS}\right)\right]}{1-fBSE_{loss}+fBSE_{source}}=-4.8\cdot\%$$

The difference in sign is due to SE leaving the bias grids (greater than unity) and not returning.

NOTE: Recall that δ_{304SS} is 80% of the SE yield maximum and η_{304SS} is an average from iron data. The above result should be seen when using a low energy incident beam (~300 eV).

Analysis of the ratio of the grid to collector currents from the experimental data reveals a curve that has the appearance of a total yield curve, which is expected. Unfortunately, the measured ratio is nearly 15% at 300 eV and reaches a maximum of 20% at energies near 900 eV. There is no reasonable source of error that could account for the factor of four discrepancy between the theoretical prediction and the experimental data.

APPENDIX D: LABVIEW VIRTUAL INSTRUMENT PROGRAM

The details of the LabView virtual instrument (VI) program used for measuring the total, SE, and BSE yields are discussed in detail. The actual file discussed here (Conrad Yield with FC and Total 2.VI) is quite similar to the program used to acquire the data for this dissertation. The main difference is the current summation method of measuring the beam current was used in this dissertation and the Faraday cup method was avoided (see Subsection 4.A.1). The VI discussed here uses the Faraday cup method, but also displays the sum of the currents within the HGRFA for reference. Other differences will be noted during the explanation. The figures in this Appendix show the front panel and each frame of the program, which will be discussed in turn.

Figure D.1 shows the front panel of the program with all the controls for the input of values and the indicators that show data values to the user. There are also charts for the monitoring of some currents in real time. Brief descriptions of each step required of the user are given in boxes along the left side of the VI front panel, beginning with “Step #1" in the upper left corner. After assigning an appropriate filename to the data set, step 1b is to enable the necessary channels and to set the range of the signal input to the data acquisition board. Enabled channels are those ready to accept data, while disabled channels are skipped. The channel information and controls are in the “DaqBoard 200A Setup” box to the right of the Step #1 box.

Step 1c is to calibrate the meters, which depends on whether the meter

calibration button is pressed. The two options are true (yes) or false (no) and are shown in Fig. D.2. The false case uses standard offset values for each channel recorded while there was no input to the channels. The true case allows for each channel to be sampled, displayed on the front panel, and those values used as the meter offsets for the rest of the data acquisition procedure. The exact method in which each channel is sampled will discussed along with Figs. F.3 and F.7. The true case

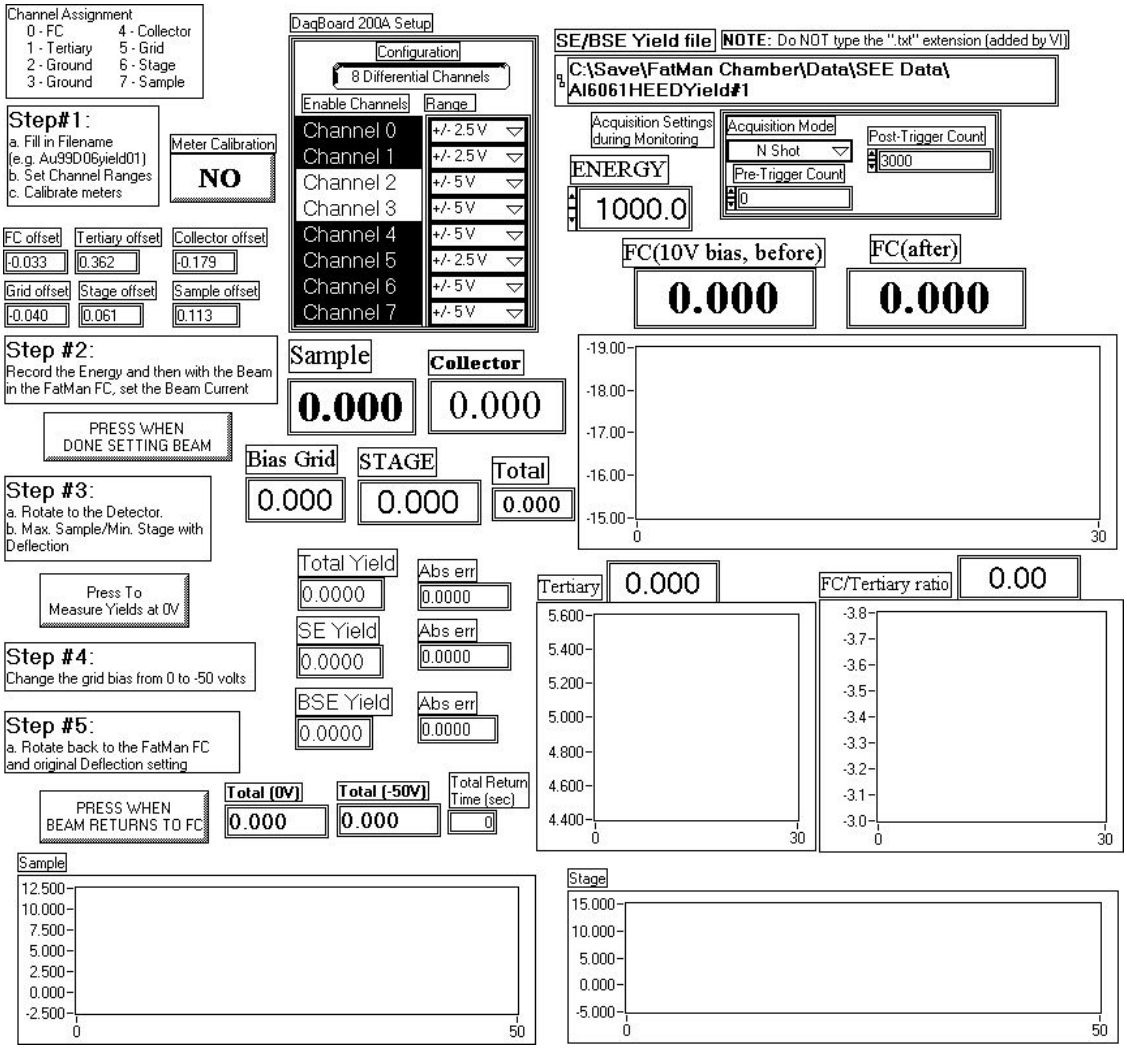


FIG. D.1: Front panel of the LabView VI that measures the total, SE, and BSE yields using the Conrad electron gun.

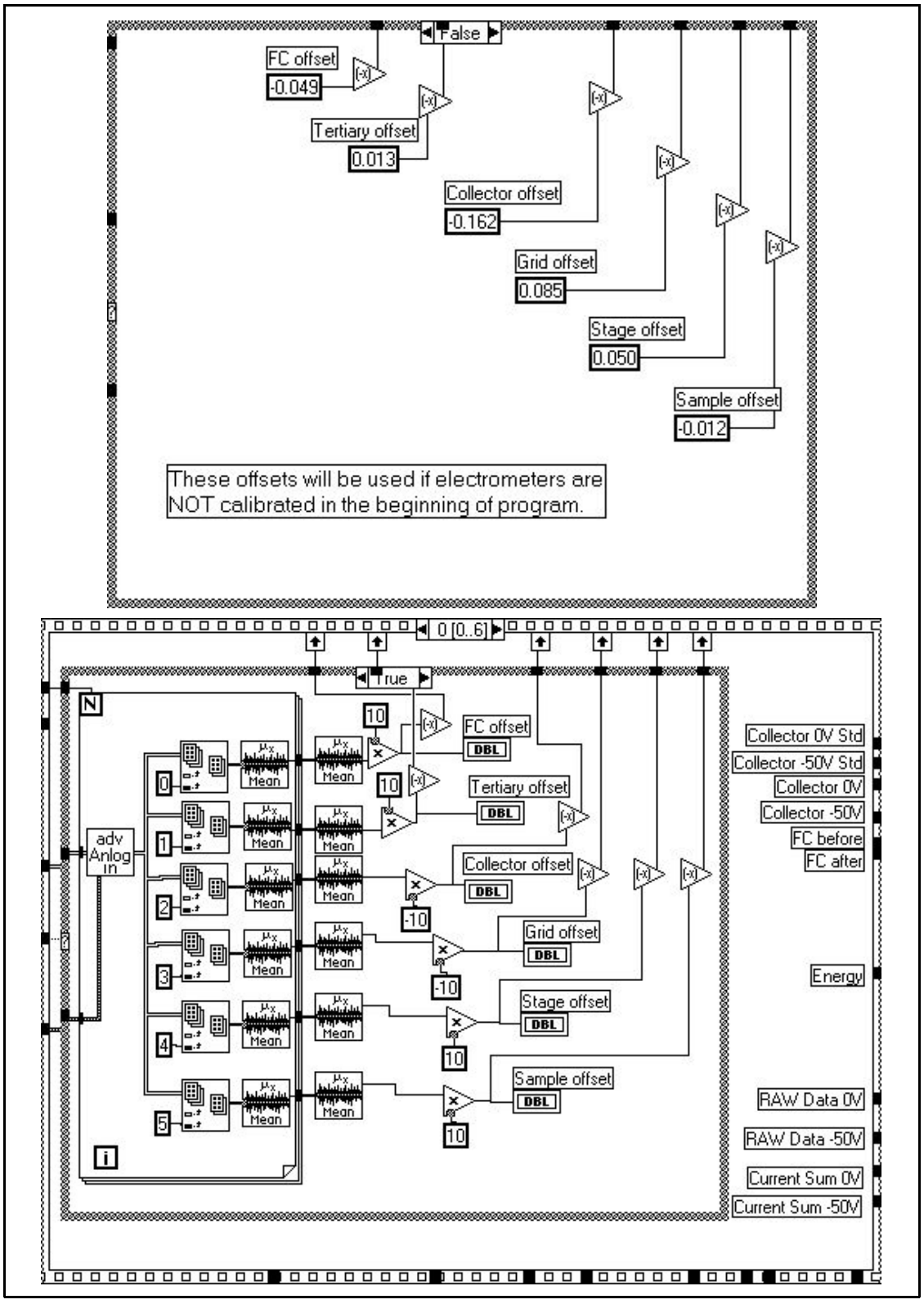


FIG. D.2: False and true cases of the meter calibration button. Part of step 1c.

allows for the compensation of any background currents appearing at the time of the measurement. Typical offsets for each channel are shown below the Step #1 box.

Returning to the front panel in Fig. D.1, step 2 involves recording the electron beam energy and monitoring the beam current while adjustments are made, then recording the beam current. Recall that this VI uses the Faraday cup to determine the beam current instead of a sum of the currents inside the HGRFA, although the current summation is later displayed in the "total" indicator for reference. With the Faraday cup method, the beam current is measured before and after the yield measurements are made, then an average of the two beam currents is taken to be the best estimate of the beam current while the yield measurements were being measured (see Subsection 4.A.1 for details). While the beam current is being adjusted, the Faraday cup current is displayed in the indicator marked "FC(10V bias, before)" and on the graph just below that indicator. The beam energy is recorded by hand in the control box just above the Faraday cup indicator. The slightly modified version of this LabView VI for taking data with the HEED gun actually measures the electron beam energy from the calibrated 0-5 volt output of the high voltage meter on HEED gun power supply.

Figure D.3 diagrams in detail the monitoring of the Faraday cup current during the setting of the beam current. The sampling of the enabled channels can now be discussed in more detail. Beginning from the left-hand side of Fig. D.3, all the enabled channels are sampled by a subVI labeled "adv Anlog in" that refers to the file "SubVI Main Unit Adv Analog Input.VI", which is taken directly from the advanced analog

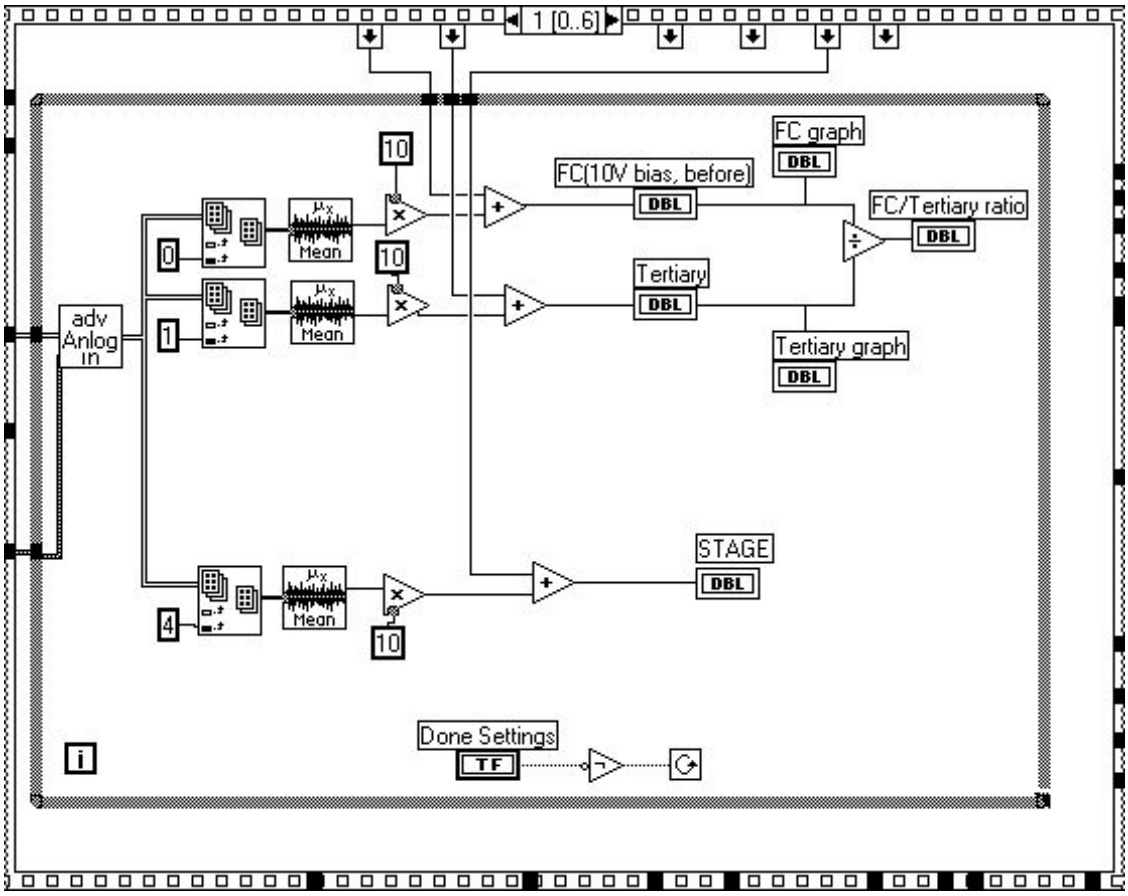


FIG. D.3: Monitoring the Faraday cup current before the yield measurements. First part of step 2.

input VI provided by Iotech that has been changed only by using specific default values and making the VI usable as a subVI. The output of the advanced analog input subVI is a matrix of all the points sampled from all the enabled channels. As seen in the upper right corner of Fig. D.1, the box labeled “acquisition setting during monitoring” controls the total number of points sampled during this and any subsequent monitoring processes. The term “N-shot” refers to a one time sampling of N points, while the pre- and post-trigger count control the number of points sampled

before and after the data acquisition board begins recording data. In Fig. D.3, the matrix from the subVI is parsed into the 0^{th}, 1^{st} and 4^{th} enabled channels that correspond to the Faraday cup, the tertiary aperture, and the stage current, respectively. A mean of the sampled points is calculated and then a slope and offset are used to convert the values into nanoamperes. The values are displayed by the "FC (10 volt bias, before)", "Tertiary", and "Stage" indicators on the front panel in Figure D.1. The step diagramed in Fig. D.3 goes further to graph the Faraday cup and tertiary currents, as well as their ratio. The graphs can be seen on the front panel in Fig. D.1. The purpose of graphing the ratio of the Faraday cup current to the tertiary current is the value gives some indication of how collimated the beam is upon entering the Faraday cup. The larger the Faraday cup/tertiary ratio, the larger the fraction of the total beam current being collected by the Faraday cup. The routine shown in Figure D.3 continuously monitors these currents until the "press when done setting beam" button in Fig. D.1 is pressed.

The second routine of step 2, diagramed in Fig. D.4, records the beam current as measured in the Faraday cup for later use in the calculating the average beam current. The routine also outputs a matrix of the Faraday cup, tertiary and stage currents as well as the time at which these currents were taken. The matrix and time becomes one of the entries in a file whose name is created by appending "TIME" to the filename for the data set entered in step 1a. The "TIME" file is created so the time dependent behavior of the beam current can be later analyzed if necessary.

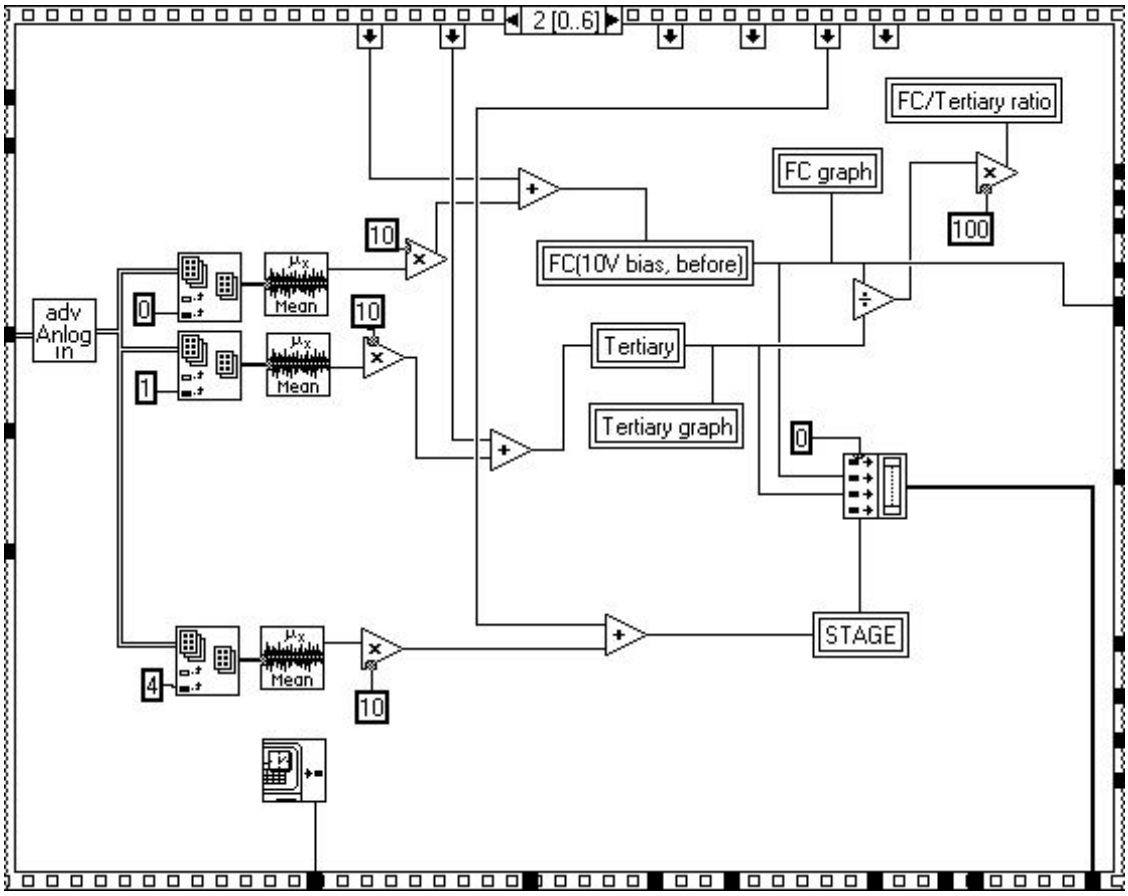


FIG. D.4: Recording the Faraday cup current. Second part of step 2.

Step 3 on the front panel involves monitoring currents within the HGRFA while the detector and sample are being positioned in front of the beam. The routine of the VI is shown in Fig. D.5 and essentially follows the same methodology as the routine diagramed in Fig. D.3. The collector, suppression grid, stage and sample currents are all monitored and the sum of these currents is computed. The sum of these HGRFA currents has been shown to be closely related to the beam current. All five currents are shown on indicators with the same names, and the sample and stage currents are graphed separately. Notice in Fig. D.5 that the collector current is

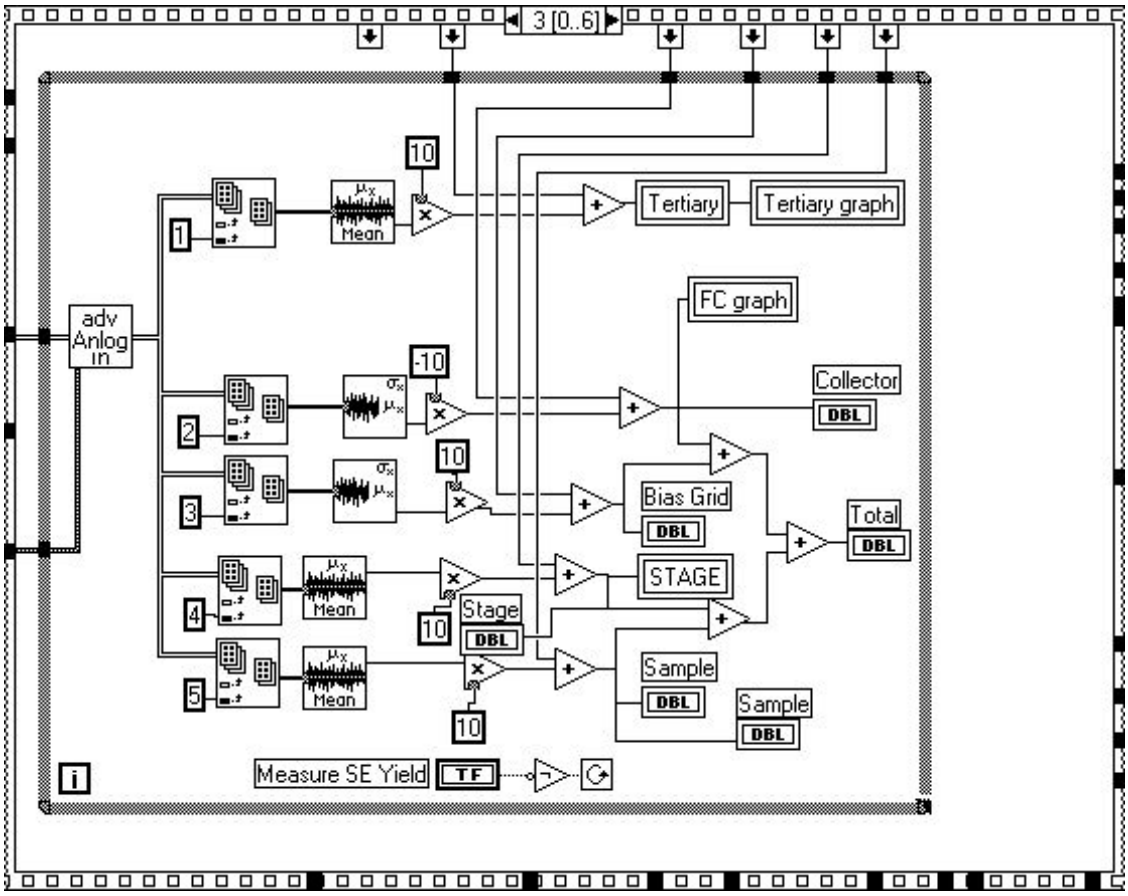


FIG. D.5: Monitoring the collector and sample currents to position the beam. First part of step 3.

displayed on the graph where the Faraday cup current had been previously displayed. These currents are monitored continuously while the sample current is maximized by the user using the electron gun beam deflection in an effort to position the beam directly down the beam pipe. After the beam has been positioned successfully, the "press to measure yields at 0V" button on the front panel is pressed and the routine ends.

Step 4 is comprised of five routines that measure the collector current during

the collection and suppression modes (see Subsection 4.A.1 for details). The first routine is shown in Fig. D.6 and is a simple action of setting the variable voltage power supply to zero volts bias on the suppression grid, which is the collection mode. The routine waits for 5 seconds to allow the fields within the detector to stabilize and the electrometers to react.

The next routine of step 4 is shown in Figure D.7 and measures the currents within the HGRFA during the collection mode. The sampling and measurements in this routine differs from the monitoring of channels previously described. Instead of a single mean of a large number of points, this routine calculates the average and

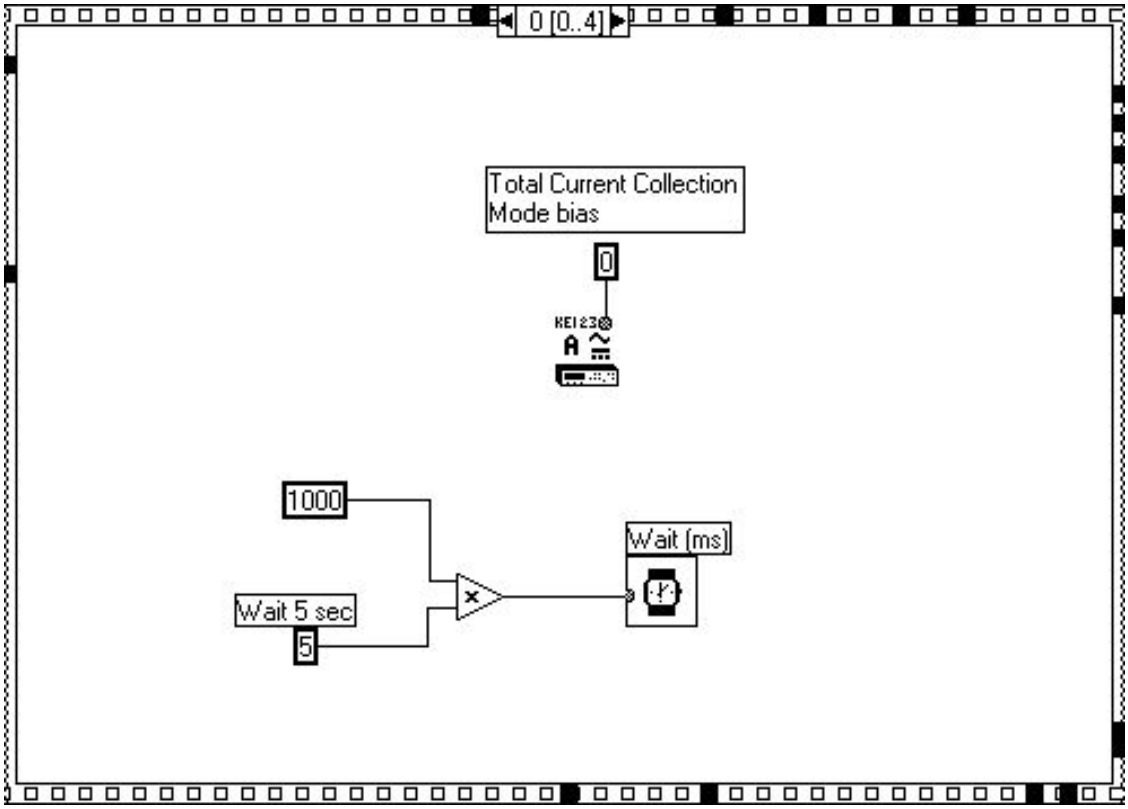


FIG. D.6: Setting the suppression grid voltage bias to 0 volts. First part of step 4.

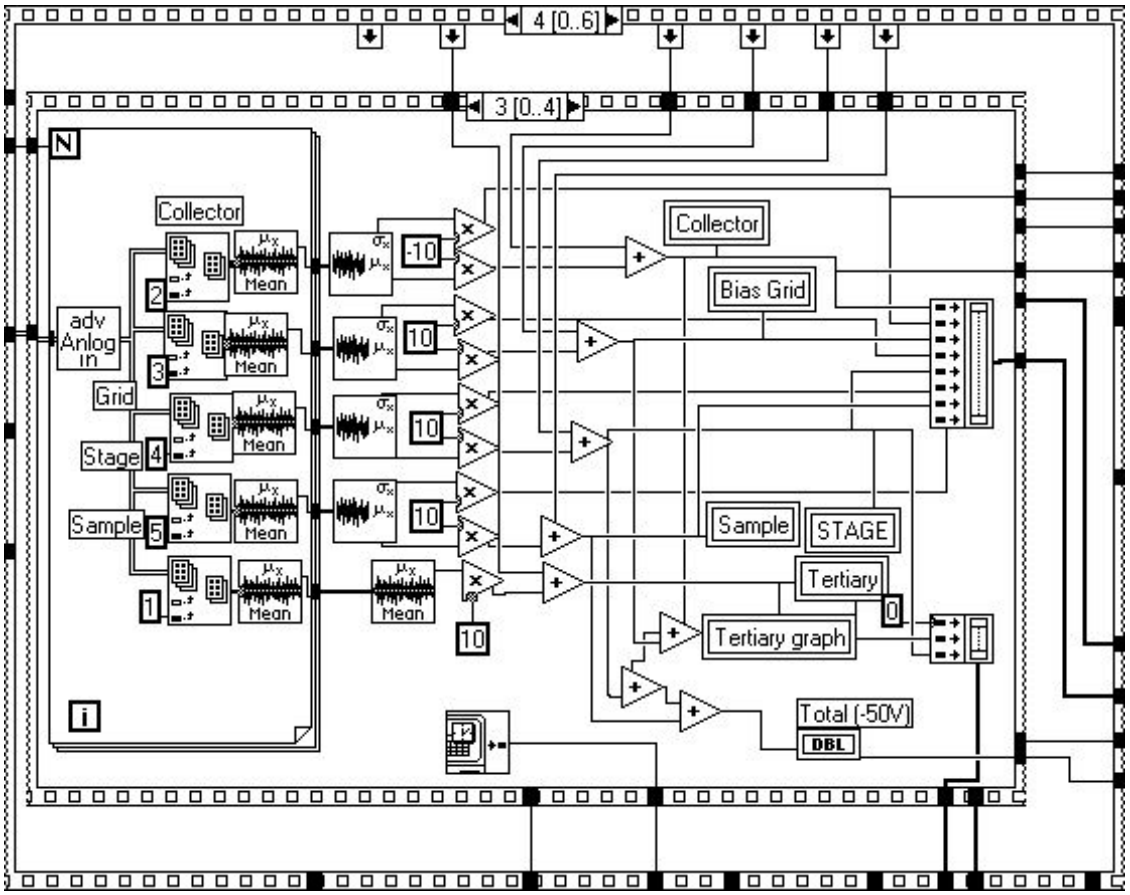


FIG. D.7: Measurement of the collector and other currents during the collection mode. This is the second routine in step 4.

standard deviation of N number of means consisting of 10,000 points. The number of means N sampled is a numerical control within the VI not shown on the front panel. The sampling of 10,000 points is the default value of the advanced analog input subVI and is also not controllable from the front panel. The data taken for this dissertation did not use this exact procedure, but only sampled 10,000 points and computed one mean value and its standard deviation. The recommended procedure in the future would be to take 20 means of 3,000 points each as a balance between sampling and

total collection time. Notice the standard deviations are shown as μ_x instead of σ_x. Calculating the standard deviation of the mean, by dividing μ_x by the square root of N, would be an improvement to this VI because the standard deviation is an overestimate of the random error by a factor of $1/\sqrt{N}$. The collector and its standard deviation leave the routine to be used in the calculation of the total and SE yield. Additionally, there are two matrices recorded. One is another entry to the "TIME" data that includes the tertiary and stage current along with the time. The other matrix is the collector, suppresion grid, stage, and sample currents along with their error, which makes up the "dataset filename"RAW0 file that refers to the raw data taken during the 0 volts of bias on the suppression grid.

There are three other routines to step 4 that are not shown in figures. The third routine involves setting the suppression grid voltage to - 50 volts and is similar to Fig. D.6. The fourth routine involves measuring the same currents as are shown in Fig. D.7. The output of the raw data from the fourth routine is to the "dataset filename"RAW50 file in reference to the raw data taken while the suppression grid was bias to -50 volts. The fifth routine returns the suppression grid to 0 volts bias and is identical to Fig. D.6.

Step 5 on the front panel in Fig. D.1 involves monitoring the Faraday cup, tertiary and stage currents while rotating the stage so the Faraday cup properly intercepts the beam. The two routines are not shown because they are identical to the routines shown in Fig. D.3 and F.4 of step 2. The only difference is the Faraday cup

current is now displayed in the “FC (after)” indicator. With the recording of the Faraday cup current after the yield measurements, the routines are complete and the data analysis and file writing commences.

An overview of the data manipulation and file writing procedures are shown in Fig. D.8. There are five files written to the directory specified in the upper right corner of the front panel. The main file contains the total, SE, and BSE yields along with their estimated uncertainties (standard deviations) and the electron beam energy at which the yields were measured. One row of the file is appended to the filename each time the program is run at a different energy. The other four output files add a short suffix to the main filename and the “TIME”, “RAW0", and “RAW50" files have been discussed previously. The only suffix that was not discussed is the “FC” file, which contains the beam energy, the Faraday cup currents before and after the yield measurements, the mean and standard deviation of those two measurements, the sum of the currents inside the detector during collection and suppression mode, and their mean and standard deviation. The file is intended for the comparison of the two methods of measuring the beam current.

Focusing in on the upper right quadrant of Fig. D.8, the data analysis involved in producing the yield file is shown in Fig. D.9. The current measurements and matrices that are the output of all the routines are labeled on the left side of Fig. D.9. Following the lines, one can track how the total, SE and BSE yields are computed from the collector current measured during the collection and suppression modes and mean value

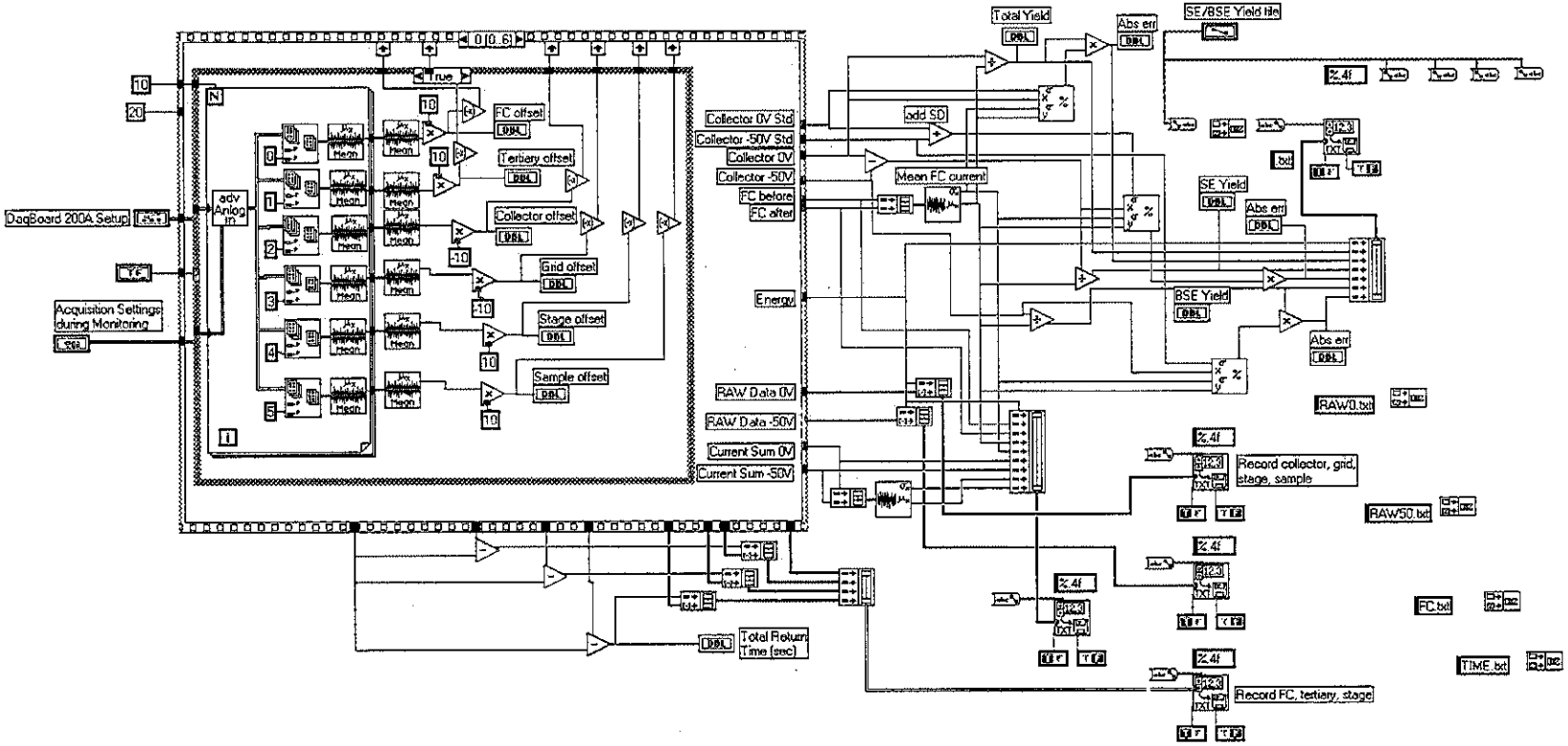


FIG. D.8: Data analysis and file writing procedures. The routine shown in the large box is an arbitrary step of the VI outline in previous Figures. The upper right-hand quadrant of this Figure contains the data analysis procedures and is expanded in Figure D.9.

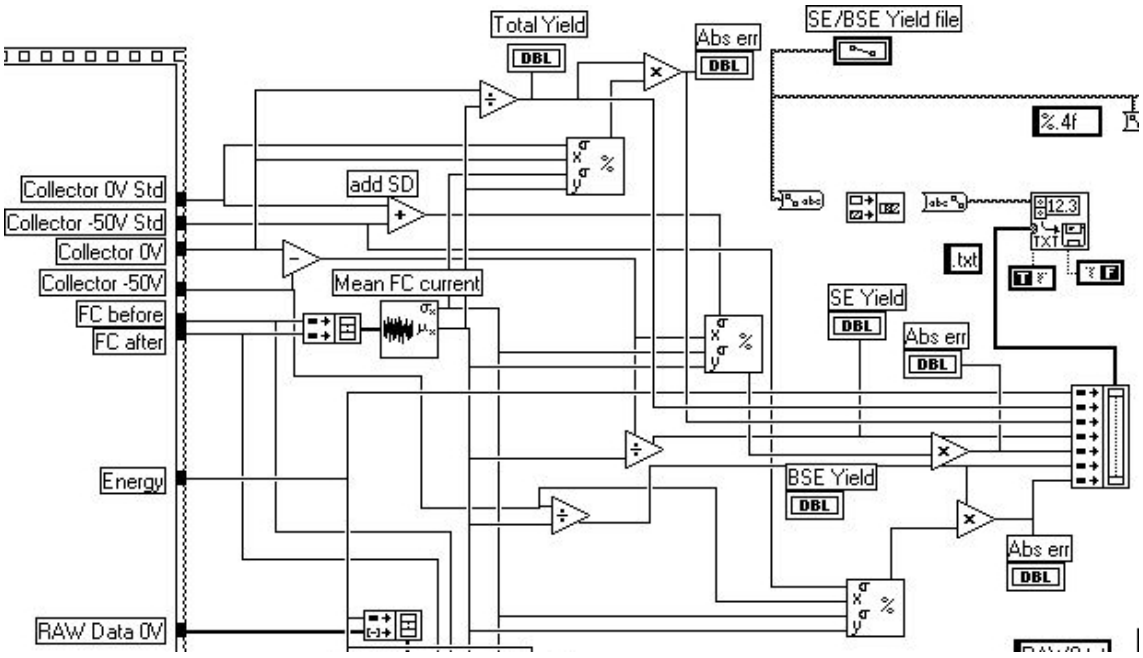


FIG. D.9: More detailed view of the upper right quadrant of Fig. D.8, showing the data analysis calculations to determine the total, SE, and BSE yields and the magnitude of their errors. The outputs of all the routines are labeled along the left side of the Figure.

of the Faraday cup current measured before and after the yield measurements. Refer to Subsection 4.1.A for the equations governing the total, SE and BSE yields. As mentioned, the beam current for this dissertation work was measured using the current summation method, rather than the Faraday cup method shown here. Since all the computed yields involve division of the beam current, the error analysis is similar.

The error analysis is propagated with the aid of a subVI (shown in Fig. D.9 as a box with an X, a Y, two σ, and a % sign) that takes an X and Y value along with their error and outputs the fractional error in a third value Z by summing the fractional X and Y errors in quadrature. The fractional error is then converted into an absolute error by multiplying by the appropriate value. The only exception in the error analysis is the SE

yield, which involves a difference of two currents and so the absolute errors are added before the error is propagated with the beam current error.

Again, the VI outlined above is not the same VI used to take the dissertation data, but is composed of all the essential elements and shows the two methods of determining the beam current as well. Changes that should be made to this VI are implement the current summation method of computing the beam current, changing the default number of samples to acquire in the advanced analog input to 20 samples of 3,000 points instead of one mean of 10,000 points, and computing the standard error in the 20 point mean instead of using the standard deviation of 10,000 points.

APPENDIX E: PERMISSIONS

AMERICAN INSTITUTE OF PHYSICS

Rights and Permissions Office

Suite 1NO1
2 Huntington Quadrangle
Melville, NY 11747-4502

Tel. 516-576-2268
Fax 516-576-2450

E-mail: rights@aip.org
http://www.aip.org

4 March 2002

Dr. Neal Nickles
Ball Aerospace &Technologies Corp
PO Box 1062
Boulder CO 80306-1062

Dear Dr. Nickles,

This is to further your request for permission to use material from American Institute of Physics publications.

Permission is hereby granted for one time reproduction – as per the requirements indicated below– of the following figures:

Figs. 1,2, Grais & Bastawros, "A study of secondary electron emission in insulators and semiconductors", *Journal of Applied Physics* 53(7), 1982, pp 5239-5242

Fig. 1, Cao & Conrad, "High *q*-resolution gun for low gun for low energy electron diffraction", *Review of Scientific Instruments* 60(8), 1989, pp 2642-2645

to be reproduced in your PhD dissertation to be published by Utah State University.

[X] 1. The following credit line must appear in all copies (please fill in the information indicated by CAPITAL LETTERS): Reprinted with permission from FULL CITATION. Copyright YEAR, American Institute of Physics.

[X] 2. NOTE: This permission does not apply to figures, tables or other materials credited to sources other than the copyright holder.

[X] 3. Obtain the Author's permission to use the material. The author's address can be obtained from the article.

[ ] 4. An invoice for permissions fee (net 30 days) of $0 will follow. Please make check payable to American Institute of Physics. Please note: Permission is not valid until payment is received.

Thank you for requesting permission to use materials copyrighted by American Institute of Physics. Please do not hesitate to contact us should you have any further questions.

Sincerely,

Ann C. Perlman

Member Societies:
The American Physical Society
Optical Society of America
Acoustical Society of America
The Society of Rheology
American Association of Physics Teachers
American Crystallographic Association
American Astronomical Society
American Association of Physicists in Medicine
American Vacuum Society
American Geophysical Union
Other Member Organizations:
Sigma Pi Sigma Physics Honor Society
Society of Physics Students
Corporate Associates

recycled paper

NATIONAL RESEARCH CENTRE
A.R. OF EGYPT

Cable : Research Cairo
Phone : 3371433
Fax : 3370931

Sh. El- Tahrir
Dokki - Cairo.

To
Dr. Neal Nickles

I hereby give you permission to reproduce the following figures in your PhD disserlation , published by Utah State University : Figure 1 and a portion of Figure 2 from Grais , Khairi I. and A.M. Bastawros ,1982, "A Study of Secondary Electron Emission in Insulators and Semiconductors , " J. Appl. Phys.53(7),5239-5242.

Sincerely,

Prof. Dr.Khairi I.Grais

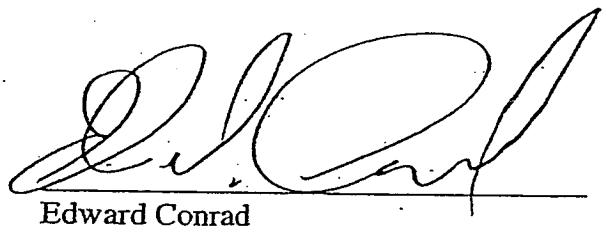
4 May, 2002

Neal Nickles,

I hereby give you permission to reproduce the following figure in your PhD dissertation, published by Utah State University:

Figure 1 from Cao, Yijian and Edward H. Conrad, 1989, "High q-resolution gun for low energy electron diffraction," Rev. Sci. Instrum. **60** (8), 2642-2645.

Sincerely,



Edward Conrad

CURRICULUM VITAE

Neal Nickles

Education:

Ph.D., Surface Physics, Utah State University 2002
Fellow, Rocky Mountain NASA Space Grant Consortium 1997-2001
Advisor: J.R. Dennison
B.A., Physics, The Colorado College 1993
Dean's list 1993

Experience:

Radiation Effects Physicist, *Ball Aerospace & Technologies Corp.*	2001-present
Research Fellowship, *Utah State University*	1997-2001
Technical Writer and Instructor, *Utah State University*	1995-1997
Teaching and Lab Assistant, *Utah State University*	1994-1995

Publications

Neal Nickles, R.E. Davies and J.R. Dennison, "Applications of Secondary Electron Energy- and Angular-Distributions to Spacecraft Charging," *Proceedings of the 6th Spacecraft Charging Technology Conference*, (Air Force Research Laboratory Science Center, Hanscom Air Force Base, MA, 1999).

Neal Nickles, J.R. Dennison, D. Mark Riffe and Beth Porter, 1998, "*Problem Solving Tutorial*," part of *Study Works 3.0* software package (Mathsoft, Cambridge, MA, 1998).

Neal Nickles, J.R. Dennison, D. Mark Riffe and Beth Porter, 1998, "*Advanced Problem Solving Tutorial*," part of *Mathcad 8.0 Profesional* software package (Mathsoft, Cambridge, MA, 1998).

R.E. Davies, Neal Nickles and J.R. Dennison, "Evolution of Secondary Electron Emission Characteristics of Spacecraft Surfaces: Importance to Spacecraft Charging," *Proceedings of the 6th Spacecraft Charging Technology Conference*, (Air Force Research Laboratory Science Center, Hanscom Air Force Base, MA, 1999).

W.Y. Chang, J.R. Dennison, Neal Nickles and R.E. Davies, "Utah State University

Ground-based Test Facility for Study of Electronic Properties of Spacecraft Materials," *Proceedings of the 6th Spacecraft Charging Technology Conference*, (Air Force Research Laboratory Science Center, Hanscom Air Force Base, MA, 1999).

Presentations

Neal Nickles, W.-Y. Chang, J.R. Dennison, "Hemispherical Grid Retarding Field Analyzer for Absolute Measurement of Secondary and Back-scattered Electron Yields," Section K40.080, American Physical Society March Meeting, Seattle, WA, 2001.

Neal Nickles, "Secondary Electron Emission and Spacecraft Charging", Rocky Mountain NASA Space Grant Consortium symposium, Salt Lake City, UT, 1998.

Neal Nickles, R.E. Davies and J.R. Dennison, "Sample Bias Influence on Angular-Resolved Secondary Electron Emission," American Physical Society Four Corners Sectional Meeting, Provo, UT, October 17, 1998.

Neal Nickles, R.E. Davies and J.R. Dennison, "Energy- and Angle-resolved Secondary Electron Cross Sections and Applications to Spacecraft Charging," 6th Spacecraft Charging Technology Conference, Air Force Research Laboratory Science Center, Hanscom Air Force Base, MA, November 3, 1998.

R.E. Davies, Neal Nickles and J.R. Dennison, "Effects of the Evolution of Spacecraft Surfaces on Secondary Electron Emission and Spacecraft Charging," 6th Spacecraft Charging Technology Conference, Air Force Research Laboratory Science Center, Hanscom Air Force Base, MA, November 3, 1998.

W.Y. Chang, N. Nickles, R.E. Davies and J.R. Dennison, "Instrumentation for Precise Energy- and Angle -Resolved Secondary Electron Emission Measurements," *Bull. Am. Phys. Soc.* **44**(1) Part I, 739 (1999). American Physical Society Four Centennial Meeting, Atlanta , GA, March 22, 1999.

J.R. Dennison, D.M. Riffe and Neal Nickles, "Using Computer-assisted Mathematics to Enhance Structured Problem-solving Techniques in Physics," Idaho-Utah Sectional Meeting of American Association of Physics Teachers, Logan, UT, April 5, 1999.

W.Y. Chang, J.R. Dennison, Neal Nickles and R.E. Davies, "Utah State University Ground-based Test Facility for Study of Electronic Properties of Spacecraft Materials," 6th Spacecraft Charging Technology Conference, Air Force Research Laboratory Science Center, Hanscom Air Force Base, MA, November 3, 1998.